



Inhibition locale par des molécules organiques de la corrosion intergranulaire précoce du cuivre et effets sur la passivation des joints de grains

Sagar Sharma

► To cite this version:

Sagar Sharma. Inhibition locale par des molécules organiques de la corrosion intergranulaire précoce du cuivre et effets sur la passivation des joints de grains. Chimie analytique. Université Paris sciences et lettres, 2021. Français. NNT : 2021UPSLC026 . tel-03956302

HAL Id: tel-03956302

<https://pastel.hal.science/tel-03956302>

Submitted on 25 Jan 2023

HAL is a multi-disciplinary open access archive for the deposit and dissemination of scientific research documents, whether they are published or not. The documents may come from teaching and research institutions in France or abroad, or from public or private research centers.

L'archive ouverte pluridisciplinaire **HAL**, est destinée au dépôt et à la diffusion de documents scientifiques de niveau recherche, publiés ou non, émanant des établissements d'enseignement et de recherche français ou étrangers, des laboratoires publics ou privés.



THÈSE DE DOCTORAT
DE L'UNIVERSITÉ PSL

Préparée à Chimie ParisTech

**Local inhibition by organic molecules of early stage
intergranular corrosion of copper and effects on
passivation of grain boundaries**

Soutenue par

Sagar Beena SHARMA

Le 07 mai 2021

Ecole doctorale n° 388

**Chimie physique et chimie
analytique de Paris centre**

Spécialité

Physico-chimie



Composition du jury :

Christine BLANC

Professeure, ENSIACET, Toulouse INP

Présidente

Frank RENNER

Professeur, Hasselt University

Rapporteur

Vincent VIGNAL

Directeur de Recherche, CNRS,
Institut Carnot de Bourgogne

Rapporteur

Ingrid MILOSEV

Professeure, Jožef Stefan Institute

Examinatrice

Cécilie DUHAMEL

Enseignante Chercheure, Mines ParisTech

Examinatrice

Vincent MAURICE

Directeur de Recherche, CNRS,
Chimie ParisTech

Co-encadrant de thèse

Philippe MARCUS

Directeur de Recherche, CNRS,
Chimie ParisTech

Directeur de thèse

"Flectere si nequeo superos, Acheronta movebo"

Acknowledgements

This is going to be a long section as I cannot help but reminisce about my past and of all the incredible people who have helped me reach this milestone. It is written earnestly. I am well aware that this is an academic thesis and I must be formal and professional. But acknowledgments and gratitude come from the heart and the language of the heart is poetry and love. So kindly pardon my way of letting my heart write this section while my logical mind will work on the remainder of the thesis. I will try my best to try to convey the deepest gratitude I hold for so many people who are behind my success.

I would like to start by thanking the two reviewers Dr. Frank RENNER and Dr. Vincent VIGNAL for reading, evaluating and correcting my thesis. Similarly, I am grateful to the other esteemed members of my jury Dr. Christine BLANC, Dr. Ingrid MILOSEV, and Dr. Cécilie DUHAMEL who has graciously agreed to examine my defense. I appreciate all of their acceptance especially during this unprecedented time of the global pandemic.

Amongst those who were directly involved throughout my Ph.D. journey, First and foremost I must say my sincerest thank to my two supervisors Professor Phillipe MARCUS and Professor Vincent MAURICE. The Sanskrit word 'Guru' has been watered down these days. It means 'Dispeller of Darkness' and I cannot find a better word for these two than Guru. I met them in unfortunate circumstances where suddenly it felt all is lost and my academic career is over. They believed in me by selecting me for this prestigious position and the rest as they say is history.

Professor MARCUS, every day was a dream come true as I was working under the guidance of a world-renowned scientist. These last years, you stood by like a rock properly guiding me. You never lost optimism even after my initial persistent failures. You are the kindest supervisor one can ask for. Your support and your words of wisdom helped me to improve myself in every way possible. Even if I never amount to much in life, I will still be proud of the fact that I have worked under the supervision of the Phenomenal Professor Marcus.

Now, my dearest co-supervisor and one of my favorite people in this world, Professor Vincent MAURICE, a true genius in every shape and form. His knowledge is so profound that I often find myself drowning in his ocean of wisdom that he possessed. I won't lie, I am a bit scared of you, not because you are scary, far from it you are incredibly kind, but I am scared of you because I hold you in such high regard that I am afraid of making a fool of myself in front of you. Sadly, most of the time I was slipped and was the silly one in the room but it is your greatness that you never once made me feel embarrassed and took everything with your witty sense of humor. You have shown me the researcher I would like to be. You are a school of patience and your attention to detail is unmatched. I can just say my kind Sir, thank you so much for everything.

I am lost for words to convey my gratitude to the colorful and charming Dr. Lorena Klein. She is the engineer in charge of the EC-STM setup. She was supposed to train and supervise me for my experiments but she ended up being much much more to me. She is a supervisor, friend, and mother to me. Dr. Klein is a master of in situ EC-STM and I was lucky to be trained by the best in the world. Not only you guided me to establish the proper procedure for these tricky experiments but you gave me a point of view to solve all the problems I faced during my measurements. Without the scientific perception that you have graciously bestowed upon me, I would still be struggling without any results. Your contribution to my thesis cannot be measured. Apart from my professional life, you help me develop my personal style, introduced me to western cultures, took me operas concert. You were kind enough to lend me a shoulder to cry on during my moments of deepest despair (in this case literally), you improved my social life, made sure I learn french, and oh so many more things! I cannot forget to mention that you made me delicious food and made sure that I was eating well. You have made such an impression on me that a mere glimpse of your silhouette is enough for me to calm down and feel that everything is going to be alright. I just cannot put to words what you mean to me Lorena, I can just say that you aren't like my mother but you are my mother, and I the utmost love and respect for you.

I cannot even if I tried, could have found a better team to work with. I like to thank my entire PCS team for their contribution to my research. Each and every one of you, are absolute legends.

A special thanks to my master supervisors Professor Sylvain FRANGER, Dr. Loïc ASSAUD, and Dr. Alireza RANJBARI who have held my hands and supervised my first steps into life as a researcher. Dr. Eric de Vito from CEA was instrumental in helping me find and secure this wonderful Ph.D. for which I am truly grateful to him. As I am going back in time I cannot overlook my roots and the momentous contribution of Dr. BKN Singh from Jai Hind College as they made me the person I am today.

Now, the remarkable Dr. Pedro ALMEIDA DE OLIVEIRA, my professor during my master's who just taught me for a handful of lectures but ended up being an integral part of my life. After my accident and injury, I lost all hope and was ready to go back to India where you came to shine a light in my darkest moments. You will always be my mentor and guru. As a thorough gentleman, you have shown me what type of man I would like to be. You are my big brother and my idol and someone I can always count on.

Now, as I have covered my professional life I have to go through people who have paid immense contributions to my life and my wellbeing. Without whom I would not reach this day. I will choose to name a few people mostly because they are more likely to read this section and I don't want to make it awkward between us. If I don't expressly mention someone's name and if you are reading it there are chances that you are really close to my heart.

My dearest friends Simon, Ludo, Florent, and Dario. You have made these past three years so light and breezy. Some days all I needed to recover was to be in your presence. My younger brother Simon, although you were a late entry into my journey the moments spent with you discussing everything have been a blessing for me. You are a younger version of me and I hope you achieve more success than you can imagine. It's no coincidence that most of my friends are all working at the I2E group which is my other family. Sincere gratitude to the ever-supportive and delightful Professor Armelle RINGUEDÉ. Armelle, you have been instrumental support and a dearest friend. You did your best to make my life as smooth as possible. Defeating you in our online word game in French was 'THE' highlight of my life something which I will never ever let you forget as I have listed it as an achievement on my CV. Also from I2E, I would like to thank someone special to me, the wonderful Madame CHAVANNE.

Thank you Dr. Sophie Griveau for being such a cheerful friend. You are an assistant professor and just like your perfection defying eye art our friendship defies the academic hierarchy. I am grateful to my beautiful friend Adeline COLLIN. Her graceful presence made is what I ever needed if and when my experiment failed (as I work with ECSTM it must have happened Seventeen thousand times in the past three years). Her office is next to the water cooler and I must have drunk millions of litre of water so that I can discuss with her to overcome my everlasting frustrations. I am not complaining as my skin never looked better. I must also thank the generous Madame Melinda TOEN who once lent me a glue stick. I know it sounds trivial but we all are aware of Chaos theory and how trivial input leads to a vastly different output. Who knows, her glue is the essence that is holding my whole thesis together so I must thank her.

The romantic in me can't help but mention my future wife. I might not have met you yet but still, I would like to mention you. We haven't been introduced yet but you already owe me as I have immortalized you by mentioning your name in my thesis and you haven't. I guess that makes me the best (future husband ever). Also to my future kids, there is a big chance that your father has a Ph.D. (if I succeed) so you have a mountain to climb to overcome the shadow of your father, so listen to your mom, eat your dinner and go do your homework!

Thank you to my brother Suraj for all sacrifices you made to make sure that your younger brother can continue to study at your expense. You are truly a father figure. Other than your generosity and spiritual support, thank you for being a guide and sharing your infinite wisdom about computers. Although only my name will appear on the degree your name and spirit are also etched on the diploma.

And last, but not at all least I would like to thank my inspiration, my strength, and my muse, who is one of the greatest inventors to have ever lived, my Mom, who invented me. Everything I am or I can ever hope to be I owe it to my beautiful mother. I can reach this summit because you have a doctorate in motherhood. I am incredibly fortunate to be your son. You made sure I never lose my way during my quest to become a Doctor. Thank you for everything you did for me Maa, I love you the most.

- Sagar SHARMA

(Note: The author did not make any attempt at the world record for the most number of adjectives used in acknowledgement, or did he?)

Table of Contents

General Introduction	1
Chapter I: Literature review and State of the Art	5
1.1 Introduction to grain boundaries	5
1.1.1 Introduction.....	5
1.1.2 Geometric construction of grain boundaries.....	6
1.1.3 Crystallographic description of grain boundaries	6
A. Crystallographic disorientation of grain boundaries	6
B. Grain boundaries defined by the angle of disorientation.	7
C. Coincidence Site Lattice (CSL) grain boundaries	8
D. Special case of triple points	12
E. Inclination of the grain boundary plane	12
1.1.4 The grain boundaries networks	12
1.1.5 Energy of grain boundaries.....	13
1.1.6 Grain boundary engineering	14
1.2 Corrosion properties of copper.....	15
1.2.1. Metal corrosion and passivation	15
1.2.2. Copper corrosion and passivation.....	17
A. Potential-pH diagram of the Cu/H ₂ O system and copper passivation.....	17
B. Potential-pH diagram of the Cu/H ₂ O/Cl system and copper passivation in the presence of chlorides	21
C. Mechanisms of dissolution of copper in the presence of chlorides.....	23
D. Special case of single crystals	24
1.2.3. Influence of microstructure on copper corrosion phenomena	25
A. Influence of grain size	25
B. Influence of grain structure	25
C. Influence grain boundary type.....	26
D. Influence of grain boundary type for other metals than copper.....	27

1.3 Corrosion protection of copper and other metals by inhibitors	27
1.3.1. Anodic, cathodic and mixed inhibitors	27
1.3.2. Inorganic inhibitors	28
1.3.3. Organic inhibitors	28
A. 2-mercaptobenzothiazole (2-MBT)	29
B. 2-mercaptobenzimidazole (2-MBI)	31
1.3.4. DFT studies of 2-MBT and 2-MBI adsorption	32
References	34

Chapter II: Experimental Techniques, Instrumentation and Protocols43

2.1 Electrochemical study.....	43
2.1.1 Electrochemical cell.....	43
2.1.2 Electrochemical STM cell.....	44
2.1.3 Cleaning the cell.....	45
2.2 Scanning Tunneling microscopy (STM)	45
2.2.1. Experimental device and operating principle	45
2.2.2 Tunneling effect.....	47
2.2.3 Theoretical aspects.....	49
2.2.4 Electrochemical application in liquid medium (EC-STM)	50
2.2.5 EC-STM Apparatus used for this thesis.	51
2.3 Preparation of sample and EC-STM tips	51
2.3.1 Preparation of microcrystalline copper	51
2.3.2 Preparation of the copper surface.....	52
A. Mechanical polishing	53
B. Electrochemical polishing	53
2.3.3 Preparation of EC-STM tips.....	54
A. Local thinning of the wire	54
B. Cutting the tip	55
C. Isolation of the tip	56
2.4 Cathodic pretreatment of microcrystalline Cu.....	57
References	58

Chapter III: Local inhibition by 2-mercaptobenzothiazole of early stage intergranular corrosion of copper61

Abstract.....	61
3.1. Introduction	61
2. Experimental.....	62

3. Results and discussion	63
3.3.1. Macroscopic electrochemical behavior	63
3.3.2. MBT inhibition effects on early stage intergranular corrosion.....	65
3.3.3. Intergranular inhibiting effects according to GB type	71
4. Conclusions.....	72
Acknowledgments.....	73
References	73
Chapter IV: In situ scanning tunneling microscopy study of 2-mercaptobenzimidazole local inhibition effects on copper corrosion at grain boundary surface terminations.....	77
Abstract.....	77
4.1. Introduction.....	77
4.2. Experimental	78
4.3. Results and discussion.....	79
4.3.1. Macroscopic MBI inhibition effects	79
4.3.2. Local MBI inhibition effects at grain boundaries	81
4.3.3. Local MBI inhibition effects according to GB type	86
4.4. Conclusions	88
Acknowledgments.....	88
Reference.....	88
Chapter V: Inhibition effects on intergranular passivation of metals: Insight from in situ scanning tunneling microscopy study for 2-mercaptobenzothiazole and 2-mercaptobenzoimidazole on copper	93
Abstract.....	93
5.1. Introduction	93
5.2. Experimental	95
5.3. Results and discussion.....	96
5.3.1. Macroscopic inhibiting effects on passivation	96
5.3.2. ECSTM images and classification of grain boundaries by their morphology	100
5.3.3. Local inhibiting effects on grain boundary network	101
5.3.4. MBT & MBI effects on local passivation properties according to GB type	112
5.4. Conclusions	114
Acknowledgments.....	115
References	115
Conclusions and perspectives	121
Annexe: Résumé Étendu de Thèse	125

General Introduction

Corrosion of metals is a natural phenomenon that is a serious economical, environmental and safety issue. According to a recent NACE study, the global cost of corrosion exceeds €2.27-trillion which is almost 3% of the world's GDP [1]. A vast majority of materials made from metals and metallic alloys are susceptible to corrosion as they are not thermodynamically stable in the conditions in which they are used. Due to this, the topmost surface of the material reacts with its environment leading to a modification of the surface than can propagate into the material and alter the bulk properties. In other words, corrosion can be defined as an electrochemical phenomenon for metallic materials that leads to chemical and mechanical degradation of a material due to its reaction to the environment.

Copper is one of the widely used metals due to its excellent mechanical, thermal and electrical properties. Materials using copper as a metal or in alloys are used in diverse environmental conditions such as underground, aquatic conditions, in pipelines for gases, in highly saline conditions, etc. Thus, it is a challenge to understand the different processes with which copper can react to its environments. This understanding is vital to develop strategies to improve the lifetime of various materials.

There are several types of corrosion depending on the mechanism of the corrosion process. Intergranular corrosion is one of the major forms of corrosion for polycrystalline materials which initiates at the grain boundaries emerging on the surface but can soon propagate in the subsurface region and to the entire microstructure which, if not controlled, often leads to total failure of the material. There are different types of grain boundaries (GBs, 'Joints de grains' in French) in the GB network. Generally, GBs are categorized in different types by the extent of the misorientation angle between the two grains. Boundaries where the misorientation angle is less than 15° are termed as 'low angle grain boundaries' while boundaries with misorientation angle higher than 15° are classified as 'high angle grain boundaries'. There is an interface energy associated with each GB. The boundary energy is defined as the excess free energy associated with the presence of a grain boundary while using the perfect lattice as a reference point [2]. Several studies have shown that intergranular corrosion depends on the energy and the type of grain boundary. Low angle GBs have much higher corrosion resistance than high angle boundaries. Even within the subclass of high angle GBs there are a few boundaries called 'Coincidence site lattices' (CSL) that have better corrosion-resistant properties against intergranular corrosion than other random high angle grain boundaries. One of the common tactics to protect the material from intergranular corrosion is by increasing the fraction of these CSL boundaries in the material. This is the objective of Grain Boundary Engineering, where the lifetime of polycrystalline material is enhanced by increasing the CSL boundaries within the GB network. The other popular method which improves the resistance of the metallic material against corrosion is by using corrosion inhibitors.

Corrosion inhibitors are organic or inorganic molecules that are used to mitigate corrosion by decreasing the rate of the corrosion process. They can be added in small quantities to the environment or encapsulated in coatings. Corrosion inhibitors such as amides, amines, esters, imidazolines, 3carboxylic acids with their derivatives and sulfur organic molecules are a few of the widely used corrosion inhibitors for copper and its alloys [3]. It has been proposed and commonly believed that the corrosion inhibitor molecules react with the topmost surface of metals to form a barrier film that protects the metallic material's surface from further reacting with the environment. 2-mercaptobenzothiazole (MBT, $C_7H_5NS_2$) and 2-mercaptobenzimidazole (MBI, $C_7H_6N_2S$) are commonly used in industry as inhibitors for copper and its alloy. Both MBT and MBI belong to the class of organic corrosion inhibitors and have two functional groups in their chemical structure. There have been many

publications that have studied the corrosion inhibition and on passivation of copper by MBT and MBI but so far, to the best of our knowledge, the effect of MBT and MBI on the inhibition of intergranular corrosion for copper remains unexplored. The main objective of this thesis is to provide new insights by studying the effect of MBT and MBI on intergranular corrosion and passivation of grain boundaries, and to correlate the inhibition efficiency of the molecules as a function of types of grain boundaries.

To this end, a surface science-based in situ analytical approach was applied to study the effect of MBT and MBI on microcrystalline copper of high purity. Copper does not form a stable oxide at low pH but undergoes the process of passivation by forming surface oxides at higher pH. To study the effect of the inhibitor on both active dissolution and passivation of copper, the effects of MBT and MBI were studied in 10 mM HCl (pH = 2) and 0.1 M NaOH (pH = 13) aqueous solutions as electrolytes, starting from a metallic surface state obtained by electrochemical reduction of the native oxide. In situ Electrochemical Scanning Tunneling Microscopy (ECSTM) was used for the work carried on for this thesis. ECSTM is a very powerful technique that can resolve surfaces at a nanometric scale and even atomic scale while being able to control the electrochemical potential of the surface and thus the initial surface state and the kinetics of the corrosion reactions.

Along with this 'General Introduction', the manuscript consists of five chapters. Chapter I presents the Literature review and State of the art. It introduces various topics necessary to understand the central theme of this thesis. It summarizes various publications and for better presentation, is divided into three parts. Part I introduces various topics on grain boundaries. This is followed by part II which briefly explains the corrosion properties of copper in different environments and factors affecting the corrosion of copper. The chapter ends with the introduction of the two corrosion inhibitors studied in this work, MBT and MBI, with their classification followed by a summary of their mode of action as a corrosion inhibitor. The chapter ends with a summary of the interaction of MBT and MBI with copper according to DFT modeling studies.

The second chapter is dedicated to experimental methods. It begins by enlisting the electrochemical techniques used for the thesis and procedure of strict protocols adhered to for cleaning of the ECSTM cell. This is followed by theoretical principles underlying STM. The third and final part of the chapter provides details regarding the procedure used for preparation of the surface by mechanical and electrochemical polishing, preparation of probes for ECSTM imaging and finally the cathodic pretreatment of microcrystalline copper.

The third chapter is dedicated to the study of the effect of MBT on local inhibition for early intergranular corrosion of copper in active state. It is a reproduction of an article published in the Journal of the Electrochemical Society. It enlists the experimental conditions used for the study followed by a discussion of macroscopic electrochemical behavior from voltammograms of microcrystalline copper obtained in 10 mM HCl without and with 0.1 mM MBT present in the electrolyte. This is followed by the discussion of parameters used to classify the different classes of grain boundaries for ECSTM images. The different types of behavior for different grain boundaries are discussed by proposing a model to have a better understanding of the results obtained. Chapter III ends by concluding the study and the new insights it brought to our understanding of early intergranular corrosion inhibition by MBT for copper in acidic medium.

The fourth chapter is dedicated to the comparative study of the the effect of MBI on intergranular corrosion in active state for different types of grain boundaries. The chapter is a reproduction of an article submitted for publication. The chapter follows the same outline as Chapter III starting with a brief introduction and experimental methods and protocol used for the work. Then we discuss the

macroscopic electrochemical behavior in presence of MBI along with its comparison with 0.1 mM MBT. The results for MBT and MBI in 10 mM HCl are presented with two different chapters due to the different electrochemical characteristics of MBT and MBI. The chapter then provides detailed discussions of ECSTM images. This is followed by a proposed model to understand the effect of MBI on intergranular behavior. Chapter V ends with a summary of the effect of MBI on each class of grain boundaries along with a comparison with data obtained by MBT.

The fifth chapter studies the role of the presence of MBT and MBI on local intergranular behavior in alkaline conditions where copper can passivate. Unlike Chapters III and IV, the study of both MBT and MBI is combined into one chapter as the observed effects of both of the inhibitors are quite similar. This is a reproduction of a publication soon to be submitted. Following the same structure as for the previous chapters, we start with an introduction followed by the experimental method and conditions used for the study. Then, we present and discuss the macroscopic electrochemical behavior observed in the voltammograms without and with MBT and MBI in the electrolyte. This is followed by a discussion of the ECSTM images particularly the similarities for both of the inhibitors. Then, the key difference observed for MBT and MBI is discussed before concluding the study.

The general conclusions of the thesis are then presented together with possible perspectives opened up by this work. A list of references for each part is added at the end of each chapter. The thesis ends with an extended summary in French.

References

- [1] "The Global Cost and Impact of Corrosion." <https://inspectioneering.com/news/2016-03-08/5202/nace-study-estimates-global-cost-of-corrosion-at-25-trillion-ann> (accessed Dec. 14, 2020).
- [2] A.D. (Tony) Rollett and S. R. Wilson, "Rodrigues vectors, unit Quaternions," presented at the Texture, Microstructure & Anisotropy, Carnegie Mellon University, Jan. 02, 2015.
- [3] M. Antonijevic and M. Petrovic Mihajlovic, "Copper Corrosion Inhibitors. A review," *International Journal of Electrochemical Science*, vol. 3, no. 1, pp. 1–28, Jan. 2008.

Chapter I

Literature review and State of the Art

This chapter is devoted to bibliographic study and will present a non-exhaustive literature review of various works and topics pertaining to this thesis. This chapter is divided into three parts. In the first part, topics related to grain boundaries are introduced. In the second part, copper corrosion is reviewed, followed by factors affecting intergranular corrosion in copper. In the final part, corrosion inhibitors are briefly presented, and specifically 2-mercaptobenzimidazole and 2-mercaptobenzothiazole as corrosion inhibitors are discussed.

1.1 Introduction to grain boundaries

1.1.1 Introduction

In this part, we will present and discuss the interfaces between two neighboring grains of polycrystalline material commonly called grain boundaries (popularly abbreviated as singular as GB and plural as GBs). Generally, a grain boundary is an interface separating two regions having different crystallographic orientations. In other words, a grain boundary is a separation of two regions sharing common atoms with the same crystal structure but whose networks are disoriented [1]. Figure 1.1 shows at high resolution an example of disorientation between two adjacent grains that leads to the formation of a quasi-periodic grain boundary.

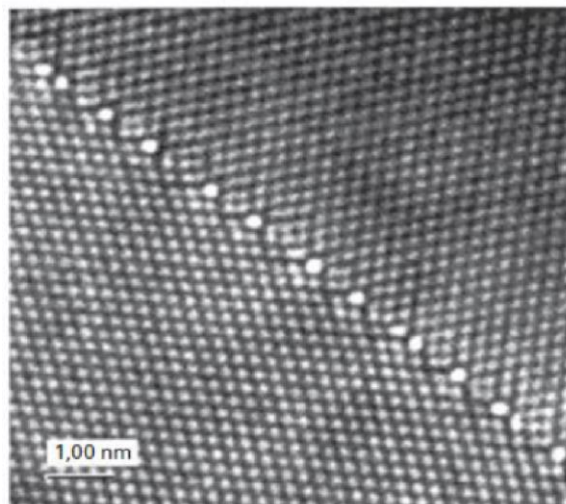


Figure 1.1: High-resolution transmission electron microscopy image of a quasi-periodic grain boundary with an angle of 90° around (001) and with a plane $(110)_1 // (100)_2$ in gold [2]

Five macroscopic rotational parameters define the geometry of a grain boundary. The orientation and inclination of the grain boundary plane are two such parameters [3]. The remaining three parameters define the rotation (or disorientation) which is necessary to make the two separate crystals to coincide [4].

It is quite challenging to define the orientation of the grain boundary plane experimentally as the slope is often not taken into account. Hence only disorientation between the two crystals is used to describe a grain boundary.

1.1.2 Geometric construction of grain boundaries

Theoretically, several symmetry operations reconstruct a grain boundary from two networks; networks 1 and 2, respectively [5]. The steps involved in the construction of a grain boundary are as follows:

- A) By application of a transformation of the A/\bar{T} type which allows us to pass from the network of crystal 1 to that of crystal 2. Here, A is a homogeneous linear transformation while \bar{T} is an associated translation. This translation is a part of $(A/\bar{T})G$ complex.
- B) By determining an interface plane using its normal \vec{n} and using the position of one of its atoms. We have to remove the atoms of network 1 and we place the atoms of network 2 on the other side of the interface.
- C) By application of a rigid translation which consists of relaxation of atoms in the vicinity of the interface followed by, if necessary, subtraction or addition of atoms to the interface.

These three steps lead to the formation of a real bicrystal. In order to have a complete geometric characterization of a grain boundary, we require definitions of nine geometrical parameters or geometric degrees of freedom. These nine geometric degrees of freedom belong to two broad categories: macroscopic degrees of freedom and microscopic degrees of freedom.

There are five macroscopic degrees of freedom:

- The angle of rotational symmetry between the two networks is the first macroscopic degree of freedom
- Further, two degrees of freedom are attributed to the direction cosines of the axis of rotation $[u \ v \ w]$.
- Two direction cosines of the unit normal vector n are the final two macroscopic degrees of freedom.

The four microscopic degrees of freedom used to define a grain boundary are as follows:

- Three define the rigid translation of crystal 1 with respect to crystal 2 (the rigid translation vector τ).
- The fourth and final microscopic degree of freedom corresponds to the amplitude d of the normal vector at the grain boundary plane. Amplitude d must be less than the amplitude of the macroscopic unit vector n .

1.1.3 Crystallographic description of grain boundaries

The crystallographic description of the grain boundaries is based on a geometric parameter which is the disorientation between the two crystal lattices on either side of the grain boundary. The value of the disorientation yields an interface with a particular atomic arrangement. The identification and study of this atomic arrangement are the foundation of the Coincidence Site Lattice (CSL) theory.

A. Crystallographic disorientation of grain boundaries

The crystallographic disorientation of a grain boundary is an angle defined around a chosen crystallographic direction $[u \ v \ w]$. This angle allows the passage from one crystal lattice to the other on either side of the grain boundary. Depending on the rotation axis of the disorientation, there are two types of grain boundaries. If the rotation axis is in the grain boundary plane, then such GBs are said to

be tilt GBs. If the rotation axis is normal to the plane of the GB, then such GBs are called twist GBs. Figure 1.2 shows the illustration for tilt and twist boundaries between two idealized grains.

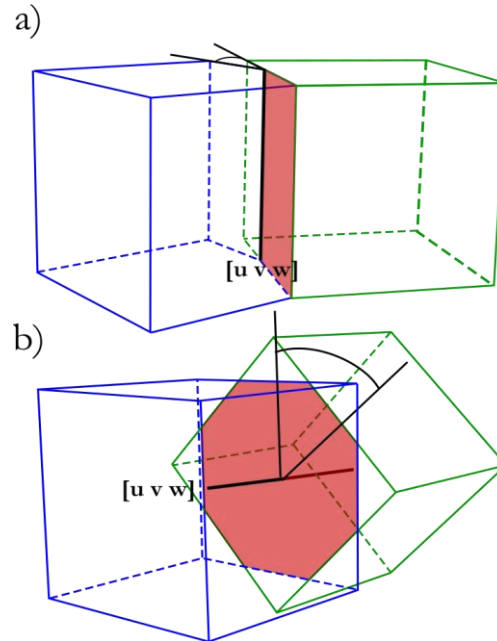


Figure 1.2: Disorientation relation around a crystallographic axis $[u \ v \ w]$ between two crystals for a grain boundary of a) tilt and b) twist type [6] [7]

Different modes of rotation can represent the same grain boundary. By convention, the smallest angle of rotation is considered. This rotation angle is the value of the disorientation between the two crystals on either side of the grain boundary. The disorientation of twist GBs in cubic networks is always less than or equal to 62° . There are several other ways of describing a grain boundary, such as the rotation matrix, the Euler angles, and the Rodrigues vector [8] [9].

B. Grain boundaries defined by the angle of disorientation.

One way to classify grain boundaries is according to their angle of disorientation θ defined above. Thus, according to θ , grain boundaries fall into two broad categories: low angle grain boundaries and high angle grain boundaries. The low θ GBs are those where the angle of disorientation is limited to 15° .

The angle of disorientation between the grains affects the energy of the grain boundaries. This energy of GBs is called grain boundary energy. It has been observed that low angle grain boundaries have lower boundary energy and lower chemical reactivity than high angle grain boundaries [3]. On the other hand, within the broad category of high-angle grain boundaries, there is a subset of GBs with comparatively lower grain boundary energy, as seen in Figure 1.3.

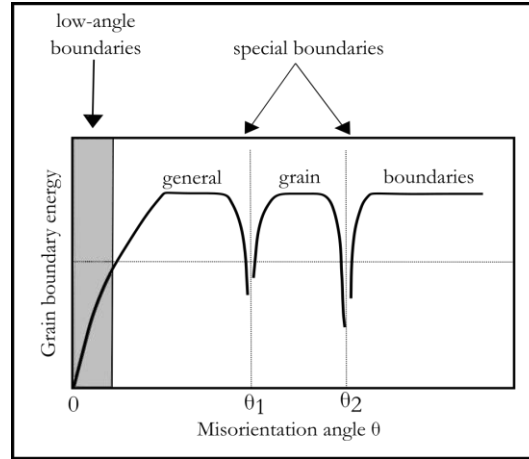


Figure 1.3: Schematic representation of the grain boundary energy variation as a function of the disorientation angle [1]

C. Coincidence Site Lattice (CSL) grain boundaries

The CSL theory helps us define a special subset of the high-angle grain boundaries that might show different susceptibility to corrosion due to lower boundary energy than the other random high angle grain boundaries. This theory helps us attribute a coincidence index noted in the form Σn to a grain boundary of known disorientation [10].

By definition, the coincidence network is the smallest network common to the two networks. At the GB, the sites thus form a network of coincidence sites. The index Σ is used to identify a CSL boundary. It is calculated as the ratio of the volume of the multiple cell of the coincidence lattice of the GB to the volume of the primitive cell of the grains' lattice (eq 1) [13].

$$\Sigma = \frac{\text{Volume of the coincidence cell}}{\text{Volume of the primitive cell}} \quad (1)$$

In other words, this is to say that the index Σ is the inverse of the density of the lattice points that are common to the lattices on each side of the GB [3].

Examples of a few CSL GBs can be seen in Figures 1.4, 1.5 and 1.6. If two crystal lattices have $1/5$ of lattice nodes that coincide as common nodes between the two lattices, then such boundary is called a Σ_5 CSL boundary as shown in Figure 1.5.

High angle grain boundaries that have in their plane a coincidence relation between the two lattices are defined as CSL boundaries if $\Sigma \leq 29$. They are defined as random boundaries if they have no coincidence relation or if their coincidence index is $\Sigma > 29$.

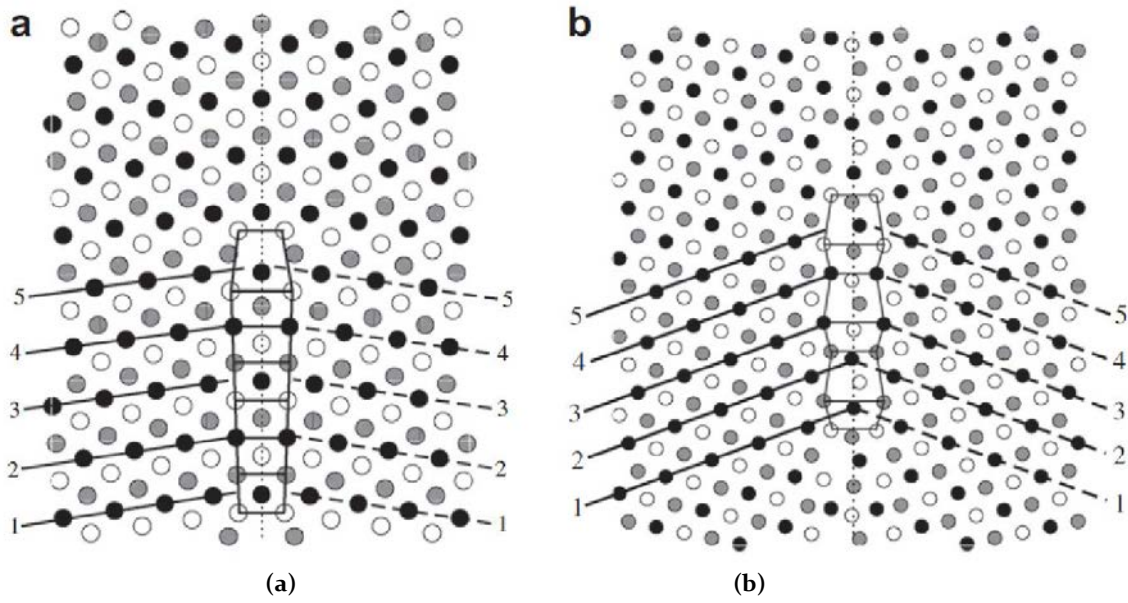


Figure 1.4: The atomic structure of (a) Σ_{57} ($\underline{187}$) ($\theta=13.17^\circ$) and (b) Σ_7 ($\underline{132}$) ($\theta=38.21^\circ$) CSL GBs $[11]$ ($[1\ 1\ 1]$ tilt axis is perpendicular to the figure plane)

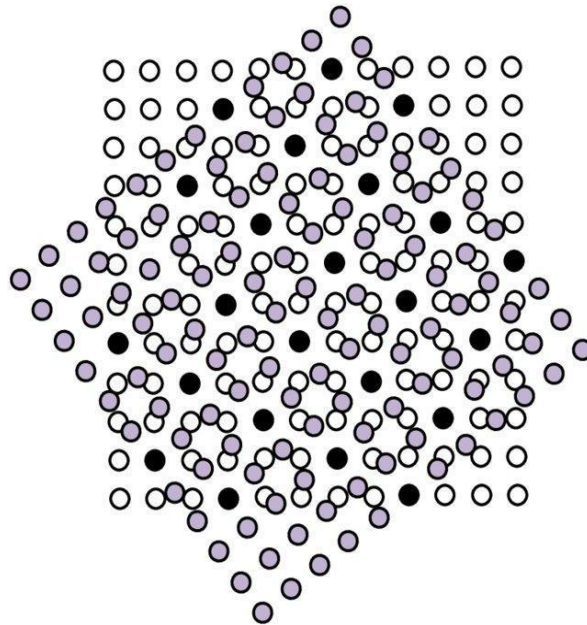


Figure 1.5: A CSL (Σ_5) formed from two simple cubic lattices rotated by 36.9° . Black circles denote sites common to both lattices $[12]$.

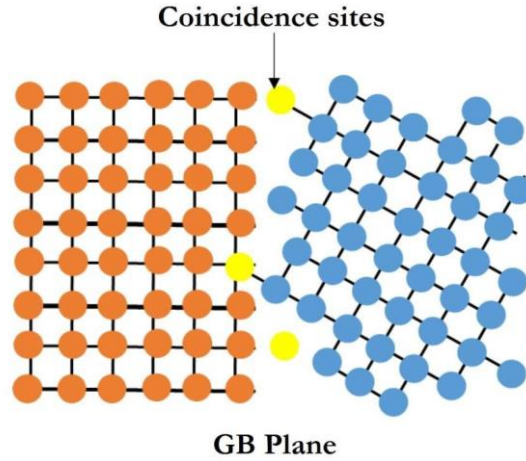


Figure 1.6: A high angle grain boundary with coinciding atoms between the two crystal lattices. The atoms common to two cubic lattices are in yellow

In a cubic network, the coincidence indices are odd. The disorientation of actual grain boundaries rarely corresponds to that of a perfect CSL network. Thus we can have a criterion of maximum angular deviation $\Delta\theta_{max}$ that can be tolerated with respect to the theoretical disorientation. The Brandon criterion is the most widely used [14]. It allows us to calculate $\Delta\theta_{max}$ from the degree of coincidence considered by the following relation:

$$\Delta\theta_{max}=15^{\circ}\Sigma^{-1/2} \quad (2)$$

This criterion is mainly used in the case where grain boundaries satisfy two coincidence relations. So, according to the Brandon criterion, grain boundaries with a disorientation angle of 30° around an axis $[100]$ would correspond to grain boundaries of type Σ_5 ($36.86^{\circ}/(100)$) for which $\Delta\theta_{max} = 6.7^{\circ}$ or to a grain boundary of type Σ_{17a} ($28.07^{\circ}/(100)$) for which $\Delta\theta_{max}=3.63^{\circ}$.

Another widely used and more restrictive criteria is the Palumbo-Aust criterion [15]. Here $\Delta\theta_{max}$ is calculated using the following relation:

$$\Delta\theta_{max}=15^{\circ}\Sigma^{-5/6} \quad (3)$$

According to the Palumbo-Aust criterion, $\Delta\theta_{max} = 3.92^{\circ}$ for a grain boundaries Σ_5 and $\Delta\theta_{max} = 1.41^{\circ}$ for a grain boundary for Σ_{17a} . The grain boundaries having an angle of disorientation of 30° would then correspond to neither of these two CSL-type grain boundaries. For $\Sigma=1$, both criteria allow a tolerance of 15° . Thus, below this value, the grain boundaries are considered to be of low disorientation. Such boundaries are called low angle grain boundaries by opposition to the so-called high angle grain boundaries for which the disorientation is greater than 15° .

Low angle grain boundaries are described by a tilt dislocation or twist dislocation leading to the formation of a tilt boundary and twist boundary [16] as seen in Figure 1.7 (a) and (b), respectively.

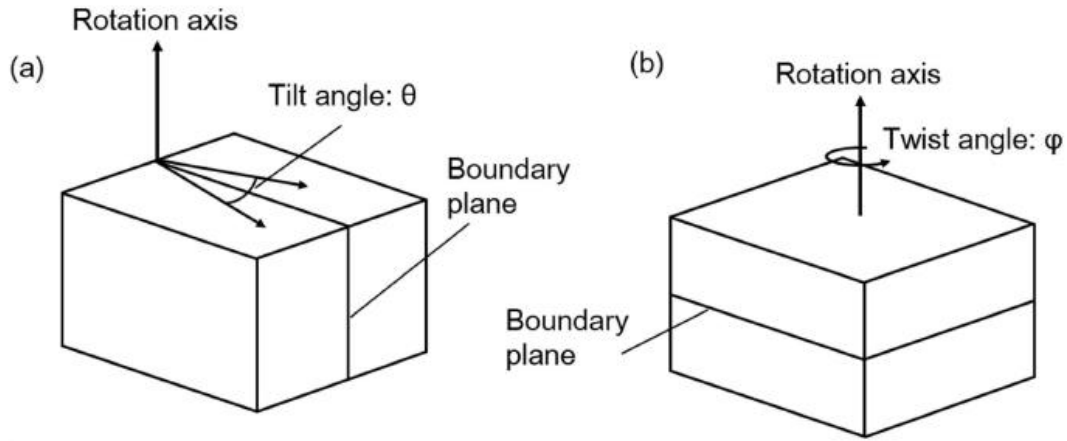


Figure 1.7: Schematic illustrations of low-angle grain boundaries: (a) tilt boundary; (b) twist boundary [16].

Table 1.1 lists the parameters characterizing the CSL grain boundaries in the cubic system ($3 < \Sigma < 29$).

Table 1.1: Disorientation Angle, Rotation Axis, and Euler Angles of CSL Grain boundaries of twist type ($3 < \Sigma < 29$) in the cubic system [19]

Σ	Θ°	$[u\ v\ w]$	Φ_1°	Φ°	Φ_2°
3	60	111	45	70.53	45
5	36.86	100	0	90	36.86
7	38.21	111	26.56	73.4	63.44
9	38.94	110	26.56	83.62	26.56
11	50.47	110	33.68	79.53	33.68
13a	22.62	100	0	90	22.62
13b	27.79	111	18.43	76.66	71.57
15	48.19	210	19.65	82.33	42.27
17a	28.07	100	0	90	28.07
17b	61.9	221	45	86.63	45
19a	20.53	110	18.44	89.98	18.44
19b	46.8	111	33.69	71.59	56.31
21a	21.78	111	14.03	70.02	75.97
21b	44.41	211	22.83	79.02	50.91
23	40.45	311	15.25	82.51	52.13
25a	16.26	100	0	90	16.26
25b	51.68	331	38.87	90	53.13
27a	31.59	110	21.8	85.75	21.8
27b	35.43	210	15.07	85.75	31.33
29a	43.6	100	0	90	43.6
29b	46.4	221	33.69	84.06	56.31

CSL grain boundaries are often called special because of the many properties distinguishing them from other types of grain boundaries. The cubic system's best known special grain boundaries are the so-called coherent twins (or CTs). This type of grain boundaries has an index of coincidence equal to 3 and

is said to be CT if they present a perfectly (111)-oriented plane. Such boundaries possess the following properties: no segregation, resistance to corrosion, no free volume at the interface, and absence of structural defects [17] [18].

To summarize, disorientation is the principal criterion for classifying GBs into two major groups: low or high angle grain boundaries. Beyond the disorientation angle of 15°, the GBs are considered to be high angle and separate into two subgroups: the CSL GBs which show a relation of coincidence between the two networks on either side of the boundary (with $\Sigma \leq 29$) and those considered to be random and which do not display a low-index coincidence Σ .

D. Special case of triple points

A triple point is formed by the meeting of three grain boundaries. The presence of a special GB in a triple point implies certain rules. Indeed, if two of the three GBs meeting at the triple point are CSLs, the third must also be of type CSL. Frary's rule [20] allows us to define the orientation of the third GB of a triple point if the first two are of type CSL. This rule is a combination rule of the Σ indices. It is expressed as follows:

$$\Sigma_1 \Sigma_2 = d^2 \Sigma_3 \quad (4)$$

Σ_1 , Σ_2 , and Σ_3 are the respective values of the coincidence indices Σ of the three CSL grain boundaries meeting at the triple point and d the common divisor, if it exists, between the values of the indices Σ_1 and Σ_2 . In the case of $\Sigma 3^n$ CSLs for which $d=1$, the combination rule can be written as follows:

$$\Sigma 3^1 + \Sigma 3^1 \rightarrow \Sigma 3^2 \quad (5)$$

$$\Sigma 3^2 + \Sigma 3^1 \rightarrow \Sigma 3^3 \quad (6)$$

$$\Sigma 3^1 + \Sigma 3^2 \rightarrow \Sigma 3^3 \quad (7)$$

E. Inclination of the grain boundary plane

Disorientation is not the only parameter that controls the atomic arrangement at the two crystal lattices interface. The GB plane's inclination can also control the index of coincidence at the interface itself [5]. The inclination of the GB plane can also lead to the introductions of intrinsic defects in the lattice.

1.1.4 The grain boundaries networks

Although the CSL theory is the most cited theory to understand the properties of these so-called 'special' high angle grain boundaries, it is only one out of many such theories to describe the grain boundaries. Few even consider that the CSL theory is incomplete as it interprets the network without taking the position of the grain boundary plane within the network under consideration.

The criterion of the significant inter-planar distance has been proposed [21] that considers the distance between the global planes of the two crystals on either side of the grain boundaries. The application of this proposed criterion to experimental measurements remains difficult because the real GBs are not plane at the atomic scale, along with the fact that the measurement of the orientation of the GBs is subject to approximations made by the observer such as the choice of the cross-sectional plane of the polycrystal. However, successive cuts allow the orientation of the grain boundary plane to be measured.

These cuts can be made manually by polishing or by localized ion beam [22]. The disorientation distribution function describes the texture of grain boundaries. Note that there is no relation between this and the distribution of various orientations [23].

1.1.5 Energy of grain boundaries

By definition, grain boundaries represent an interface between two crystals, which has the effect of increasing the overall energy of the polycrystalline material. The GB energy is directly related to the atomic arrangement of each type of GBs. Compact atomic planes at the interface lead to lower GB energy due to the reduction in the free volume of the network. Some GBs may be listed as special because of their lower energy, not necessarily due to the fact that these boundaries have a special structure. In these cases, the special properties can result from this lower energy due to the reduction of free volume owing to the compactness of their atomic planes.

A geometric condition has been proposed to predict the energy of GBs [24]. Under this condition, it has been proposed that a higher density of coincidence sites, $\rho = 1/\Sigma$, which corresponds to low indices Σ , induces lower energy of the GB. Experimentally, it has been established for fcc material that lower coincidence index for GBs does indeed correspond to lower energy. Thus, Σ_3 type GBs owe their properties to their very low energy compared to other special GBs [25]. Low energy stacking fault materials, such as superalloys, exhibit the lowest energy class of GBs [26]. These are the grain boundaries resulting from the multiple twinning. This condition was confirmed by studying the influence of interplanar distance on the energy of grain boundaries [27].

In the case of low angle GBs, the specific energy of each GB is a function of its disorientation [28]. The energy of low disorientation GBs can be calculated using the Read-Shockley formula [26] [29] [30]. This formula allows the calculation of the energy of a succession of edge dislocations. Its expression is:

$$\gamma_{ij} = \begin{cases} \gamma_{max} \frac{\theta}{\theta_0} (1 - \log(\theta/\theta_0)) & / \theta < \theta_0 \\ \gamma_{max} & / \theta > \theta_0 \end{cases} \quad (8)$$

Where, θ is the disorientation of the GB and θ_0 the limit of disorientation of low angle GBs ($\theta_0 = 15^\circ$). γ_{max} is the energy of a GB with a disorientation angle greater than θ_0 . γ_{max} is calculated using the following equation

$$\gamma_{max} = \frac{\mu b \theta_0}{4 \pi (1 - \nu)} \quad (9)$$

Where μ is the shear modulus, b the Burgers vector, and ν the Poisson's coefficient.

For disoriented high angle grain boundaries, no relationship between the values of angles of disorientation and that of the energy of GBs has been established. Nevertheless, studies have cited an energy difference between tilt and twist grain boundaries. Figure 1.8 presents the evolution of the CSL-type grain boundary energy as a function of the disorientation angle.

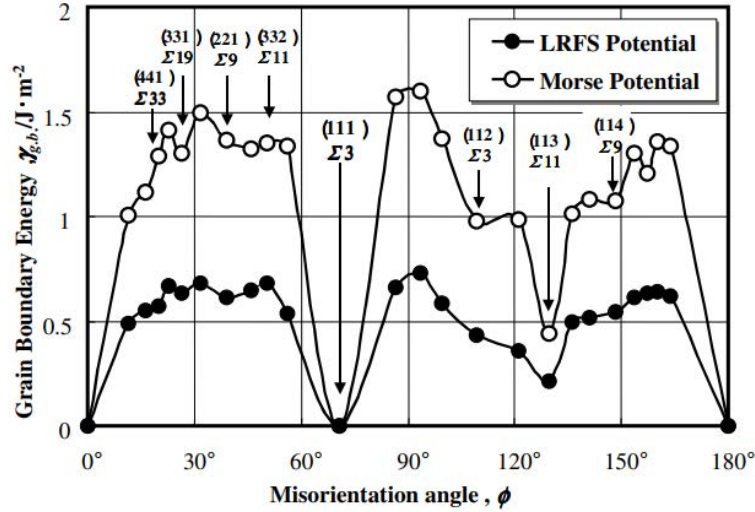


Figure 1.8: Energy of the grain boundaries according to the angle of disorientation along an axis of inclination (110) for copper [31]

For identical disorientation, the orientation (or inclination defined above) of the GB plane with respect to the crystal can influence the GB energy. This is the case of type Σ_3 grain boundaries. Indeed, the energy of coherent grain boundaries (Σ_3 CT) is less than that of incoherent Σ_3 grain boundaries. This lower energy results from compact and ordered stacking of coherent Σ_3 grain boundaries as well as from their planar morphologies (Figure 1.9) [32]. The plane of the incoherent GBs is locally deviated from its perfect theoretical orientation by introducing disordered segments, which results in the overall increase in its energy.

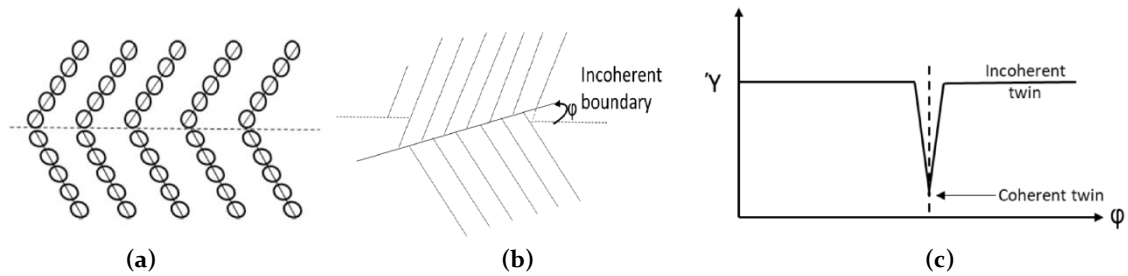


Figure 1.9: Grain boundaries of type (a) Σ_3 coherent and (b) Σ_3 incoherent, and evolution (c) of the energy of the grain boundaries with the deviation angle from perfect geometry ϕ [32]

1.1.6 Grain boundary engineering

Grain boundary engineering is the set of methods and processes applied in order to improve the behavior of the intergranular region of polycrystalline materials with respect to environment or mechanical stress (corrosion, segregation, rupture, etc). Since grain boundaries are classified in categories with different properties, it is considered for grain boundary engineering that the proportion of each category in a polycrystal has a direct influence on the macroscopic properties of the latter. So, the fraction of each type of grain boundary is defined after each stage of the elaboration of the material. The aim of grain boundary engineering is to control the polycrystalline material's properties by controlling the fractions of different categories of grain boundaries introduced into the polycrystalline material. The most used analysis technique to measure the fraction of a particular category of grain boundaries is electron back scatter diffraction (EBSD).

Two types of processing are used to control the proportions of each category of grain boundaries. They consist of alternating mechanical and thermal treatments. According to the deformation rate introduced, it can be either strain-annealing or strain-recrystallization [33]. Annealing for a few hours precedes the mechanical treatment.

Restoration treatments follow a mechanical treatment introducing a low rate of deformation (5-10%). Thermal annealing is carried out at a low temperature in order to avoid the recrystallization of the grains. However, temperatures must be high enough to allow rearrangement of grain boundaries to minimize their energy. The energy generated by mechanical deformations is stored and then reused for the creation of new intergranular interfaces during the heat treatment.

For recrystallization treatments, the initial deformation rate is higher (20-30%). Heat treatments are performed at higher temperatures allowing the rapid recrystallization of the grains. The recrystallization is of static type and follows a cold deformation. After a number of cycles of cold deformation and recrystallization, and depending on the type of materials, the proportion of special grain boundaries increases considerably [33]. This is the method used at Ghent University to develop the microcrystalline copper samples that we used during this thesis, where the microcrystalline copper is produced from high purity electrolytic copper with cryogenic rolling.

1.2 Corrosion properties of copper

1.2.1 Metal corrosion and passivation

According to the International Union of Pure and Applied Chemistry (IUPAC), corrosion is defined as "an irreversible interfacial reaction between a material and its environment, leading to the degradation of the material."

The interaction of a metal with an aqueous corrosive environment can lead to soluble or insoluble corrosion products. In a liquid medium, the corrosion phenomenon is driven by two simultaneous chemical reactions of electronic exchanges: the oxidation of the material, an anodic process, and the reduction of the medium, a cathodic process. . The oxidation of metal leads to the formation of corrosion products.



When the material is immersed, it is placed at the free potential of the material in that medium. This potential is called the corrosion potential, E_{corr} . At this potential, the anodic current is associated with the oxidation of the material, and the cathodic current is associated with the reduction of the medium. These two currents are equal, in absolute value, and define the corrosion current i_{corr} . The process of corrosion by the anodic and cathodic processes is summarized in the Figure 1.10.

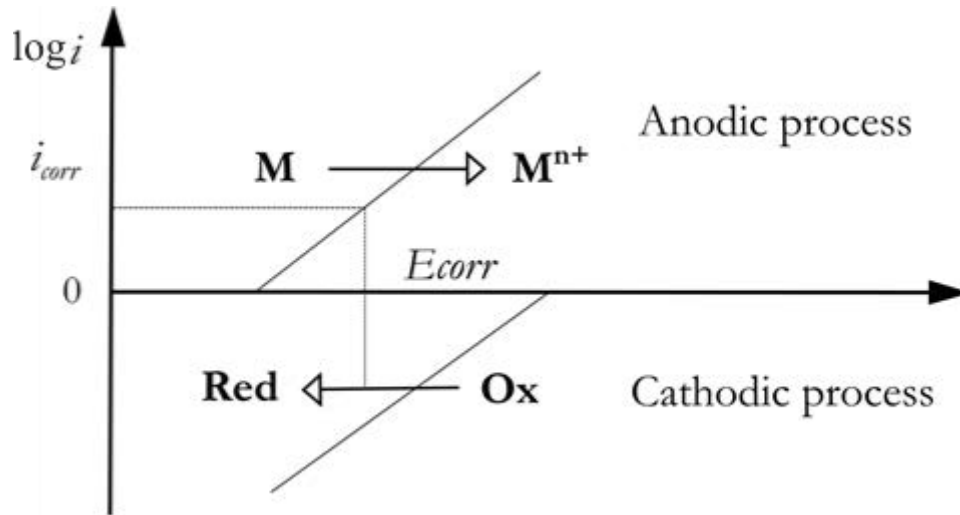


Figure 1.10: Schematic representation of the electrochemical behavior of a metal M in an oxidizing medium Ox (corrected from reference) [34]

Metallic cations (M^{n+}), as formed in equation 10, can react with the anions in the medium (A^{m-}) to form more or less soluble compounds depending on the reaction:



Insoluble products can form directly on the surface or be redeposited after formation in solution to cover the surface either partially or entirely. The insoluble corrosion products formed in an aqueous medium are most often metal oxides or hydroxides.

In the case of metals and alloys that are passive, the oxidation of the metal in an aqueous medium leads to the formation of a protective film on the surface. This film consists of insoluble oxides or very slowly dissolving oxides and/or hydroxides that form a compact, adherent, and continuous layer that insulate the metallic substrate from the surrounding aggressive medium. This protective barrier slows down the atomic transport across the liquid/solid interface, thus limiting the rate of metal dissolution in the form of ions in the medium [35]–[38].

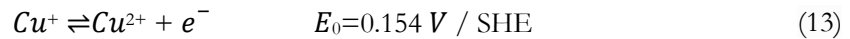
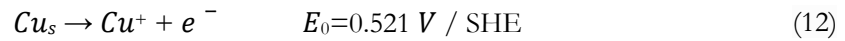
Passivation generally is a spontaneous phenomenon but in few instances, it is necessary to promote it by an oxidizing anodic treatment. Stainless steels, aluminum alloys, and copper and copper alloys, to name a few, are examples of metals and alloys that undergo passivation and are widely used in different fields of application.

There are several factors that can modify the reaction kinetics and influence the corrosion and passivation mechanisms of metals and alloys. When the nature of the material is a predominating factor then, the main factors: are the chemical nature of the metal and alloys, the presence of additional elements, the structure and microstructure of the surface, and chemical and mechanical states of the surface [39] [40]. When environmental effects are predominant, the main factors are the pH of the electrolyte, temperature, the oxygen content of the environment, as well as the presence of species of chemical or microbiological origin [41]–[46].

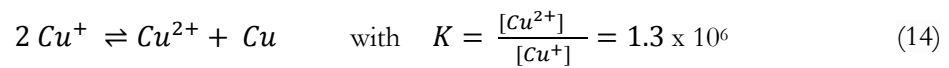
1.2.2 Copper corrosion and passivation

Copper (atomic number 29) belongs to the group of transition metals. Its electronic configuration is [Ar] 3d¹⁰4s¹ and its molar mass 63.546 g.mol⁻¹. It exists in metallic, Cu(o), or oxidized, Cu(I) and Cu (II), form. Copper is one of the first metals used by humans and possesses attractive properties such as its malleability and the fact that it is an excellent conductor of heat and electricity.

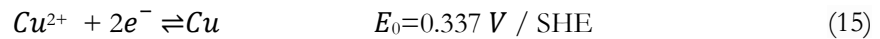
In an aqueous solution, copper can oxidize according to the following equilibrium reactions:



The Cu^+ species is unstable and dissociate according to the following reaction:



The equilibrium constant K indicates that Cu^+ and Cu^{2+} ions predominate at low and high ionic concentrations, respectively. Thus, only metallic copper Cu and Cu^{2+} ion are stable at higher concentrations. The transition from one species to another is done according to the following equilibrium:



A. Potential-pH diagram of the Cu/H₂O system and copper passivation

The potential-pH diagram makes it possible to predict, on a thermodynamic basis, the areas of predominance of each of the different compounds formed by metallic copper and its ions.

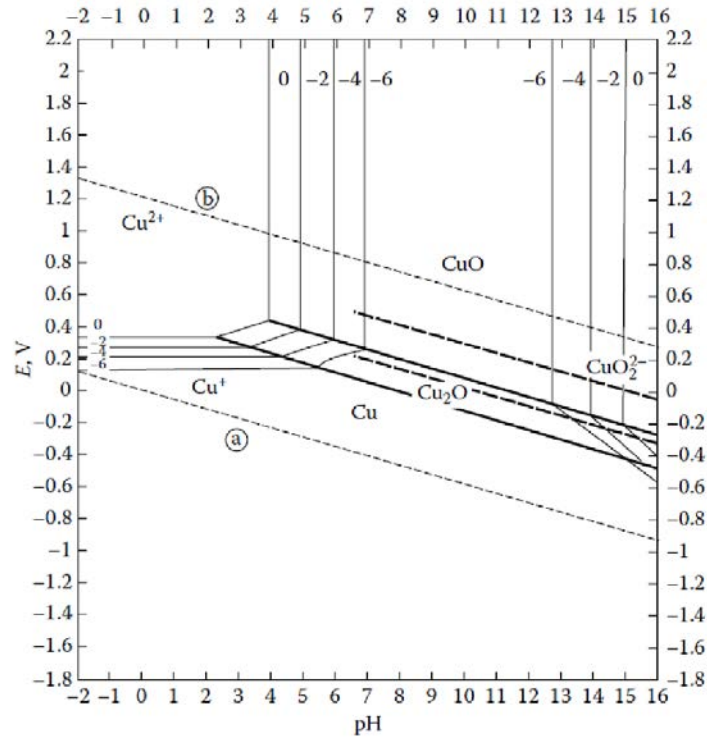
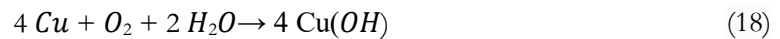


Figure 1.11: Pourbaix diagram of the Cu/H₂O system, at 25° C and for concentrations of 10⁻⁶ mol/L [47] [48]

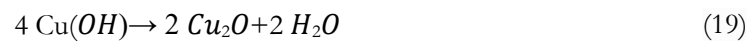
The diagram established by Pourbaix [47], also known as Pourbaix diagram, for the Cu/H₂O system illustrates the extent of the domains of immunity of copper, when it is in its stable metallic form, of corrosion, when it is dissolved in soluble ionic form, and of passivity, when it forms a stable oxide. These different domains are included in the domain of water stability (Figure 1.11).

The oxidation-reduction potential of the Cu/Cu⁺ couple is greater than that of the H⁺/H₂ couple in a wide range of pH. Therefore copper corrodes very little in an aqueous solution under weak oxidizing conditions. On the other hand, the redox potential of the O₂/H₂O couple is greater than that of the Cu/Cu⁺ couple—an increase in the concentration of dissolved oxygen results in the corrosion of copper.

At open circuit potential and in the presence of dissolved oxygen, the oxidation of metallic copper leads to the formation of copper hydroxide according to the following reactions:

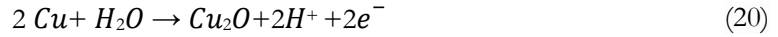


The dehydration of the hydroxide leads to the formation of cuprite (Cu₂O):



Thus, the presence of dissolved oxygen can promote the formation of Cu₂O oxide.

This oxide can also be formed from the dissociation of water according to the following anodic reaction:



Cuprite is a copper oxide with an oxidation number +1 (Cu(I)). Figure 1.12 illustrates its mineral occurrence and Table 1.2 summarizes its properties. This oxide is stable on the surface of copper when the pH is greater than 5.5 and at relatively low oxidizing potential, as seen in the Pourbaix diagram in Figure 1.11.



Figure 1.12: Cuprite ore found in nature. From left to right: found in Oshikoto, Namibia; Tuscany, Italy; Leicestershire, England [49]

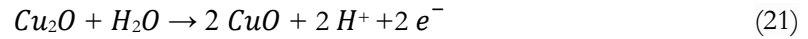
Table 1.2: Physical and crystallographic properties of cuprite [49] [50]

Properties	Values
Chemical Formula	Cu_2O
Colour	Dark red to cochineal red, sometimes almost black.
Lustre	Adamantine, Sub-Metallic, Earthy
Molar mass	$143.09 \text{ g.mol}^{-1}$
Melting point	$1232 \text{ }^\circ\text{C}$
Boiling point	$1800 \text{ }^\circ\text{C}$
Band gap	2.137 eV
Crystal	Cubic
Space Group	$\text{Pn}\bar{3}\text{m}$
Cell Parameters	$a = 4.2685 \text{ \AA}$
Locality	Commonly in the copper deposits of SW, USA, and in Chile.

Cuprite, Cu_2O , has a cubic structure in which the Cu^+ and O^{2-} ions are positioned on two distinct sub-lattices. The protective role of this oxide formed on pure copper and copper-nickel alloys has been attributed due to its semiconductor properties [51] [52]. Cuprite is a p-type non-stoichiometric semiconductor due to a deficiency of Cu^+ ions [51]–[58]. The diffusion of cuprous ions is drained by a gradient of vacancies, which are more concentrated at the oxide/electrolyte interface than at the metal/oxide interface [59]–[61]. Oxygen is reduced at the surface of the oxide to O^{2-} and is incorporated into the mesh of the oxide.

The diffusion of Cu^+ ions through the cuprite layer is the limiting factor in the growth kinetics of the oxide formed in the passive Cu(I) domain. It is this same diffusion through the passive layer that slows down the corrosion kinetics of copper in the passive state.

At higher oxidizing potential, the Cu_2O cuprite layer is transformed into tenorite (CuO) by oxidation of Cu^+ ions into Cu^{2+} ions [62]-[64]. Figure 1.13 illustrates the mineral form of tenorite and Table 1.3 summarizes its properties. The oxidation reaction of cuprite to tenorite is as follows:



The formation of CuO is only possible at the surface where there is a sufficiently thick layer of Cu_2O . Tenorite formation can be accompanied by the dissolution of part of the cuprite layer according to the following reaction [65]:

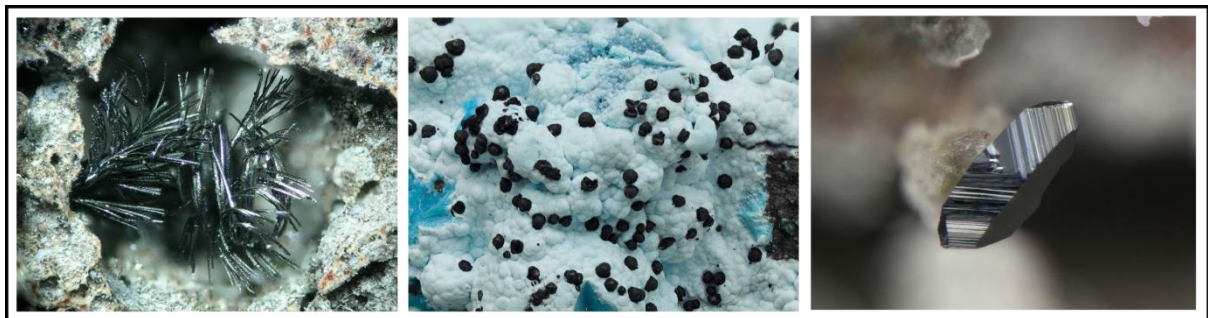
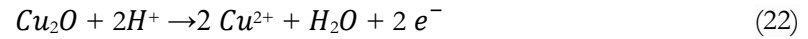


Figure 1.13: Tenorite ore found in nature. From left to right: found in Kamchatka krai, Russia; Arizona, USA; Rhineland-Palatinate, Germany [65]

Table 1.3: Physical and crystallographic properties of tenorite [52][53][67][68][69]

Properties	Values
Chemical Formula	CuO
Colour	Grey, black
Lustre	Metallic
Molar mass	79.55 g.mol^{-1}
Melting point	1326°C
Boiling point	2000°C
Band gap	1.2 eV
Crystal Data	monoclinic
Space Group	C2/c
Cell Parameters	$a = 4.6837 \text{ \AA}$, $b = 3.4226 \text{ \AA}$, $c = 5.1288 \text{ \AA}$ $\alpha = 90^\circ$, $\beta = 99.54^\circ$, $\gamma = 90^\circ$
Locality	Vesuvio (Vesuvius), Napoli, Campania, Italy

The passive layer formed in the region of formation of the Cu(II) oxide is a duplex layer of nanometric thickness with the inner part consisting of Cu(I) oxide (Cu_2O) and the outer part of Cu(II) oxide (CuO) (Figure 1.14) [70] [63] [71]. It has been shown that the outer layer may contain Cu(II) hydroxide (Cu(OH)_2) [63] [71].

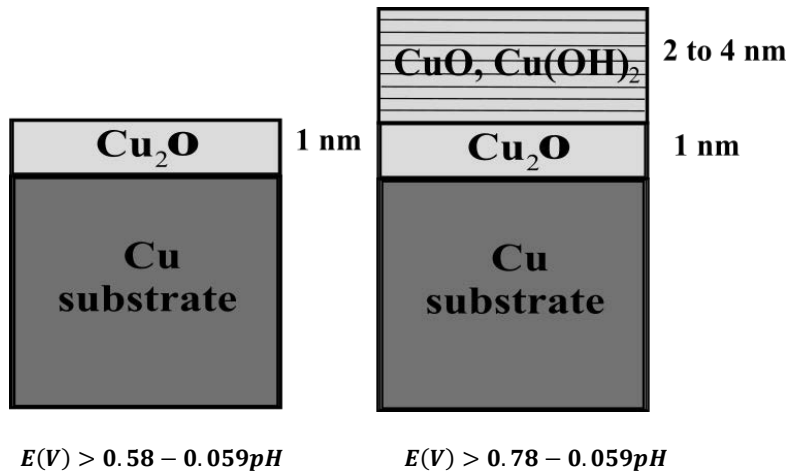


Figure 1.14: Schematic of the layers formed on copper in the Cu(I) and Cu(II) passive domains [71]

This duplex oxide is formed by a thin layer of Cu_2O oxide no more than 2 nm thick and an outer layer of CuO oxide up to 4 nm thick. These two oxides are p-type semiconductors [72] [73], and are both non-toxic. A metastable structure of the gross formula Cu_4O_3 has been identified as an intermediate between the two known forms of copper oxides [74]. CuO oxide has a monoclinic structure, while Cu_2O oxide has a cubic structure, the latter having a larger gap layer than that of CuO [75]–[77].

At a pH lower than 5, the oxides Cu(I) and Cu(II) are not stable, and it is impossible to form a protective copper oxide film. The concentrations of Cu^+ and Cu^{2+} ions, therefore, increase as the dissolution progresses. They are dependent on the pH of the solution [78]:

$$\text{Log} [\text{Cu}^+] = -0.84 - \text{pH} \quad (23)$$

$$\text{Log} [\text{Cu}^{2+}] = 9.21 - 2\text{pH} \quad (24)$$

B. Potential-pH diagram of the $\text{Cu}/\text{H}_2\text{O}/\text{Cl}$ system and copper passivation in the presence of chlorides

In the presence of aggressive species, copper can behave differently with respect to its corrosion reactions. For example, the presence of chloride ions poisons the formation of the passive film, or it weakens it [79], which makes copper vulnerable to localized corrosion even at alkaline pH values. The proposed potential-pH diagram for the $\text{Cu}/\text{H}_2\text{O}/\text{Cl}$ system is shown in Figure 1.15 [80].

From a thermodynamic point of view, the stable species that may be present at the metal/electrolyte interface are copper chloride CuCl , copper oxide Cu(I) (Cu_2O), copper hydroxide Cu(I) ($\text{Cu}(\text{OH})_2$), copper oxide Cu(II) (CuO), acatamite $\text{Cu}_2(\text{OH})_3\text{Cl}$ or malachite $\text{CuCO}_3 \cdot \text{Cu}(\text{OH})_2$ [55] [81] [82]. Figure 1.16 shows the order in which these compounds were observed on the copper surface [55] [81].

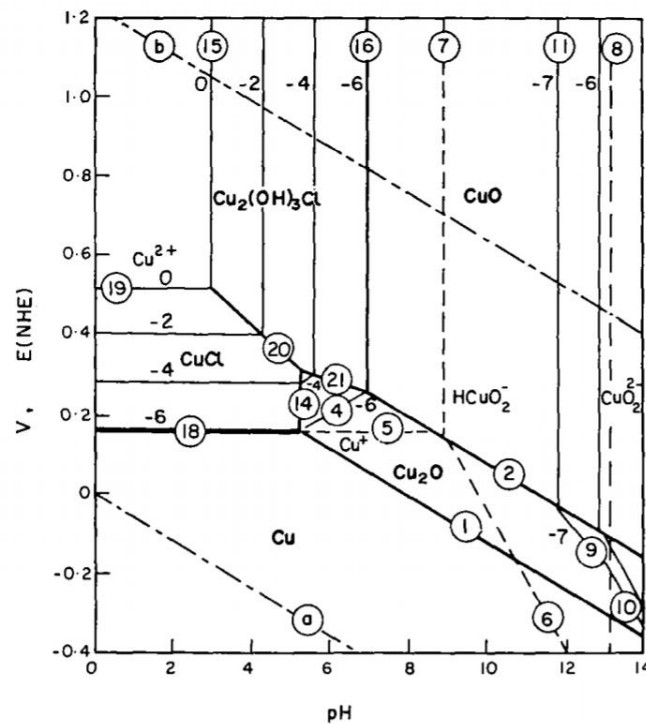


Figure 1.15: E-pH diagram of the Cu/H₂O/Cl⁻ system at T = 25 °C, Solid phases taken into account: Cu, Cu₂O, CuCl, CuO, Cu₂(OH)₃Cl (dashed lines indicate the water stability domain) [80]

<div style="display: flex; justify-content: space-around; align-items: center;"> <div style="background-color: #000080; color: white; border-radius: 50%; width: 40px; height: 40px; display: flex; align-items: center; justify-content: center;">Cl⁻</div> <div style="text-align: center;">Electrolyte</div> <div style="background-color: #000080; color: white; border-radius: 50%; width: 40px; height: 40px; display: flex; align-items: center; justify-content: center;">Cl⁻</div> </div>		
Atacamite (Cu ₂ (OH) ₃ Cl) or malachite (CuCO ₃ ·Cu(OH) ₂)		
Cupric hydroxide Cu(OH) ₂ or oxide (CuO)		
Cuprous oxide (Cu ₂ O)		
Cuprous chloride (CuCl)		
Copper metal		

Figure 1.16: Corrosion products observed on copper in an aqueous medium containing chlorides [55] [81]

These corrosion products are soluble; however, some such as copper oxide Cu₂O, acatamite, and malachite may be partially protective. These three species have been observed experimentally at open circuit potential. It would not be possible to observe acatamite and malachite simultaneously because the precipitation of these two species is competitive [80].

Chloride ions stabilize the dissolution of copper by binding itself to the Cu(I) species. The film formed on the surface of the copper is then covered with a layer of Cu₂O oxide, the main constituent of the layer formed by corrosion products on the surface of the copper in a chloride medium. The stability of the oxide in a chlorinated medium depends mainly on the pH and the amount of dissolved oxygen. CuO oxide can also appear by dissolving copper as Cu²⁺. At open circuit potential, there is, in reality, a balance between the dissolution of copper in its two ionized forms (Cu(I) and Cu(II)) and the reduction of these ions to metallic copper [83], [84].

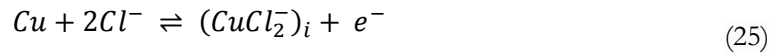
Localized corrosion of copper in contact with chloride ions is inevitable. This has been attributed to the adsorption of chloride ions on the surface of the bare copper. Indeed, $CuCl_2^-$ ions destabilize the formation and growth of Cu_2O oxide [75] [76].

Other soluble compounds can be formed such as $Cu_2(OH)_2^{2+}$, $Cu_2(OH)_3^-$, $Cu_2(OH)_4^{2-}$. These hydroxyl complexes disrupt the growth mechanisms of oxide layers, which accelerates the phenomena associated with copper corrosion. Therefore, it is possible to form copper oxides Cu(I) and Cu(II) in an aqueous medium in the presence of chlorides. However, the growth of these oxides to form a sufficiently thick and compact layer to effectively protect copper against corrosion is impossible [57] [80] [85]–[92].

C. Mechanisms of dissolution of copper in the presence of chlorides

Three mechanisms have been proposed to explain the species formed.

It has been proposed that the dissolution of copper in chloride media is controlled only by the diffusion of $CuCl_2^-$ ions [93]. The reactions involved would be:



Where i and s refer to the species at the copper/solution interface and in the solution, respectively. The kinetics is limited by reaction 26, which corresponds to the diffusion of the $CuCl_2^-$ from the interface to the solution. The oxidation of copper in $CuCl_2^-$ is assumed to be at equilibrium, and the application of the Nernst equation makes it possible to obtain the concentration $(CuCl_2^-)_i$ as follows:

$$(CuCl_2^-)_i = E^0 + \frac{RT}{F} \ln\left(\frac{[(CuCl_2^-)_i]}{(Cl^-)^2}\right) \quad (27)$$

The rate of diffusion is obtained by applying Fick's law of diffusion:

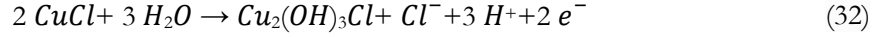
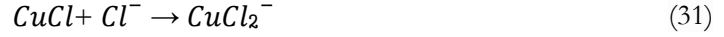
$$i = \frac{zFD[(CuCl_2^-)_i]}{\delta} \quad (28)$$

where i is the diffusion flux, z the charge of the diffusing species, D the diffusion coefficient and δ the thickness of the diffusion layer. Taking into account the activation energy of the diffusion (ΔH_d^*), equation 28 becomes:

$$i = \frac{zFD_0}{\delta} Cl^{-2} \exp\left(-\frac{\Delta H_d^*}{RT}\right) \exp\left(\frac{F(E-E^0)}{RT}\right) \quad (29)$$

A study has shown three distinct regions on the $\log i$ vs E curves obtained by cyclic voltammetry [94]. The first region corresponds to the oxidation-reduction of the $Cu/CuCl_2^-$ couple. The kinetics of the reaction in this region is governed by the diffusion of $CuCl_2^-$ species. A second region corresponds to the formation and reduction of an insoluble compound, identified as $CuCl$ by X-ray diffraction. This compound can partially cover the copper surface, but the uncovered part continues to form the two soluble species. In the third region, X-ray diffraction analysis also identified the formation of $CuCl$ and $Cu_2(OH)_3Cl$ compounds. Thus, the following three reactions have been proposed to describe the observed formation of the species:





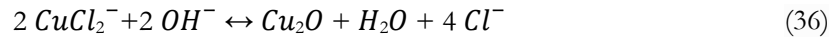
The first reaction is not stationary, CuCl is an insoluble compound which only partially covers the copper surface, and the mass transport is limited by a single product $CuCl_2^-$. Other studies have confirmed these mechanisms [88]-[96].

It has been proposed that the insoluble compound $CuCl_2^-$ would be the first to form and would be followed by the precipitation of CuCl, the two compounds forming a porous and non-adherent film [97]. However, during anodic polarization, equilibrium could be established between $CuCl$ and $CuCl_2^-$.

These dissolution mechanisms are still widely debated till this day. It nevertheless emerges that, in the initiation stages of the dissolution studied in this thesis, copper first oxidizes to Cu^+ to form $CuCl$ and/or $CuCl_2^-$ according to the following reactions:



The same corrosion mechanisms occur in a neutral or acidic chloride environment. The only difference would be the transformation of $CuCl_2^-$ into Cu_2O according to the following reaction [80] [85] [91] [93] [95] [97]-[100].



The concentration of chloride ions can alter the response of copper to corrosion. Thus, it has been shown that some species only appear above a particular chloride concentration (between 0.7 and 1 mol/L). These species are the $CuCl_3^{2-}$ and $CuCl_4^{3-}$ complexes which are formed according to the following reactions [80]:



There is competition for the formation of the Cu_2O and CuCl compounds. The oxide predominates for chloride concentrations below 1mM, while CuCl predominates for chloride concentrations above 0.1M [101].

D. Special case of single crystals

On a monocrystalline material, the dissolution and passivation reactions are preferentially initiated at the step edges. The step edges delimit the terraces which have the nominal crystallographic orientation of the surface. The presence of these step edges results from the residual disorientation of the surface

with respect to its nominal orientation. At the step edges, the coordination of the atoms is reduced as compared to that of the atoms of the terraces, which increases their reactivity. For the cubic system, the density of step edges increases sharply in the cases of complex orientations, far from those of poles (001), (101), and (111)). The dissolution kinetics therefore is greatly increased [102]-[105].

1.2.3 Influence of microstructure on copper corrosion phenomena

Several studies have shown that the corrosion rate of polycrystalline copper is influenced by the microstructure (grain size and orientation of the grains) and microstructure defects (grain boundaries, dislocation, and other imperfections).

A. Influence of grain size

It has been observed in studies dealing with the effect of grain size in polycrystalline copper that the corrosion kinetics of ultra-fine-grained copper is significantly lower than that of coarse-grained copper. Hence ultra-fine-grained copper exhibits better corrosion resistance [106]. This effect has been attributed to a greater density of dislocations and grain boundaries in ultra-fine-grained copper, promoting the formation of passive layers [106] [107]. This interpretation implies that the formation of a passive layer would be favored at the emergence at the surface of grain boundaries or other imperfections.

In order to better understand the relationship between grain size and corrosion rate, gold nano plating experiments were performed on high purity copper with different grain sizes. At the same time, other parameters, like internal stresses and texture, were kept constant [108]. It was observed that the smaller the average size of the grain, the more negative was its corrosion potential. The smallest grains were found to be more uniformly corroding than the larger grains.

B. Influence of grain structure

As passivation is a phenomenon occurring on the surface of materials, it is strongly related to the density of reactive sites and, therefore to the crystallographic orientation of the grains on the surface of the metal. This dependence has been studied. Thus, it has been reported that a thicker passive layer would form on grains with a low index (*h*, *k*, *l*). This effect has been attributed to a greater density of surface atoms [109].

The formation of copper oxide layers would also depend on the crystallographic orientation of the grains as reported in a study of the crystallinity of the duplex Cu(I)/Cu(II) passive film formed on Cu(001) and Cu(111) [71]. The duplex film formed on a Cu(111) copper substrate is always crystalline and terminated with terraces up to 20 nm in width and step height of the order of one atomic monolayer of oriented CuO(001). CuO oxide forming the outer layer of this duplex film, its structure in orientation (001) consists of an alternation between planes of Cu²⁺ ions and O²⁻ ions. The duplex film formed on Cu(001) is terminated by a crystalline or amorphous structure. In the case of a crystalline termination, the structure observed was the same as that of the oxide formed on Cu(111). The formation of an amorphous CuO layer has been explained by the redeposition of corrosion products. A mechanism of dissolution and precipitation has been proposed to explain the oxidation of Cu⁺ ions to Cu²⁺ ions in the case of an intense anodic oxidation peak [110]. The dissolution of copper is, therefore, followed by the redeposition of corrosion products at the electrode/electrolyte interface [63].

C. Influence grain boundary type

It is well established that intergranular corrosion of polycrystalline materials results from the particular corrosion properties of grain boundaries which are less resistant than grains. Intergranular corrosion has been defined as a "phenomenon of localized attack at the grain boundaries of metals and alloys" [111]. In such instances, the corrosion rate of a grain boundary is greater than that of the adjacent grains. An intergranular attack groove will then form between the grains. Ultimately, this can lead to propagation in the sub-surface region and thus greatly accelerate the degradation of the material.

Studies of the relationships between type of GBs and intergranular corrosion are most often carried out by characterizing the microstructure and the GB network after a chemical attack in more or less advanced stages where corrosion has penetrated below the surface and has spread into the GB network. Such studies have shown that low angle GBs are just as resistant to corrosion as grains [112]. In particular, it has been shown that a low disorientation of the grain boundaries is significant of low energy and confers a greater resistance to corrosion, thus confirming that the energy is stored at the level of the grain boundaries. Grains play a very important role in the resistance of metals to intergranular corrosion [113].

GBs of CSL Σ_3 type are common in face-centered cubic crystalline materials, especially copper. Depending on the inclination of the GB plane, they can be divided into two groups: Σ_3 coherent twins (or CT) and Σ_3 incoherent boundaries (or twins). It has been observed that among these two groups, only Σ_3 CTs are resistant to the propagation of intergranular corrosion [114]. This property was also observed at the extreme surface by electrochemical scanning tunneling microscopy (ECSTM) in the initiation stages of intergranular corrosion for GBs of linear morphology and arranged in parallel [108].

Among high angle GBs, CSL type GBs differ from random type GBs by the presence of a network of coincident sites at the interface. However, and despite this peculiarity, these special GBs, except for the Σ_3 coherent twins, would be just as sensitive to intergranular corrosion as random grain boundaries [114] [115].

In the ECSTM study of microcrystalline copper in 1 mM HCl, it was observed that the initiation of intergranular corrosion depends on the grain boundary character as the extent of intergranular attack depended on the nature of the GBs [116]. It was observed that only Σ_3 coherent twins were resistant to intergranular corrosion. Incoherent Σ_3 GBs, i.e. those Σ_3 that deviate from the ideal orientation, have shown a transition from resistance to susceptibility observed in a range of deviation from 1° to 1.7° . Random GBs were found to be susceptible to the aggressive acidic medium.

For the study of copper in basic medium, i.e. where a stable passive film can form, an ECSTM study of microcrystalline copper in NaOH showed that the passive film formed in the Cu(I) oxidation range was thicker at grain boundaries than on the grains [40]. Similarly, thicker passive films formed at the surface termination of random GBs than at the surface termination of Σ_3 coherent twins. The passivation properties were thus shown to be dependent on the type of grain boundaries.

Later on, in the study of microcrystalline copper in 0.1 M NaOH combining EBSD and in situ ECSTM local analysis, it was confirmed that the passivation by anodic oxidation in the Cu(I) range leads to the formation of a passive film which was locally thicker than formed on the adjacent grains due to higher consumption of copper at these GBs [117]. It was also confirmed that the Cu(I) passivation was in fact, less efficient at the edges of random boundaries than formed on the Σ_3 CSL boundaries. Also, it was established that even for Σ_3 CSL boundaries, the efficiency of formation of the passive film was not uniform but depends on the deviation of such boundaries from the ideal (111) plane; the lower the value of the deviation of angle, the more efficient will be the formation of the passive film.

The influence of grain boundary character distribution and connectivity in the network of high angle grain boundaries was explored in a recent study by potentiodynamic polarization tests of high purity copper in 0.1 M sodium chloride [118]. The study was focused on investigating the contribution of multiple twinning processes to interrupt the connectivity of random boundaries. It was again confirmed that low Σ CSL boundaries showed better resistance to intergranular corrosion, and the random boundaries network interrupted by multiple twinning during the annealing process was shown to exhibit better resistance to intergranular corrosion.

D. Influence of grain boundary type for other metals than copper

Before moving on to the final part of this literature review, a summary of the influence of the type of grain boundaries on metals other than copper is covered briefly in this part.

Aluminium is another very widely used metal, utilized either in its pure metallic form or as an alloy. A study on high purity aluminium was performed to identify the relationship between the susceptibility of different types of GBs to intergranular corrosion in HCl in three different concentrations (8, 16 and 38%)[119]. It was observed that low angle boundaries showed resistance against intergranular corrosion in all concentrations of HCl. Σ_3 twin boundaries showed higher resistance than random boundaries in 16 and 8% HCl. However, it was observed that to denote whether or not Σ_3 CSL boundaries displayed the so-called 'special' properties in a higher concentration of HCl (16 and 38%) was subject to which criterion, Brandon or Palumbo-Aust (See I.1.2 C), was employed to classify the GBs.

There are not many studies reported on the effect of grain boundaries type on intergranular corrosion for pure chromium. However, a model developed and applied to polarization and impedance measurements on chromium single crystals and polycrystalline material hypothesized that the dissolution of material at the grain boundaries was diffusion controlled [120].

1.3 Corrosion protection of copper and other metals by inhibitors

Corrosion inhibitors are defined as chemical compounds that are added at a low concentration to the corrosive medium to decrease the rate of corrosion of the material [121]. There are different criteria used to categorize corrosion inhibitors: by their mode of action (anodic, cathodic, or mixed) or by their chemical nature (organic or inorganic)

1.3.1 Anodic, cathodic and mixed inhibitors

Anodic inhibitors are those inhibitors that increase the value of the corrosion potential of the material. This increase in the corrosion potential promotes and favors the formation of a protective film on the surface [121]. Anodic inhibitors need to be introduced in sufficiently large quantities. If the quantity of inhibitors is not sufficient for the formation of a passivating layer to cover the entire surface, then this can result in creation of 'anodic zones' which are small surface areas that are prone to pitting corrosion.

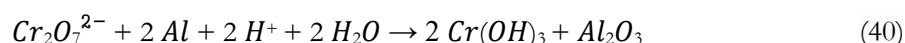
In contrast, cathodic inhibitors are a class of corrosion inhibitors that work by decreasing the rate of the cathodic reaction and therefore the corrosion potential. These are usually cations that precipitate on the surface to protect it. In comparison to anodic inhibitors, their efficiency is often lower but their use is simpler and, if they are used in an insufficient amount, they do not promote corrosion [121].

Mixed corrosion inhibitors are molecules that have both anodic and cathodic actions. Another way to categorize inhibitors is by their chemical nature.

1.3.2 Inorganic inhibitors

Inorganic inhibitors can themselves be classified into two categories: non-passivating inhibitors and passivating inhibitors. Non-passivating inhibitor form a precipitate on the surface that protects the surface while passivating inhibitors promotes the formation of a homogenous and insulating oxide layer.

CrO_4^{2-} chromate ions and $\text{Cr}_2\text{O}_7^{2-}$ dichromates are the majorly used inorganic inhibitors, commonly in the aeronautical sector for their exceptional properties and low cost. The Cr^{6+} ion adsorbs on the surface and proceeds to react with aluminium, which becomes passive according to the following equation:



Chromates, on the other hand, promote the formation of protective layers of alumina containing chromium oxide that helps to stabilize the natural oxide. Further, they are also known to inhibit intermetallic copper compounds [122] [123]. However, the major drawback of these widely used chromates and dichromates ions is that they are cancerogenic.

Several studies were undertaken to replace chromates with molybdates and tungstates. As molybdenum and tungsten are present within the same column of the periodic table as chromium, both MoO_4^{2-} and WO_4^{2-} have the same electronic structure as chromates. However, several studies have shown that the inhibition efficiency of these replacement ions is less than those of chromate due to their lower oxidizing power. Unlike Cr^{6+} ions, Mo^{6+} and W^{6+} ions cannot spontaneously passivate the surface and need an oxidant's contribution to form a protecting layer [124]–[126].

The phosphates PO_4^{3-} ions are other ions with similar protection behavior, but just like molybdates and tungstates, phosphate ions only passivate the metals in the presence of an oxidant [126] [127].

Lanthanide salts (La, Ce, Pr, Nd, etc.), commonly known as Rare Earths, have also shown to be promising substituents as an inorganic inhibitor to the toxic chromates. Cerium and lanthanum are cathodic inhibitors that form insoluble precipitates on the copper intermetallics. Ce^{3+} ions contained within the residues can be oxidized to Ce^{4+} to form an insoluble and protective CeO_2 precipitate on the surface. This prevents the transport of oxygen to the metal. This property makes cerium one of the most exploited rare earth elements [128] [129].

1.3.3 Organic inhibitors

The effectiveness of organic inhibitors is directly linked to their structures. They are mainly composed of benzene ring structure with a functional group that allows the molecule to be strongly adsorbed on the surface, leading to formation of a physical barrier that protects the metal from the aggressive medium, and possibly with a terminal functional group that makes the surface hydrophobic. Some organic inhibitors might have heteroatoms (nitrogen, sulfur, oxygen, etc.), interacting with the metal by σ bonds. The most commonly studied and used organic inhibitors have mercapto ($-\text{SH}$), amine (NH_2), phosphonates ($\text{C}-\text{PO}(\text{OR})_2$) and phosphate ($-\text{PO}_3^{2-}$) functional groups within their structure.

Triazoles and thiazoles are the most commonly used organic inhibitors. These classes of organic inhibitors have a structure including heterocycles with five constituents. In the case of triazoles, three of these five atoms in the heterocycle are nitrogen atoms. While in the case of thiazoles, within the heterocycle, one of the atoms is nitrogen, and there is one atom of sulfur. Benzotriazole is one of the most widely used inhibitors for the protection of copper. Other well-known and widely used organic inhibitors for copper and its alloys are 2-mercaptobenzothiazole and 2-mercaptobenzimidazole, both of which are the subject of this manuscript.

A. 2-mercaptobenzothiazole (2-MBT)

2-mercaptobenzothiazole (2-MBT) is a widely used organic inhibitor, particularly for the protection of copper and its alloys. It is also used for the protection of aluminium alloy 2024. Other than being a corrosion inhibitor, it has fungicidal properties. Due to its chelating properties, it is widely used in the mining industry to extract gold from ores [130]. It is used in the rubber industry, where it serves as a vulcanization accelerator, but it also acts as an agent for the manufacturing of other accelerators. These compounds catalyze the formation of disulfide bridges between unsaturated elastomeric polymers, leading to flexible and elastic materials.

2-MBT has an acid-base character with a pKa of ~6.9. 2-MBT has two possible structures and, due to tautomeric equilibrium, can adopt either a thiol form or a thione form (Figure 1.17). 2-MBT can also exist as an ionized thiolate form. Studies have shown that in solid-state the thione form of 2-MBT predominates [131]. The thione form of 2-MBT can oxidize to form 2-2'-dithiobis (benzothiazole) which is a dithiolate as can be seen in Figure 1.18.

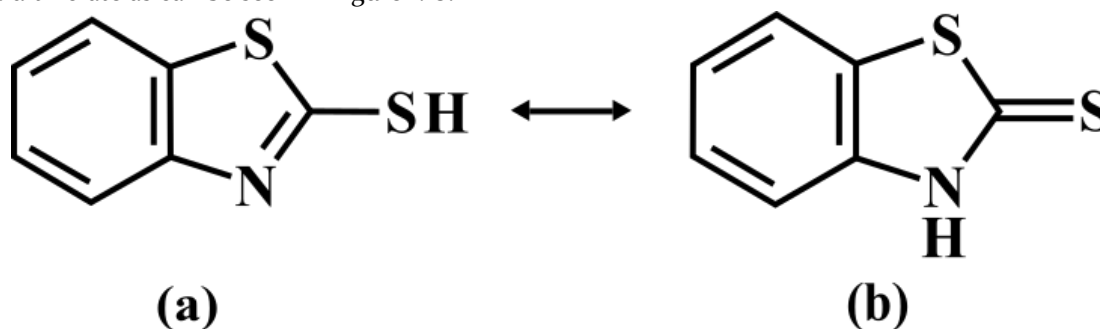


Figure 1.17: 2-MBT in its thiol form (a) and thione form (b)

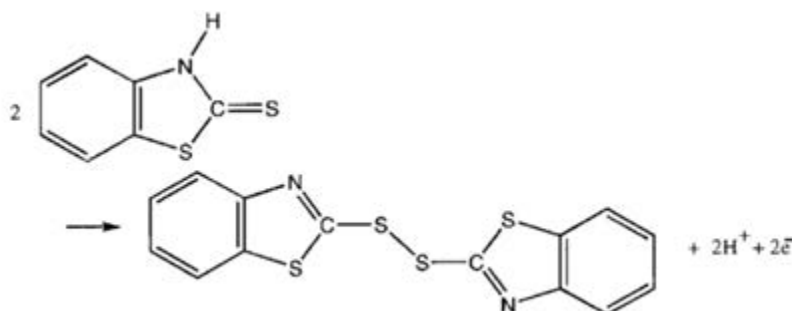


Figure 1.18: 2-2'-dithiobis (benzothiazole), a dithiolate formed from the thiol form of 2-MBT

One major drawback of 2-MBT is that it is recognized as harmful to the environment. 2-MBT exhibits allergen properties in humans, and one study has reported that 2-MBT might be carcinogenic [132].

As a corrosion inhibitor, 2-MBT was first used for copper and its alloys. It is now also very commonly used on aluminium alloys containing copper. Studies have shown that 2-MBT reacts with intermetallics rich in copper and reduces their cathodic and anodic activities [129]. However, the precise mechanism of action of the molecule is still subject to debate and depends strongly on the experimental conditions.

On copper, the mechanism of 2-MBT action was studied in acid, neutral and alkaline media. In acidic medium [133], it was shown that the addition of 2-MBT into the electrolyte inhibits both the anodic reaction, i.e. the metal dissolution, and the cathodic reactions. The presence of 2-MBT considerably reduces the current density in contrast to a reference without an inhibitor. The inhibition effect of 2-MBT would be due to the formation of Cu^+ -MBT complexes. However, overtime, the oxidation of 2-MBT takes place leading to the formation of a 2,2'-dithiobis (benzothiazol) dimer, which reacts with Cu^{2+} ions degrading the quality of the protective film. In another study in acidic medium, it was shown that 2-MBT acts as a mixed inhibitor for copper but this was attributed to adsorption by formation of non-covalent bonds of the electrostatic type. Similar observations were made regarding 2-MBI [134].

In a study of 2-MBT effects on copper in neutral phosphate solutions [135], electrochemical measurements associated with X-ray photoelectron spectroscopy (XPS) measurements showed that 2-MBT inhibits the anodic reaction by interacting with Cu^+ ions present at the surface via its nitrogen and exocyclic sulfur atoms. The film formed on the surface prevents the formation of Cu(II) phosphates, and the thickness of this film increases with time. Within the context of this study, it was shown that 2-MBT coordinated with two Cu^+ cations.

In another study in an alkaline medium, it was shown that the sulfur of the thiol form is ionized, favoring the adsorption of the molecule on the surface. This ionized thiol group then forms a thick and protective polymeric film [136].

Regarding the effect of 2-MBT in chlorinated media, using XPS surface analysis, it was shown that the presence of 2-MBT in the medium prevents the formation of copper species and chlorine compounds on the surface [137]. A comparison of the XPS spectra of the powdered molecule and the adsorbed molecule allowed the authors to determine that the molecule bound to the surface via its nitrogen atom and exocyclic sulfur atom. From the electrochemical impedance measurements, it was concluded that 2-MBT indeed acted as a mixed inhibitor acting on both cathodic and anodic reactions.

In another study of 2-MBT in a chlorinated medium [138], the presence of oxygen was shown to cause the gradual degradation of the protective film formed by 2-MBT. Due to the presence of O_2 , the molecule eventually oxidizes and forms the 2,2'- dimerdithiobis (benzothiazole) desorbing from the surface. Similar results were observed in a previous study [139].

2-MBT adsorption on copper was also studied by deposition from the vapor at ultra-low pressure on a Cu(111) single crystal [131] [132]. At room temperature, it was found by XPS that the molecule adsorbed on the oxide-free metallic surface through S bonding. In the initial stages of adsorption, the molecule partially decomposed, leaving atomic sulfur on the surface. The intact molecule remained flat in the monolayer adsorption regime with its two S atoms bonded to Cu atoms. The initial decomposition was found to be prevented by the pre-oxidation of the surface, with dissociation of the pre-formed 2D oxide accelerating the initial 2-MBT adsorption. Multilayers were formed with increasing exposure to 2-MBT vapor with the outermost molecules lying flat. In the case of the pre-oxidized Cu(111) surface, a more

homogenous and compact molecular layer was formed after dissociation of the pre-formed 2D-oxide as observed by STM.

For temperature higher than 100°C, the 2-MBT adsorbed layer decomposed to form an atomic sulfur layer characterized by a $(\sqrt{7} \times \sqrt{7})R19.1^\circ$ surface structure. Upon adsorption at ultra-low pressure at 150°C, a Moiré structure was formed that transformed into the $(\sqrt{7} \times \sqrt{7})R19.1^\circ$ structure at 250°C [130]. From examining copper surface oxidation behavior by dosing oxygen to this pre-adsorbed Moiré structure, it was concluded that the surface is better protected by this pre-adsorbed Moiré structure formed at 150°C than by the 2-MBT monolayer formed at room temperature.

The effect of the presence of 2-MBT has also been studied on other materials. With electrochemical impedance measurements, it was shown that 2-MBT had corrosion inhibition effects on silver and zinc in a solution of potassium chloride. Surface-enhanced Raman scattering (SERS) was employed to show that the orientation of the molecule depends on the surface. Thus, on silver, the molecule is tilted so as to form a bridge adsorbed configuration between its exocyclic sulfur atom and its nitrogen atom and the surface atoms. While on zinc, it is also tilted, but adsorption occurs via its two sulfur atoms [133].

A review of the various previous works confirmed that the 2-MBT reactivity and mechanism of action are dependent on the surface and the environment studied [134].

B. 2-mercaptobenzimidazole (2-MBI)

2-mercaptobenzimidazole (2-MBI) has a molecular structure very similar to that of 2-MBT (Figure 1.19). Just like 2-MBT, it is commonly used as an inhibitor on copper and as an antioxidant in the rubber industry. Also like 2-MBT, 2-MBI is affected by a tautomeric equilibrium and an acid-base equilibrium. The pKa of 2-MBI is ~10.4.

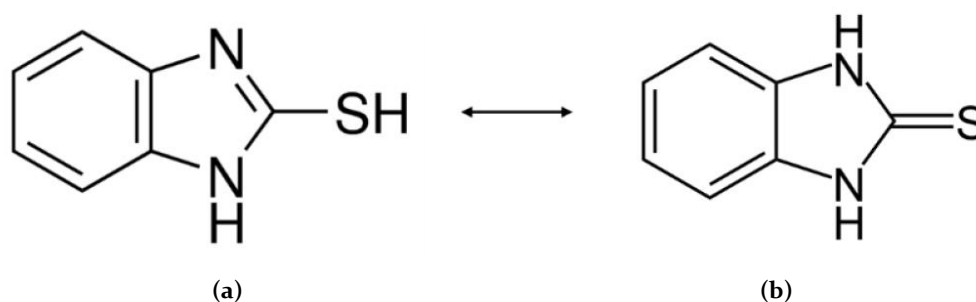


Figure 1.19: 2-MBT in it thiol form (a) and in its thione form (b)

Unlike 2-MBT, 2-MBI is not classified as dangerous for the environment but a few studies have shown its toxicity for humans and in particular on the thyroid and it is now classified SGH06 (toxic) according to regulations.

Like 2-MBT, 2-MBI is considered to be a mixed corrosion inhibitor. It is commonly used in applications of copper and its alloys. Other studies have also highlighted its effectiveness on steel [145].

In 1991, adsorption of 2-MBI on copper was studied using XPS and IR analysis [146]. The surface film formed by 2-MBI was reported to involve bonding via the S and N atoms of the molecule, and to be protective in acidic and alkaline environments.

The properties of 2-MBI on copper in a concentrated solution of NaCl (3 w%) were also investigated [147]. Using XPS, it was concluded that the molecule probably binds to the oxidized surface via its sulfur and nitrogen atom, forming a bridge configuration. The addition of 2-MBI prevents the formation of Cu(II)-containing species and the adsorption of chloride to the surface.

Note that as for 2-MBT, it was shown that the presence of oxygen promotes the formation of 2-MBI dimers (oxidation of the thiol function) over time, leading to the degradation of the protective film formed initially [139].

A synergistic effect between 2-MBI and potassium iodide to protect copper in acidic conditions was reported [159]. This effect was attributed to the formation of a relatively stable CuI_2 complex and the formation of a film (Cu^+ -MBI) protecting the surface. The iodide ions were not found to be directly incorporated into the protective film but were shown to promote the formation of the Cu^+ -MBI film.

Like for 2-MBT, STM, Auger electron spectroscopy (AES) and XPS were employed to study the adsorption of 2-MBI from the vapor at ultra-low pressure on model Cu(111) surfaces. On the metallic surface, it was observed the formation of a flat-lying and complete molecular layer bonded to the Cu atoms via the S and N atoms of the molecule [149]. Compared with 2-MBT, 2-MBI was concluded to form a thermally more stable molecular layer on the oxide-free surface but to be less effective against surface oxidation due to the presence of local defects in the molecular layer. From this comparative study between 2-MBT and 2-MBI, it was concluded that, at room temperature for copper, 2-MBT might offer better corrosion inhibition.

Several other studies have reported the effect of 2-MBI on the protection of stainless steels. For instance, in one study, the impact of 2-MBI on the protection of 316L stainless steel in NaCl solution was studied [150] [144]. The result showed that the effectiveness of the 2-MBI protection increases with its concentration but decreases with temperature. Electrochemical measurements also showed the efficiency of 2-MBI for the protection of 316L stainless steel against pitting corrosion.

1.3.4 DFT studies of 2-MBT and 2-MBI adsorption

DFT modeling has been employed to investigate the adsorption at low coverage of 2-MBI in its neutral and deprotonated forms on Cu(111) surfaces [151]. It was shown that when the molecule is neutral, two orientations are stable: either with the molecular plane parallel to the surface, and in this case, the molecule is physisorbed, or with the molecular plane perpendicular to the surface, and in this case, 2-MBI is chemisorbed via its sulfur and nitrogen atoms. For the deprotonated molecule, the authors reported that the adsorption energy is stronger. Again, the most stable orientation was when 2-MBI adsorbs via its sulfur and nitrogen atoms. This work showed that in this deprotonated state, the molecule cannot be physisorbed parallel to the surface like for the neutral molecule. The projection of the electron density of states of the molecule on the surface allowed the authors to understand the electronic properties associated with the metal/molecule interaction and confirm the formation of strong bonds between copper and the sulfur and nitrogen atoms. In the end, by comparing the adsorption energy of MBI with that of other studied molecules, a good correlation between adsorption force and inhibitory efficiency was reported.

In another study, DFT modelling was also used to study the adsorption of 2-MBI on Cu(111) and Al(111) surfaces at low coverage [152]. Studying the molecule alone allowed the authors to confirm that the thione form of the molecule was the most stable and that it could adsorb flat on both surfaces. They explain this orientation by the fact that the distribution of the HOMO and LUMO orbitals is relatively

equal over the whole molecule and that the reactive sites are distributed between the sulfur and nitrogen atoms and the electrons of the molecule.

In another study, the electronic properties, determined by quantum calculations, of different corrosion inhibitors, including 2-MBT, were found to be correlated with the effectiveness of the molecules against corrosion [153]. To supplement these data, the adsorption energy of an isolated molecule on Al(111) was calculated, and a good correlation between adsorption strength and efficiency of the inhibitor was reported.

Another work also employed DFT in an effort to rationalize the different corrosion inhibition efficiency of 5 imidazole derivatives (including 2-MBI) previously measured experimentally on copper [82]. It was shown that the adsorption energy is not sufficient to explain the results obtained experimentally. The thione form of the molecule was indeed found the most stable and the one that gets most strongly adsorbed to the surface. However, it was also shown that the thiol form is more prone to deprotonation (breaking an SH bond) than the thione form (breaking an NH bond), and that the resulting thiolate form interacts more strongly with the surface than the intact molecule. This work showed that the molecule is adsorbed in a bridge configuration via its nitrogen and sulfur atoms. In this work, DFT was also applied to study the formation of soluble complexes between molecules and the potentially dissolved Cu^{2+} ions coming from the surface, which would be detrimental for the protection of the surface. This reaction is not favored with 2-MBI, unlike with other inhibitors, which explains its better efficiency despite similar absorption energy. In this work, the authors also addressed the solubility of the molecule in the medium as another possible factor to consider. Thus, if the solubility of the molecule is too high, its affinity with the medium will be greater than with the surface thus reducing its adsorption.

DFT was also applied to compare the adsorption of 2-MBT and 2-MBI in thiol, thiolate and thione forms on Cu(111) [154]. It was found that the formation of a 2-MBI surface film was more exothermic than that of a 2-MBT film. At the interface with water in the low pH range, where Cu metal is in its non-oxidized form, the thione form of both 2-MBT and 2-MBI was found to predominate. Due to the lateral interactions between molecules within the organic layer, it was found that a 2-MBI molecular film adsorbs more strongly than a 2-MBT molecular film.

A recent DFT study of the interaction of 2-MBT on Cu(111) surface covered by an ultrathin $\text{Cu}_2\text{O}(111)$ film was also reported [155]. It was found that both the thione and the thiolate form of 2-MBT strongly interact with the oxidized copper surface and may substitute a terminal H_2O or OH layer at the surface of the Cu_2O film. This substitution would lead to the formation of a protective layer on the oxidized copper surface in an aqueous environment, explaining the corrosion protection efficiency of the 2-MBT molecule.

A similar DFT study of the adsorption of 2-MBI in thione and thiolate forms on model Cu(111)|| $\text{Cu}_2\text{O}(111)$ was also reported [156]. It was concluded that the formation of the protective monolayer of thione or thiolate species at full coverage was favored over adsorption at low coverage, with the molecular planes in perpendicular orientation. Amongst the two forms of 2-MBI, the thiolate formed showed stronger adsorption with the oxide-covered surface. The molecule bonded to the surface by forming a covalent bond between its most reactive site, the S atom, and the Cu atoms of the oxidized surface. Additional hydrogen bonds were formed between the NH group and the surface oxygen atoms. Overall, the calculations suggested that the stabilized thiolate form of 2-MBI might substitute water and hydroxyl terminal groups at the oxidized copper surface, and thus form a protective layer in an aqueous environment like in the case of 2-MBT.

References

- [1] Gottstein, G and Shvindelerman, L.S., *Grain boundary migration in metals: Thermodynamics, Kinetics, Applications.*, Materials Science and Technology. C. Press, 2010.
- [2] J.-M. Pénisson, F. Lançon, and U. Dahmen, "High Resolution Study of a Quasiperiodic Grain Boundary in Gold," *Materials Science Forum*, 1999. <https://www.scientific.net/MSF.294-296.27> (accessed Nov. 08, 2020).
- [3] L. Priester., *Les joints de grains, de la théorie à la pratique*. EDP Sciences, 2006.
- [4] H. K. D. H. Bhadeshia, *Worked examples in the geometry of crystals*. London: Institute of Metals, 1987.
- [5] L. Priester, "Geometrical speciality and special properties of grain boundaries," *Revue de Physique Appliquée*, vol. 24, no. 4, pp. 419–438, 1989, doi: 10.1051/rphysap:01989002404041900.
- [6] V. Randle, *The measurement of grain boundary geometry*. Bristol, Philadelphia: Institute of Physics Pub., 1993.
- [7] U. Puppet, *English: Illustration of tilt and twist grain boundaries. Remade in 3D to clarify details and rotation planes/axis (original: TiltAndTwistBoundaries.png)*. 2007.
- [8] A. R. Bausch et al., "Grain Boundary Scars and Spherical Crystallography," *Science*, vol. 299, no. 5613, pp. 1716–1718, Mar. 2003, doi: 10.1126/science.1081160.
- [9] A.D. (Tony) Rollett and S. R. Wilson, "Rodrigues vectors, unit Quaternions," presented at the Texture, Microstructure & Anisotropy, Carnegie melllon university, Jan. 02, 2015.
- [10] H. T. D. Montcel, L. Nazé, V. Maurel, N. Souaï, R. E. Logé, and J. Y. Guedou, "Ingénierie des joints de grain dans les alliages à base de Nickel," Aug. 2009, p. 6 p., Accessed: Oct. 24, 2020. [Online]. Available: <https://hal-mines-paristech.archives-ouvertes.fr/hal-00664517>.
- [11] D. Bachurin, D. Weygand, and P. Gumbsch, "Dislocation—grain boundary interaction in $\langle 111 \rangle$ textured thin metal films," 2010, doi: 10.1016/J.ACTAMAT.2010.05.037.
- [12] F.J. Humphreys and M. Hatherly, "Recrystallization and related annealing phenomena," Boston, MA: Elsevier, 2004, pp. 98–100.
- [13] O. Hardouin Duparc, "A review of some elements in the history of grain boundaries, centered on Georges Friedel, the coincident 'site' lattice and the twin index," *Journal of Materials Science*, vol. 46, pp. 4116–4134, Jun. 2011, doi: 10.1007/s10853-011-5367-1.
- [14] D. G. Brandon, "The structure of high-angle grain boundaries," *Acta Metallurgica*, vol. 14, no. 11, pp. 1479–1484, Nov. 1966, doi: 10.1016/0001-6160(66)90168-4.
- [15] G. Palumbo and K. T. Aust, "Structure-dependence of intergranular corrosion in high purity nickel," *Acta Metallurgica et Materialia*, vol. 38, no. 11, pp. 2343–2352, Nov. 1990, doi: 10.1016/0956-7151(90)90101-L.
- [16] Eita Tochigi, Atsutomo Nakamura, Naoya Shibata, and Yuichi Ikuhara, "Dislocation Structures in Low-Angle Grain Boundaries of α -Al₂O₃," *Crystals*, vol. 8, no. 3, p. 133, Mar. 2018, doi: <https://doi.org/10.3390/cryst8030133>.
- [17] M.A. Meyers and C. McCowan, "The formation of annealing twins: overview and new thoughts.," presented at the International Symposium on Interface Migration and Control of Microstructure, Detroit, Michigan, USA, Sep. 1984.
- [18] R. L. Fullman, "Crystallography and Interfacial Free Energy of Noncoherent Twin Boundaries in Copper," *Journal of Applied Physics*, vol. 22, no. 4, pp. 456–460, Apr. 1951, doi: 10.1063/1.1699983.
- [19] L. Priester, "Approche géométrique des joints de grains. Intérêt et limite," *Rev. Phys. Appl. (Paris)*, vol. 15, no. 4, pp. 789–830, Apr. 1980, doi: 10.1051/rphysap:01980001504078900.
- [20] M. Frary and C. A. Schuh, "Co2-MBlnation rule for deviant CSL grain boundaries at triple junctions," *Acta Materialia*, vol. 51, no. 13, pp. 3731–3743, Aug. 2003, doi: 10.1016/S1359-6454(03)00188-5.
- [21] D. Wolf, "Structure-energy correlation for grain boundaries in f.c.c. metals—IV. Asymmetrical twist (general) boundaries," *Acta Metallurgica et Materialia*, vol. 38, no. 5, pp. 791–798, May 1990, doi: 10.1016/0956-7151(90)90031-B.
- [22] W. Xu, M. Ferry, N. Mateescu, J. Cairney, and F. Humphreys, "Techniques for generating 3-D EBSD microstructures by FIB tomography," *Materials Characterization - MATER CHARACTER*, vol. 58, pp. 961–967, Oct. 2007, doi: 10.1016/j.matchar.2006.10.001.

- [23] A. J. Schwartz, "The potential engineering of grain boundaries through thermomechanical processing," *JOM*, vol. 50, no. 2, pp. 50–55, Feb. 1998, doi: 10.1007/s11837-998-0250-5.
- [24] J. K. MACKENZIE M. J. THOMSON, "SOME STATISTICS ASSOCIATED WITH THE RANDOM DISORIENTATION OF CUBES | Biometrika | Oxford Academic," *Biometrika*, vol. 44, no. 1–2, pp. 205–210, Jun. 1957.
- [25] S. Ratanaphan, T. Boonkird, R. Sarochawikasisit, H. Beladi, K. Barmak, and G. S. Rohrer, "Atomistic simulations of grain boundary energies in tungsten," *Materials Letters*, vol. 186, pp. 116–118, Jan. 2017, doi: 10.1016/j.matlet.2016.09.104.
- [26] T. Skidmore, R. G. Buchheit, and M. C. Juhas, "Grain boundary energy vs. misorientation in Inconel® 600 alloy as measured by thermal groove and OIM analysis correlation," *Scripta Materialia*, vol. 50, no. 6, pp. 873–877, Mar. 2004, doi: 10.1016/j.scriptamat.2003.12.004.
- [27] L. S. Shvindlerman and B. B. Straumal, "Regions of existence of special and non-special grain boundaries," *Acta Metallurgica*, vol. 33, no. 9, pp. 1735–1749, Sep. 1985, doi: 10.1016/0001-6160(85)90168-3.
- [28] K. K. Shih and J. C. M. Li, "Energy of grain boundaries between cusp misorientations," *Surface Science*, vol. 50, no. 1, pp. 109–124, May 1975, doi: 10.1016/0039-6028(75)90176-4.
- [29] G. C. Hasson and C. Goux, "Interfacial energies of tilt boundaries in aluminium. Experimental and theoretical determination," *Scripta Metallurgica*, vol. 5, no. 10, pp. 889–894, Oct. 1971, doi: 10.1016/0036-9748(71)90064-0.
- [30] W. T. Read and W. Shockley, "Dislocation Models of Crystal Grain Boundaries," *Phys. Rev.*, vol. 78, no. 3, pp. 275–289, May 1950, doi: 10.1103/PhysRev.78.275.
- [31] Takata, Naoki, Kenichi Ikeda, Fusahito Yoshida, H. Nakashima, and Hiroshi Abe. "Grain Boundary Structure and Its Energy of <110> Symmetric Tilt Boundary in Copper." *Materials Science Forum* 467–470, pp. 807–12, October 2004 <https://doi.org/10.4028/www.scientific.net/msf.467-470.807>.
- [32] "9780412450303: Phase Transformations in Metals and Alloys - AbeBooks - Porter, David A.; Easterling, Kenneth E.: 0412450305." <https://www.abebooks.fr/9780412450303/Phase-Transformations-Metals-Alloys-Porter-0412450305/plp> (accessed Oct. 24, 2020).
- [33] J. A. Zelinski, "An evaluation of grain boundary engineering technology and processing scale-up," Thesis, Massachusetts Institute of Technology, 2005.
- [34] L. T. Gillard Elsa, "Passivité et rupture de passivité de l'acier 304L en milieu acide nitrique concentré et chaud," Theses, Université Pierre et Marie Curie - Paris VI, 2014.
- [35] A. D'Aloya and A. N. Nikoloski, "The passivation of iron in ammoniacal solutions containing copper (II) ions," *Hydrometallurgy*, vol. 111–112, pp. 58–64, Jan. 2012, doi: 10.1016/j.hydromet.2011.10.003.
- [36] B. Narayanan, S. A. Deshmukh, S. K. R. S. Sankaranarayanan, and S. Ramanathan, "Strong correlations between structural order and passive state at water–copper oxide interfaces," *Electrochimica Acta*, vol. 179, pp. 386–393, 2015, doi: 10.1016/j.electacta.2015.03.221.
- [37] Q. Xu, K. Gao, Y. Wang, and X. Pang, "Characterization of corrosion products formed on different surfaces of steel exposed to simulated groundwater solution," *Applied Surface Science*, vol. 345, pp. 10–17, Aug. 2015, doi: 10.1016/j.apsusc.2015.03.143.
- [38] X. Gai *et al.*, "Electrochemical behaviour of passive film formed on the surface of Ti-6Al-4V alloys fabricated by electron beam melting," *Corrosion Science*, vol. 145, pp. 80–89, Dec. 2018, doi: 10.1016/j.corsci.2018.09.010.
- [39] M. Alvarez-Lopez *et al.*, "Corrosion behaviour of AZ31 magnesium alloy with different grain sizes in simulated biological fluids," *Acta Biomaterialia*, vol. 6, no. 5, pp. 1763–1771, May 2010, doi: 10.1016/j.actbio.2009.04.041.
- [40] H. Chen *et al.*, "Local passivation of metals at grain boundaries: In situ scanning tunneling microscopy study on copper," *Corrosion Science*, vol. 111, pp. 659–666, Oct. 2016, doi: 10.1016/j.corsci.2016.04.013.
- [41] A. Alfantazi, T. Ahmed, and D. Tromans, "Corrosion behavior of copper alloys in chloride media," *Materials & Design*, vol. 30, pp. 2425–2430, Aug. 2009, doi: 10.1016/j.matdes.2008.10.015.
- [42] S. G. Choudhary, "Emerging microbial control issues in cooling water systems," *Hydrocarbon Processing*, vol. 77, no. 5, May 1998, Accessed: Oct. 24, 2020. [Online]. Available: <https://www.osti.gov/biblio/616311-emerging-microbial-control-issues-cooling-water-systems>.
- [43] J. M. Cieslewicz and P.A. Schweitzer, *Copper and Copper Alloys, Corrosion and Corrosion Protection Handbook*, Second edition. Marcel Dekker, 1989.

- [44] G. J. Licina, *MIC in the Power Industry, Microbiologically Influenced Corrosion*. NACE International, 1993.
- [45] T. Y. Soror, "Scale and Corrosion Prevention in Cooling Water Systems Part I: Calcium Carbonate," *The Open Corrosion Journal*, vol. 2, no. 1, Mar. 2009, Accessed: Oct. 24, 2020. [Online]. Available: <https://benthamopen.com/ABSTRACT/TOCORRJ-2-45>.
- [46] H. A. Videla, "Prevention and control of biocorrosion," *International Biodeterioration & Biodegradation*, vol. 49, no. 4, pp. 259–270, Jun. 2002, doi: 10.1016/S0964-8305(02)00053-7.
- [47] M. J. N. Pourbaix and N. de Zoubov, *Atlas d'équilibres électrochimiques*. Paris: Gauthier-Villars, 1963.
- [48] Philippe Marcus, *Corrosion Mechanisms in Theory and Practice*, Third. CRC press, 2012.
- [49] "Cuprite." <https://www.mindat.org/min-1172.html> (accessed Nov. 08, 2020).
- [50] "Cuprite Mineral Data." <http://webmineral.com/data/Cuprite.shtml> (accessed Nov. 08, 2020).
- [51] R.G. Blundy, "The potential dependence of reaction product composition on copper-nickel alloys," *Corrosion Science*, vol. 12, pp. 65–75, 1972.
- [52] R. F. North and M. J. Pryor, "The influence of corrosion product structure on the corrosion rate of Cu-Ni alloys," *Corrosion Science*, vol. 10, no. 5, pp. 297–311, Jan. 1970, doi: 10.1016/S0010-938X(70)80022-1.
- [53] B. D. Craig, *Fundamental Aspects of Corrosion Films in Corrosion Science*. Springer US, 1991.
- [54] L. E. Eiselstein, B. C. Syrett, S. S. Wing, and R. D. Caligiuri, "The accelerated corrosion of Cu Ni alloys in sulphide-polluted seawater: Mechanism no. 2," *Corrosion Science*, vol. 23, no. 3, pp. 223–239, Jan. 1983, doi: 10.1016/0010-938X(83)90104-X.
- [55] G. Kear, B. D. Barker, and F. C. Walsh, "Electrochemical corrosion of unalloyed copper in chloride media—a critical review," *Corrosion Science*, vol. 46, no. 1, pp. 109–135, Jan. 2004, doi: 10.1016/S0010-938X(02)00257-3.
- [56] A. M. S. El Din and F. M. A. El Wahab, "The behaviour of the copper electrode in alkaline solutions upon alternate anodic and cathodic polarization," *Electrochimica Acta*, vol. 9, no. 1, pp. 113–121, Jan. 1964, doi: 10.1016/0013-4686(64)80010-4.
- [57] M. V. Vazquez, S. R. de Sanchez, E. J. Calvo, and D. J. Schiffrin, "The electrochemical reduction of hydrogen peroxide on polycrystalline copper in borax buffer," *Journal of Electroanalytical Chemistry*, vol. 374, no. 1, pp. 179–187, Aug. 1994, doi: 10.1016/0022-0728(94)03342-0.
- [58] M. Yamashita, K. Omura, and D. Hirayama, "Passivating behavior of copper anodes and its illumination effects in alkaline solutions," *Surface Science*, vol. 96, no. 1, pp. 443–460, Jun. 1980, doi: 10.1016/0039-6028(80)90319-2.
- [59] B. Millet, C. Fiaud, C. Hinnen, and E. M. M. Sutter, "A correlation between electrochemical behaviour, composition and semiconducting properties of naturally grown oxide films on copper," *Corrosion Science*, vol. 37, no. 12, pp. 1903–1918, Dec. 1995, doi: 10.1016/0010-938X(95)00072-R.
- [60] B. Millet, "Etude électrochimique et photoélectrochimique de couches d'oxydes de cuivre semi-conductrices. Rôle d'un inhibiteur de corrosion du cuivre," l'université Paris VI, 1994.
- [61] K.R. Trethewey and J. Chamberlain, *Passivation behavior of copper anodes and its illumination effect in alkaline solutions*. Longman, Harlow, 1995.
- [62] J. C. Hamilton, J. C. Farmer, and R. J. Anderson, "In Situ Raman Spectroscopy of Anodic Films Formed on Copper and Silver in Sodium Hydroxide Solution," *J. Electrochem. Soc.*, vol. 133, no. 4, p. 739, Apr. 1986, doi: 10.1149/1.2108666.
- [63] H.-H. Strehblow and B. Titze, "The investigation of the passive behaviour of copper in weakly acid and alkaline solutions and the examination of the passive film by esca and ISS," *Electrochimica Acta*, vol. 25, no. 6, pp. 839–850, Jun. 1980, doi: 10.1016/0013-4686(80)90036-5.
- [64] Y. Van Ingelgem, E. Tourwé, J. Vereecken, and A. Hubin, "Application of multisine impedance spectroscopy, FE-AES and FE-SEM to study the early stages of copper corrosion," *Electrochimica Acta*, vol. 53, no. 25, pp. 7523–7530, Oct. 2008, doi: 10.1016/j.electacta.2008.01.052.
- [65] K. P. FitzGerald, J. Nairn, G. Skennerton, and A. Atrens, "Atmospheric corrosion of copper and the colour, structure and composition of natural patinas on copper," *Corrosion Science*, vol. 48, no. 9, pp. 2480–2509, Sep. 2006, doi: 10.1016/j.corsci.2005.09.011.
- [66] "Tenorite." <https://www.mindat.org/min-3912.html> (accessed Nov. 08, 2020).
- [67] "Tenorite Mineral Data." <http://webmineral.com/data/Tenorite.shtml> (accessed Nov. 08, 2020).
- [68] G. Tunell, E. Posnjak, and C. J. Ksanda, "Geometrical and Optical Properties, and Crystal Structure of Tenorite," *Zeitschrift für Kristallographie - Crystalline Materials*, vol. 90, no. 1–6, Jan. 1935, doi: 10.1524/zkri.1935.90.1.120.

- [69] PubChem, "Copper(II) oxide." <https://pubchem.ncbi.nlm.nih.gov/compound/14829> (accessed Nov. 08, 2020).
- [70] J.-B. He, D.-Y. Lu, and G.-P. Jin, "Potential dependence of cuprous/cupric duplex film growth on copper electrode in alkaline media," *Applied Surface Science*, vol. 253, no. 2, pp. 689–697, Nov. 2006, doi: 10.1016/j.apsusc.2005.12.159.
- [71] J. Kunze, V. Maurice, L. H. Klein, H.-H. Strehblow, and P. Marcus, "In situ STM study of the duplex passive films formed on Cu(111) and Cu(001) in 0.1 M NaOH," *Corrosion Science*, vol. 46, no. 1, pp. 245–264, Jan. 2004, doi: 10.1016/S0010-938X(03)00140-9.
- [72] A. H. Jayatissa, K. Guo, and A. C. Jayasuriya, "Fabrication of cuprous and cupric oxide thin films by heat treatment," *Applied Surface Science*, vol. 255, no. 23, pp. 9474–9479, Sep. 2009, doi: 10.1016/j.apsusc.2009.07.072.
- [73] Bari RH, Patil SB, and Bari AR, "Spray-pyrolized nanostructured CuO thin films for H₂S gas sensor," *International Nano Letters*, vol. 3, pp. 1–5, 2013.
- [74] H. Zhu, J. Zhang, C. Li, F. Pan, T. Wang, and B. Huang, "Cu₂O thin films deposited by reactive direct current magnetron sputtering," *Thin Solid Films*, vol. 517, no. 19, pp. 5700–5704, Aug. 2009, doi: 10.1016/j.tsf.2009.02.127.
- [75] M. Heinemann, B. Eifert, and C. Heiliger, "Band structure and phase stability of the copper oxides Cu₂O, CuO, and Cu₄O₃" *Phys. Rev. B*, vol. 87, no. 11, p. 115111, Mar. 2013, doi: 10.1103/PhysRevB.87.115111.
- [76] Thien Viet Pham, Manohar Rao, P. Andreasson, Yuan Peng, Junling Wang, and K. B. Jinesh, "Photocurrent generation in Cu_xO thin films deposited by radio frequency sputtering," *Appl. Phys. Lett.*, vol. 102, no. 3, pp. 32–101, 2013.
- [77] N. Serin, T. Serin, Ş. Horzum, and Y. Çelik, "Annealing effects on the properties of copper oxide thin films prepared by chemical deposition," *Semicond. Sci. Technol.*, vol. 20, no. 5, pp. 398–401, Mar. 2005, doi: 10.1088/0268-1242/20/5/012.
- [78] Y. Feng, K.-S. Siow, W.-K. Teo, K.-L. Tan, and A.-K. Hsieh, "Corrosion Mechanisms and Products of Copper in Aqueous Solutions at Various pH Values," *corrosion science*, vol. 53, pp. 389–398, 1997.
- [79] S. Sathiyarayanan, M. Sahre, and W. Kautek, "In-situ grazing incidence X-ray diffractometry observation of pitting corrosion of copper in chloride solutions," *Corrosion Science*, vol. 41, no. 10, pp. 1899–1909, Oct. 1999, doi: 10.1016/S0010-938X(99)00021-9.
- [80] G. Bianchi and P. Longhi, "Copper in sea-water, potential-pH diagrams," *Corrosion Science*, vol. 13, no. 11, pp. 853–864, Jan. 1973, doi: 10.1016/S0010-938X(73)80067-8.
- [81] "G. D. Bengough, R. M. Jones, R. Pirret," *Journal of the Institute of Metals*, vol. 23, p. 65, 1920.
- [82] Francis Dabosi, Gérard Béranger, and Bernard Baroux, *Corrosion localisée*, Les Editions de physique., French, France, 1994.
- [83] J. Kruger, "The Oxide Films Formed on Copper Single Crystal Surfaces in Pure Water: I. Nature of the Films Formed at Room Temperature," *J. Electrochem. Soc.*, vol. 106, no. 10, p. 847, Oct. 1959, doi: 10.1149/1.2427161.
- [84] B. Miller and M. I. Bellavance, "Rotating Ring-Disk Electrode Studies of Corrosion Rates and Partial Currents: Cu and Cu₃₀Zn in Oxygenated Chloride Solutions," *J. Electrochem. Soc.*, vol. 119, no. 11, p. 1510, Nov. 1972, doi: 10.1149/1.2404033.
- [85] H. P. Dhar, R. E. White, G. Burnell, L. R. Cornwell, R. B. Griffin, and R. Darby, "Corrosion of Cu and Cu-Ni Alloys in 0.5M NaCl and in Synthetic Seawater," *CORROSION*, vol. 41, no. 6, pp. 317–323, Jun. 1985, doi: 10.5006/1.3582011.
- [86] U. R. Evans, "Oxygen Distribution as a Factor in the Corrosion of Metals.," *Ind. Eng. Chem.*, vol. 17, no. 4, pp. 363–372, Apr. 1925, doi: 10.1021/ie50184a012.
- [87] G. Faïta, G. Fiori, and D. Salvatore, "Copper behaviour in acid and alkaline brines—I kinetics of anodic dissolution in 0.5M NaCl and free-corrosion rates in the presence of oxygen," *Corrosion Science*, vol. 15, no. 6, pp. 383–392, Jan. 1975, doi: 10.1016/0010-938X(75)90005-0.
- [88] H. P. Lee and K. Nobe, "Kinetics and Mechanisms of Cu Electrodeposition in Chloride Media," *J. Electrochem. Soc.*, vol. 133, no. 10, p. 2035, Oct. 1986, doi: 10.1149/1.2108335.
- [89] J. Mathiyarasu, N. Palaniswamy, and V.S. Muralidharan, "Proceedings of the Indian Academy of Sciences," *Chemical Sciences*, vol. 111, pp. 377–386, 1999.
- [90] D. D. Macdonald, "Cyclic Voltammetry of Copper Metal in Lithium Hydroxide Solution at Elevated Temperatures," *J. Electrochem. Soc.*, vol. 121, no. 5, p. 651, May 1974, doi: 10.1149/1.2401879.

- [91] F. Mansfeld, G. Liu, H. Xiao, C. H. Tsai, and B. J. Little, "The corrosion behavior of copper alloys, stainless steels and titanium in seawater," *Corrosion Science*, vol. 36, no. 12, pp. 2063–2095, Dec. 1994, doi: 10.1016/0010-938X(94)90008-6.
- [92] G.D. Preston and L.L. Bircumshaw, "Studies on the oxidation of metals Part II. Copper, brass, aluminium-brass, aluminium-bronze, magnesium and magnesium alloys," *Philosophical Magazine*, vol. 20, pp. 706–720, 1935.
- [93] A. L. Bacarella and J. C. G. Jr, "The Anodic Dissolution of Copper in Flowing Sodium Chloride Solutions Between 25° and 175°C," *J. Electrochem. Soc.*, vol. 120, no. 4, p. 459, Apr. 1973, doi: 10.1149/1.2403477.
- [94] A. Moreau, J. P. Frayret, F. D. Rey, and R. Pointeau, "Etude des phenomenes electrochimiques et des transports de matiere d'un systeme metal electrolytique: cas d'un disque tournant en cuivre dans des solutions aqueuses d'acide chlorhydrique," *Electrochimica Acta*, vol. 27, no. 9, pp. 1281–1291, Sep. 1982, doi: 10.1016/0013-4686(82)80149-7.
- [95] C. Deslouis, B. Tribollet, G. Mengoli, and M. M. Musiani, "Electrochemical behaviour of copper in neutral aerated chloride solution. I. Steady-state investigation," *J Appl Electrochem*, vol. 18, no. 3, pp. 374–383, May 1988, doi: 10.1007/BF01093751.
- [96] C. Deslouis, O. R. Mattos, M. M. Musiani, and B. Tribollet, "Comments on mechanisms of copper electrodisolution in chloride media," *Electrochimica Acta*, vol. 38, no. 18, pp. 2781–2783, Dec. 1993, doi: 10.1016/0013-4686(93)85099-K.
- [97] J. Crousier, L. Pardessus, and J.P. Crousier, "Voltamétrie study of copper in chloride solution," *Electrochimica Acta*, vol. 33, pp. 1039–1042, 1988.
- [98] G. Kiliççeker and H. Galip, "The effects of acetate ions (CH₃COO⁻) on electrochemical behavior of copper in chloride solutions," *Materials Chemistry and Physics*, vol. 110, no. 2, pp. 380–386, Aug. 2008, doi: 10.1016/j.matchemphys.2008.02.026.
- [99] J. Newman and B. Tribollet, "Impedance Model for A Concentrated-Solution - Application to the Electrodisolution of Copper in Chloride Solutions," Dec. 1983, Accessed: Nov. 10, 2020. [Online]. Available: <https://www.rti.org/publication/impedance-model-concentrated-solution-application-electrodisolution-copper-chloride>.
- [100] R. J. K. Wood, S. P. Hutton, and D. J. Schiffrin, "Mass transfer effects of non-cavitating seawater on the corrosion of Cu and 70Cu-30Ni," *Corrosion Science*, vol. 30, no. 12, pp. 1177–1201, Jan. 1990, doi: 10.1016/0010-938X(90)90198-E.
- [101] A. El Warraky, H. A. El Shayeb, and E. M. Sherif, "Pitting corrosion of copper in chloride solutions," *Anti-Corrosion Methods and Materials*, vol. 51, no. 1, pp. 52–61, Jan. 2004, doi: 10.1108/00035590410512735.
- [102] T. Dickinson, A.F. Povey, and P.M.A. Sherwood, "Dissolution and passivation of nickel, an X-ray photoelectron spectroscopie study," *Chem. Soc. Faraday Trans*, vol. 73, no. 1, pp. 327–343, 1977.
- [103] V. Maurice, H.H. Strehblow, and P. Marcus, "In Situ STM Study of the Passivation of Cu(III)," *J. Electrochem. Soc.*, vol. 146, pp. 524–540, 1999.
- [104] V. Maurice, L.H. Klein, and P. Marcus, "Atomic Structure of Metastable Pits Formed on Nickel," *Electrochem. Solid-State Lett.*, vol. 4, pp. B1–B3, 2001.
- [105] P. Marcus, J. Oudar, I. Olefjord, and J. Microsc, "XPS-Study of The Passive Film on Nickel," *Spectrosc. Electron*, vol. 4, p. 63, 1979.
- [106] H. Miyamoto, K. Harada, T. Mimaki, A. Vinogradov, and S. Hashimoto, "Corrosion of ultra-fine grained copper fabricated by equal-channel angular pressing," *Corrosion Science*, vol. 50, no. 5, pp. 1215–1220, May 2008, doi: 10.1016/j.corsci.2008.01.024.
- [107] A. Vinogradov, H. Miyamoto, T. Mimaki, and S. Hashimoto, "Corrosion, stress corrosion cracking and fatigue of ultra-fine grain copper fabricated by severe plastic deformation," *Annales de Chimie Science des Matériaux*, vol. 27, no. 3, pp. 65–75, May 2002.
- [108] L. Lapeire, E. Martinez Lombardia, I. De Graeve, H. Terry, and K. Verbeken, "Influence of grain size on the electrochemical behavior of pure copper," *J Mater Sci*, vol. 52, no. 3, pp. 1501–1510, Feb. 2017, doi: 10.1007/s10853-016-0445-z.
- [109] M. Zhao, H. Song, J. Li, G. He, G. He, and Y. Gui, "Origin of the Zn-induced Al intergranular corrosion of the outermost surface layer of the aluminium grain boundary: An ab initio study," *Computational Materials Science*, vol. 102, pp. 78–84, 2015.
- [110] D. W. Shoesmith, T. E. Rummery, D. Owen, and W. Lee, "Anodic Oxidation of Copper in Alkaline Solutions: I. Nucleation and Growth of Cupric Hydroxide Films," *J. Electrochem. Soc.*, vol. 123, no. 6, p. 790, Jun. 1976, doi: 10.1149/1.2132934.

- [111] Beaunier, L., Beranger, G., Charbonnier, J.C., and Cihal, V., "Corrosion intergranulaire," *Corrosion localisée*, Les Editions de Physique, pp. 286–320, 1994.
- [112] R. D. Leggeti and H. W. Paxton, "The corrosion of single crystals, bicrystals and polycrystals of an austenitic stainless steel in boiling nitric acid," *Corrosion Science*, vol. 2, no. 3, pp. 211–223, Jan. 1962, doi: 10.1016/0010-938X(62)90022-7.
- [113] T. Watanabe, "Approach to grain boundary design for strong and ductile polycrystals," *Res Mechanica*, vol. 11, pp. 47–84, 1984.
- [114] C. Hu *et al.*, "Improving the intergranular corrosion resistance of 304 stainless steel by grain boundary network control," *Corrosion Science*, vol. 53, no. 5, pp. 1880–1886, May 2011, doi: 10.1016/j.corsci.2011.02.005.
- [115] M. Michiuchi, H. Kokawa, Z. J. Wang, Y. S. Sato, and K. Sakai, "Twin-induced grain boundary engineering for 316 austenitic stainless steel," *Acta Materialia*, vol. 54, no. 19, pp. 5179–5184, Nov. 2006, doi: 10.1016/j.actamat.2006.06.030.
- [116] M. Bettayeb, V. MAURICE, L. H. Klein, L. Lapeire, K. Verbeken, and P. Marcus, "Nanoscale Intergranular Corrosion and Relation with Grain Boundary Character as Studied In Situ on Copper," *Journal of The Electrochemical Society*, vol. 165, no. 11, pp. 835–841, 2018, doi: 10.1149/2.134181jes.
- [117] M. Bettayeb, V. Maurice, L. H. Klein, L. Lapeire, K. Verbeken, and P. Marcus, "Co₂-MBIned in situ microstructural study of the relationships between local grain boundary structure and passivation on microcrystalline copper," *Electrochimica Acta*, vol. 305, pp. 240–246, May 2019, doi: 10.1016/j.electacta.2019.03.054.
- [118] Y. Yuan, Y. Jiang, J. Zhou, G. Liu, and X. Ren, "Influence of grain boundary character distribution and random high angle grain boundaries networks on intergranular corrosion in high purity copper," *Materials Letters*, vol. 253, pp. 424–426, Oct. 2019, doi: 10.1016/j.matlet.2019.07.125.
- [119] S. Kim, U. Erb, K. Aust, and G. Palumbo, "Grain boundary character distribution and intergranular corrosion behavior in high purity aluminum," 2001, doi: 10.1016/S1359-6462(00)00682-5.
- [120] J. a. L. Dobbelaar and J. H. W. de Wit, "The Corrosion Behavior of Polycrystalline and Single Crystal Chromium: A Revised Model," *J. Electrochem. Soc.*, vol. 139, no. 3, p. 716, Mar. 1992, doi: 10.1149/1.2069290.
- [121] "Corrosion Vieillissement," Jul. 10, 1990. <https://www.techniques-ingenieur.fr/base-documentaire/materiaux-th11/methodes-de-prevention-et-lutte-contre-la-corrosion-42374210/inhibiteurs-de-corrosion-cor1005/> (accessed Nov. 11, 2020).
- [122] R. L. Twite and G. P. Bierwagen, "Review of alternatives to chromate for corrosion protection of aluminum aerospace alloys," *Progress in Organic Coatings*, vol. 33, no. 2, pp. 91–100, Feb. 1998, doi: 10.1016/S0300-9440(98)00015-0.
- [123] M. Kendig, S. Jeanjaquet, R. Addison, and J. Waldrop, "Role of hexavalent chromium in the inhibition of corrosion of aluminum alloys," *Surface and Coatings Technology*, vol. 140, no. 1, pp. 58–66, May 2001, doi: 10.1016/S0257-8972(01)01099-4.
- [124] K. C. Emregül and A. A. Aksüt, "The effect of sodium molybdate on the pitting corrosion of aluminum," *Corrosion Science*, vol. 45, no. 11, pp. 2415–2433, Nov. 2003, doi: 10.1016/S0010-938X(03)00097-0.
- [125] C. B. Breslin, G. Treacy, and W. M. Carroll, "Studies on the passivation of aluminium in chromate and molybdate solutions," *Corrosion Science*, vol. 36, no. 7, pp. 1143–1154, Jul. 1994, doi: 10.1016/0010-938X(94)90139-2.
- [126] J. Sinko, "Challenges of chromate inhibitor pigments replacement in organic coatings," *Progress in Organic Coatings*, vol. 42, no. 3, pp. 267–282, Sep. 2001, doi: 10.1016/S0300-9440(01)00202-8.
- [127] H. Konno, S. Kobayashi, H. Takahashi, and M. Nagayama, "The hydration of barrier oxide films on aluminium and its inhibition by chromate and phosphate ions," *Corrosion Science*, vol. 22, no. 10, pp. 913–923, Jan. 1982, doi: 10.1016/0010-938X(82)90061-0.
- [128] A. Kolics, A. S. Besing, P. Baradlai, and A. Wieckowski, "Cerium Deposition on Aluminum Alloy 2024-T3 in Acidic NaCl Solutions," *J. Electrochem. Soc.*, vol. 150, no. 11, p. B512, Sep. 2003, doi: 10.1149/1.1615995.
- [129] S. V. Lamaka, M. L. Zheludkevich, K. A. Yasakau, M. F. Montemor, and M. G. S. Ferreira, "High effective organic corrosion inhibitors for 2024 aluminium alloy," *Electrochimica Acta*, vol. 52, no. 25, pp. 7231–7247, Sep. 2007, doi: 10.1016/j.electacta.2007.05.058.

- [130] "A SERS spectroelectrochemical investigation of the interaction of 2-mercaptobenzothiazole with copper, silver and gold surfaces | SpringerLink." <https://link.springer.com/article/10.1023%2FA%3A1026561914338> (accessed Nov. 11, 2020).
- [131] A. L. R. Silva and M. D. M. C. Ribeiro da Silva, "Energetic, structural and tautomeric analysis of 2-mercaptobenzimidazole," *J Therm Anal Calorim*, vol. 129, no. 3, pp. 1679–1688, Sep. 2017, doi: 10.1007/s10973-017-6353-x.
- [132] M. H. Whittaker, A. M. Gebhart, T. C. Miller, and F. Hammer, "Human health risk assessment of 2-mercaptobenzothiazole in drinking water," *Toxicol Ind Health*, vol. 20, no. 6–10, pp. 149–163, Jul. 2004, doi: 10.1191/0748233704th1990a.
- [133] J. C. Marconato, L. O. Bulhões, and M. L. Temperini, "A spectroelectrochemical study of the inhibition of the electrode process on copper by 2-mercaptobenzothiazole in ethanolic solutions," *Electrochimica Acta*, vol. 43, no. 7, pp. 771–780, Jan. 1998, doi: 10.1016/S0013-4686(97)00204-1.
- [134] T. Shahrabi, H. Tavakholi, and M. G. Hosseini, "Corrosion inhibition of copper in sulphuric acid by some nitrogen heterocyclic compounds," *Anti-Corrosion Methods and Materials*, vol. 54, no. 5, pp. 308–313, Jan. 2007, doi: 10.1108/00035590710822161.
- [135] L. P. Kazansky, I. A. Selyaninov, and Yu. I. Kuznetsov, "Adsorption of 2-mercaptobenzothiazole on copper surface from phosphate solutions," *Applied Surface Science*, vol. 258, no. 18, pp. 6807–6813, Jul. 2012, doi: 10.1016/j.apsusc.2012.03.097.
- [136] R. Subramanian and V. Lakshminarayanan, "Effect of adsorption of some azoles on copper passivation in alkaline medium," *Corrosion Science*, vol. 44, no. 3, pp. 535–554, Mar. 2002, doi: 10.1016/S0010-938X(01)00085-3.
- [137] M. Finšgar and D. Kek Merl, "An electrochemical, long-term immersion, and XPS study of 2-mercaptobenzothiazole as a copper corrosion inhibitor in chloride solution," *Corrosion Science*, vol. 83, pp. 164–175, Jun. 2014, doi: 10.1016/j.corsci.2014.02.016.
- [138] J. Li, C. W. Du, Z. Y. Liu, X. G. Li, and M. Liu, "Inhibition Film Formed by 2-mercaptobenzothiazole on Copper Surface and Its Degradation Mechanism in Sodium Chloride Solution," *Int. J. Electrochem. Sci*, vol. 11, pp. 10690–10705, 2016.
- [139] D. Chadwick and T. Hashemi, "Electron spectroscopy of corrosion inhibitors: Surface films formed by 2-mercaptobenzothiazole and 2-mercaptobenzimidazole on copper," *Surface Science*, vol. 89, no. 1, pp. 649–659, Jan. 1979, doi: 10.1016/0039-6028(79)90646-0.
- [140] X. Wu, F. Wiame, V. Maurice, and P. Marcus, "Moiré Structure of the 2-Mercaptobenzothiazole Corrosion Inhibitor Adsorbed on a (111)-Oriented Copper Surface," *J. Phys. Chem. C*, vol. 124, no. 29, pp. 15995–16001, Jul. 2020, doi: 10.1021/acs.jpcc.0c04083.
- [141] X. Wu, F. Wiame, V. Maurice, and P. Marcus, "Adsorption and thermal stability of 2-mercaptobenzothiazole corrosion inhibitor on metallic and pre-oxidized Cu(111) model surfaces," *Applied Surface Science*, vol. 508, p. 145132, Apr. 2020, doi: 10.1016/j.apsusc.2019.145132.
- [142] X. Wu, F. Wiame, V. Maurice, and P. Marcus, "2-Mercaptobenzothiazole corrosion inhibitor deposited at ultra-low pressure on model copper surfaces," *Corrosion Science*, vol. 166, p. 108464, Apr. 2020, doi: 10.1016/j.corsci.2020.108464.
- [143] H. Yang *et al.*, "2-Mercaptobenzothiazole monolayers on zinc and silver surfaces for anticorrosion," *Corrosion Science*, vol. 50, no. 11, pp. 3160–3167, Nov. 2008, doi: 10.1016/j.corsci.2008.08.036.
- [144] M. Antonijevic and M. Petrovic Mihajlovic, "Copper Corrosion Inhibitors. A review," *International Journal of Electrochemical Science*, vol. 3, no. 1, pp. 1–28, Jan. 2008.
- [145] "Suitability and Stability of 2-Mercaptobenzimidazole as a Corrosion Inhibitor in a Post-Combustion CO₂ Capture System CORROSION." <https://www.corrosionjournal.org/doi/abs/10.5006/1524> (accessed Nov. 11, 2020).
- [146] G. Xue, X.-Y. Huang, J. Dong, and J. Zhang, "The formation of an effective anti-corrosion film on copper surfaces from 2-mercaptobenzimidazole solution," *Journal of Electroanalytical Chemistry and Interfacial Electrochemistry*, vol. 310, no. 1, pp. 139–148, Jul. 1991, doi: 10.1016/0022-0728(91)85257-P.
- [147] M. Finšgar, "2-Mercaptobenzimidazole as a copper corrosion inhibitor: Part II. Surface analysis using X-ray photoelectron spectroscopy," *Corrosion Science*, vol. 72, pp. 90–98, Jul. 2013, doi: 10.1016/j.corsci.2013.03.010.
- [148] D.-Q. Zhang, L.-X. Gao, and G.-D. Zhou, "Synergistic effect of 2-mercapto benzimidazole and KI on copper corrosion inhibition in aerated sulfuric acid solution," *Journal of Applied Electrochemistry*, vol. 33, no. 5, pp. 361–366, May 2003, doi: 10.1023/A:1024403314993.

- [149] Xiaocui WU, Frederic Wiame, Vincent Maurice, and Philippe Marcus, "2-MBI deposition on pristine and pre-oxidized Cu(111) surfaces at room temperature," *Applied Surface Science*.
- [150] S. A. M. Refaey, F. Taha, and A. M. A. El-malak, "Corrosion and Inhibition of 316L stainless steel in neutral medium by 2-Mercaptobenzimidazole," *Int. J. Electrochem. Sci*, vol. 1, pp. 80–91, 2006.
- [151] S. Sun, Y. Geng, L. Tian, S. Chen, Y. Yan, and S. Hu, "Density functional theory study of imidazole, benzimidazole and 2-mercaptobenzimidazole adsorption onto clean Cu(111) surface," *Corrosion Science*, vol. 63, pp. 140–147, Oct. 2012, doi: 10.1016/j.corsci.2012.05.024.
- [152] B. Obot, Z. M. Gasem, and S. A. Umoren, "Understanding the mechanism of 2-mercaptobenzimidazole adsorption on Fe (110), Cu (111) and Al (111) surfaces: DFT and molecular dynamics simulations approaches," *Int. J. Electrochem. Sci*, vol. 9, no. 5, pp. 2367–2378, 2014.
- [153] M. K. Awad, M. R. Mustafa, and M. M. Abouelnga, "Quantum chemical studies and atomistic simulations of some inhibitors for the corrosion of al surface," *Prot Met Phys Chem Surf*, vol. 52, no. 1, pp. 156–168, Jan. 2016, doi: 10.1134/S2070205116010032.
- [154] E. Vernack, D. Costa, P. Tingaut, and P. Marcus, "DFT studies of 2-mercaptobenzothiazole and 2-mercaptobenzimidazole as corrosion inhibitors for copper," *Corrosion Science*, vol. 174, p. 108840, Sep. 2020, doi: 10.1016/j.corsci.2020.108840.
- [155] F. Chiter, D. Costa, V. Maurice, and P. Marcus, "DFT investigation of 2-mercaptobenzothiazole adsorption on model oxidized copper surfaces and relationship with corrosion inhibition," *Applied Surface Science*, vol. 537, p. 147802, Jan. 2021, doi: 10.1016/j.apsusc.2020.147802.
- [156] Fatah Chiter, Dominique Costa, Vincent Maurice, and Philippe Marcus, "Adsorption of 2-mercaptobenzimidazole corrosion inhibitor on copper: DFT study on model oxidized interfaces," *Journal of the Electrochemical Society*, in press.

Chapter II

Experimental Techniques, Instrumentation and Protocol

This chapter is dedicated to a brief presentation of the experimental techniques and instrumentations used in this study. Various electrochemical polarization techniques have been used for the characterization, preparation, and control of the surface state of polycrystalline copper samples. Electrochemical Scanning tunneling microscopy (EC-STM) allowed us to characterize the topography and morphology of the copper surface at the nanometric scale while applying to the sample the electrochemical potential corresponding to the surface state that we wanted to study. This chapter also presents the conditions for sample preparation, surface preparation and tip preparation required for the EC-STM measurements.

2.1 Electrochemical study

The electrochemical study was carried out by dynamic or static polarization of the microcrystalline copper sample in acidic and alkaline electrolyte in order to study the effect of the presence of two corrosion inhibitors, namely 2-mercaptobenzothiazole (2-MBT) and 2-mercaptobenzimidazole (2-MBI). The two electrolytes selected are aqueous solutions of sodium hydroxide (0.1M NaOH, pH ~ 13) prepared from a 10 M concentrated solution and ultra-pure water (resistivity > 18MΩ cm) and hydrochloric acid (10 mM HCl, pH ~ 2) prepared from a solution of ultra-pure HCl and ultra-pure water.

For the study of the effect of the presence of corrosion inhibitors in acidic conditions, a solution of 1 mM of 2-MBI was made in 10 mM HCl. However, due to the low solubility of 2-MBT, a solution of 0.1 mM of 2-MBT was made in 10 mM HCl. For the study of the effect of the presence of corrosion inhibitors in alkaline conditions, two solutions of 1 mM 2-MBT and 1 mM 2-MBI were prepared, each in 0.1 M NaOH.

Dynamic polarization by linear or cyclic voltammetry provided the polarization curves or voltammograms for determining the electroactivity domains of copper in both of the mediums. Using this technique, the oxidation and reduction potentials of the different copper states are thus defined. These studies provided the information enabling us to set the polarization conditions making it possible to passivate the surface or to dissolve it. The analysis of the transferred charge densities makes it possible to quantify the number of oxide monolayers formed or the amount of copper dissolved. Potentiostatic polarization was used to maintain the sample at the desired electrochemical potentials and thus to characterize the copper surface in different surface states.

2.1.1 Electrochemical cell

Before the EC-STM measurements, we carried out conventional electrochemical cell polarization curves in order to confirm the electrochemical behavior of polycrystalline copper in the selected electrolytes and applied electrochemical potentials compared to a real reference. This was done in a classical three-electrode electrochemical cell.

The cell is made up of glass with three inputs: the main entrance dedicated to the working electrode and two other inputs located on the top of the cell to insert the counter-electrode and the reference

electrode. The counter electrode is a simple platinum wire having a surface approximately 10 times larger than that of the working electrode. The reference electrode is a Saturated Calomel Electrode (+0.248 V/SHE). An electrolytic bridge serves to protect the reference electrode. The bridge is equipped with sintered glass at its end and is filled with calomel solution. A Kel-F sample holder holds the copper sample (working electrode) and is sealed by a VITON® O-ring with a working area of 0.3 cm².

A methodical cleaning procedure for the cell, Kel-F sample holder and VITON seal minimizes any kind of organic or metallic contamination. This procedure is the same as that used for cleaning STM cells (see 2.1.3).

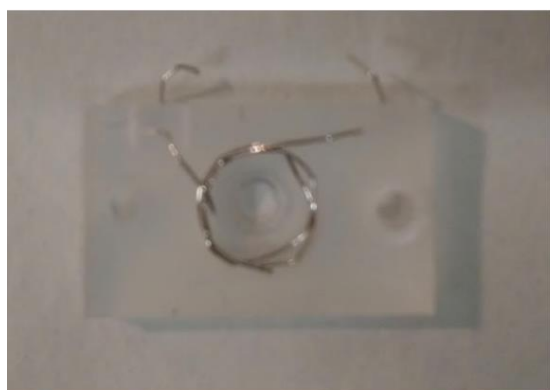
The cell is connected to a potentiostat PGSTAT30 (AUTOLAB) and the whole setup is controlled by the GPES software.

The potentiodynamic measurements were carried out at a scan rate of 20 mV/ s to define the domains of electroactivity that is of our interest:

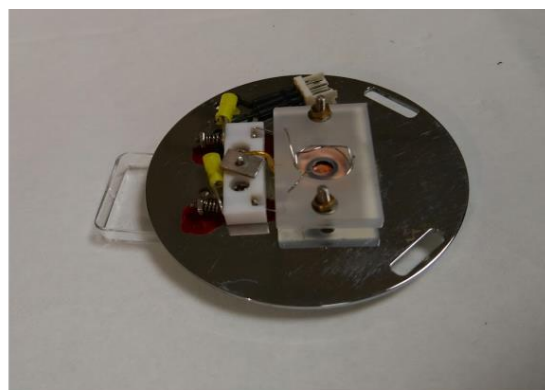
- (i) the metallic and passive states of surface in alkaline NaOH (0.1 M) in the presence of 2-MBI and 2-MBT (scanning between -0.75 V and +0.16 V / SCE).
- (ii) the inert and active states of surface in acidic HCl (10 mM) in the presence of 2-MBI and 2-MBT (scanning between -0.35 V and 0.063 V / SCE).

2.1.2 Electrochemical STM cell

The electrochemical STM cell was designed and manufactured by our group. It fits on a Scanning tunneling microscopy (STM) plate. The cell is made up of Kel-F. Both the STM plate and the Kel-F cell can be seen in Figure 2.1. The electrochemical STM cell has three electrodes: (i) a working electrode (sample) (ii) a pseudoreference electrode (RE) made up of platinum calibrated with respect to the saturated hydrogen electrode and (iii) a counter-electrode (CE) also made up of platinum. Unlike a conventional cell, the EC-STM setup has a fourth electrode which is the STM tip, immersed in the electrolytic solution and on which electrochemical reactions can occur which can generate a faradic current. Between the sample and the cell, a VITON® O-ring seal ensures tightness and delimits a working surface of approximately 0.16 cm². The cell has a volume of approximately 360 µL. This system allows the surface of the sample to be characterized simultaneously by conventional electrochemistry and as well as with scanning tunneling microscopy. This cell is cleaned according to the same procedure as that of the conventional cell as briefly explained in the next section.



a



b

Figure 2.1: (a) EC-STM cell made of Kel-F. (b) electrochemical cell along with a microcrystalline copper sample mounted on the STM plate

The polarization curves made in EC-STM cells were similar to those obtained in conventional cells, taking into account the potential shift between the SCE and that of the standard platinum electrode. The curves were carried out at a scan rate of 20 mV/ s in the same range of copper electroactivity, between -0.6 V / SHE and -0.18 V / SHE in HCl and between -1.2 V / SHE and -0.08 V / SHE in NaOH.

Before beginning any electrochemical analysis, in a conventional cell or in EC-STM cell, pretreatment of the surface with cathodic scanning is carried out in order to reduce the native oxide which forms spontaneously on the surface of the copper when exposed to air after polishing. This is done to ensure a metallic initial state prior to any further electrochemical analysis.

Based on the type of study to be performed, the surface state is changed from metallic and inert state either to the region corresponding to a passive state in alkaline solution or an active state in acid solution. This is achieved by jumping or by scanning the applied potential. The residual reactivity of the tip also conditions the choice of conditions to be adopted to vary the potential applied to the sample.

2.1.3 Cleaning the cell

The cell and the O-rings are first rinsed with a cold solution of 2:1 mixture of concentrated H_2SO_4 and 30% hydrogen peroxide. The remaining procedure for the cleaning of the cell is carried out in the following manner:

1. The cell is rinsed with ultrapure water and then boiled in concentrated HNO_3 for 5 minutes. This step serves to eliminate metal contaminations that accumulate mainly on the reference electrode. The O-rings are not boiled in HNO_3 .
2. The cell is rinsed with ultrapure water and then the cell and the O-rings are heated in the 2:1 mixture of concentrated H_2SO_4 and 30% hydrogen peroxide till the disappearance of the bubbles, which is the sign of consumption of hydrogen peroxide, in order to eliminate organic contaminations.
3. After this, the cell and the O-rings are boiled in ultra-pure water for at least 7 times to remove the residual traces of the acid from steps A and B. The cell and O-ring are dried with pressurized air prior to use.

2.2 Scanning Tunneling microscopy (STM)

2.2.1 Experimental device and operating principle

Scanning Tunneling Microscopy, or STM, is a very powerful tool for characterizing conductive and semiconducting surfaces. Its major asset is undoubtedly its ability to translate the topography of surfaces from the nanometric scale to the atomic scale resolution. Indeed, before the creation of the first tunneling microscope, the existing microscopy techniques were of two types: (i) Optical or conventional microscopy whose resolution power depended on the wavelength of the incident radiation and (ii) Electron microscopy (scanning electron microscope or transmission electron microscope). These microscopic techniques were unable to observe the atomic structures of the surfaces. Only Field ion microscopy (FIM) allowed us to visualize atoms on the sample surface with a small radius of curvature (equivalent to that of an STM tip).

The first tunneling microscope was developed in 1981 at IBM's Zurich laboratories by G. Binnig and H. Rohrer [1], [2] which earned them the Nobel Prize in 1986 [3], [4]. The operating principle of STM is shown in Figure 2.2.

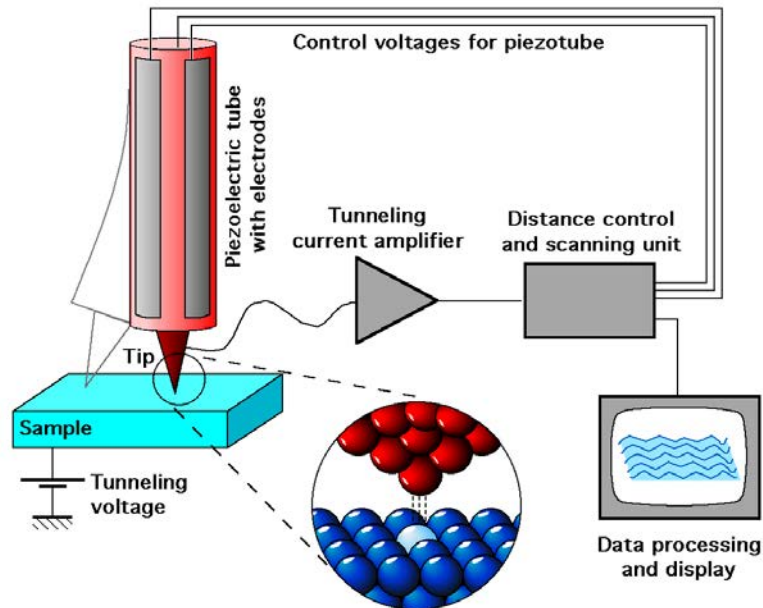


Figure 2.2: Diagram illustrating the principle of Scanning Tunneling Microscopy

To obtain a surface mapping, a very thin metallic tip that can be made of W or Pt / Ir, is used to scan the surface and it acts as a probe. The tip approaches the surface at a distance of a few angstroms controlled with the help of a piezoelectric tube manufactured with PZT (Lead zirconate titanate). The piezoelectric tube is also called an STM scanner. The piezoelectric tube contracts or relax depending on the polarization applied to it. This tube provides excellent control of the position of the tip and thus the tunneling current exchanges with the surface provided that a potential difference is applied between the two electrodes. If the potential difference is positive, the electrons will pass predominantly from the highest occupied levels of the tip to the lowest unoccupied energy levels of the sample through tunneling effect and vice versa if this potential difference is negative.

The tip then scans the surface along the x and y axes and measures the intensity of the tunnel current point by point. The piezoelectric tube adjusts the position of the tip along the z-axis. The tip/sample distance is thus controlled with a precision of the order of a few picometers (hundredths of angstroms). This control is carried out by means of a feedback loop which adjusts the height of the tip point by point according to the variations of the tunneling current.

This precise control with the help of a piezoelectric tube keeps the tip at a constant distance from the sample surface. When the surface is imaged at a constant distance it is called 'constant current imaging mode'. A scheme of this is seen in Figure 2.3. In this case, it is the variations of the tunneling current that translate to the topography of the surface. If the tip detects an increase in tunnel current, this indicates a decrease in the tip/surface distance and thus a protuberance is detected. This STM imaging mode is the most commonly used because it allows you to follow the surface topography while keeping the probe safer. The study of highly rough surfaces requires optimizing the servo gains of the feedback loop. However, in imaging highly rough surfaces, the risk of deterioration of the tip by contact with the surface is high. This is the imaging mode used in this work.

Another imaging mode called 'constant height imaging mode' can also be used. In this case, the height of the tip is not adjusted by the feedback loop and the images produced are images of the current

measured point by point at a constant height. This mode of imaging of the STM is little used and reserved for the study of highly smooth surfaces at the atomic scale.

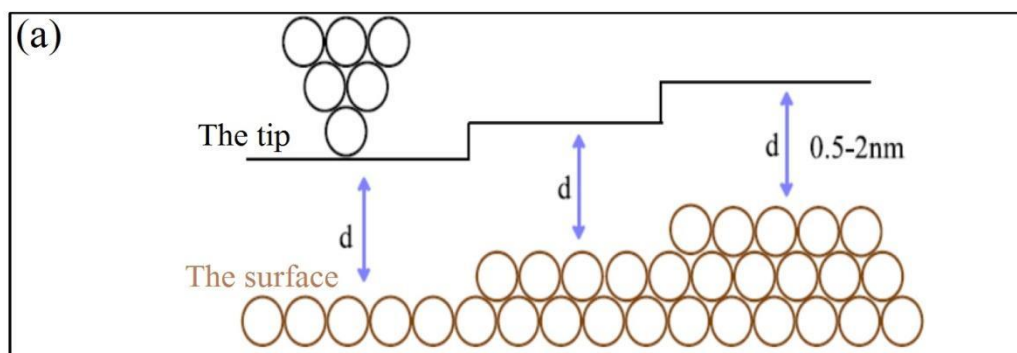


Figure 2.3: Diagram of the constant current topographic mode STM imaging mode used in this work

STM measurements strongly depend on the behavior of the piezoelectric tube and are very sensitive to the non-linearity between the applied voltage and the displacement. Parameters such as temperature, depolarization, and hysteresis can cause compression or stretching of the images. To find a normal behavior of the piezoelectric tube several methods of calibration are possible. Among them one of the methods developed consists of the detection of the reciprocal cell in the Fourier space to estimate the lateral calibration factors and the drift in the scanning direction [5]. In our case, we chose highly oriented pyrolytic graphite (HOPG) as a reference for calibrating our STM scanners. Thus, we compared the values of the interatomic distances obtained experimentally with those theoretically known and we adjusted our scanners so as to minimize the error and to correlate the two values. In most cases, the manufacturer of the piezoelectric tube already provides calibration files to optimize the working of the scanner. But during experimentation, it can be found that the STM scanner is not well calibrated.

The good quality of the STM tips is essential for obtaining good images, especially for measurements in situ in an electrochemical environment. An ideal STM tip is one whose summit is very thin and ended with an atom. This shape favors the presence of a dz^2 orbital which points perpendicular to the surface. This is the ideal configuration for collecting tunneling electrons from the orbitals of surface atoms.

Due to the extreme proximity of the tip to the surface of the samples, the surrounding vibrations can induce the crashing of the tip onto the surface and the stopping thus leading to a failed STM experiment. To avoid such an undesirable situation, the STM microscope must be positioned on a very heavy platform, suspended with the help of elastics to damp the external vibrations. In addition, the setup must be placed in an airtight noise-canceling box which can help to reduce the sensitivity of STM setup to sound waves.

2.2.2 Tunneling effect

G. Gamow was the first to introduce the tunneling effect. He represented the atom as a potential sink and coulombic interactions as a potential barrier to explain the nature of alpha radiation. Thus the disintegration became coherent from an energy point of view. This resulted in several papers and articles on the Appelbaum Tunnel Effect, 1969 [6], [7]. To understand the tunneling effect, one has to describe the electron as a wave set, but also to present the wave function as an ephemeral wave beyond the surface of the crystal. If two metal surfaces are separated by a vacuum, the spatial probability of the presence of this ephemeral wave is $|\Psi(t)|^2$ and thus the tunneling effect is typically of the order of one nanometer.

In the case of Figure 2.4, simplifying the representation and understanding of the phenomenon, the work functions (Φ) and Fermi energy levels of the two electrodes are assumed to be equal. The electrons transit from left to right and exactly the same number of electrons take the opposite path, which corresponds to a zero flux difference and therefore a zero current.

To detect the tunneling current it is necessary to provide an energy imbalance to the system. By applying a voltage V , the junction between the two electrodes is polarized (Figure 2.5). The potential barrier is deformed following the appearance of an electric field. Fermi levels are no longer aligned thus allowing the possibility of spontaneous passage of the tunneling current.

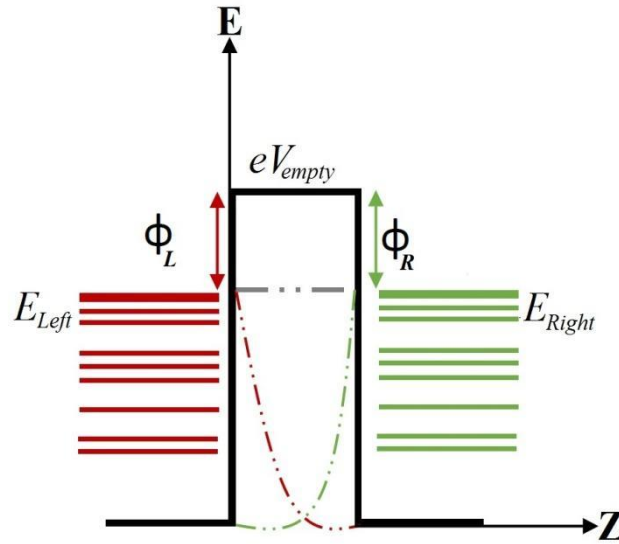


Figure 2.4: Diagram of a potential barrier between two electrodes separated by a vacuum. Fermi levels on both sides eventually line up. In this case, the number of electrons transiting the junction is the same in both directions, no tunnel current is measured.

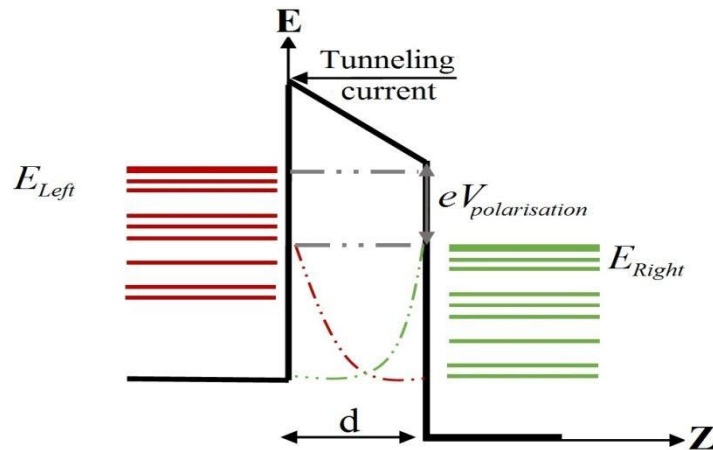


Figure 2.5: Diagram of a polarized junction between two electrodes. The electrons pass by tunneling from the left to the right towards the positive electrode.

In a simple one-dimensional model, the current is given by

$$I \propto A \cdot V_{polarisation} \cdot \exp(-B \cdot \sqrt{\phi} \cdot d) \quad (1)$$

Where 'A' and 'B' are constants and 'd' is the distance between the two surfaces.

Thus, from equation 3.1 we can see that there is an exponential dependence of the tunneling current with the distance between the tip and the sample. This exponential variation of the current explains the good spatial resolution of scanning tunneling microscopy (<0.01 nm) in the direction perpendicular to the surface.

2.2.3 Theoretical aspects

Theoretically, STM tip can be considered as a spherical wave function [8]. When the potential difference V applied is smaller than the work functions of the electrodes, then the tunneling current is expressed as follows:

$$I \propto V \cdot (E_f) \exp(-2kR) n_s(E_f, Z_0) \quad (2)$$

Where Z_0 is the distance from the top of the tip to the surface, E_f is the Fermi level of the tip, and $n_s(E_f, Z_0)$ is the state density at the Fermi level of the surface. R is the radius of the curvature of the tip. For a given value of V , this equation translates that the tunneling current as being proportional to the state density of the tip and the analyzed surface in the vicinity of their respective Fermi levels. This equation is limited to low bias voltages V .

Taking into account the high voltages, the expression of the current becomes:

$$I \propto \int_0^{eV} n_s(E, Z_0) \cdot n_p(E - eV) T(E, eV) dE \quad (3)$$

Where $n_p(E - eV)$ and $n_s(E, Z_0)$ are the state densities at the Fermi levels of the tip and the surface respectively. $T(E, eV)$ is the transmission coefficient of an electron across the potential barrier.

Since the tip is metallic in nature, its density of the state is not very variable as a function of the voltage and can be simplified. Deriving this expression from V , it becomes:

$$\frac{dI}{dV} \propto e n_s(eV) T(eV, eV) + \int_0^{eV} n_s(E) \frac{dT}{dV}(E, eV) dE \quad (4)$$

Here the derivative of the current, the differential conductance, is given by the sum of (i) the product of the surface state density by the tunnel transmission probability $T(eV, eV)$ and (ii) an integral that expresses the probability of tunnel transmission for a given applied voltage. If we divide the whole by I/V and simplify $T(E, eV)$ and $T(eV, eV)$, we can express the normalized differential conductivity as follows:

$$\frac{dI/dV}{I/V} \propto \frac{n_s(eV)C + X(V)}{Y(V)} \quad (5)$$

Where C is a constant $X(V)$ and $Y(V)$ vary very little with the applied voltage. Only the number of states accessible according to a given surface can influence the value of the standardized differential conductivity which can be expressed as follows:

$$\frac{dI/dV}{I/V} \propto n_s(eV) \quad (6)$$

In other words, depending on the positive or negative polarization of the junction, only the empty or occupied energetic states of the surface participate in the production of the tunnel current. It is indeed an interaction between occupied states of the surface and empty state of the tip or vice versa. In further work, the polarization effect of the potential barrier was taken into account [9].

In this simplified treatment, the effect of temperature was not taken into account. Indeed, energetic states are represented by the Dirac distribution, which is true only if $T=0$. For non-zero temperatures and because of the Pauli Exclusion Principle, the temperature has an effect only if there is a free state between $E_0 - K_B T$ and $E_0 + K_B T$, where E_0 is the energy of the state in the question and $K_B T$ is the thermal energy brought by a non-zero temperature.

2.2.4 Electrochemical application in liquid medium (EC-STM)

Corrosion studies require the characterization of samples by chemical and surface analytical techniques. The most widely used surface chemical analysis techniques (XPS, SIMS) operate ex-situ and require ultra-high vacuum (UHV) chambers. However, in the field of corrosion, the information collected may be very sensitive to the change of environment to which the surface is subjected during transfer to these UHV chambers[10]. To avoid characterization artifacts, the transfer conditions must be the best controlled possible. Another strategy is to use characterization methods operating in situ. The EC-STM technique (for electrochemical scanning tunneling microscopy) makes it possible to study the metal surface in an aqueous medium and under electrochemical control, and thus to characterize the in situ topographic alterations of a surface subjected to corrosion reactions.

The theory of the tunneling current is based on the presence of a potential barrier between the studied surface and the tip. It has been shown that an aqueous medium can replace air or vacuum and constitute this barrier of potential. Indeed, several previous EC-STM studies have demonstrated the possibility of studying and imaging passivated metal substrates in well-defined electrochemical environments [11]–[15]

The electrochemical control of the surface involves adding to the STM device the electrochemical cell presented previously (3.1.2). The device obtained after the assembly is shown in Figure 2.6. This four-electrode cell (the surface, the tip, the reference electrode, and the counter-electrode) requires the use of a bipotentiostat which allows the independent control of potentials applied to the sample and the tip with respect to the same reference. Thus, the bias voltage for the tunneling transfer corresponds to the difference between the potentials applied independently to the sample and the tip.

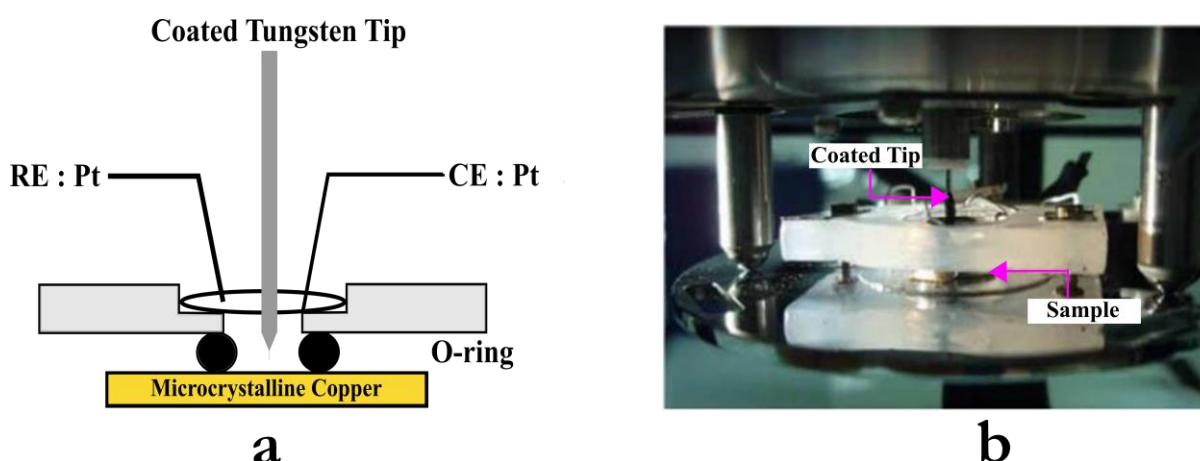


Figure 2.6: Scheme of the EC-STM setup (left) along with actual EC-STM assembled setup (right)

Immersed in the solution, the tip is the seat of electrochemical reactions that generates a faradic current. These currents disturb significantly the current measurements on the tip since the servo circuit is unable to differentiate faradic current I_f (parasite) from tunneling current I_t . To make EC-STM imagery possible, one must avoid the faradic current as much as possible by minimizing the electrochemical

reactions on the surface of the tip. We will detail the different stages of the preparation of an ECSTM tip in a later section (section 2.3.3).

2.2.5 EC-STM Apparatus used for this thesis.

The EC-STM microscope consists of a base that includes a platform for positioning sample and tip, as well as a step approach motor that allows the approach (and withdrawal) between the tip and the sample. The precise control of the position (x, y, z) of the tip is done by means of an STM scanner on which the tip is fixed.

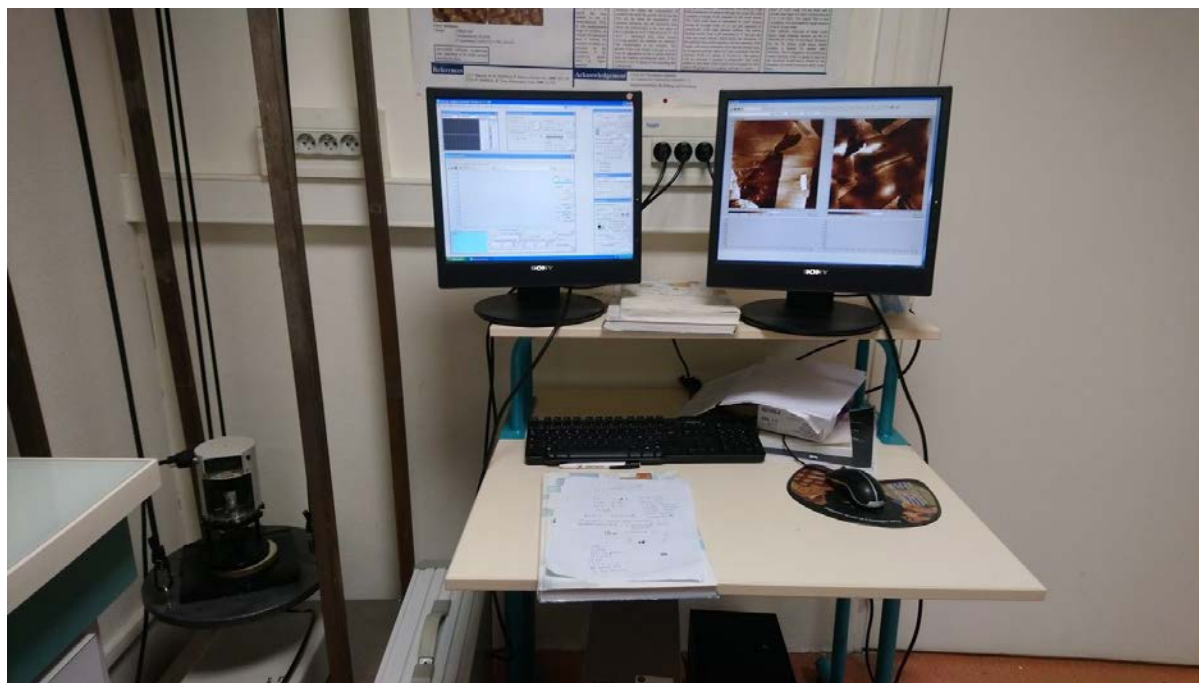


Figure 2.7: EC-STM microscope used for this thesis

The EC-STM setup used for the purpose of this thesis is shown in Figure 2.7. It is an Agilent (Model 4500, Pico SPM). It allows working in an open-air condition or in a liquid medium with or without electrochemical control. The software used for system control is PicoScan 5.3.3. Because EC-STM microscopy is very sensitive to vibrations, an isolation platform is used to minimize the impact of surrounding vibrations.

2.3 Preparation of sample and EC-STM tips

2.3.1 Preparation of microcrystalline copper

The maximum field of view of the EC-STM microscope used is $30 \times 30 \mu\text{m}^2$. The goal of this project was to the study of grain boundaries using EC-STM setup. The probability of observing grain boundaries with our EC-STM setup would be almost zero if the size of the grains exceeds that of the maximum field of view allowed by our set up. It is, therefore, necessary to reduce the size of the grains to increase the mesh size of the grain boundaries network. For this purpose, micro polycrystalline samples were used. These samples were prepared at the University of Ghent in Belgium by A. Laureys and K. Verbeken, on the occasion of a collaboration with the Université Libre de Bruxelles (E. Martinez-Lombardia, I Degraeve, H. Terryn) [16], [17], from a high purity copper widely used in electrical engineering. They are

prepared by cycles of two stages each: (i) cryogenic lamination after immersion in liquid nitrogen and (ii) annealing treatment limited in time and temperature. The size of grains is reduced up to 90% after cryogenic rolling. The final step is heat treatments at 200 °C for about 2 mins. This is done for 2 to 6 cycles.

According to the EBSD analyzes carried out at the University of Ghent after preparation (Figure 2.8), the average grain size is 1.4 μm with very wide dispersion, ranging from 0.1 to 37 μm . The absence of preferential crystallographic orientation and thus a random texture of the samples produced are observed. This random texture of the studied surfaces makes it possible to overcome the effects of preferential orientation of the surrounding grains on the local behavior of the grain boundaries with respect to corrosion and passivation phenomena.

The EBSD data also reveal that Σ_3 -type grain boundaries are dominant and represent 66% of all grain boundaries present in the analyzed area. It is known that special and precisely Σ_3 grain boundaries are very abundant in face-centered cubic materials such as copper.

The high purity of the microcrystalline copper used and the annealing conditions achieved helped to minimize the contamination of the grain boundaries with sulfur and other species that can segregate at the grain boundaries. Measurements by ToF-SIMS showed that the sulfur and the oxygen were below the limit of detection of the technique, and therefore in trace amounts, if present, in the samples. Similarly, the absence of alloying element makes it possible to avoid segregation effects at the grain boundaries that can modify the behavior of the copper. The behavior studied can be considered as that of pure copper.

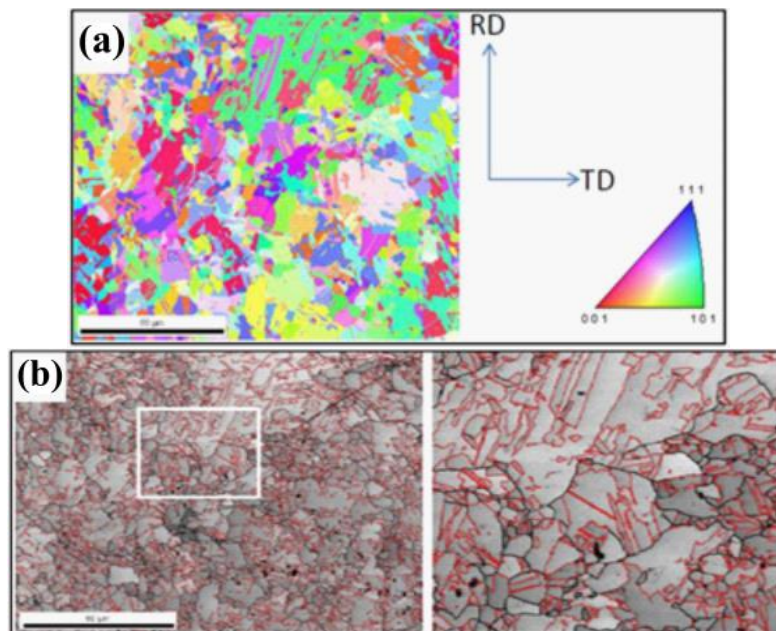


Figure 2.8: EBSD analysis of microcrystalline copper samples. (a) IFP mapping of grains and (b) IQ mapping of grain boundaries. In (b) the Σ_3 grain boundaries are shown in red and the random grain boundaries and other types of grain boundaries are shown in black. The right IQ image is a zoom in the square on the left IQ image

2.3.2 Preparation of the copper surface

For any surface analysis and especially for EC-STM and EBSD analyzes, it is necessary to proceed with a surface preparation that reveals the surface crystallography sharply during the measurements. For this purpose, two polishing steps have been used: mechanical polishing and electrochemical polishing.

A. Mechanical polishing

A polishing disc is used on which a lubricated and diamond solution is applied. Mechanical polishing is done by applying a constant force to the sample while rotating it in the opposite direction of rotation of the disc (Figure 2.9). In this work, we successively used diamond solutions of 6 μm , 3 μm , 1 μm , and 0.25 μm . This type of polishing allows us to eliminate any roughness or scratches of a depth greater than or equal to about 0.25 μm . Thick layers of corrosion or other surface-formed products are also removed.



Figure 2.9: Mechanical polishing device

Before going from one diamond solution to another it is necessary to check that all the scratches present on the surface are of the same depth. However, to go from the diamond solution to 1 μm to that to 0.25 μm no scratches should be visible to the naked eye. Polishing time should also be increased from one solution to another to avoid dented surfaces. In general, the average polishing time for each of the four steps was 20, 30, 40 and 60 minutes respectively. The mentioned time duration was an average time which sometimes had to be increased in order to get a well-polished and highly flat surface required for EC-STM analysis. The samples are rinsed successively in ultrasonically agitated baths of acetone, ethanol, then of ultra-pure water and finally dried with filtered compressed air at the end of the polishing.

B. Electrochemical polishing

This step makes it possible to eliminate the hardened cold work layer formed on the surface by mechanical polishing. An electrochemical polishing device with two electrodes is used (Figure 2.10). A voltage of 3 V is applied between the cathode (in copper) and the anode which is our sample for about 15 s. The electrolyte used is orthophosphoric acid (66%). Then the sample is rinsed with 10% orthophosphoric acid then abundantly rinsed with ultrapure water (about 0.5 L). It must be quickly dried with nitrogen. It is an electrochemical surface treatment process during which the surface layer of the metal sample is etched after its anodic dissolution. Pickling allows the sample to get rid of its native oxide layer. After this polishing step, the surface of the copper has overall roughness not exceeding 30 nm. A few holes due to high potential (3 V) used for electropolishing may be present. Exposing the surface to such high potential for a short amount of time during the electropolishing step ensures etching of grain boundaries which results in high resolved EC-STM images.

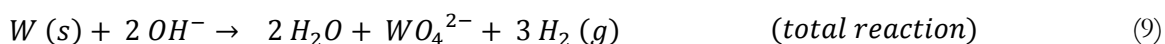


Figure 2.10: Electrochemical polishing cell of copper

2.3.3 Preparation of EC-STM tips

The STM is a very powerful analysis technique capable of providing surface images resolved at the atomic scale. However, the shape of the tip and the electronic properties of its active region strongly influence image resolution [18]. Several types of metallic or non-metallic tip exist, but the most widely used are those made of W or Pt/Ir. Theoretical work has shown that the dz^2 orbital is the most suitable for well-tuned tunneling current conduction and imaging at the nanometric/atomic scale.

There are two methods of preparation for STM tips: (i) mechanical cleavage or (ii) electrochemical erosion. Mechanical cleavage is not widely used because it produces coarse tips inappropriate for the nanometric study of relatively rough surfaces like those studied in this thesis. The electrochemical erosion method was opted, which involves dissolving a wire of tungsten metal using a two-electrode electrochemical cell in which the tungsten constitutes the anode while a platinum wire is the cathode. The two half-reactions and the overall reaction are as follows:



In order to obtain a very sharp tip, the electrochemical erosion was carried in two stages.

A. Local thinning of the wire

This step is performed with the device shown in Figure 2.11. About 2 cm tungsten wire (0.25 mm diameter, approx 99.95% purity) is cut and straightened. About 0.5 cm of this cut wire is dipped in a solution of 3 M NaOH. A platinum wire acting as cathode is also placed in the beaker.

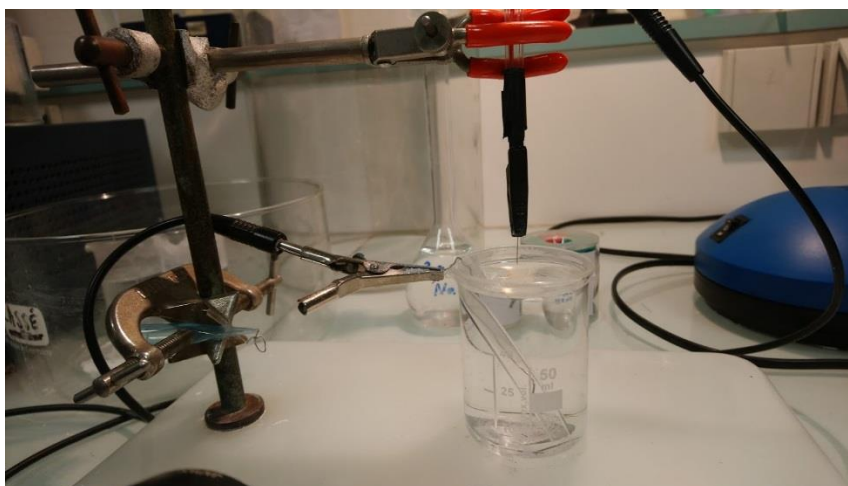


Figure 2.11: Electrochemical assembly for the localized dissolution of tungsten wire

A voltage of 10 V is then applied between the two electrodes for a few minutes. In order to obtain a correct shape (in the shape of a figure '8'), the tungsten wire must be placed in a position perpendicular to the surface of the solution. The tungsten wire at the solution/air interface corrodes in priority and its diameter decreases considerably (Figure 2.12). The application of potential is stopped just before the other end of the wire falls. The wire is rinsed with ultrapure water and dried with compressed air.

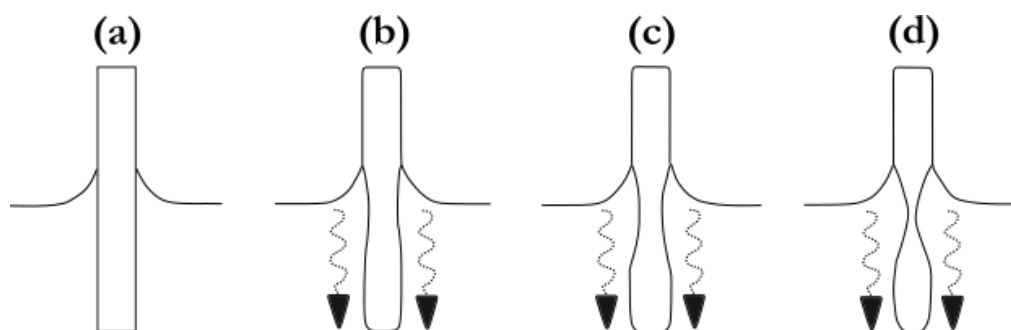
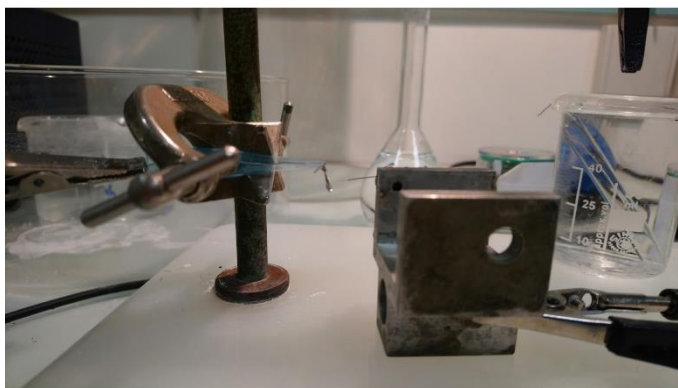


Figure 2.12: local thinning scheme by the preferential dissolution of a tungsten wire at the solution/air interface

B. Cutting the tip

This second step is performed using the assembly shown in Figure 2.13 (a). It consists of cutting the thinned portion of the tungsten rod to produce the tip. This step results in the formation of a straight and a very sharp, cone-shaped tip (Figure 2.13 (b)). The voltage applied between the two electrodes during this step is less than 1 V. The cathode consists of a platinum ring filled with a drop of electrolyte 3 M NaOH solution. The tungsten wire (anode) is inserted and cut at the thinned zone using small repetitive movements around this area. Again, the tip is thoroughly rinsed with ultra-pure water.



a

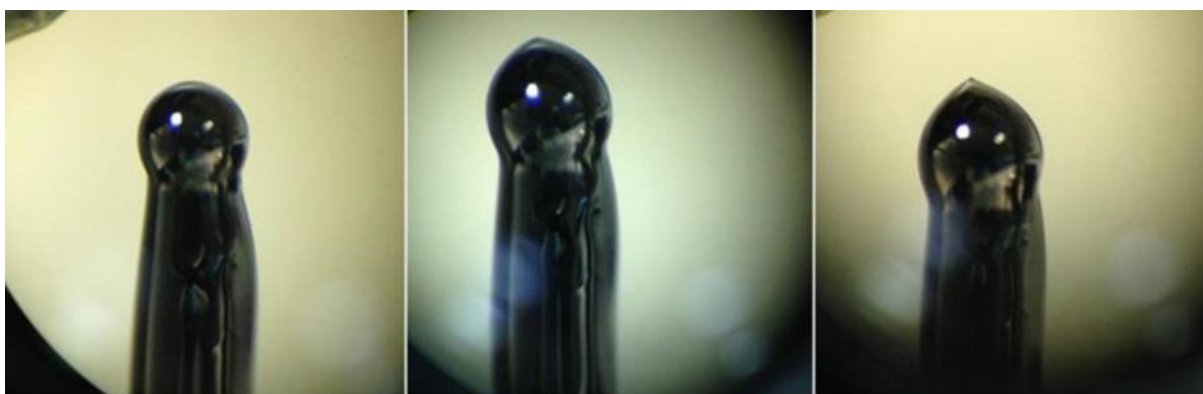
b

Figure 2.13: (a) assembly for electrochemically cutting the tip, (b) final shape of a tip STM

C. Isolation of the tip

To finalize the preparation of an EC-STM tip, the part to be immersed in solution (length 6-7 mm) must be isolated in order to minimize the faradic current (i_F) associated with the electrochemical reactions occurring at the surface of the tip in solution. Indeed, in an electrochemical environment, the total current i_t measured by the tip is the sum of the tunneling current and the faradic current: $i_t = i_T + i_F$. To be able to image the surface, the faradic current must be as small as possible. The tip is thus covered by an insulator (Apiezon wax) so that the faradic current is negligible.

A U-shaped oven is used to coat the Apiezon wax tip (Figure 2.14). At first, the tip is completely coated with Apiezon wax by passing through a drop of liquid wax (Figure 2.14 (a)). In a second step, the furnace is warmly approached from the end of the tungsten wire to cause the wax to flow (Figure 2.14 (b)). The tip emerges from the wax as a cone forms at the end of the coated wire (Figure 2.14 (c)).



(a)

(b)

(c)

Figure 2.14: (a) tip fully coated with Apiezon wax, (b, c) tip partially uncovered by Apiezon wax flow

Control of the electrochemical potential applied to the tip when it is immersed in solution after assembly of the EC-STM cell is also used to minimize the faradic current (i_F). Thus, for each new system studied (solution/sample), the potential of the tip (E_t) is adjusted to obtain the minimum faradic current. Since the quality of the STM images obtained is sensitive to the bias voltage, i.e. the potential difference between the tip and the surface ($E_s - E_t$), it is, therefore, necessary to find a compromise between the stable electrochemical potential window of the tip and the quality of the STM images.

2.4 Cathodic pretreatment of microcrystalline Cu

Before the reactivity of the surface can be electrochemically studied starting from its metallic state, it is necessary to reduce the native oxide spontaneously formed on the surface after electropolishing. This is done by applying a cathodic reduction pretreatment. Once the electrolyte is introduced in the ECSTM cell, the Open Circuit Potential (OCP) is recorded and the bipotentiostat is switched on. After this, the surface is polarized at a scan rate of 20 mV/s, first cathodically down till a cathodic vertex corresponding to the beginning of the hydrogen evolution region and then up until an anodic vertex in the domain of inertness of the metallic state (i.e. before anodic oxidation). Three reduction cycles are applied to ensure complete removal of the surface native oxide. Two examples of such a pretreatment are shown in figure 2.15 and 2.16 in 10mM HCl and 0.1 M NaOH electrolytes, respectively, both in the presence of the 2-mercaptobenzothiazole (2-MBT) inhibitor. In the acid electrolyte, no cathodic reduction peak is observed unlike in the alkaline electrolyte. This is in agreement with the spontaneous dissolution of the oxide expected at pH lower than 5, and here taking place in 10mM HCl (pH 2) after immersion at OCP and before cathodic polarization. In 0.1 M NaOH, no spontaneous dissolution takes place at OCP and a cathodic reduction peak is observed at -0.71 V/SHE. The peak is strongly attenuated in the 2nd cycle and vanishes in the 3rd cycle showing that the native oxide has been fully dissociated by the cathodic reduction pretreatment.

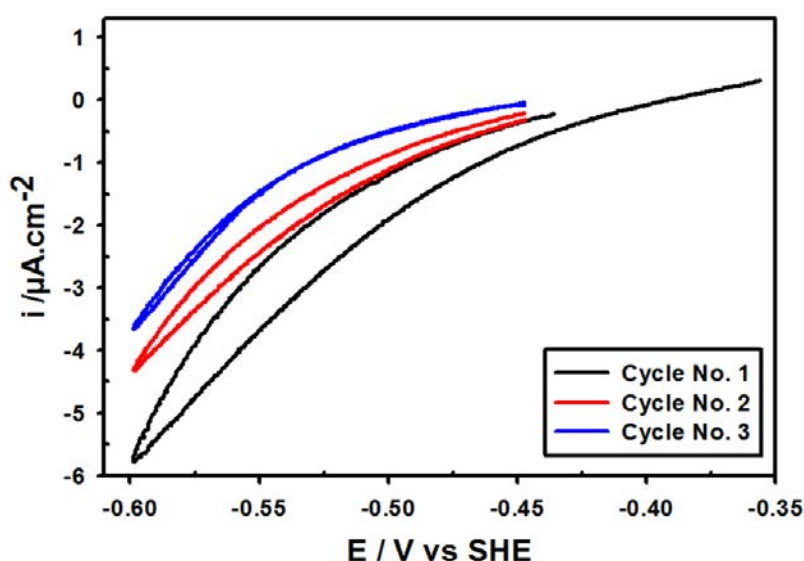


Figure 2.15: Cathodic reduction for microcrystalline Cu in 0.1 mM 2S-MBT + 10 mM HCl.

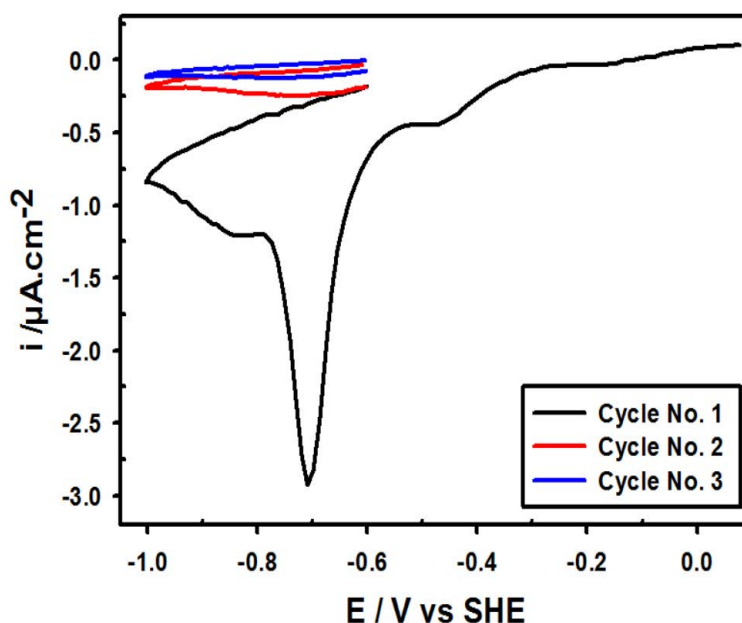


Figure 2.16: Cathodic reduction for microcrystalline Cu in 1 mM 2-MBT + 0.1 M NaOH.

References

- [1] G. Binnig and H. Rohrer, "Scanning Tunneling Microscopy—from Birth to Adolescence (Nobel Lecture)," *Angewandte Chemie International Edition in English*, vol. 26, no. 7, pp. 606–614, 1987, doi: <https://doi.org/10.1002/anie.198706061>.
- [2] G. Binnig, H. Rohrer, Ch. Gerber, and E. Weibel, "Surface Studies by Scanning Tunneling Microscopy," *Phys. Rev. Lett.*, vol. 49, no. 1, pp. 57–61, Jul. 1982, doi: [10.1103/PhysRevLett.49.57](https://doi.org/10.1103/PhysRevLett.49.57).
- [3] R. J. Behm, N. García, and H. Rohrer, Eds., *Scanning Tunneling Microscopy and Related Methods*. Springer Netherlands, 1990.
- [4] G. Binnig and H. Rohrer, "In touch with atoms," *Rev. Mod. Phys.*, vol. 71, no. 2, pp. S324–S330, Mar. 1999, doi: [10.1103/RevModPhys.71.S324](https://doi.org/10.1103/RevModPhys.71.S324).
- [5] J. F. Joergensen, L. L. Madsen, J. Garnaes, K. Carneiro, and K. Schaumburg, "Calibration, drift elimination, and molecular structure analysis," *Journal of Vacuum Science & Technology B: Microelectronics and Nanometer Structures Processing, Measurement, and Phenomena*, vol. 12, no. 3, pp. 1698–1701, May 1994, doi: [10.1116/1.587266](https://doi.org/10.1116/1.587266).
- [6] J. G. Simmons, "Generalized Formula for the Electric Tunnel Effect between Similar Electrodes Separated by a Thin Insulating Film," *Journal of Applied Physics*, vol. 34, no. 6, pp. 1793–1803, Jun. 1963, doi: [10.1063/1.1702682](https://doi.org/10.1063/1.1702682).
- [7] J. H. Weiner and Y. Partom, "Quantum Rate Theory for Solids. II. One-Dimensional Tunneling Effects," *Phys. Rev.*, vol. 187, no. 3, pp. 1134–1146, Nov. 1969, doi: [10.1103/PhysRev.187.1134](https://doi.org/10.1103/PhysRev.187.1134).
- [8] J. Tersoff and D. R. Hamann, "Theory of the scanning tunneling microscope," *Phys. Rev. B*, vol. 31, no. 2, pp. 805–813, Jan. 1985, doi: [10.1103/PhysRevB.31.805](https://doi.org/10.1103/PhysRevB.31.805).
- [9] N. D. Lang, "Spectroscopy of single atoms in the scanning tunneling microscope," *Phys. Rev. B*, vol. 34, no. 8, pp. 5947–5950, Oct. 1986, doi: [10.1103/PhysRevB.34.5947](https://doi.org/10.1103/PhysRevB.34.5947).
- [10] Philippe Marcus, *Corrosion Mechanisms in Theory and Practice*, Third. CRC press, 2012.
- [11] V. Maurice, H.H. Strehblow, and P. Marcus, "In Situ STM Study of the Passivation of Cu(111)," *J. Electrochem. Soc.*, vol. 146, pp. 524–540, 1999.
- [12] E. Martinez Lombardia, L. Lapeire, I. De Graeve, H. Terryn, and K. Verbeken, "Influence of grain size on the electrochemical behavior of pure copper," *J Mater Sci*, vol. 52, no. 3, pp. 1501–1510, Feb. 2017, doi: [10.1007/s10853-016-0445-z](https://doi.org/10.1007/s10853-016-0445-z).

- [13] H. Chen *et al.*, "Local passivation of metals at grain boundaries: In situ scanning tunneling microscopy study on copper," *Corrosion Science*, vol. 111, pp. 659–666, Oct. 2016, doi: 10.1016/j.corsci.2016.04.013.
- [14] J. Kunze, V. Maurice, L. H. Klein, H.-H. Strehblow, and P. Marcus, "In situ STM study of the duplex passive films formed on Cu(111) and Cu(001) in 0.1 M NaOH," *Corrosion Science*, vol. 46, no. 1, pp. 245–264, Jan. 2004, doi: 10.1016/S0010-938X(03)00140-9.
- [15] M. C. del Barrio, D. R. Salinas, and S. G. García, "Electrochemical and in-situ stm study of the surface alloy formation in the system Au(100)/Cd," *Electrochimica Acta*, vol. 130, pp. 164–169, Jun. 2014, doi: 10.1016/j.electacta.2014.02.143.
- [16] E. Martinez-Lombardia *et al.*, "In situ scanning tunneling microscopy study of the intergranular corrosion of copper, electrochemistry communication," *Electrochemistry Communication*, vol. 41, 2014.
- [17] H. Chen *et al.*, "Grain boundary passivation studied by in situ scanning tunneling microscopy on microcrystalline copper," *J Solid State Electrochem*, vol. 19, no. 12, pp. 3501–3509, Dec. 2015, doi: 10.1007/s10008-015-2787-x.
- [18] S. Ohnishi and M. Tsukada, "Effect of the microscopic electronic states of the tip on the scanning tunneling microscopy image," *Journal of Vacuum Science & Technology A*, vol. 8, no. 1, pp. 174–176, Jan. 1990, doi: 10.1116/1.577058.

Chapter III

Local inhibition by 2-mercaptobenzothiazole of early stage intergranular corrosion of copper

This chapter reproduces an original manuscript with reference: Sagar B. Sharma, Vincent Maurice, Lorena H. Klein, Philippe Marcus, Local inhibition by 2-mercaptobenzothiazole of early stage intergranular corrosion of copper, Journal of The Electrochemical Society 167 (2020) 161504, DOI: 10.1149/1945-7111/abcc36

Abstract

Corrosion inhibition by 2-mercaptobenzothiazole (MBT) at the surface termination of various types of grain boundaries (GBs) was studied at the nanometer scale on microcrystalline copper in HCl acid solution using *in situ* electrochemical scanning tunneling microscopy (ECSTM). Macroscopic electrochemical analysis by cyclic voltammetry showed highly effective inhibition of Cu(I) active dissolution blocked by MBT pre-adsorption in a potential range of 0.15-0.2 V. ECSTM analysis of the initial stages of intergranular corrosion confirmed the mitigation of net intergranular dissolution by the pre-adsorbed MBT surface layer but also revealed the local accumulation of reaction products in the GB regions. For Coincidence Site Lattice boundaries other than coherent twins, intergranular dissolution, mitigated by the pre-adsorbed MBT layer, and protection by intergranular formation of a film of reaction products were observed. For random GBs, protection by reaction products was dominant, in agreement with their more reactive intrinsic character, generating more Cu(I) ions under anodic polarization and thus promoting the formation of a protective film of reaction products. Coherent twins did not show preferential intergranular reactivity compared to adjacent grains, indicating equally strong efficiency than on grains. These results bring new insight on how inhibition operates locally at various types of GBs.

3.1 Introduction

At the surface, polycrystalline metallic materials expose a grain boundary (GB) network to the environment, which can limit their durability because of intergranular corrosion. The degradation, localized at the GBs, initiates at the topmost surface before penetrating in the sub-surface, and eventually propagates to the entire GB network. Intergranular corrosion is known to relate to the GB character and GB energy from previous studies of GB engineered materials submitted to intergranular sub-surface penetrating attack [1-21]. Based on such knowledge, GB engineering aims at producing polycrystals having the most stable GB network, and thus mitigate their susceptibility to intergranular corrosion.

There are two main classes of GBs depending on their misorientation angle: i) low angle ($< 15^\circ$) GBs that can be described by a network of edge dislocations in the GB plane, and ii) high angle ($> 15^\circ$) GBs that do not obey such a crystallographic description and are more reactive because of their higher energy compared to low angle GBs. Among high angle GBs, those that can be described by a coincidence site lattice (CSL) are labeled Σn with $1/n$ defining the fraction of lattice sites shared by the two grains in the GB plane. The low Σ GBs, i.e. those with a high fraction of common lattice sites, have lower energies and are so-called “special” when they resist degradation as opposed to the high Σ ones, and the random high angle grain boundaries that cannot be described by a coincidence site lattice [2,6,8,11-13,16]. In *fcc* materials such as copper, Σ_3 boundaries (also called twins) are most common and can resist intergranular sub-surface penetrating attack [6,9,12,13,16]. Depending on the specific orientation of their

GB plane, Σ_3 twins can be coherent or incoherent. It has been reported that only the Σ_3 coherent twins (with a {111}-oriented GB plane) would better resist intergranular sub-surface penetrating attack [3,13].

Improving our knowledge of intergranular corrosion also requires to investigate the initial stages of reaction, i.e. early intergranular corrosion, at the surface termination of grain boundaries before penetration in the sub-surface region and propagation. The alterations of the topmost surface of the metallic material must be characterized locally, with sufficient high space resolution, and preferably *in situ* and under electrochemical control in order to monitor the kinetics of the corrosion reaction. Recently, this has been achieved on microcrystalline copper using electrochemical scanning tunneling microscopy (ECSTM) [22-25]. Dissolution in the active state [22], as well as transient dissolution during passivation [23,25], observed at the nanometer scale, were found weaker at the GB edges assigned to coherent twin boundaries than at other GB edges assigned to random or other CSL boundaries. Coupling with Electron Back-Scatter Diffraction (EBSD) characterization of the local GB character showed the susceptibility to early intergranular corrosion for high angle boundaries as well as Σ_9 CSL boundaries. For Σ_3 coherent twins, the behavior was found dependent on the deviation angle of the GB plane from the exact orientation with a transition from resistance to susceptibility between 1° and 1.7° of deviation [26].

The use of corrosion inhibitors has been proven to be an effective approach to mitigate the corrosion of metals and alloys in contact with aggressive environments. Azole derivatives such as 2-mercaptobenzothiazole (MBT, $C_7H_5NS_2$) are often used as corrosion inhibitors for copper or its alloys [27-41]. MBT has been reported to have a remarkable efficiency under neutral saline, acid and alkaline conditions [27,28,30,32,37-40] and to act as a mixed-type inhibitor [29,37,]. There are two sulfur atoms and one nitrogen atom in the MBT molecule, that can, concomitantly or individually, strongly bond to copper atoms and thus enable chemisorption to form a stable molecular film protecting the copper surface from corrosion [30,36,37,40,43-48]. The formation of a Cu-MBT film has been proposed [27,28] and the film thickness would depend on pH with only a monolayer film forming in the range of Cu_2O stability ($pH > 4$) whereas multilayers would form in the range of Cu_2O instability ($pH < 3$) [27]. The mechanism would consist of a surface reaction of Cu(I) ions with pre-adsorbed MBT, and not of a complex precipitated from the solution [29]. If pre-adsorbed on a copper surface in the metallic state, MBT forms a monolayer that prevents oxide formation as observed in alkaline aqueous solution [40] and in the gas phase [44-46].

Here, we report on the nanoscale local characterization using ECSTM of the inhibition of early intergranular corrosion of copper by MBT in HCl acid solution in which no stable copper oxide is formed. Despite the well-established corrosion inhibition properties of MBT and other inhibitors on polycrystalline copper, there are, to the best of our knowledge, no studies on the local aspect of early stage intergranular corrosion in the presence of inhibitors and the mechanisms of inhibition at the surface termination of grain boundaries. The results reported here bring new insight on the inhibition process at various types of GBs.

3.2 Experimental

Microcrystalline copper samples were used [19,22-26,]. They were obtained from high-purity cast electrolytic tough pitch copper, (ETP-)Cu, by cryogenic rolling after freezing in liquid nitrogen. Annealing was limited to 1 min at 200 °C to ensure full recrystallization while preserving a GB network of suitable cell size for the relatively small STM field of view, as confirmed by EBSD [22,23] and the data presented hereafter. No preferential grain orientation, i.e. a nearly random texture, was obtained [23] and 66% of the GB length corresponded to Σ_3 CSL boundaries, the other 34% being random boundaries for the most part [22,23]. Samples were mechanically polished with diamond spray down to a final grade of 0.25 μm for surface preparation, which was followed by electrochemical polishing in 66%

orthophosphoric acid at 3 V versus a copper counter electrode for 15 s in order to remove the cold work layer.

ECSTM analysis was performed with an Agilent Technologies system (PicoSPM base, Keysight STM S scanner, PicoScan 2100 controller, PicoStat bi-potentiostat and Picoscan software). The homemade ECSTM cell is made of Kel-F and contains ~350 μl of electrolyte. The working electrode area is 0.16 cm^2 delimited using a VITON® O-ring. Two Pt wires served as counter electrode and pseudo reference electrode (+0.20 V/SHE). ECSTM cell cleaning and tip preparation have been detailed elsewhere [51-55].

A non-deaerated 10 mM HCl(aq) aqueous acid solution (pH 2) was used as electrolyte, prepared from ultrapure HCl and Millipore water (resistivity > 18 $\text{M}\Omega\text{ cm}$). MBT was added at a concentration of 0.1 mM obtained by dissolution from the powder physical state. In order to avoid any uncontrolled corrosion, the samples were exposed to the electrolyte at -0.45 V/SHE, i.e. below the open-circuit potential value of -0.35 V/SHE. Then, a cathodic reduction pre-treatment was applied in order to reduce the native oxide film. The potential was repeatedly cycled (0.2 V s^{-1}) down to -0.60 V/SHE at the onset of hydrogen evolution and backward to the value of -0.45 V/SHE until the cyclic voltammograms (CVs) showed no cathodic peak associated with Cu(I) to Cu(0) reduction. Two cycles were enough to fully reduce the native oxide formed after electropolishing.

After this pre-treatment, ECSTM images of the microcrystalline copper surface in the metallic state were taken at -0.45 V/SHE for localization of grain boundaries of interest. Afterwards, anodic oxidation was forced by cycling (1 mV s^{-1}) the potential first up to the anodic apex of -0.18 V/SHE then backward to the cathodic apex of -0.60 V/SHE and finally upward to the initial value of -0.45 V/SHE. This cycle was repeated up to 4 times and new ECSTM images of the surface were taken at -0.45 V/SHE after 2 and 4 cycles. During electrochemical treatment, the STM tip was kept engaged but not scanning the surface, so as to keep the area of interest in the STM field of view after cycling. The evolution of the local topography could thus be followed after electrochemical cycling. The ECSTM images were acquired in the constant current mode. No filtering was used and the recorded images were processed with the Gwyddion software [56].

Line profile analysis was applied to measure the topography across the GB regions. The line profiles were obtained by averaging 30 adjacent line scans drawn across the grain boundary, covering a local distance of ~170 nm along the boundary [24,26]. The GB depth was measured as the local difference in topographic height between the bottom of the GB regions and the surface level of the grains directly above. Ten different measurements were performed for each selected site and the reported error bar is the standard deviation for these ten measurements.

3.3 Results and discussion

3.3.1 Macroscopic electrochemical behavior

Figure 3.1 shows the effect of MBT on the electrochemical behavior of copper in 10 mM HCl(aq) as characterized by cyclic voltammetry. The CV measurements characterize the macroscopic electrochemical response of the surface. When showing substantial activity, this response can be assigned essentially to the reactivity of the grains since the exposed surface fraction of the GB network is very small compared to that of the grains, as confirmed by the ECSTM images presented below. In contrast, if only residual activity is observed, it corresponds to the sites of preferential reactivity, and thus emphasizes the response of the exposed GB network.

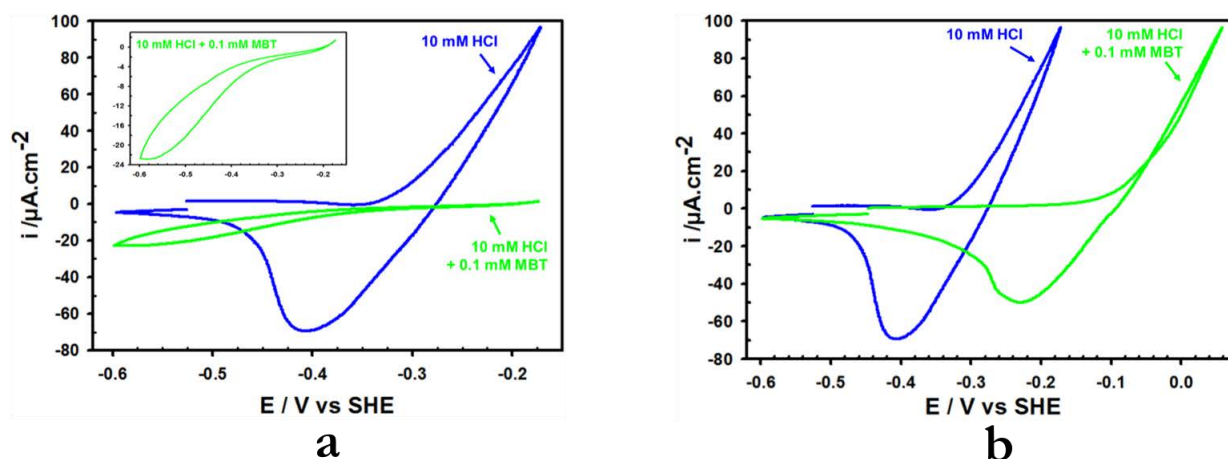


Figure 3.1: Cyclic voltammograms in the ECTM cell for microcrystalline copper in 10 mM HCl(aq), first cycle, scan rate = 1 mV/s: (a) CVs recorded without and with 0.1 mM MBT in the solution until anodic apex of -0.18 V. Inset shows enlarged CV obtained in the presence of MBT. (b) CVs recorded without and with 0.1 mM MBT in the solution until an anodic apex corresponding to the anodic current of 100 $\mu\text{A}\cdot\text{cm}^{-2}$.

Figure 3.1(a) shows the CVs obtained after reduction of the native oxide and starting at -0.45 V/SHE in the metallic state (first cycle is shown). In the absence of MBT, the increase of the anodic current for $E > -0.35$ V/SHE is assigned to the anodic oxidation of copper ($\text{Cu}(0) \rightarrow \text{Cu}(I) + e^-$). No stable copper oxide is formed at pH 2 and the Cu(I) ions formed in this potential range dissolve as CuCl_2^- in HCl medium [57-60]. In the reverse scan, a cathodic peak is observed like in previous studies [26,60,61-65]. It is assigned to the reductive deposition of dissolved Cu(I) and observed in the present experimental conditions at -0.40 V/SHE.

The integration of the positive current density measured during the anodic and reverse cathodic scans yields a total value of the anodic charge density transfer of 26 885 $\mu\text{C}\cdot\text{cm}^{-2}$. This charge transfer amounts to an equivalent thickness δ of reacting copper of 19.7 nm as calculated using Eq. (1),

$$\delta = \frac{qV_m}{zF} \quad \text{Eq. (1)}$$

where q is the charge density, V_m the molar volume of metallic copper ($7.1\text{ cm}^3\text{ mol}^{-1}$), z the number of exchanged electrons (1), and F the Faraday constant. This value of 19.7 nm corresponds to 95 equivalent monolayers (ML) of copper being dissolved since one (111)-oriented ML of copper is 0.208 nm thick from the bulk fcc structure. A 3-dimensional (3D) volume of material was thus consumed by the dissolution reaction in these testing conditions. The cathodic charge density transfer measured during the cathodic scan is 22 007 $\mu\text{C}\cdot\text{cm}^{-2}$, lower than the anodic one and indicating that about ~17 ML of copper irreversibly dissolved during the CV treatment.

In the presence of MBT, the CV is nearly completely flat until the anodic apex (Figure 3.1(a)), showing highly efficient inhibition of the dissolution of copper. In our testing conditions, MBT pre-adsorbs on copper covered by the native oxide and the reduction process of the native oxide occurs in the presence of a surface layer of MBT. As a result, the Cu atoms dissociated from oxygen by electro-reduction may be captured by the molecular surface layer, and it can be expected that the MBT film pre-formed in these conditions includes copper. The enlarged CV is shown in the inset. The increase of the anodic current is shifted anodically indicating that the anodic oxidation of copper and atomic transport across the interface requires a higher driving force. At the anodic apex, the current is much lower due to the barrier effect of the pre-adsorbed MBT molecular layer. In the reverse scan, no cathodic peak is observed in the range of -0.3 to -0.50 V/SHE unlike in the absence of the inhibitor. This is consistent with the

MBT pre-formed surface layer blocking dissolution in these conditions of anodic polarization, and thus the subsequent reductive deposition of copper.

Figure 3.1(b) shows the first CV obtained when increasing anodic polarization potential in the presence of MBT. For $E > -0.20$ to -0.15 V/SHE, the anodic current increases continuously until the anodic apex and a cathodic peak is observed in the reverse scan. Like in the absence of MBT, this behavior indicates a regime of anodic dissolution followed by reductive redeposition of dissolved copper upon reverse polarization. The anodic shift of the regime of anodic dissolution confirms that the MBT pre-adsorbed layer inhibits dissolution by a barrier effect in a potential window of about 0.15-0.2 V. However, this barrier effect does not resist the further increase of the driving force for Cu dissolution. The results obtained in this range of anodic polarization do not support the view that the reacting copper atoms could be directly captured by the pre-adsorbed MBT surface layer to form a protective Cu(I)-MBT film by a surface reaction [29], since a dissolution/redeposition behavior is observed like at lower potential in the absence of MBT as seen in Figure 3.1(b). However, the previously proposed formation of a Cu-containing film [27,28] by redeposition from the solution cannot be excluded.

In the presence of MBT, the anodic charge density transfer cumulated until the anodic apex of -0.18 V/SHE and in the reverse scan is $36 \mu\text{C cm}^{-2}$. This corresponds to only 0.03 nm (0.13 ML) of copper having reacted to be compared with 19.7 nm (95 ML) without MBT, showing extremely high anodic inhibition efficiency (99.9%) in these test conditions. The residual anodic activity observed at the apex of -0.18 V/SHE likely occurs at the most reactive surface sites, and thus at the emergence of the grain boundaries while the grain surfaces remain better protected. Hereafter, we discuss the ECSTM data obtained in the presence of the MBT inhibitor in these conditions of low residual activity generated at the apex of -0.18 V/SHE. The ECSTM data obtained in similar conditions of residual activity in MBT-free 1 mM HCl solution were discussed previously [22,26].

3.3.2 MBT inhibition effects on early stage intergranular corrosion

Figure 3.2 shows a typical local area at the topmost surface of microcrystalline copper where the microstructure could be repeatedly imaged *in situ* by ECSTM before (Figure 3.2 (a)) and after 2 (Figure 3.2(b)) and 4 (Figure 3.2(c)) CVs in the 10 mM HCl(aq) + 0.1mM MBT solution. In this area of interest, the microstructure exposes grains and sub-grains. Some of the grains are measured at a lower topographic height, which is attributed to differences of local surface reactivity during surface preparation by electrochemical polishing (etching) and subsequent *in situ* reduction of the native oxide film. The GB edges, i.e. the termination of the GB planes, and their immediate vicinity, hereafter referred to as the GB regions, are also well marked by the surface preparation. Some GB regions are measured lower, also as a result of higher local surface reactivity revealed by surface preparation while others can be located thanks to topography variations between the adjacent grains.

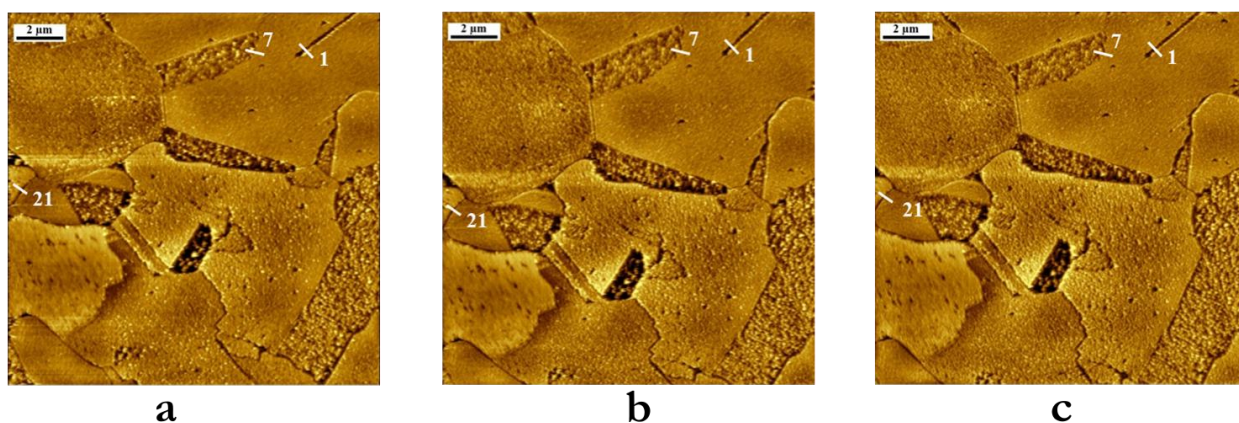


Figure 3.2: Topographic ECSTM images of microcrystalline copper as obtained *in situ* at $U = -0.45$ V/SHE before and after cycling in 10 mM HCl(aq) + 0.1 mM MBT (Z range $\Delta Z = 7$ nm, tip potential $U_{\text{tip}} = -0.8$ V

SHE, tunneling current $I_t = 1$ nA): (a) Initial surface state; (b) Surface state after 2 CVs; (c) Surface state after 4 CVs.

Based on our previous work [22,24-26], the different types of observed grains boundaries were assigned according to the GB morphology in the surface plane. Two parallel GBs separating a sub-grain is a configuration typical of Σ_3 coherent twins (with a $\{111\}$ -oriented GB plane). Short and straight GBs are assigned to low Σ CSL boundaries. Straight segments observed along a GB of locally straight or curved morphology are assigned to high Σ CSL boundaries. Curved GBs are assigned to random boundaries.

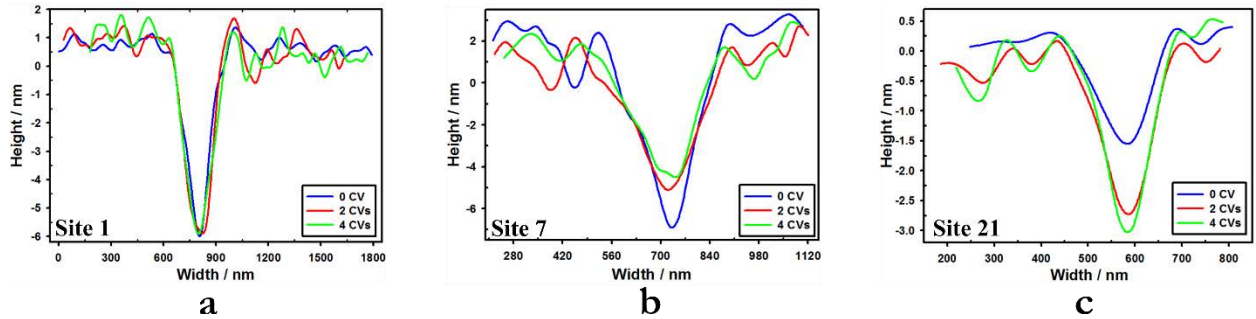


Figure 3.3: Average topographic line profiles measured across the GB at sites # 1, 7 and 21 in Figure 3.2.

In total, 43 local sites were identified at which the depth at the bottom of the GB region could be geometrically measured before and after 2 and 4 CV cycles. Typical examples are shown in Figure 3.3 for sites 1, 7 and 21 in Figure 3.2. Comparative analysis of the variations of the GB depth in this population of 43 sites revealed five types of local intergranular behavior after 2 and 4 CVs: i) no variation of the GB depth, ii) repeated increase, iii) repeated decrease, iv) decrease followed by increase, and v) increase followed by decrease.

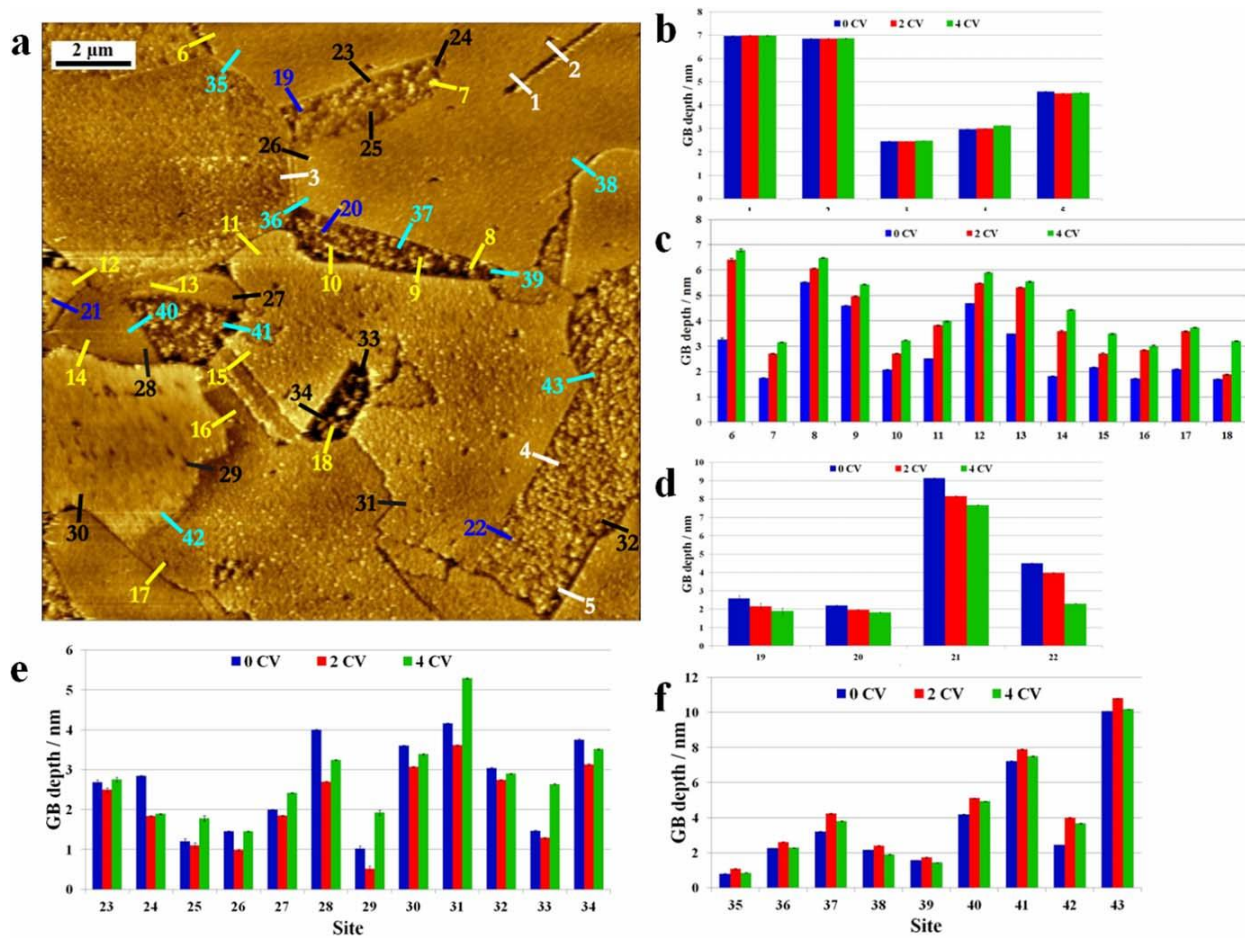


Figure 3.4: Identification of early stage intergranular corrosion behavior of microcrystalline copper sites in 10 mM HCl(aq) + 0.1 mM MBT: (a) Topographic ECSTM image with grain boundary sites labelled 1 to 43; (b) Bar graph of the depth measured across the GB sites showing no preferential reactivity after 2 and 4 CVs; (c) Bar graph of the GB sites showing depth increase after 2 and 4 CVs; (d) Bar graph of the GB sites showing depth decrease after 2 and 4 CVs; (e) Bar graph of the GB sites showing depth decrease and subsequent increase after 2 and 4 CVs, respectively. (f) Bar graph of the GB sites showing depth increase and subsequent decrease after 2 and 4 CVs, respectively.

There were five sites, labelled 1 to 5 in Figure 3.4(a), at which no net variation of the depth of the GB region was measured after 2 and 4 CVs. The depth measured across all five sites is different due to differences of local surface reactivity during surface preparation. The bar graph in Figure 3.4(b) shows no significant increase nor decrease of the depth of the GB region that would characterize a different behavior than on the adjacent grains caused by intergranular corrosion. In the absence of inhibitors, this intergranular corrosion resistant behavior is typical of Σ_3 coherent twins like characterized in testing conditions of sub-surface penetrating attack [3,13] and like also observed by *in situ* ECSTM measurements of early intergranular corrosion [22,26]. Here, it is observed for sites 1 and 2 which are located along two parallel GBs separating a sub-grain, a configuration typical of Σ_3 coherent twins. Thus, the absence of preferential local reactivity in these sites cases can be assigned to the intrinsic resistance of the Σ_3 coherent twins rather than to the presence of the MBT inhibitor. This locally resistant intergranular behavior is also observed for sites 3 to 5. Site 3 is located at a short and straight boundary assigned to a low Σ CSL boundary. Sites 4 and 5 are located along straight segments of GBs assigned to high Σ CSLs. In these local sites, which would be attacked without inhibitor [22,26], the pre-adsorbed MBT layer provides equal protection to the GB region than to the adjacent grains, like schematically illustrated in Figure 3.5a.

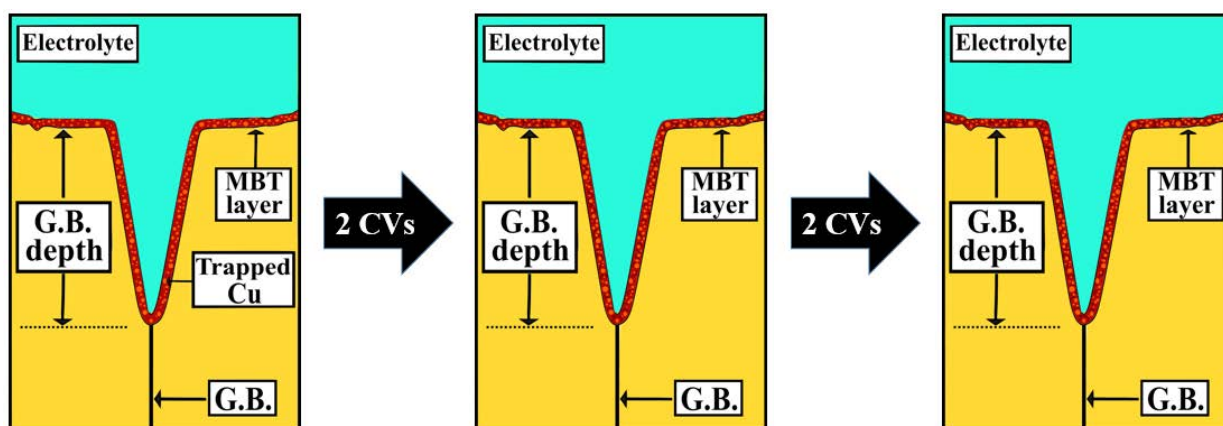


Figure 3.5a: Schematic illustration of observed MBT inhibiting effects on early intergranular corrosion of copper in acid electrolyte: protection by pre-adsorbed MBT layer and there is no dissolution at the GBs after 2 CVs and 4 CVs.

For thirteen sites, labelled 6 to 18 in Figure 3.4(a), a net increase of the depth of the GB region could be measured after 2 and 4 CVs (Figure 3.4(c)). The increase of the GB depth is indicative of the preferential local consumption of the material by irreversible and faster dissolution than on the adjacent grains. It has been previously observed for early intergranular corrosion of copper in 1 mM HCl(aq) solution without inhibitor with an amplitude of the increase of the GB depth not exceeding 2 nm [26]. In the present work performed in more acidic 10 mM HCl(aq) + 0.1 mM MBT, it was observed with a maximum amplitude reaching 3 nm, which is assigned to the effect of MBT mitigating, but not fully blocking, preferential dissolution at the less resistive GBs because of less efficient MBT protection than on the adjacent grains (Figure 3.5b). Among the sites where this imperfect MBT protection is observed, sites 8-10 and 15 are located along straight GB segments assigned to high Σ CSLs. For these high Σ CSL boundaries, local intergranular irreversible dissolution is observed but mitigated by the MBT surface layer given the relatively small increase of the GB depth. Sites 6,7,11-14,16-18 belong to curved GBs or GB segments assigned to random boundaries. Note that the highest amplitude of the GB depth increase resulting from the imperfect MBT protection is measured at site 6 assigned to a random GB.

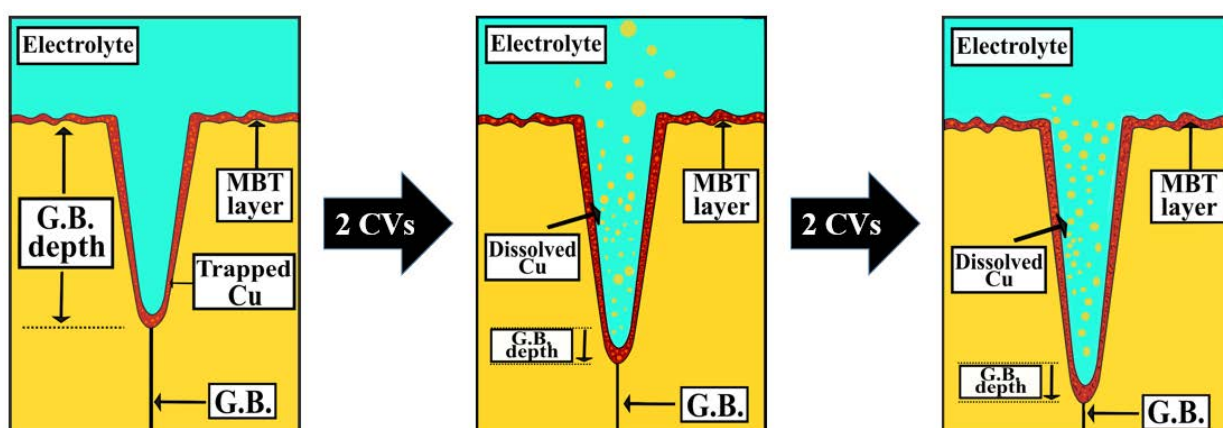


Figure 3.5b: Schematic illustration of observed MBT inhibiting effects on early intergranular corrosion of copper in acid electrolyte: imperfect protection by pre-adsorbed MBT layer and there is mitigated dissolution at the GBs after 2 CVs and 4 CVs.

The four sites labelled 19 to 22 in Figure 3.4(a) are those at which a net decrease of the depth of the GB region could be measured after 2 and 4 CVs (Figure 3.4(d)). The decrease of the GB depth is indicative of a local accumulation of reaction products, more important in the GB region than on the adjacent grains. It has been observed in previous ECSTM studies of passivation of copper in 0.1 M NaOH(aq) and

attributed to the formation of the Cu(I) passive oxide film locally thicker in the GB regions than on the adjacent grains [24,25,]. In 10 mM HCl(aq) + 0.1 mM MBT, the electrochemical response does not show a passivation-like behavior of the grains in the potential range tested but only a displaced onset of anodic oxidation. However the anodic oxidation could preferentially occur in the GB regions because of their higher reactivity, generating locally more Cu(I) ions and thus leading to the local growth of a layer of reaction products, possibly Cu(I)-MBT species [27,28], protecting more efficiently against anodic dissolution than the MBT film formed by pre-adsorption. No such layer would form on the less reactive adjacent grains (Figure 3.5c). The growth process would be repeated at each treatment cycle thus leading to an increased thickness of the film formed in the GB region. This local formation of a film of reaction products is observed at sites 19, 20 and 22 along straight GB segments assigned to high Σ CSL boundaries. It is also observed at site 21 along a random GB characterized by a curved morphology.

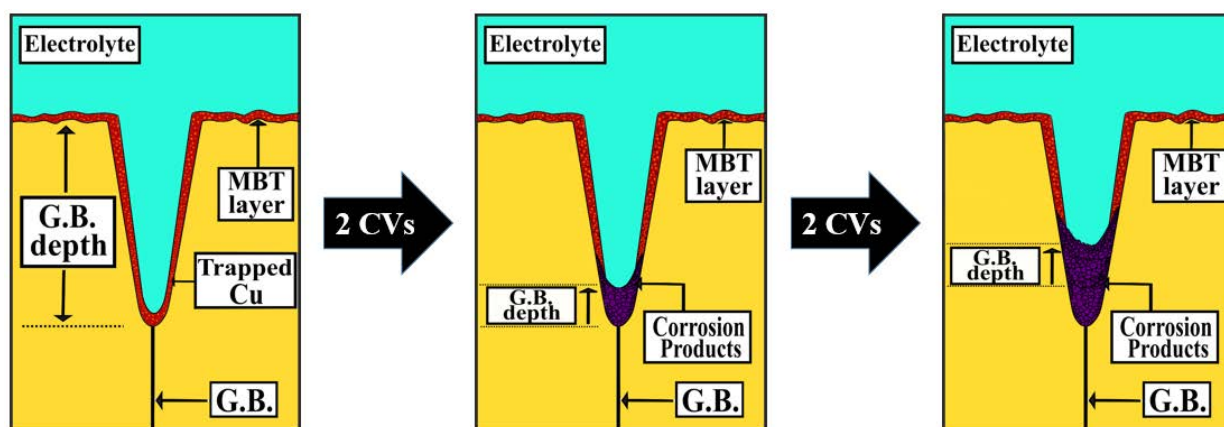


Figure 3.5c: Schematic illustration of observed MBT inhibiting effects on early intergranular corrosion of copper in acid electrolyte: protection by corrosion products at the GBs after 2 CVs and 4 CVs.

For the twelve sites labelled 23 to 34 in Figure 3.4(a), the behavior was first characterized by a decrease of the GB depth after 2 CVs and subsequently by an increase after 4 CVs (Figure 3.4(e)). These variations can be small (e.g. site 23) or more pronounced (e.g. site 31). Like for sites 19 to 22, the decrease of the GB depth measured after 2 CVs is indicative of the preferential accumulation in the GB region of reaction products that leads to the formation of a film mitigating, at least temporarily, preferential dissolution in the GB region. However, this protective effect does not persist since after 2 more CVs the GB depth increases due to dissolution (Figure 3.5d). This unstable behavior suggests transient protection provided by the local film initially formed and likely altered during the subsequent CV treatments. Among the GB sites where this behavior is observed, sites 23 and 34 belong to straight GB segments assigned to high Σ CSLs. Note that at these two sites the GB depth variations are small indicating little alterations of the local early intergranular corrosion behavior. All the other sites belong to curved or locally curved boundaries assigned to random boundaries. Half of them (25, 27, 29, 31 and 33) show an increase of the GB depth after 4 CVs to a value higher than the initial value measured before cycling, indicating a pronounced alteration of the transient protection against anodic dissolution brought by the initial growth of the surface film of reaction products.

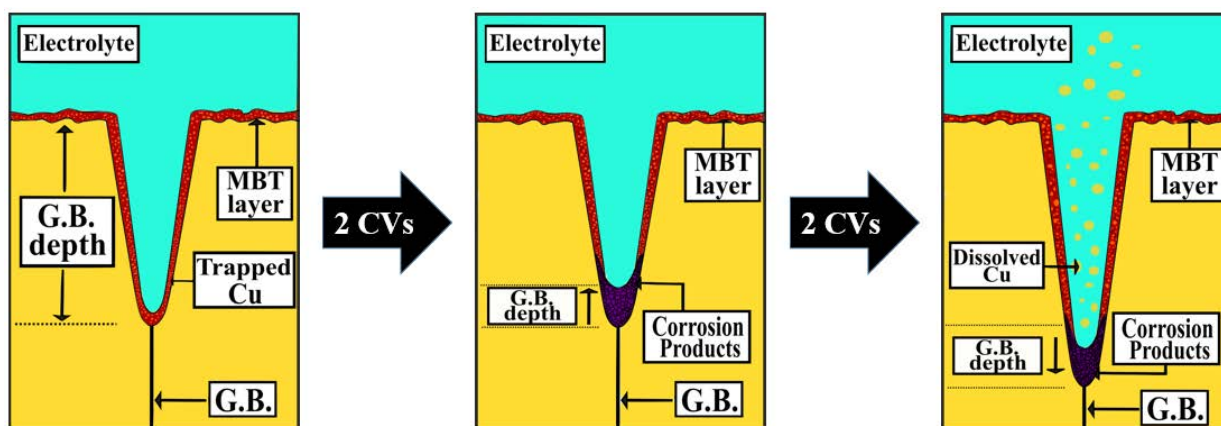


Figure 3.5d: Schematic illustration of observed MBT inhibiting effects on early intergranular corrosion of copper in acid electrolyte: transient protection by corrosion products at the GBs after 2 CVs and 4 CVs.

Labels 35 to 43 in Figure 3.4(a) correspond to the nine sites at which the behavior was first characterized by an increase of the GB depth after 2 CVs and subsequently by a decrease after 4 CVs (Figure 3.4(f)). Like for sites 6 to 18, the increase of the GB depth measured after 2 CVs is indicative of intergranular net dissolution. Mitigation by the MBT is supported by the relatively small increase of the GB depth reaching 1 nm at the most, less than in the less aggressive 1 mM HCl(aq) solution in the absence of MBT [26]. However, after 2 more CVs, the local accumulation of reaction products decreases the GB depth with formation of a protective film against dissolution. In this case, the repeated alterations of the MBT surface layer brought by the CV treatment promote the delayed formation of a protecting film in the GB regions (Figure 3.5e). Three sites (37, 38 and 40) at which this behavior is observed belong to straight GB segments assigned to high Σ CSLs. The other six sites (35, 36, 39, 41-43) belong to curved or locally curved boundaries assigned to random GBs.

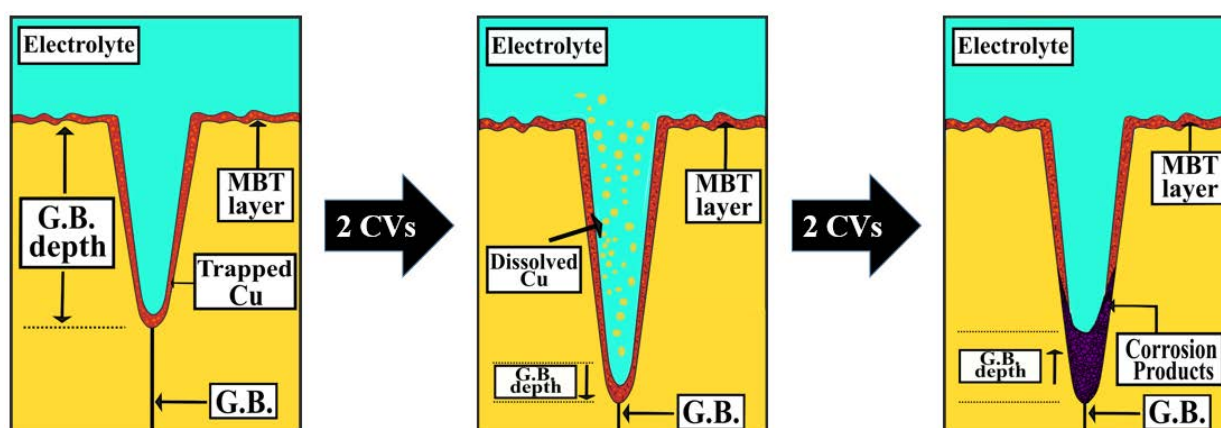


Figure 3.5e: Schematic illustration of observed MBT inhibiting effects on early intergranular corrosion of copper in acid electrolyte: delayed protection by corrosion products at the GBs after 2 CVs and 4 CVs.

3.3.3 Intergranular inhibiting effects according to GB type

Table 3.1: Observed occurrences of each type intergranular corrosion behavior for various types of grain boundaries for microcrystalline copper in 10 mM HCl(aq) + 0.1 mM MBT

Intergranular behavior	CTs	Low Σ CSLs	High Σ CSLs	Random GBs
Resistance (intrinsic)	2	--	--	--
Protection by pre-adsorbed MBT layer (no dissolution)	--	1	2	--
Imperfect protection by pre-adsorbed MBT layer (mitigated dissolution)	--	--	4	9
Protection by corrosion products	--	--	3	1
Transient protection by corrosion products	--	--	2	10
Delayed protection by corrosion products	--	--	3	6

Table 3.1 and Figure 3.6 compile the occurrences for the different types of observed local intergranular corrosion behaviors. They are sorted according to GB type as derived from the morphology of the GBs at the topmost surface. It can be seen that all types of GBs except the Σ_3 coherent twins show preferential reactivity compared to the adjacent grains. For the coherent twins, the absence of early intergranular corrosion is assigned to the intrinsic resistant character of these boundaries to intergranular corrosion. For low Σ CSLs, full protection by the pre-adsorbed MBT layer was the only observed behavior, in agreement with the lower intrinsic reactivity expected for these boundaries compared to high Σ CSLs and random boundaries. In other words, the MBT layer pre-adsorbed in low Σ CSLs, i.e. before CV cycling in the Cu(I) oxidation range, is protective enough so that preferential intergranular electrochemical reactivity is completely inhibited. Whereas, in the high Σ CSLs and random boundaries, intergranular reactivity is only mitigated, because of the higher electrochemical reactivity of these boundaries and possibly because of the more defective character of the MBT layer pre-formed in these boundaries.

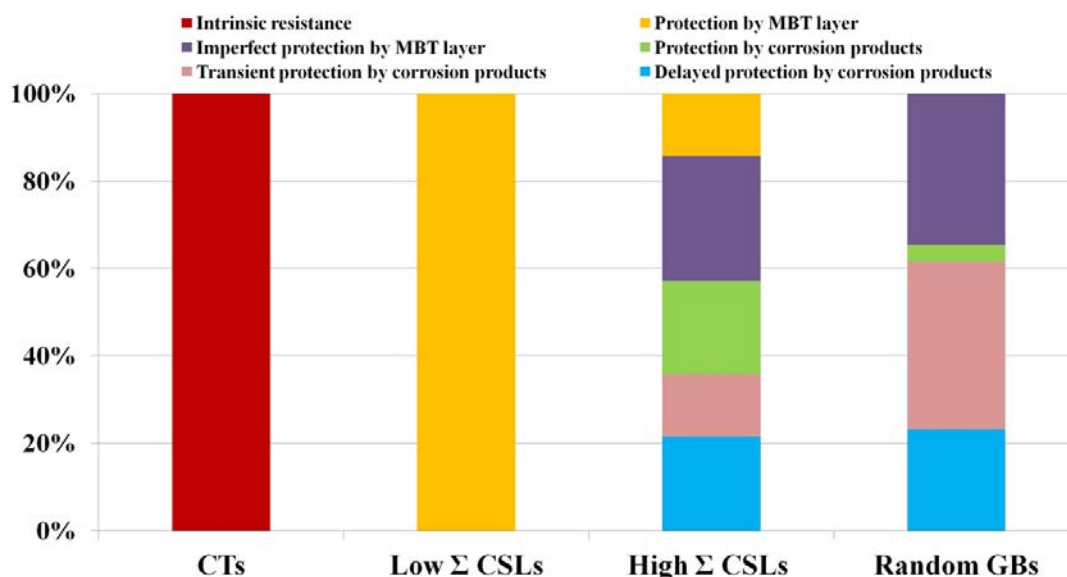


Figure 3.6: Percentage of each type of intergranular corrosion behavior observed on various types of grain boundaries for microcrystalline copper in 10 mM HCl(aq) + 0.1 mM MBT.

For the random GBs, characterized by curved morphologies at the topmost surface, protection against active dissolution by the accumulation of reaction products forming a protective film predominates protection by the pre-adsorbed MBT layer. This is consistent with more intense activity occurring initially in the GB region, as expected from the ill-defined crystallographic character of the random boundaries, and producing transiently the Cu(I) ions leading to the formation of corrosion products. A major part of the measured random GB sites show transient protection after repeated anodic polarization, showing the fragile protectiveness provided by the reaction products accumulated in the random GBs.

Fewer of the measured GB sites could be associated with the other types of GBs. For the high Σ CSLs, characterized by short straight segments, protection by a film of corrosion products is also observed but more concurrently with protection by the pre-adsorbed MBT layer, which suggests a lower initial reactivity of these GBs compared to most random GBs. A major part of the measured high Σ CSLs show stable or delayed protection by a film of corrosion products in contrast with the random GBs whose major part show transient protection, which suggests lower protectiveness of the film grown in the random grain boundaries.

3.4 Conclusions

ECSTM and cyclic voltammetry have been applied to characterize the inhibiting effects of MBT on the early stages of intergranular corrosion of microcrystalline copper in a 10 mM HCl(aq) acid solution. CV analysis of the macroscopic electrochemical response showed that MBT efficiently inhibits the active dissolution of copper in the acid medium by shifting to higher potential the onset of anodic dissolution and markedly lowering its intensity in an overpotential window of 0.15-0.2 V, owing to pre-adsorption and formation of a protective surface layer before CV cycling.

ECSTM analysis of the local intergranular corrosion behavior showed that the Σ_3 coherent twins do not react preferentially compared to grains, in agreement with their intrinsic resistant character to intergranular corrosion. Low Σ CSL was observed to be protected by the pre-adsorbed MBT layer against net preferential dissolution in the GB region. All high Σ CSLs and random GBs were observed to react preferentially compared to grains. For these intrinsically more reactive boundaries, net dissolution, mitigated by the MBT layer pre-formed before CV cycling, was observed concurrently with protection

resulting from preferential formation of reaction products in the GB regions. This protective effect of accumulated corrosion products was observed to be stable, transient or delayed in the conditions of repeated anodic cycling applied to force dissolution. For the high Σ CSL boundaries, this protection effect was more stable upon repeated cycling. For the random boundaries, this protection effect is generally transient, which is assigned to the intrinsically more reactive character of such GBs, less effectively protected by the local formation of a film of reaction products.

Acknowledgments

This project has received funding from the European Research Council (ERC) under the European Union's Horizon 2020 research and innovation programme (Advanced Grant CIMNAS, Corrosion Initiation Mechanisms at the Nanometric or Atomic Scale. Grant agreement No 741123).

References

- [1] J. Mieluch, M. Smialowski, The Behaviour of Grain Boundaries in Iron During Anodic Polarization in Ammonium Nitrate Solution, *Corrosion Science* 4 (1964) 237–243.
- [2] P. Lin, G. Palumbo, U. Erb, K.T. Aust, Influence of Grain Boundary Character Distribution on Sensitization and Intergranular Corrosion of Alloy 600, *Scripta Metallurgica et Materialia* 33 (1995) 1387–1392.
- [3] A. Vinogradov, T. Mimaki, S. Hashimoto, R.Z. Valiev, On the Corrosion Behaviour of Ultra-Fine Grain Copper, *Scripta Materialia* 41 (1999) 316–326.
- [4] L. Lu, M.L. Sui, K. Lu, Superplastic Extensibility of Nanocrystalline Copper at Room Temperature, *Science* 287 (2000) 1463–1466.
- [5] V.Y. Gertsman, S.M. Gruemer, Study of Grain Boundary Character Along Intergranular Stress Corrosion Crack Paths in Austenitic Alloys, *Acta Materialia* 49 (2001) 1589–1598.
- [6] S.H. Kim, U. Erb, K.T. Aust, G. Palumbo, Grain Boundary Character Distribution and Intergranular Corrosion Behavior in High Purity Aluminum, *Scripta Materialia* 44 (2001) 835–839.
- [7] H. Miyamoto, K. Yoshimura, T. Mimaki, M. Yamashita, Behavior of Intergranular Corrosion of $\langle 011 \rangle$ Tilt Grain Boundaries of Pure Copper Bicrystals, *Corrosion Science* 44 (2002) 1835–1846.
- [8] M. Shimada, H. Kokawa, Z.J. Wang, Y.S. Sato, I. Karibe, Optimization of grain boundary character distribution for intergranular corrosion resistant 304 stainless steel by twininduced grain boundary engineering, *Acta Materialia* 50 (2002) 2331–2341.
- [9] E.M. Lehecky, A.M. Brennenstuhl, I. Thompson, On the relationship between grain boundary connectivity, coincident site lattice boundaries, and intergranular stress corrosion cracking, *Corrosion Science* 46 (2004) 2383–2404.
- [10] V. Randle, 'Special' Boundaries and Grain Boundary Plane Engineering, *Scripta Materialia* 54 (2006) 1011–1015.
- [11] S. Xia, B. Zhou, W. Chen, Effect of single-step strain and annealing on grain boundary character distribution and intergranular corrosion in Alloy 690, *Journal of Materials Science* 43 (2008) 2990–3000.
- [12] R. Jones, V. Randle, Sensitisation behaviour of grain boundary engineered austenitic stainless steel, *Materials Science and Engineering A* 527 (2010) 4275–4280.
- [13] K. D. Ralston, N. Birbilis, Effect of Grain Size on Corrosion: A Review, *Corrosion* 66 (2010) 075005–075005-13.
- [14] CL Changliang, S.Xi, H. Li, TG. Liu, BX. Zhou, WJ. Chen, N. Wang, Ning, Improving the intergranular corrosion resistance of 304 stainless steel by grain boundary network control, *Corrosion Science* 53 (2011) 1880–1886.
- [15] C. Luo, X. Zhou, G.E. Thompson, A.E. Hughes, Observations of intergranular corrosion in AA2024-T351: The influence of grain stored energy, *Corrosion Science* 61 (2012) 35–44.
- [16] S. Kumar, B.S. Sai Prasad, V. Kain, J. Reddy, Methods for making alloy 600 resistant to sensitization and intergranular corrosion, *Corrosion Science* 70 (2013) 55–61.

- [17] Y. Takehara, H. Fujiwara, H. Miyamoto, "Special" to "general" transition of intergranular corrosion in Sigma 3{111} grain boundary with gradually changed misorientation, *Corrosion Science* 77 (2013) 171-175.
- [18] A. Stratulat, J.A. Duff, T.J. Marrow, T. James, Grain boundary structure and intergranular stress corrosion crack initiation in high temperature water of a thermally sensitised austenitic stainless steel, observed in situ, *Corrosion Science* 85 (2014) 428-435.
- [19] E. Martinez-Lombardia, Y. Gonzalez-Garcia, L. Lapeire, I. De Graeve, K. Verbeken, L. Kestens, J. Mol, H. Terryn, Scanning Electrochemical Microscopy to Study the Effect of Crystallographic Orientation on the Electrochemical Activity of Pure Copper, *Electrochimica Acta* 116 (2014) 89-96.
- [20] B.V. Mahesh, R.K. Singh Raman, Role of Nanostructure in Electrochemical Corrosion and High Temperature Oxidation: A Review, *Metallic Materials Transactions A* 45A (2014) 5799-5822.
- [21] N. Srinivasan, V. Kain, N. Birbilis, K.V. Mani Krishna, S. Shekhawat, I. Samajdar, Near boundary gradient zone and sensitization control in austenitic stainless steel, *Corrosion Science* 100 (2015) 544-555.
- [22] E. Martinez-Lombardia, L. Lapeire, V. Maurice, I. De Graeve, K. Verbeken, L.H. Klein, L. Kestens, P. Marcus, H. Terryn, In Situ Scanning Tunneling Microscopy Study of the Intergranular Corrosion of Copper, *Electrochemistry Communications* 41 (2014) 1-4.
- [23] E. Martinez-Lombardia, V. Maurice, L. Lapeire, I. De Graeve, K. Verbeken, L.H. Klein, L. Kestens, P. Marcus, H. Terryn, In Situ Scanning Tunneling Microscopy Study of Grain-Dependent Corrosion on Microcrystalline Copper, *Journal of Physical Chemistry C* 118 (2014) 25421-25428.
- [24] H. Chen, V. Maurice, L.H. Klein, L. Lapeire, K. Verbeken, H. Terryn, P. Marcus, Grain Boundary Passivation Studied by In Situ Scanning Tunneling Microscopy on Microcrystalline Copper, *Journal of Solid State Electrochemistry* 19 (2015) 3501-3509.
- [25] H. Chen, M. Bettayeb, V. Maurice, L.H. Klein, L. Lapeire, K. Verbeken, H. Terryn, P. Marcus, Local passivation of metals at grain boundaries: In situ scanning tunneling microscopy study on copper, *Corrosion Science* 111 (2016) 659-666.
- [26] M. Bettayeb, V. Maurice, L.H. Klein, L. Lapeire, K. Verbeken, P. Marcus, Nanoscale Intergranular Corrosion and Relation With Grain Boundary Character as Studied In Situ on Copper, *Journal of the Electrochemical Society* 165 (2018) C835-C841.
- [27] D. Chadwick, T. Hashemi, Electron spectroscopy of corrosion inhibitors: Surface film formed by 2-mercaptobenzothiazole and 2-mercaptobenzimidazole on copper, *Surface Science* 89 (1-3) (1979) 649-659.
- [28] M. Ohsawa, W. Suëtaka, Spectro-electrochemical studies of the corrosion inhibition of copper by mercaptobenzothiazole, *Corrosion Science* 19 (1979) 709-722.
- [29] J. C. Marconato, L. O. Bulboes, M. L. Temperini, A spectroelectrochemical study of the inhibition of the electrode process on copper by 2-mercaptobenzothiazole in ethanolic solutions, *Electrochimica Acta* 43 (1998) 771-780.
- [30] R. Woods, G. A. Hope, K. Watling, A SERS spectroelectrochemical investigation of the interaction of 2-mercaptobenzothiazole with copper, silver and gold surfaces, *Journal of Applied Electrochemistry* 30 (2000) 1209-1222.
- [31] C. W. Yan, H. C. Lin, C. N. Cao, Investigation of inhibition of 2-mercaptobenzothiazole for copper corrosion, *Electrochimica Acta* 45 (2000) 2815-2821.
- [32] M. Antonijevic, M. Petrovic Mihajlovic, Copper corrosion inhibitors. A review, *International Journal of Electrochemical Science* 3 (1) (2008) 1-28.
- [33] M. M. Antonijevic, S. M. Milic, M. B. Petrovic, Films formed on copper surface in chloride media in the presence of azoles, *Corrosion Science* 51 (2009) 1228-1237.
- [34] F. M. A. Kharafi, N. A. Al-Awadi, I. M. Ghayad, R.M. Abdullah, M.R. Ibrahim, Novel technique for the application of azole corrosion inhibitors on copper surface, *Materials Transactions* 51 (2010) 1671-1676.
- [35] G. Gece, Drugs: A review of promising corrosion inhibitors, *Corrosion Science* 53 (2011) 3873-3898.
- [36] L. P. Kazansky, I. A. Selyaninov, Y. I. Kuznetsov, Adsorption of 2-mercaptobenzothiazole on copper surface from phosphate solutions, *Applied Surface Science* 258 (2012) 6807-6813.
- [37] M. Finsgar, D.K. Merl, An electrochemical, long-term immersion, and XPS study of 2-mercaptobenzothiazole as a copper corrosion inhibitor in chloride solution, *Corrosion Science* 83 (2014) 64-175.

- [38] I. Milosev, N. Kovacevic, J. Kovac, A. Kokalj, The roles of mercapto, benzene and methyl groups in the corrosion inhibition of imidazoles on copper: I. experimental characterization, *Corrosion Science* 98 (2015) 107-118.
- [39] M. Petrovic Mihajlovic, M. Antonijevic, Copper corrosion inhibitors. period 2008-2014. a review, *International Journal of Electrochemical Science* 10 (2015) 1027-1053.
- [40] Y.-H. Chen, A. Erbe, The multiple roles of an organic corrosion inhibitor on copper investigated by a combination of electrochemistry-coupled optical in situ spectroscopies, *Corrosion Science* 145 (2018) 232-238.
- [41] A. Fateh, M. Aliofkhazraei, A. R. Rezvanian, Review of corrosive environments for copper and its corrosion inhibitors, *Arabian Journal of Chemistry* 13 (2020) 481-544.
- [42] T. Shahrabadi, H. Tavakholi, M. G. Hosseini, Corrosion inhibition of copper in sulphuric acid by some nitrogen heterocyclic compounds, *Anti-Corrosion Methods and Materials* 54 (2007) 308-313.
- [43] Z. Zhang, Q. Wang, X. Wang, L. Gao, The influence of crystal faces on corrosion behavior of copper surface: First-principle and experiment study, *Applied Surface Science* 396 (2017) 746-753.
- [44] X. Wu, F. Wiame, V. Maurice, P. Marcus, Adsorption and thermal stability of 2-mercaptobenzothiazole corrosion inhibitor on metallic and pre-oxidized Cu(111) model surfaces, *Applied Surface Science* 508 (2020) 145132.
- [45] X. Wu, F. Wiame, V. Maurice, P. Marcus, 2-Mercaptobenzothiazole corrosion inhibitor deposited at ultra-low pressure on model copper surfaces, *Corrosion Science* 166 (2020) 108464.
- [46] X. Wu, F. Wiame, V. Maurice, P. Marcus, Moiré Structure of 2-Mercaptobenzothiazole Corrosion Inhibitor Adsorbed on (111)-Oriented Copper Surface, *Journal of Physical Chemistry C* 124 (2020) 15995-16001.
- [47] E. Vernack, D. Costa, P. Tingaut, P. Marcus, DFT studies of 2-mercaptobenzothiazole and 2-mercaptobenzimidazole as corrosion inhibitors for copper, *Corrosion Science* 174 (2020) 108840.
- [48] F. Chiter, D. Costa, V. Maurice, P. Marcus, DFT investigation of 2-mercaptobenzothiazole adsorption on model oxidized copper surfaces and relationship with corrosion inhibition, *Applied Surface Science* 537 (2021) 147802.
- [49] L. Lapeire, E. Martinez Lombardia, K. Verbeken, I. De Graeve, L. Kestens, H. Terryn, Effect of Neighboring Grains on the Microscopic Corrosion Behavior of a Grain in Polycrystalline Copper, *Corrosion Science* 67 (2013) 179-183.
- [50] L. Lapeire, E. Martinez Lombardia, K. Verbeken, I. De Graeve, L. Kestens, H. Terryn, Structural Dependence of Gold Deposition by Nanoplatin in Polycrystalline Copper, *Journal of Materials Science* 49 (2014) 3909-3916.
- [51] D. Zuili, V. Maurice, P. Marcus, Surface Structure of Nickel in Acid Solution Studied by In Situ STM, *Journal of the Electrochemical Society* 147 (2000) 1393-1400.
- [52] A. Seyeux, V. Maurice, L. H. Klein, P. Marcus, In Situ STM Study of the Initial Stages of Growth and of the Structure of the Passive Film on Ni(111) in 1 mM NaOH(aq), *Journal of Solid State Electrochemistry* 9 (2005) 337-346.
- [53] A. Seyeux, V. Maurice, L. H. Klein, P. Marcus, In Situ STM Study of the Effect of Chloride on the Growth Mechanism and Structure of the Passive Film on Nickel in Alkaline Solution. *Journal of the Electrochemical Society* 153 (2006) B453-463.
- [54] V. Maurice, L. H. Klein, H.-H. Strehblow, P. Marcus, In situ STM Study of the Surface Structure, Dissolution and Early Stages of Electrochemical Oxidation of the Ag(111) Electrode, *Journal of Physical Chemistry C* 111 (2007) 16351-16361.
- [55] N. Li, V. Maurice, L. H. Klein, P. Marcus, Structure and Morphology Modifications of Silver Surface in the Early Stages of Sulphide Growth in Alkaline Solution, *Journal of Physical Chemistry C* 116 (2012) 7062-7072.
- [56] Gwyddion – Free SPM (AFM, SNOM/NSOM, STM, MFM ...) data analysis software. <http://gwyddion.net/>
- [57] H.-H. Strehblow, B. Titze, The Investigation of the Passive Behaviour of Copper in Weakly Acid and Alkaline Solutions and the Examination of the Passive Film by Esca and ISS, *Electrochimica Acta* 25 (1980) 839-850.
- [58] Y. Feng, K.S. Siow, W.K.Teo, K.L.TanL, A.K Hsieh, Corrosion Mechanisms and Products of Copper in Aqueous Solutions at Various pH Values, *Corrosion* 53 (1997) 389-398.
- [59] B. Beverskog, I. Puigdomenech, Pourbaix Diagrams for the System copper-chlorine at 5-100 C. SKI, Nyköping, 1998

- [60] O. Magnussen, L. Zitzler, B. Gleich, M. Vogt, R.J. Behm, In-Situ Atomic-Scale Studies of the Mechanisms and Dynamics of Metal Dissolution by High-Speed STM, *Electrochimica Acta* 46 (2001) 3725-3733.
- [61] M. Kruft, B. Wohlmann, C. Stuhlmann, K. Wandelt, Chloride Adsorption on Cu(111) Electrodes in Dilute HCl Solutions, *Surface Science* 377 (1997) 601-604.
- [62] M. Vogt, A. Lachenwitzer, O. Magnussen, R.J. Behm, In-Situ STM Study of the Initial Stages of Corrosion of Cu(100) Electrodes in Sulfuric and Hydrochloric Acid Solution. *Surface Science* 399 (1998) 49-69.
- [63] L.-J. Wan, K. Itaya, In Situ Scanning Tunneling Microscopy of Cu(110): Atomic Structures of Halide Adlayers and Anodic Dissolution, *Journal of Electroanalytical Chemistry* 473 (1999) 10-18.
- [64] W.H. Li, Y. Wang, J.H. Ye, S. F. Y. Li, In Situ STM Study of Chloride Adsorption on Cu(110) Electrode in Hydrochloric Acid Aqueous Solution, *Journal of Physical Chemistry B* 105 (2001) 1829-1833.
- [65] T. Hai Phan, T. Kosmala, K. Wandelt, Potential dependence of self-assembled porphyrin layers on a Cu(111) electrode surface: In-situ STM study, *Surface Science* 631 (2015) 207-212.
- [66] M. Bettayeb, V. Maurice, L.H. Klein, L. Lapeire, K. Verbeken, P. Marcus, Combined in situ microstructural study of the relationships between local grain boundary structure and passivation on microcrystalline copper, *Electrochimica Acta* 305 (2019) 240-246.

Chapter IV

In situ scanning tunneling microscopy study of 2-mercaptobenzimidazole local inhibition effects on copper corrosion at grain boundary surface terminations

This chapter reproduces an original manuscript with reference: Sagar B. Sharma, Vincent Maurice, Lorena H. Klein, Philippe Marcus, In situ scanning tunneling microscopy study of 2-mercaptobenzimidazole local inhibition effects on copper corrosion at grain boundary surface terminations, *Electrochimica Acta* (2021), in press.

Abstract

New insight on local inhibition effects of 2-mercaptobenzimidazole (MBI) on early stage intergranular corrosion of copper in hydrochloric acid solution is reported from *in situ* analysis at the nanometer scale and comparison with 2-mercaptobenzothiazole (MBT) effects in the same pre-adsorption and corrosion testing conditions. Macroscopic cyclic voltammetry analysis, including grains and grain boundary (GB) network, showed a passivation-like behavior in the Cu(I) oxidation range, specific to MBI since not observed with MBT and assigned to the anodic formation of a surface film of Cu(I)-MBI reaction products protecting against dissolution. Electrochemical scanning tunneling microscopy analysis revealed net intergranular dissolution, mitigated by the imperfect protection provided by the anodically formed MBI layer. It also showed local accumulation of reaction products in the GB surface regions, blocking preferential dissolution. For random GBs, blocking by local accumulation of reaction products was dominant, in agreement with the expected higher reactivity of these GBs generating more Cu(I) ions under anodic polarization and thus less efficiently protected by the anodically formed MBI layer. For Coincidence Site Lattice (CSL) boundaries, mitigated net dissolution was more frequently observed. Coherent twins showed equally efficient inhibition in the GB surface region than on adjacent grains. MBI inhibition was less efficient than MBT inhibition with more Cu(I) reaction products generated on the grains to form a surface film and their preferential local accumulation more frequently observed in the GB surface regions.

4.1 Introduction

Intergranular corrosion is a major form of degradation for polycrystalline metallic materials. It initiates locally at the surface termination of grain boundaries (GBs), and eventually propagates to attack the GB network, which can compromise the entire microstructure after penetration in the sub-surface. This form of localized corrosion can be combated by engineering polycrystals having the GB network the most resistant to corrosive attack. GB engineering is based on the knowledge of the relationships between crystallographic type and energy of grain boundaries and their susceptibility to intergranular corrosion, as developed from studies of GB engineered materials submitted to intergranular corrosion tests and studied with microstructural analytical techniques [1-26].

One efficient and widely applied mean to mitigate corrosion is to add inhibitors to the aggressive environment contacting the material. On copper and its alloys, azole derivatives such as the widely used and most studied benzotriazole (BTAH, $C_6H_5N_3$) but also mercaptoazoles derivatives such as 2-mercaptobenzothiazole (MBT, $C_7H_5NS_2$) and 2-mercaptobenzimidazole (MBI, $C_7H_6N_2S$) have been shown to be effective corrosion inhibitors [27-30]. The MBT and MBI molecules, the latter being studied in this work, contain sulfur and nitrogen atoms that act as active sites that enable chemisorption to the

metal substrate by strongly bonding, individually or concomitantly, to copper atoms, and thus form a stable and protective molecular film at the solid/liquid interface [30-45]. For MBI, the formation of a polymeric film has been proposed [35,37,40,41,] with the presence of Cu reaction products in the film - Cu-MBI [37] or Cu₂-MBI [35] organo-metallic complexes have been suggested - conditioned by the initial surface state of copper, metallic or oxidized, prior to formation of the protective film [37], and also by the reactivity of copper during the film formation.

The efficiency of corrosion inhibitors to mitigate intergranular corrosion and the relationship between GB crystallographic type and inhibition mechanism remains to be investigated. Recently, this was studied on copper by investigating the effects of MBT on early stage intergranular corrosion at the surface termination of grain boundaries, i.e. before penetration in the sub-surface region and propagation [46] (see Chapter III). Electro-Chemical Scanning Tunneling Microscopy (ECSTM) was used to study *in situ* in HCl acid solution the local alterations of the topmost surface of the metallic material at the nanometer scale. Among high angle GBs that are susceptible to intergranular corrosion in the absence of inhibitors [2,6,8,9,11-13,16,22,26], only coherent twins – which are Σ_3 coincidence site lattice (CSL) boundaries with a {111}-oriented GB plane - did not show preferential intergranular reactivity compared to adjacent grains, which was assigned to the intrinsic resistance of these GBs also observed without the inhibitor [3,13,22,26]. Low Σ Coincidence Site Lattice (CSL) boundaries were observed to be protected by the pre-adsorbed MBT layer against net preferential dissolution whereas high Σ CSLs and random GBs were observed to react preferentially compared to grains. For these intrinsically more reactive boundaries, net dissolution, mitigated by the pre-adsorbed MBT layer, was observed as well as protection resulting from preferential formation of reaction products in the GB regions. For random GBs, protection by reaction products was more frequently observed but less stable upon repeated anodic cycling applied to force dissolution.

Here, we report new insight for MBI and its local inhibiting effects at the surface termination of grain boundaries of various crystallographic types. ECSTM and CV (cyclic voltammetry) analysis was applied to microcrystalline copper in HCl aqueous acid solution in which no stable copper oxide is formed. Comparative analysis of the results obtained here with MBI with those obtained with MBT [46] in the same pre-adsorption and corrosion testing conditions provides deeper understanding on local inhibition mechanisms as well as their dependence on GB type and inhibiting molecule.

4.2 Experimental

The high purity microcrystalline copper samples were the same as in previous work [19,22-26,47,48]. From previous microstructural characterization [22,23], texture is nearly random and Σ_3 CSL and random boundaries correspond to 66% and most of remaining 34% of the GB length, respectively. The surface was prepared by mechanical polishing (diamond spray, 0.25 μm final grade) followed by electrochemical polishing (15 s in 66% orthophosphoric acid at 3 V versus Cu counter electrode) in order to remove the cold work layer and reveal the GB surface terminations.

An Agilent Technologies ECSTM system (PicoSPM base, Keysight STM S scanner, PicoScan 2100 controller, PicoStat bi-potentiostat and Picoscan software) was used. ECSTM cell, cleaning and tip preparation have been detailed elsewhere [49-53]. The ECSTM cell exposes a working electrode area of 0.16 cm² to ~350 μl of electrolyte. Two Pt wires served as counter electrode and pseudo reference electrode (+0.20 V/SHE). The 10 mM HCl(aq) (pH 2) electrolyte was prepared from ultrapure HCl and Millipore water (resistivity > 18 M Ω cm) and non-deaerated. MBI was dissolved from the powder physical state at a concentration of 1 mM. After exposing the sample to the electrolyte at -0.45 V/SHE, below the open-circuit potential value of -0.35 V/SHE, the native oxide film formed after electropolishing was reduced by CV treatment in the cathodic potential range as described before [22,26]. The cathodic peak associated with Cu(I) to Cu(0) reduction in the CVs was suppressed after two cycles,

independently of the presence or absence of MBI in the solution during the cathodic reduction pre-treatment.

After reduction of the native oxide, the microcrystalline copper surface was imaged by ECSTM in the metallic state at -0.45 V/SHE to ensure localization of grain boundaries in the field of view. CV was also used to force anodic oxidation by cycling between the anodic and cathodic apexes of -0.18 and -0.60 V/SHE (1 mV s⁻¹), respectively, like applied in our MBT study [46] (Chapter III). Up to 4 cycles were applied and new ECSTM images of the same surface field of view were taken at -0.45 V/SHE after 2 and 4 cycles, thus enabling to follow the evolution of the local topography after electrochemical cycling. The images were acquired in the constant current mode. No filtering was used during acquisition and the recorded images were processed with the Gwyddion software [54]. At the surface, the terminations of the GB planes correspond to the GB edges. These GB edges and their immediate vicinity are referred to as the GB surface regions, easily identified in the STM images. The local difference in topographic height between the bottom of the GB surface regions and the two adjacent grains, hereafter called GB depth, was determined by line profile analysis as previously described [24,26,46].

4.3 Results and discussion

4.3.1 Macroscopic MBI inhibition effects

Cyclic voltammetry was applied with the same protocol as for the ECSTM study in order to characterize the effects of MBI on the macroscopic corrosion behavior. The exposed surface fraction of the grains being very large compared to that of the GB network, the macroscopic electrochemical response can be assigned to the surface properties of the grains. Figure 4.1(a) shows CVs started in the metallic state at -0.45 V/SHE after reduction of the native oxide. At pH 2, no stable oxide is formed on copper and the Cu(I) ions dissolve as $CuCl_2^-$ in the investigated anodic potential range [55-58]. In the absence of MBI, anodic dissolution is observed for $E > -0.35$ V/SHE. The cathodic peak observed in the reverse scan corresponds to the reductive deposition of dissolved Cu(I) [26,58,59-63]. As discussed previously [46], the equivalent thickness of reacting copper can be deduced from the total positive current density (26 885 $\mu C\ cm^{-2}$) using Eq. (1),

$$\delta = \frac{qV_m}{zF} \quad \text{Eq. (1)}$$

where q is the charge density, V_m the molar volume of metallic copper (7.1 cm³ mol⁻¹), z the number of exchanged electrons (1), and F the Faraday constant. The obtained value is 19.7 nm, which indicates that a nanometer thick layer of material has reacted in these testing conditions.

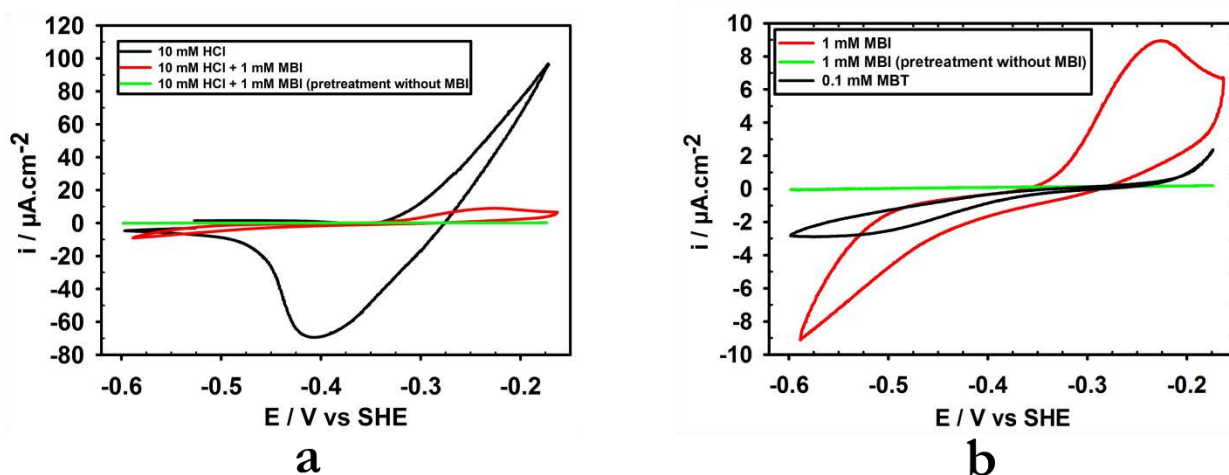


Figure 4.1: CV analysis of macroscopic electrochemical behavior of microcrystalline copper in 10 mM HCl(aq) (ECTM cell, scan rate = 1 mV/s): (a) CVs recorded without and with 1 mM MBI in the solution. (b) Enlarged CVs obtained in the presence of MBI after cathodic pre-treatment with and without MBI in the solution. In (b), the CV obtained in 10 mM HCl(aq) + 0.1 M MBT is shown for comparison.

The CVs obtained in the presence of MBI are superimposed in Figure 4.1(a) and enlarged in Figure 4.1(b). The observed behavior depends on the presence or absence of MBI during the reduction pre-treatment of the native oxide. After pre-treatment in the absence MBI in the solution, the CV is flat showing highly efficient inhibition of the anodic dissolution of copper as well as of the cathodic activity. In this case, MBI adsorbs on the copper surface in the metallic state obtained after reduction of the native oxide, and controlled by setting the potential to -0.45 V/SHE while adding MBI to the electrolyte. The obtained CV shows that these pre-adsorption conditions optimize the inhibition efficiency of the molecular adsorbed layer in the potential range tested, due to formation of a molecular barrier efficiently blocking atomic transport across the interface.

After pre-treatment in the presence of MBI in the solution, the CV shows a higher copper electrochemical activity, however markedly reduced compared to that measured in the absence of the inhibitor. In this case, MBI pre-adsorbs on copper covered by the native oxide and the reduction process occurs in the presence of a surface layer of MBI. As a result, the Cu atoms dissociated from oxygen by electro-reduction may be captured by the molecular surface layer, resulting in the formation of a barrier film less effective to block atomic transport across the interface as indicated by the residual electrochemical response in the Cu(I) oxidation range. The anodic current also increases for $E > -0.35$ V/SHE indicating that the anodic oxidation of copper and its transport across the interface leading to dissolution is initiated in the same potential range as in the absence of MBI. However, the current increase is much slower due to the mitigating effect of the MBI molecular layer pre-adsorbed on the surface. With increasing potential, a peak is observed at -0.23 V/SHE. The anodic reaction decreases in intensity in a process similar to passivation. Copper transport and dissolution appear blocked by the anodic formation of a modified, compared to pre-adsorbed layer, but protective surface layer. The charge density transfer cumulated at the anodic apex is $2\,292\,\mu\text{C}\cdot\text{cm}^{-2}$. Using Eq. (1), this corresponds to 1.7 nm of copper having reacted and captured by the formation of the protective surface film grown at this stage (if one assumes no transient dissolution). Given that several monolayers of copper were consumed, it is suggested that this surface layer is 3D in thickness and constituted of Cu(I)-MBI reaction products, possibly organic-metallic complexes [35,37], since grown in the Cu(I) oxidation range. It cannot be excluded that during the growth of the protective surface film some Cu(I) ions dissolved in the solution although no redeposition peak is observed in the subsequent cathodic scan.

In the reverse scan performed after reaching the anodic apex at -0.18 V/SHE, no cathodic peak is observed in the range of -0.3 to -0.50 V/SHE unlike in the absence of the inhibitor. This is consistent with the grown surface layer blocking anodic dissolution and thus the reductive deposition of copper.

The cathodic current increase observed for $E < -0.30$ V/SHE may correspond to the electro-reduction of the surface film of Cu(I)-MBI reaction products. A cathodic charge density transfer of $2107 \mu\text{C cm}^{-2}$ is obtained from the integration of the negative current density measured during cycling, which corresponds to an equivalent thickness of 1.55 nm of reacting copper. This value confirms the 3D thickness of the protecting surface layer grown by anodic oxidation of copper in the presence of the MBI inhibitor.

The CV previously obtained in the same testing conditions after pre-treatment in the presence of MBT [46] (Chapter III) is reproduced in Figure 4.1(b) for comparison. The surface is much less reactive than in the presence of MBI with no anodic peak indicative of anodic formation of a 3D layer constituted of Cu(I)-MBT reaction products. The total measured positive current density is $36 \mu\text{C cm}^{-2}$, corresponding to only a fraction of a monolayer of copper (0.03 nm equivalent thickness) having reacted [46] (Chapter III). For the same conditions of pre-treatment of the surface, comparison between the two molecules shows higher anodic inhibition efficiency for MBT than for MBI. For MBT, the pre-adsorbed molecular layer nearly fully blocks the macroscopic anodic activity. It can be deduced that the surface of grains is fully protected by the interfacial molecular layer in the test conditions, and that the residual activity may be associated to the most reactive (i.e. imperfectly protected) sites, including the GB network. For MBI, the pre-adsorbed molecular layer only mitigates anodic oxidation, leading to a passivation-like behavior with the buildup of a protective 3D surface layer of Cu(I)-MBI reaction products. This surface layer forms at the surface of the grains as deduced from the macroscopic electrochemical response. It also forms in the GB regions as deduced from the local analysis of the topography variations discussed hereafter.

4.3.2 Local MBI inhibition effects at grain boundaries

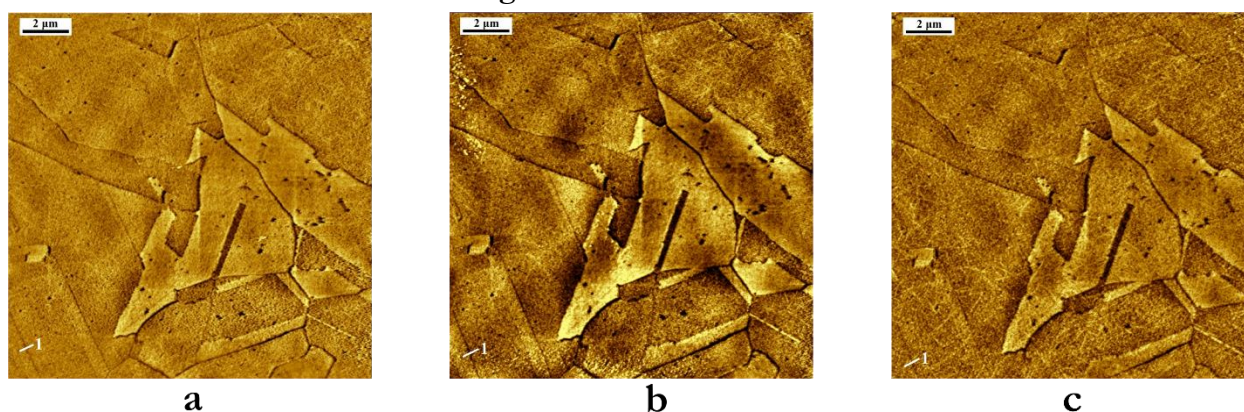


Figure 4.2: Topographic ECSTM images of microstructure obtained at $U = -0.45$ V/SHE in 10 mM HCl(aq) + 1 mM MBI (Z range $\Delta Z = 6$ nm, tip potential $U_{\text{tip}} = -0.5$ V/SHE, tunneling current $I_t = 0.6$ nA): (a) Initial surface state; (b) Surface state after 2 CV treatments; (c) Surface state after 4 CV treatments.

Figure 4.2(a) shows a typical local area at the topmost surface of microcrystalline copper as obtained *in situ* after reduction of the native oxide in the presence of MBI. ECSTM images of this local microstructure could be repeatedly obtained and after 2 (Figure 4.2(b)) and 4 (Figure 4.2(c)) CVs. Grains and sub-grains delimited by grain boundaries are observed at varying topographic levels owing to differences of local reactivity during surface preparation. In each image, the depth at the bottom of the GB region could be geometrically measured in the same local position after 0, 2 and 4 CVs for 74 sites. A typical example of the line profile obtained for site #1 in Figure 4.2 before and after 2 and 4 CVs is shown in Figure 4.3. In this example, no variation of the GB depth is observed.

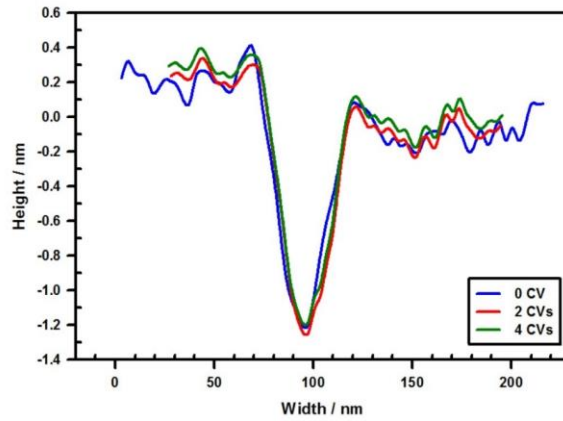


Figure 4.3: Average topographic line profiles measured across the GB at site # 1 in Figure 4.2 after 0, 2 and 4 CV treatments.

The comparative analysis of the GB depth before and after the CV treatments in the 74 sites revealed 5 types of local intergranular behavior: i) unchanged GB depth, ii) repeated increase, iii) repeated decrease, iv) decrease followed by increase, and v) increase followed by decrease. The distribution of these observed behaviors is shown in Figure 4.4.

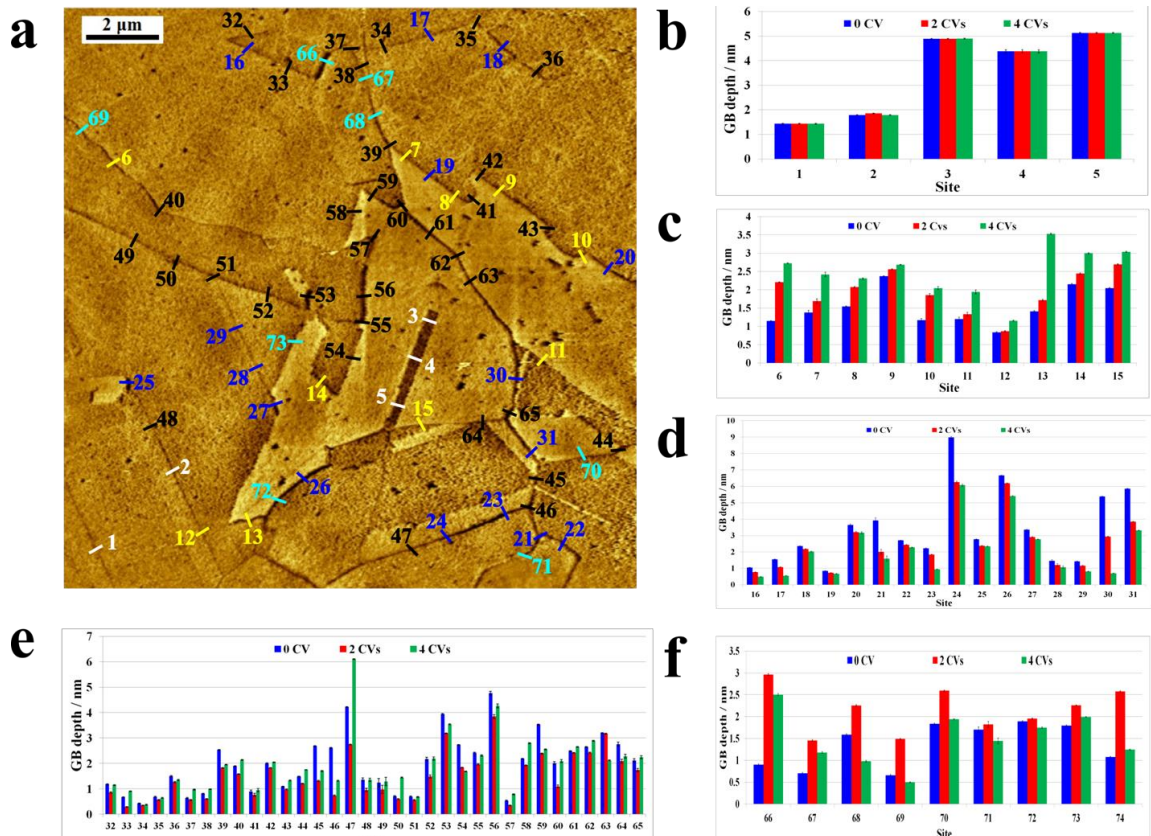


Figure 4.4: ECSTM evaluation of the intergranular behavior in the early stage corrosion of microcrystalline copper sites in 10 mM HCl(aq) + 1 mM MBI: (a) Topographic image with GB sites labelled 1 to 74; (b) Bar graph of the GB depth measured across the sites (labelled in white in (a)) showing no preferential reactivity after 2 and 4 CVs; (c) Bar graph of the GB sites (labelled in yellow in (a)) showing depth increase after 2 and 4 CVs; (d) Bar graph of the GB sites (labelled in dark blue in (a)) showing depth decrease after 2 and 4 CVs; (e) Bar graph of the GB sites (labelled in black in (a)) showing depth decrease and subsequent increase after 2 and 4 CVs, respectively. (f) Bar graph of the GB sites (labelled in light blue in (a)) showing depth increase and subsequent decrease after 2 and 4 CVs, respectively.

The 5 sites showing no specific local behavior caused by intergranular corrosion after 2 and 4 CVs are labelled 1 to 5 in Figure 4.4(a). The bar graph of the GB depth confirms no net variation of the depth of the GB region compared to the adjacent grains (Figure 4.4(b)). In the absence of inhibitors, such an absence of preferential local intergranular reactivity is typical of coherent twins (Σ_3 CSL with a $\{111\}$ -oriented GB plane) [3,13,22,26,46]. In the present case, it is observed along two parallel GBs separating a narrow sub-grain (sites 3 to 5), a configuration typical of Σ_3 coherent twins. It is also observed for sites 1 and 2 also located along two parallel GBs and separating a wider sub-grain. At these sites, the absence of preferential local reactivity is thus assigned to the intrinsic intergranular properties of the Σ_3 coherent twins rather than to a local effect of the MBI inhibitor. The surface layer of Cu(I)-MBI reaction products formed indifferently in the GB region and on the adjacent grains, and the Σ_3 coherent twins did not react preferentially owing to their intrinsic resistance against intergranular corrosion (Figure 4.5(a)).

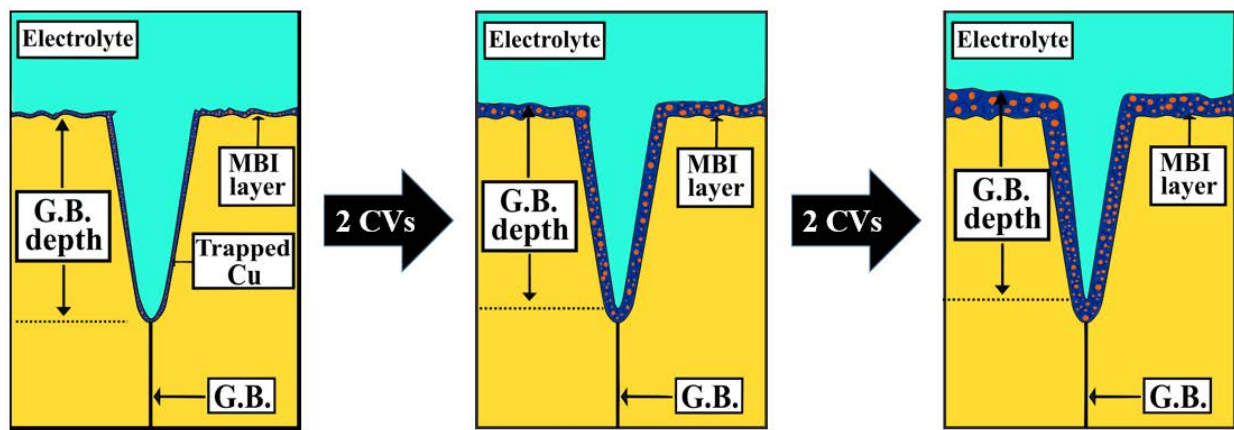


Figure 4.5a: Schematic illustration of observed MBI inhibiting effects on early intergranular corrosion of copper in acid electrolyte: anodic formation of MBI layer and there is no preferential activity at the GBs after 2 CVs and 4 CVs.

The 10 sites showing a repeated net increase of the depth of the GB region after 2 and 4 CVs are labelled 6 to 15 in Figure 4.4(a) and (c). In the absence of formation of a passive film, the increase of the GB depth is indicative of the preferential local consumption of the material by irreversible and faster dissolution than on the adjacent grains as previously observed for early stage intergranular corrosion of copper in 1 mM HCl(aq) in the absence of inhibitor [22,26]. In the present case, a surface layer of Cu(I)-MBI reaction products is formed as shown by the CV analysis. The formation of a thinner layer in the GB regions than on the adjacent grains would result in an increase of the GB depth. However, this is not consistent with the preferential reactivity expected in the GB regions. In contrast, the formation in the GB regions of a surface layer less efficiently mitigating anodic dissolution than on the adjacent grains is consistent with the more reactive character of the GBs, and would result in an increase of the GB depth owing to the preferential consumption of copper in the GBs regions (Figure 4.5(b)). Among the 10 GB sites where preferential although mitigated irreversible dissolution is observed, only site 12 can correspond to a Σ_3 coherent and incoherent twin (the same as for site 2). This coherent twin is possibly locally deviated from the perfect geometry since exhibiting local preferential dissolution [26]. Among the 9 other sites, site 14 is located at a short and straight boundary, assigned to a low Σ CSL boundary. Sites 7 to 9 are located along straight segments of a GB whose morphology is locally straight or curved and assigned to a high Σ CSL. Sites 6, 10, 11, 13 and 15 belong to GBs with curved morphologies indicating their random character. For these high Σ CSL and random boundaries, local intergranular irreversible dissolution is observed but mitigated by the MBI surface layer given the relatively small increase of the GB depth.

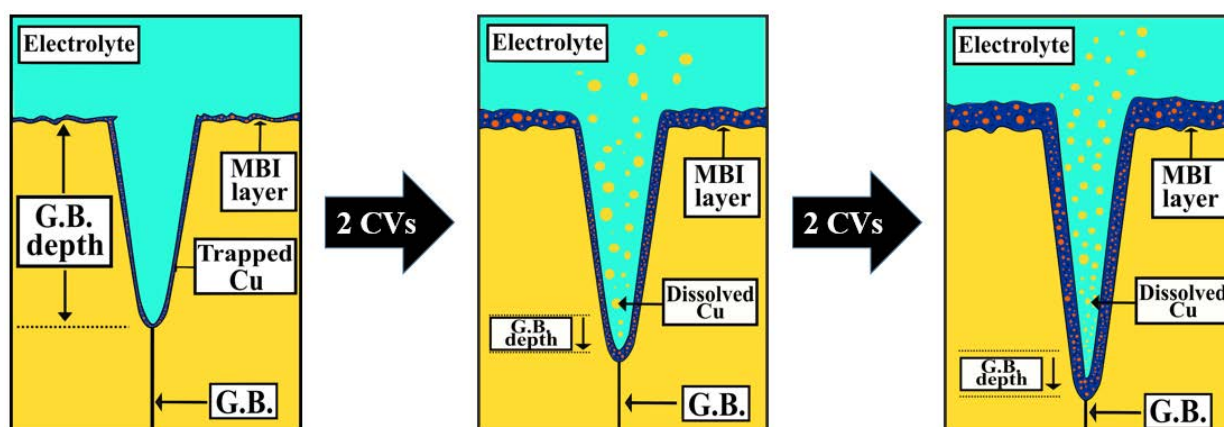


Figure 4.5b: Schematic illustration of observed MBI inhibiting effects on early intergranular corrosion of copper in acid electrolyte: imperfect GB protection by anodically formed MBI layer and there is mitigated dissolution at the GBs after 2 CVs and 4 CVs.

The repeated net decrease of the depth of the GB region after 2 and 4 CVs could be measured in 16 sites, labelled 16 to 31 in Figure 4.4(a) and (d). The decrease of the GB depth is consistent with the local accumulation of reaction products, more important in the GB region because of the locally higher reactivity. Such a local GB behavior has been observed by ECSTM for copper passivated in 0.1 M NaOH(aq) and attributed to a locally thicker Cu(I) passive oxide film formed in the GB regions [24,25,]. In 10 mM HCl(aq) + 1 mM MBI, the electrochemical response is indicative of a passivation-like behavior not observed in the absence of MBI. More copper would react in the GB region during anodic polarization leading to the formation of a thicker layer of Cu(I) reaction products than on the adjacent grains. The process would be repeated at each treatment cycle thus leading to the thickness increase of the film formed in the GB regions (Figure 4.5(c)). This formation of a thicker film of Cu(I) reaction products than on the adjacent grains is observed at sites 16, 28 and 29 along straight GBs that can be assigned to low Σ CSL GBs. It is also observed at site 19 along the same straight GB segment as at sites 7 and 8 and corresponding to a high Σ CSL, thereby showing that the inhibitor effect may be dependent on the local structure along the same GB edge. Sites 17, 18, 20-27, 30 and 31 all belong to random GBs characterized by curved morphologies. It is at such GBs that the largest decrease of the GB depth is observed (sites 21, 24, 30 and 31), which is consistent with more copper being consumed in these more reactive GBs leading to increased accumulation of Cu(I)-MBI reaction products with formation of a thicker film.

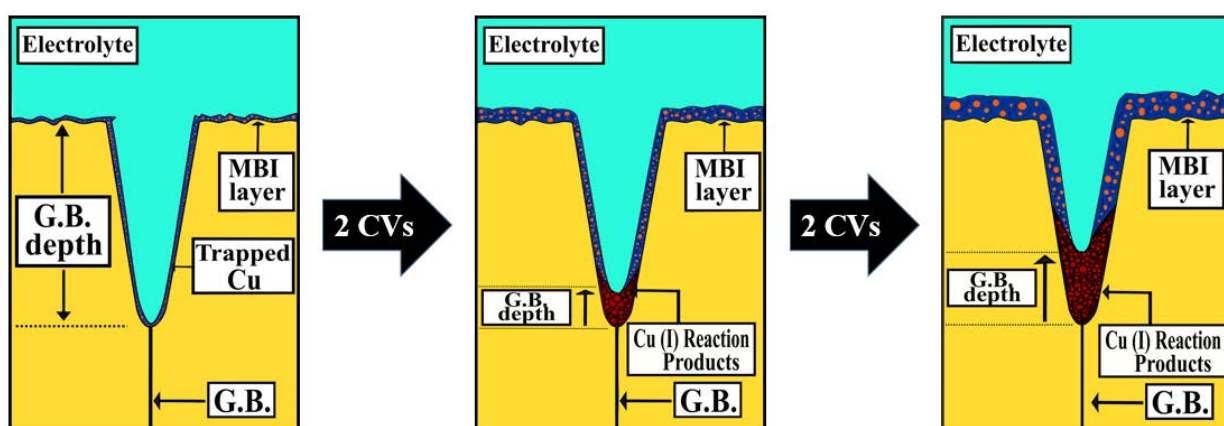


Figure 4.5c: Schematic illustration of observed MBI inhibiting effects on early intergranular corrosion of copper in acid electrolyte: GB protection by corrosion products and there is blocked dissolution at the GBs after 2 CVs and 4 CVs.

Figure 4.4(a) and (e) shows the 34 GB sites, labelled 32 to 65, where, after 2 CVs, the behavior was first characterized by a decrease of the GB depth and subsequently, after 4 CVs, by an increase. Like for the GB sites 16 to 31 discussed above, the initial decrease of the GB depth is assigned to the preferential accumulation in the GB region of Cu(I) reaction products leading to the formation of a locally thicker surface layer than on the adjacent grains. The subsequent increase of the GB depth after 2 more CVs is indicative of net dissolution by anodic oxidation. This unstable behavior suggests that the thicker layer of Cu(I) reaction products formed in the GB regions first provides local protection against anodic dissolution, like observed on the grains by CV. However, this initial protection provided by the surface layer is not stable since altered during the subsequent CV treatments as shown by the increase of the GB depth resulting from net dissolution (Figure 4.5(d)). Among the GB sites where this behavior is observed, site 48 can be assigned to a Σ_3 coherent twin of locally imperfect geometry like at site 12. Site 33 can be assigned to a low Σ CSL boundary, the same as site 16 discussed above. Site 42 belongs to a straight segment that can be assigned to a high Σ CSL boundary. Note that at these 3 sites the GB depth variations are small indicating little alterations of the local early intergranular corrosion behavior. All the other 31 sites belong to curved or locally curved boundaries assigned to random boundaries. Among them only a minority of 10 sites (37, 38, 40, 43, 44, 47, 50, 58, 61 and 62) show an increase of the GB depth after 4 CVs to a value higher than the initial value measured before cycling, indicating a pronounced alteration of the transient protection brought by the formation of the surface layer of reaction products.

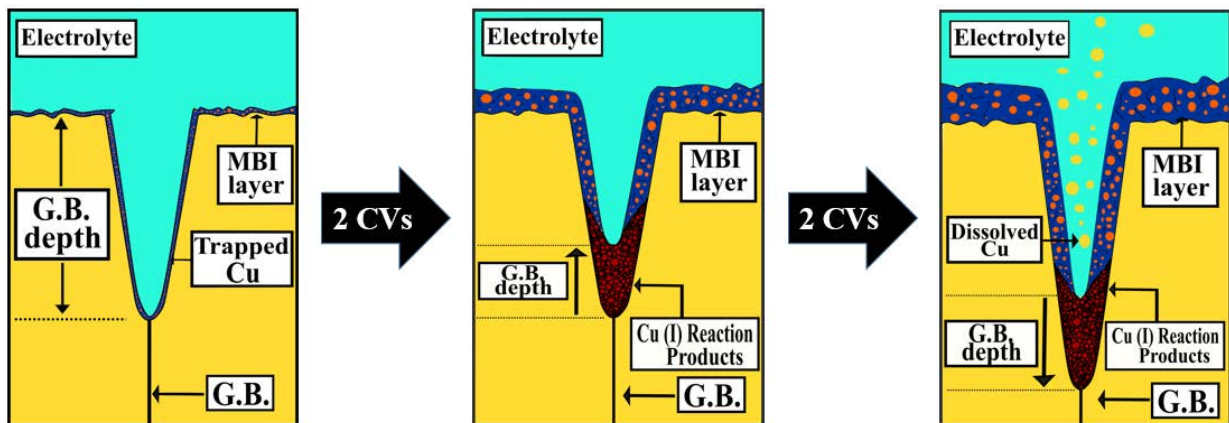


Figure 4.5d: Schematic illustration of observed MBI inhibiting effects on early intergranular corrosion of copper in acid electrolyte: transient GB protection by corrosion products at the GBs after 2 CVs and 4 CVs.

We found 9 GB sites where the behavior was first characterized by an increase of the GB depth after 2 CVs and subsequently by a decrease after 4 CVs. They are labelled 66 to 74 in Figure 4.4(a) and (f). Like for sites 6 to 15 discussed above, we assign the increase of the GB depth measured after 2 CVs to net irreversible dissolution, less mitigated by the surface layer of Cu(I) reaction products at the GBs than on the adjacent grains. After 2 more CVs, the preferential accumulation of Cu(I) reaction products in the GB region decreases the GB depth owing to the formation of a thicker surface layer than on the adjacent grains. In this case, the repeated alterations of the surface layer brought by the CV treatment promote a delayed protection in the GB regions (Figure 4.5(e)). All GB sites except one (site 66) at which this behavior was observed belong to curved or locally curved boundaries characteristic of random GBs. Site 66 belongs to short and straight boundary, assigned to a low Σ CSL boundary.

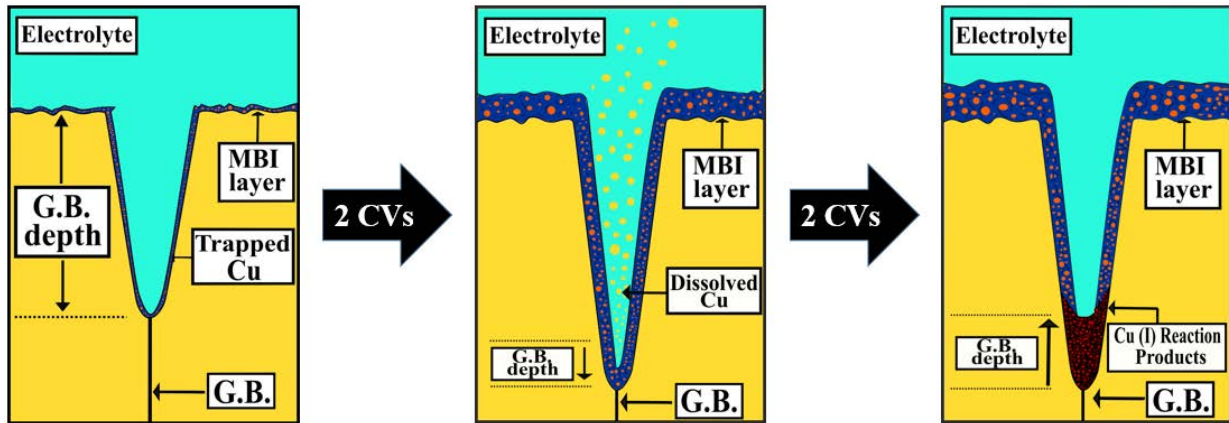


Figure 4.5e: Schematic illustration of observed MBI inhibiting effects on early intergranular corrosion of copper in acid electrolyte: delayed GB protection by corrosion products at the GBs after 2 CVs and 4 CVs.

4.3.3 Local MBI inhibition effects according to GB type

Table 4.1: Total number of occurrences of each type of early intergranular corrosion behavior for various types of grain boundaries for microcrystalline copper in 10 mM HCl(aq) + 1 mM MBI

Intergranular behavior	CTs	Low Σ CSLs	High Σ CSLs	Random GBs
Resistance (intrinsic)	2	--	--	--
Protection by pre-adsorbed MBI layer (no dissolution)	--	1	2	--
Imperfect protection by pre-adsorbed MBI layer (mitigated dissolution)	--	--	4	9
Protection by corrosion products	--	--	3	1
Transient protection by corrosion products	--	--	2	10
Delayed protection by corrosion products	--	--	3	6

The 5 types of local intergranular corrosion behavior observed in this work in the presence of MBI and their occurrences according to GB crystallographic type are compiled in Table 4.1 and Figure 4.6. The distribution of behavior observed with MBT [46] (Chapter III) is also reported in Figure 4.6 for comparison.

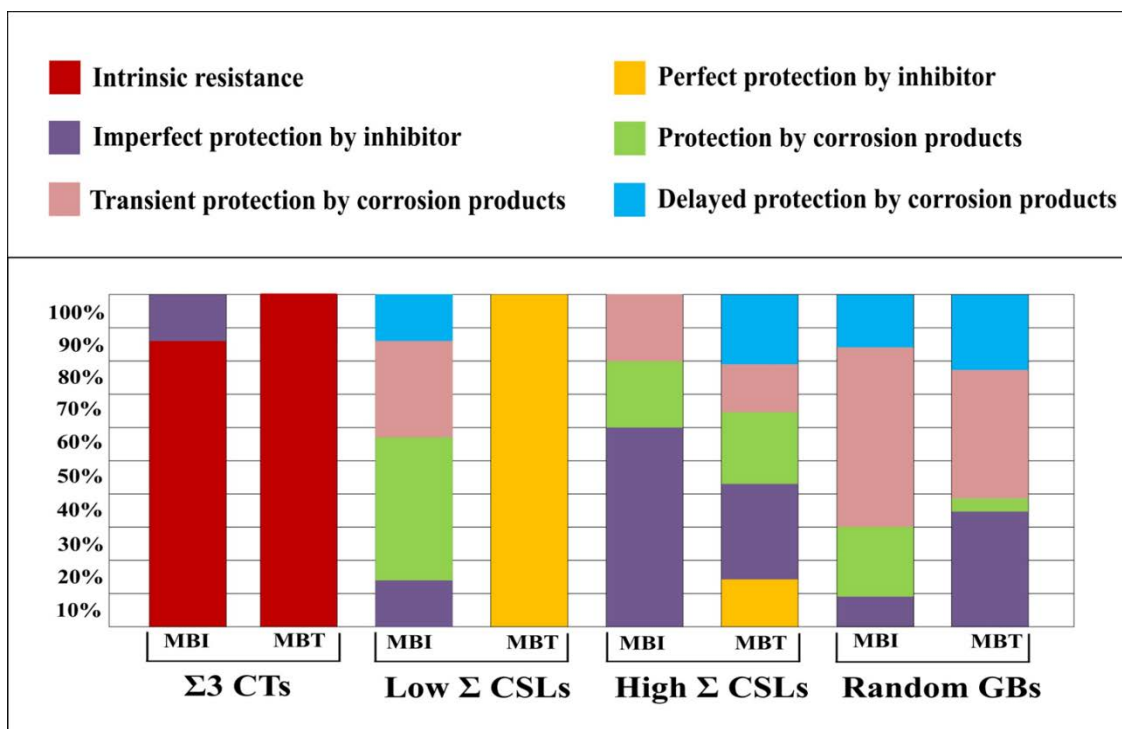


Figure 4.6: Percentage of each type of early intergranular corrosion behavior observed on various types of grain boundaries for microcrystalline copper in 10 mM HCl(aq) + 1 mM MBI and comparison in 10 mM HCl(aq) + 0.1 mM MBT

In most cases and independently of the presence of the MBI or MBT inhibitors in the solution, the Σ_3 coherent twins showed no preferential intergranular reactivity compared to the adjacent grains. This is in agreement with intrinsic resistance of these grain boundaries to intergranular corrosion [3,13,22,26], and thus equally efficient inhibition in the GB surface region than on adjacent grains can be concluded for the Σ_3 coherent twins. Local preferential reactivity was observed in two cases despite the presence of MBI, likely owing to the local deviation of the grain boundary plane from the perfect geometry as observed previously in the absence of inhibitor [26]. In these cases, the anodically formed surface layer of Cu(I)-MBI corrosion products provided imperfect or only transient protection against anodic dissolution.

All other types of grain boundaries showed preferential reactivity. For the most reactive random GBs, protection by accumulation of reaction products was found to largely predominate protection by mitigated dissolution. For MBI, with which a passivation-like behavior of the grains is observed by CV, this mode of protection results from the formation of a thicker film of Cu(I) corrosion products in the GB region than on the adjacent grains. For MBT, with which no passivation-like anodic behavior of the grains is observed, this mode of protection results from the local accumulation of Cu(I) corrosion products in the GB region. With both inhibitors, the preferential formation of corrosion products in the GB region is consistent with more intense activity occurring at the surface terminations of random GBs, as expected from the ill-defined crystallographic character of these boundaries, and producing upon anodic polarization more Cu(I) corrosion products than in CSL boundaries. With MBI, as well as with MBT, the major part of the measured random GB sites did not show stable protection after repeated anodic polarization, showing the fragile protectiveness provided by the reaction products accumulated in the surface regions of the random GBs.

Much fewer occurrences of the locally observed intergranular behavior could be associated with CSL boundaries. For the high Σ CSLs, protection by a thicker layer of Cu(I)-MBI corrosion products is also observed but mitigated dissolution by the anodically formed MBI layer is more frequent, in agreement with a lower reactivity of high Σ CSLs compared to most random GBs. A more balanced distribution of

these two types of local inhibition effects was also observed with MBT. For low Σ CSLs, protection by a thicker layer of Cu(I)-MBI corrosion products is more frequent than mitigated dissolution by the MBI layer. This suggests that some CSL boundaries could be initially as reactive as random GBs for forming Cu(I)-MBI corrosion products. A larger fraction of the low CSLs than of random GBs would form a stable protective layer of corrosion products.

4.4 Conclusions

The local inhibiting effects of MBI on the initial stages of intergranular corrosion of copper were studied *in situ* by ECSTM in 10 mM HCl(aq) acid solution. Macroscopic analysis by CV of the grains and GB network electrochemical response in the Cu(I) oxidation range confirmed that MBI inhibits the active dissolution of copper and showed that the inhibition efficiency markedly depends on the conditions of pre-adsorption of the molecule. If pre-adsorbed on the surface in the metallic state, anodic as well as cathodic activity is suppressed, most likely by formation of a homogeneous barrier molecular film efficiently blocking atomic transport across the interface. If pre-adsorbed on the surface covered by its native oxide and subsequently reduced, the residual activity is higher and characteristic of a passivation-like behavior assigned to the anodic formation of a protective surface film of Cu(I)-MBI reaction products.

Local ECSTM analysis at the surface termination of the GB network showed no preferential intergranular corrosion of the Σ_3 coherent twins compared to grains, in agreement with their intrinsic resistance to intergranular corrosion. All other types of GBs reacted preferentially compared to adjacent grains. They showed preferential dissolution mitigated by the imperfect protection provided by the anodically formed Cu(I)-MBI surface film, or preferential accumulation of Cu(I) reaction products protecting the GB surface regions against intergranular dissolution. Local GB protection by preferential accumulation of Cu(I) reaction products was observed to be transient, delayed or stable in the conditions of repeated anodic cycling applied to force anodic oxidation. For CSL grain boundaries other than Σ_3 coherent twins, mitigated preferential dissolution occurred more frequently than blocking by accumulated reaction products, indicating more efficient protection by the anodically formed MBI surface layer. For the random boundaries, local protection by preferential accumulation of Cu(I) reaction products was dominant like previously observed with MBT. This is assigned to the intrinsically more reactive character of the random GBs, less efficiently protected by the anodically formed MBI layer and with the generation of more Cu(I) ions under anodic polarization resulting in the local accumulation of Cu(I)-MBI reaction products.

Comparison with MBT effects studied in the same pre-adsorption and testing conditions shows less efficient inhibition by MBI, with more Cu(I) reaction products generated on the grains to form a surface film and the preferential accumulation of reaction products more frequently observed in the GB surface regions.

Acknowledgments

This project has received funding from the European Research Council (ERC) under the European Union's Horizon 2020 research and innovation programme (ERC Advanced Grant agreement No 741123).

Reference

- [1] J. Mieluch, M. Smialowski, The Behaviour of Grain Boundaries in Iron During Anodic Polarization in Ammonium Nitrate Solution, *Corrosion Science* 4 (1964) 237–243.

- [2] P. Lin, G. Palumbo, U. Erb, K.T. Aust, Influence of Grain Boundary Character Distribution on Sensitization and Intergranular Corrosion of Alloy 600, *Scripta Metallurgica et Materiala* 33 (1995) 1387-1392.
- [3] A. Vinogradov, T. Mimaki, S. Hashimoto, R.Z. Valiev, On the Corrosion Behaviour of Ultra-Fine Grain Copper, *Scripta Materialia* 41 (1999) 316-326.
- [4] L. Lu, M.L. Sui, K. Lu, Superplastic Extensibility of Nanocrystalline Copper at Room Temperature, *Science* 287 (2000) 1463-1466.
- [5] V.Y. Gertsman, S.M. Gruemer, Study of Grain Boundary Character Along Intergranular Stress Corrosion Crack Paths in Austenitic Alloys, *Acta Materialia* 49 (2001) 1589-1598.
- [6] S.H. Kim, U. Erb, K.T. Aust, G. Palumbo, Grain Boundary Character Distribution and Intergranular Corrosion Behavior in High Purity Aluminum, *Scripta Materialia* 44 (2001) 835-839.
- [7] H. Miyamoto, K. Yoshimura, T. Mimaki, M. Yamashita, Behavior of Intergranular Corrosion of $\langle 011 \rangle$ Tilt Grain Boundaries of Pure Copper Bicrystals, *Corros. Sci.* 44 (2002) 1835-1846. *Acta Materialia* 50 (2002) 2331-2341.
- [8] M. Shimada, H. Kokawa, Z.J. Wang, Y.S. Sato, I. Karibe, Optimization of grain boundary character distribution for intergranular corrosion resistant 304 stainless steel by twin-induced grain boundary engineering, *Acta Materialia* 50 (2002) 2331-2341.
- [9] E.M. Lehockey, A.M. Brennenstuhl, I. Thompson, On the relationship between grain boundary connectivity, coincident site lattice boundaries, and intergranular stress corrosion cracking, *Corrosion Science* 46 (2004) 2383-2404.
- [10] V. Randle, 'Special' Boundaries and Grain Boundary Plane Engineering, *Scripta Materialia*. 54 (2006) 1011-1015.
- [11] S. Xia, B. Zhou, W. Chen, Effect of single-step strain and annealing on grain boundary character distribution and intergranular corrosion in Alloy 690, *Journal of Material Science* 43 (2008) 2990-3000.
- [12] R. Jones, V. Randle, Sensitisation behaviour of grain boundary engineered austenitic stainless steel, *Materials Science and Engineering A* 527 (2010) 4275-4280.
- [13] K. D. Ralston, N. Birbilis, Effect of Grain Size on Corrosion: A Review, *Corrosion* 66 (2010) 075005-075005-13.
- [14] CL Changliang, S.Xi, H. Li, TG. Liu, BX. Zhou, WJ. Chen, N. Wang, Ning, Improving the intergranular corrosion resistance of 304 stainless steel by grain boundary network control, *Corrosion Science* 53 (2011) 1880-1886.
- [15] C. Luo, X. Zhou, G.E. Thompson, A.E. Hughes, Observations of intergranular corrosion in AA2024-T351: The influence of grain stored energy, *Corrosion Science* 61 (2012) 35-44.
- [16] Sunil Kumar B., Balla Sai Prasad, Vivekanand Kain, Jayanth Reddy, Methods for making alloy 600 resistant to sensitization and intergranular corrosion, *Corrosion Science* 70 (2013) 55-61.
- [17] Y. Takehara, H. Fujiwara, H. Miyamoto, "Special" to "general" transition of intergranular corrosion in Sigma 3{111} grain boundary with gradually changed misorientation, *Corrosion Science* 77 (2013) 171-175.
- [18] A. Stratulat, J.A. Duff, T.J. Marrow, T. James, Grain boundary structure and intergranular stress corrosion crack initiation in high temperature water of a thermally sensitised austenitic stainless steel, observed in situ, *Corrosion Science* 85 (2014) 428-435.
- [19] E. Martinez-Lombardia, Y. Gonzalez-Garcia, L. Lapeire, I. De Graeve, K. Verbeken, L. Kestens, J. Mol, H. Terryn, Scanning Electrochemical Microscopy to Study the Effect of Crystallographic Orientation on the Electrochemical Activity of Pure Copper, *Electrochimica Acta* 116 (2014) 89-96.
- [20] B.V. Mahesh, R.K. Singh Raman, Role of Nanostructure in Electrochemical Corrosion and High Temperature Oxidation: A Review, *Metallic Materials Transactions A* 45A (2014) 5799-5822.
- [21] N. Srinivasan, V. Kain, N. Birbilis, K.V. Mani Krishna, S. Shekhawat, I. Samajdar, Near boundary gradient zone and sensitization control in austenitic stainless steel, *Corrosion Science* 100 (2015) 544-555.
- [22] E. Martinez-Lombardia, L. Lapeire, V. Maurice, I. De Graeve, K. Verbeken, L.H. Klein, L. Kestens, P. Marcus, H. Terryn, In Situ Scanning Tunneling Microscopy Study of the Intergranular Corrosion of Copper, *Electrochemistry Communications* 41 (2014) 1-4.
- [23] E. Martinez-Lombardia, V. Maurice, L. Lapeire, I. De Graeve, K. Verbeken, L.H. Klein, L. Kestens, P. Marcus, H. Terryn, In Situ Scanning Tunneling Microscopy Study of Grain-Dependent Corrosion on Microcrystalline Copper, *Journal of Physical Chemistry C* 118 (2014) 25421-25428.

- [24] H. Chen, V. Maurice, L.H. Klein, L. Lapeire, K. Verbeken, H. Terryn, P. Marcus, Grain Boundary Passivation Studied by In Situ Scanning Tunneling Microscopy on Microcrystalline Copper, *Journal of Solid State Electrochemistry* 19 (2015) 3501-3509.
- [25] H. Chen, M. Bettayeb, V. Maurice, L.H. Klein, L. Lapeire, K. Verbeken, H. Terryn, P. Marcus, Local passivation of metals at grain boundaries: In situ scanningtunneling microscopy study on copper, *Corrosion Science* 111 (2016) 659-666.
- [26] M. Bettayeb, V. Maurice, L.H. Klein, L. Lapeire, K. Verbeken, P. Marcus, Nanoscale Intergranular Corrosion and Relation With Grain Boundary Character as Studied In Situ on Copper, *Journal of the Electrochemical Society* 165 (2018) C835-C841.
- [27] M. Antonijevic, M. Petrovic Mihajlovic, Copper corrosion inhibitors. A review, *International Journal of Electrochemical Science* 3 (1) (2008) 1-28.
- [28] M. M. Antonijevic, S. M. Milic, M. B. Petrovic, Films formed on copper surface in chloride media in the presence of azoles, *Corrosion Science* 51 (2009) 1228-1237.
- [29] M. Petrovic Mihajlovic, M. Antonijevic, Copper corrosion inhibitors. period 2008-2014. a review, *International Journal of Electrochemical Science* 10 (2015) 1027-1053.
- [30] T. Shahrabi, H. Tavakholi, M. G. Hosseini, Corrosion inhibition of copper in sulphuric acid by some nitrogen heterocyclic compounds, *Anti-Corrosion Methods and Materials* 54 (2007) 308-313.
- [31] P. M. Niamien, F. K. Essy, A. Trokourey, A. Yapi, H. K. Aka, D. DIABATE, Correlation between the molecular structure and the inhibiting effect of some benzimidazole derivatives, *Materials Chemistry and Physics* 619 136 (2012) 59-65.
- [32] M. Finsgar, 2-mercaptobenzimidazole as a copper corrosion inhibitor: Part i. long-term immersion, 3D-profilometry, and electrochemistry, *Corrosion Science* 72 (2013) 82-89.
- [33] I. Milosev, N. Kovacevic, J. Kovac, A. Kokalj, The roles of mercapto, benzene and methyl groups in the corrosion inhibition of imidazoles on copper: I. experimental characterization, *Corrosion Science* 98 (2015) 107-118.
- [34] G. Zerjav, I. Milosev, Protection of copper against corrosion in simulated urban rain by the combined action of benzotriazole, 2-mercaptobenzimidazole and stearic acid, *Corrosion Science* 98 (2015) 180-191.
- [35] D. Chadwick, T. Hashemi, Electron spectroscopy of corrosion inhibitors: Surface film formed by 2-mercaptobenzothiazole and 2-mercaptobenzimidazole on copper, *Surface Science* 89 (1-3) (1979) 649-659.
- [36] Y. Tooru, An X-ray photoelectron spectroscopic study of several metal complexes of 2-mercaptobenzimidazole and 2-mercaptobenzoxazole, *The Chemical Society of Japan* 53 (5) (1980) 1449-1450.
- [37] G. Xue, X.-Y. Huang, J. Dong, J. Zhang, The formation of an effective anti-corrosion film on copper surfaces from 2-mercaptobenzimidazole solution, *Journal of Electroanalytical Chemistry* 310 (1991) 139-148.
- [38] G. Xue, X. Huang, J. Ding, Surface reaction of 2-mercaptobenzimidazole on metals and its application in adhesion promotion, *Journal of the Chemical Society Faraday Transactions* 87 (8) (1991) 1229-1232.
- [39] G. Xue, Q. Dai, SERS and IR studies of the reaction of an oxidized surface and an etched surface of copper with 2-mercaptobenzimidazole, *Spectroscopy Letters* 27 (3) (1994) 341-351.
- [40] F. Perrin, J. Pagetti, Characterization and mechanism of direct film formation on a Cu electrode through electro-oxidation of 2-mercaptobenzimidazole, *Corrosion science* 40 (10) (1998) 1647-1662.
- [41] B. Trachli, M. Keddami, H. Takenouti, A. Srhiri, Protective effect of electropolymerized 2-mercaptobenzimidazole upon copper corrosion, *Progress in Organic Coatings* 44 (2002) 17-23.
- [42] J. Izquierdo, J. J. Santana, S. Gonzalez, R. M. Souto, Scanning microelectrochemical characterization of the anti-corrosion performance of inhibitor films formed by 2-mercaptobenzimidazole on copper, *Progress in Organic Coatings* 74 (3) (2012) 526-533.
- [43] M. Finsgar, 2-mercaptobenzimidazole as a copper corrosion inhibitor: Part ii. surface analysis using X-ray photoelectron spectroscopy, *Corrosion Science* 72 (2013) 90-98.
- [44] X. Wu, F. Wiame, V. Maurice, P. Marcus, 2-mercaptobenzimidazole films formed at ultra-low pressure on copper: adsorption, thermal stability and corrosion inhibition performance, *Applied Surface Science* 527 (2020) 146814.
- [45] D. quan Zhang, L. xin Gao, G. ding Zhou, Inhibition of copper corrosion in aerated hydrochloric acid solution by heterocyclic compounds containing a mercapto group, *Corrosion Science* 46 (2004) 3031-3040.

- [46] S.B. Sharma, V. Maurice, L.H. Klein, P. Marcus, Local inhibition by 2-mercaptobenzothiazole of early stage intergranular corrosion of copper, *Journal of the Electrochemical Society*, J. Electrochem. Soc. 167 (2020) 161504.
- [47] L. Lapeire, E. Martinez Lombardia, K. Verbeken, I. De Graeve, L. Kestens, H. Terryn, Effect of Neighboring Grains on the Microscopic Corrosion Behavior of a Grain in Polycrystalline Copper, *Corrosion Science* 67 (2013) 179–183.
- [48] L. Lapeire, E. Martinez Lombardia, K. Verbeken, I. De Graeve, L. Kestens, H. Terryn, Structural Dependence of Gold Deposition by Nanoplatin in Polycrystalline Copper, *Journal of Materials Science* 49 (2014) 3909–3916.
- [49] D. Zuili, V. Maurice, P. Marcus, Surface Structure of Nickel in Acid Solution Studied by In Situ STM, *Journal of the Electrochemical Society* 147 (2000) 1393–1400.
- [50] A. Seyeux, V. Maurice, L. H. Klein, P. Marcus, In Situ STM Study of the Initial Stages of Growth and of the Structure of the Passive Film on Ni(111) in 1 mM NaOH(aq), *Journal of Solid State Electrochemistry* 9 (2005) 337–346.
- [51] A. Seyeux, V. Maurice, L. H. Klein, P. Marcus, In Situ STM Study of the Effect of Chloride on the Growth Mechanism and Structure of the Passive Film on Nickel in Alkaline Solution, *Journal of the Electrochemical Society* 153 (2006) B453–463.
- [52] V. Maurice, L. H. Klein, H.-H. Strehblow, P. Marcus, In situ STM Study of the Surface Structure, Dissolution and Early Stages of Electrochemical Oxidation of the Ag(111) Electrode, *Journal of Physical Chemistry C* 111 (2007) 16351–16361.
- [53] N. Li, V. Maurice, L. H. Klein, P. Marcus, Structure and Morphology Modifications of Silver Surface in the Early Stages of Sulphide Growth in Alkaline Solution, *Journal of Physical Chemistry C* 116 (2012) 7062–7072.
- [54] Gwyddion – Free SPM (AFM, SNOM/NSOM, STM, MFM ...) data analysis software. <http://gwyddion.net/>
- [55] H.-H. Strehblow, B. Titze, The Investigation of the Passive Behaviour of Copper in Weakly Acid and Alkaline Solutions and the Examination of the Passive Film by Esca and ISS, *Electrochimica Acta* 25 (1980) 839–850.
- [56] Y. Feng, K.S. Siow, W.K. Teo, K.L. Tan, A.K. Hsieh, Corrosion Mechanisms and Products of Copper in Aqueous Solutions at Various pH Values, *Corrosion* 53 (1997) 389–398.
- [57] B. Beverskog, I. Puigdomenech, Pourbaix Diagrams for the System Copper-Chlorine at 5–100 C. SKI, Nyköping, 1998
- [58] O. Magnussen, L. Zitzler, B. Gleich, M. Vogt, R.J. Behm, In-Situ Atomic-Scale Studies of the Mechanisms and Dynamics of Metal Dissolution by High-Speed STM, *Electrochimica Acta* 46 (2001) 3725–3733.
- [59] M. Kruff, B. Wohlmann, C. Stuhlmann, K. Wandelt, Chloride Adsorption on Cu(111) Electrodes in Dilute HCl Solutions, *Surface Science* 377 (1997) 601–604.
- [60] M. Vogt, A. Lachenwitzer, O. Magnussen, R.J. Behm, In-Situ STM Study of the Initial Stages of Corrosion of Cu(100) Electrodes in Sulfuric and Hydrochloric Acid Solution. *Surface Science* 399 (1998) 49–69.
- [61] L.-J. Wan, K. Itaya, In Situ Scanning Tunneling Microscopy of Cu(110): Atomic Structures of Halide Adlayers and Anodic Dissolution, *Journal of Electroanalytical Chemistry* 473 (1999) 10–18.
- [62] W.H. Li, Y. Wang, J.H. Ye, S. F. Y. Li, In Situ STM Study of Chloride Adsorption on Cu(110) Electrode in Hydrochloric Acid Aqueous Solution, *Journal of Physical Chemistry B* 105 (2001) 1829–1833.
- [63] T. Hai Phan, T. Kosmala, K. Wandelt, Potential dependence of self-assembled porphyrin layers on a Cu(111) electrode surface: In-situ STM study, *Surface Science* 631 (2015) 207–212.
- [64] M. Bettayeb, V. Maurice, L.H. Klein, L. Lapeire, K. Verbeken, P. Marcus, Combined in situ microstructural study of the relationships between local grain boundary structure and passivation on microcrystalline copper, *Electrochimica Acta* 305 (2019) 240–246.

Chapter V

Inhibition effects on intergranular passivation of metals: Insight from in situ scanning tunneling microscopy study for 2-mercaptobenzothiazole and 2- mercaptobenzoimidazole on copper

This chapter reproduces an original manuscript with reference: Sagar B. Sharma, Vincent Maurice, Lorena H. Klein, Philippe Marcus, Inhibition effects of 2-mercaptobenzothiazole and 2-mercaptobenzoimidazole on local passivation of metals at grain boundaries: In situ scanning tunneling microscopy study on copper, *to be submitted for publication as an article*.

Abstract

The effects of 2-mercaptobenzothiazole (MBT) and 2-mercaptobenzoimidazole (MBI) on the passivation of copper at the surface termination of various types of grain boundaries (GBs) was investigated *in situ* at the nanometer scale in 0.1 M NaOH(aq) alkaline solution using electrochemical scanning tunneling microscopy (ECSTM). Macroscopic electrochemical analysis by cyclic voltammetry showed that the organic surface layers, pre-formed by reductive dissociation of the native oxide in the presence of the inhibitors, block passivation and the formation of a Cu(I) surface oxide but does not entirely suppress residual reactivity. Local ECSTM analysis in initial metallic, subsequently oxidized, and final reduced states confirmed residual intergranular reactivity except for coherent twins close to ideal geometry. On Coincidence Site Lattice (CSL) and random boundaries, passivation was either blocked with residual dissolution and accumulation of corrosion products or incompletely blocked with residual accumulation of passivation products, depending on the barrier effect of the pre-formed inhibitor layer. For low Σ CSLs, passivation was observed to be equally blocked or incompletely blocked, with no difference of barrier effect for MBT and MBI. For more reactive high Σ CSLs and random boundaries, passivation was more frequently blocked by the pre-formed MBT surface layer than by the pre-formed MBI surface layer. The results provide deeper understanding of how passivation of different types of GBs is altered by a pre-formed surface layer of organic corrosion inhibitor.

5.1 Introduction

Intergranular corrosion initiates at the surface of metallic materials, on grain boundaries (GBs) emerging at the surface, but soon can propagate into the sub-surface region and eventually lead to failure of the entire microstructure if not combated. This localized corrosion process remains a significant challenge to overcome for the widespread durable use of microcrystalline and nanomaterials rich in surface terminations of grain boundaries. Developing our knowledge of intergranular corrosion is also a prerequisite for improving the durability of polycrystalline metallic materials.

Previous GB engineering studies have shown that intergranular corrosion depends on the energy and type of grain boundaries [1]–[21]. GBs are divided into two classes based on their misorientation angle: i) low angle GBs ($<15^\circ$) and ii) high angle GBs ($>15^\circ$). Amongst the two classes, high angle GBs are more reactive owing to their higher energy. The class of high-angle GBs can be further divided into two: a) coincidence site lattices GBs (CSL GBs) and b) random grain boundaries. Some CSL boundaries are also

called 'special boundaries' as they have comparatively lower reactivity, owing to their lower boundary energy, than random boundaries. CSLs are denoted by a Σn index, where $1/n$ refers to the fraction of lattice sites shared by the two crystals at the GB. Coherent twins (CTs), which are CSL Σ_3 boundaries having a GB plane of (111) orientation, are most common in face-centered cubic materials such as copper and have better resistance to corrosion than any other CSLs. Thus, with GB engineering, it is aimed to increase the lifetime of polycrystalline material by increasing the fraction of CSL boundaries and of the most resistive CTs in the grain boundary network.

A practical approach to mitigate and control metals and alloys corrosion in aggressive environments is by using corrosion inhibitor molecules. Organic molecules such as azole derivatives are frequently used as corrosion inhibitors for copper and its alloys [22]. Two such inhibitor molecules are 2-mercaptobenzothiazole (MBT, $C_7H_5NS_2$) and 2-mercaptobenzimidazole (MBI, $C_7H_6N_2S$), which have shown to be very efficient inhibitors for copper systems [22]-[50]. Being classified as mixed-type inhibitors [25], [33], [38] [41], [49], [50], MBT and MBI have been reported as efficient inhibitors in neutral, acidic, or alkaline conditions [23], [24], [26], [28], [33], [35], [40], [42]-[47], [49]. What makes MBT and MBI very efficient inhibitors is that they include sulfur and nitrogen atoms within their heterocyclic structure, two S and one N atom in MBT and one S and two N atoms in MBI. These atoms can, simultaneously or individually, strongly bond to the copper atoms of the surface. Thus a stable molecular film that protects the copper surface from its environment is stabilized by chemisorption [23], [26], [29], [32], [33], [35], [40], [43], [45], [46], [51]-[56] [52]-[54], [57].

For MBT, several studies have proposed the formation of a Cu-MBT film whose thickness depends on the pH of the medium [23], [24], ranging from only a monolayer film in conditions where a stable Cu_2O oxide is formed ($pH > 4$) to the formation of multilayers in acidic conditions where no stable Cu_2O film can be formed ($pH < 3$) [23]. The proposed mechanism is one where surface ions of Cu(I) react to the pre-adsorbed MBT [25]. However, if MBT pre-adsorption occurs on the copper in the metallic state, in that case, the MBT monolayer prevents the formation of a surface oxide as observed in the gaseous phase [51]-[53] or alkaline conditions [31], [34]. For MBI, several studies have proposed the formation of a polymeric film [23], [43], [46], [47], [50] with Cu reaction products included in the film - Cu-MBI [43] or Cu_2 -MBI [23] organo-metallic complexes have been suggested - depending on the initial surface state of copper, metallic or oxidized, before the formation of the protective film [43]. Due to their attractive quality as inhibitors, there is renewed interest in studying MBT and MBI as corrosion inhibitors for copper [23], [28], [35], [38]-[44], [46]-[49], [52], [53], [53]-[56], [58]. However, little is known about the role of MBT and MBI to inhibit intergranular corrosion in copper and their local effects on surface passivation at the surface terminations of grain boundaries.

So as to better understand early stage intergranular corrosion and the passivation behaviour at the surface terminations of grain boundaries, we need a technique that can characterize the alterations of the topmost surface of metals locally with a high spatial resolution and possibly under in situ conditions allowing the electrochemical control of the kinetics of the surface corrosion reactions. In situ electrochemical scanning tunneling microscopy (ECSTM) is one such analytical technique that fulfills all the above criteria. Recently, ECSTM has been successfully employed to study intergranular copper's dissolution in the active state and transient dissolution during passivation [59]-[62]. Studied at the nanometric scale, it was found that the GB edges assigned to Σ_3 coherent twins showed weaker dissolution, both in active and passive states, than those GB edges assigned to other CSL or random boundaries. Combining ECSTM with electron back-scatter diffraction (EBSD) characterization of the same local GB sites, the passivation behavior of CSL Σ_3 coherent twins was found to depend on the deviation angle of the GB plane from its perfect (111) orientation with a transition from more to less efficient passivation for a deviation angle of 0.4 - 0.5° [62]. For random boundaries, passivation in the

Cu(I) oxidation range was characterized by a decrease of the depth of GB edge region due to the formation of a passive film locally thicker than on the adjacent grains, and thus to anodic oxidation being locally less efficient since consuming more copper at the grain boundaries [62].

Here, we report the nanometric local characterization by ECSTM of the effects of the presence of MBT and MBI on the local passivation properties of copper at GB surface terminations. The study was conducted in alkaline NaOH(aq) aqueous solutions in the potential range of Cu(I) anodic oxidation where, in the absence of inhibitor, a stable Cu₂O passive film is formed [19], [59], [60]. Although MBT and MBI are well established as corrosion inhibitors for polycrystalline copper, copper alloys and other materials [23], [24], [24]–[26], [26]–[33], [36], [37], [40]–[48], [58], and further substantiated by our work on early stage intergranular corrosion in acid solution presented in Chapters 3 and 4 [63] [64], there are no studies, to the best of our knowledge, that has addressed the impact of MBT and MBI on copper passivation at grain boundaries terminations. This work aims to bring new insight and compare the passivation behavior of different types of GBs in the presence of corrosion inhibitors.

5.2 Experimental

The experiments were performed with microcrystalline samples obtained by cryogenic rolling after freezing in liquid nitrogen of high-purity cast electrolytic tough pitch copper [59]–[67]. In order to ensure the relatively smaller grain size necessary for the microstructure to be included in the STM field of view, the annealing treatment for full recrystallization of the samples was limited in time and temperature of 1 min and 200 °C, respectively. The resulting samples showed no preferential grain orientation, i.e. nearly random texture, as confirmed by EBSD. 66% of GB length corresponded to $\Sigma 3$ CSL boundaries, while the remaining 34% were, for the most part, random boundaries [66], [67]. The surface preparation was done following the protocol previously reported starting with mechanical polishing with diamond spray from 6 μm down to 0.25 μm . The sample was subjected to electrochemical polishing in 66% orthophosphoric acid for 15 s at 3 V versus a copper counter electrode to remove the cold work layer [68].

The ECSTM analysis was carried using an Agilent Technologies system ((PicoSPM base, Keysight STM S scanner, PicoScan 2100 controller, PicoStat bi-potentiostat and Picoscan software). The ECSTM cell, homemade from Kel-f, can contain ~350 μl of electrolyte. The working electrode area was delimited to 0.16 cm^2 by using a VITON® O-ring. The counter electrode and the pseudo reference electrode (+0.20 V/SHE) were made from two 0.5 mm Pt wires. All potentials reported hereafter are relative to the standard hydrogen electrode. The ECSTM cell was cleaned using the previously established procedure and tips were prepared using an electrochemical etching of a 0.25 mm diameter tungsten wire and were covered with Apiezon wax [68].

A non-deaerated 0.1 M NaOH(aq) electrolyte solution (pH 13) was prepared from ultrapure NaOH and Millipore water (resistivity > 18 M Ω cm). Solutions of MBT and MBI in the concentration of 1 mM were prepared by dissolution in the electrolyte from the physical powder states. The sample was exposed to the electrolyte to the open circuit potential ($E_{\text{OCP}} = -0.03$ V/SHE). The air-formed surface oxide was reduced by cathodic reduction of the sample (scanning at 20 mV/s) down to $E = -1.20$ V/SHE at the onset of hydrogen evolution and upward to $E = -0.75$ V/SHE. Three such cathodic reductions were enough to reduce the native oxide fully as shown in Chapter 2. The ECSTM images of the microcrystalline copper surface were first taken in the metallic state at $E = -0.75$ V/SHE in a local area rich in different types of grain boundaries. Surface imaging in the metallic state was followed by imaging the surface in the Cu(I) range of anodic oxidation. This was done by polarizing the sample anodically up until $E = -0.08$ V/SHE at the scan rate of 1 mV/s. The tip was always kept engaged (but not scanning) during the potential scan

so as to not lose the previously observed area of interest. The surface was imaged again in the Cu(I) oxidation range at $E = -0.08$ V/SHE. Following this, the surface was imaged again in the reduced state. This is done by sweeping the sample's potential down to $E = -1.20$ V/SHE, followed by upward to $E = -0.75$ V/SHE at 1 mV/s. Again the tip was kept engaged but not scanning. Images of the surface in the initial metallic, subsequently oxidized and final reduced states were recorded in constant current mode without the usage of any filters. The recorded images were processed with Gwyddion software [69].

The topography across the GB regions was measured by line profile analysis. For analysis, a GB site was selected and 30 adjacent line scans covering a local distance of ~ 170 nm along the boundary were drawn across the grain boundary. The GB depth was taken as to be the local difference in topographic height between the bottom of the GB regions and the surface level of the corresponding grains on either side of the GB. Each such selected site was subject to ten different measurements and the standard deviations of these ten measurements are reported in the form of an error bar.

5.3 Results and discussion

5.3.1 Macroscopic inhibiting effects on passivation

Before discussing the ECSTM data, it is important to understand the macroscopic electrochemical behavior of the surface. For this, cyclic voltammetry was applied using the same protocol as for the ECSTM study in order to understand the effect of the presence of MBT and MBI in the NaOH alkaline electrolyte on macroscopic passivation. The CVs were obtained in the ECSTM cell after the cathodic reduction of the native oxide and recorded starting from -0.75 V/SHE up to the anodic apex of -0.08 V/SHE, in the domain of Cu(I) anodic oxidation, then down to the cathodic apex of -1.2 V/SHE, at the beginning of the hydrogen evolution region, and back to the starting point. The recorded macroscopic electrochemical response can be assigned to the properties of the grains since, for the total exposed surface, the surface fraction of the grains is much larger than that of the GBs.

Figure 5.1 shows the superimposed CVs of microcrystalline copper obtained in 0.1 M NaOH(aq), in 0.1 M NaOH(aq) + 1 mM MBT, and in 0.1 M NaOH(aq) + 1 mM MBI. The analysis of the anodic and cathodic reactions for all three cases is made according to the drawn baseline. The baseline was drawn for 0.1 M NaOH(aq) so that it is well centered in the potential region of -0.9 to -0.7 V/SHE, where the measured current is minimum. The same procedure was used for the two cases with inhibitors, and the current offsets were adjusted so that the baselines superimpose with that in the pure electrolyte.

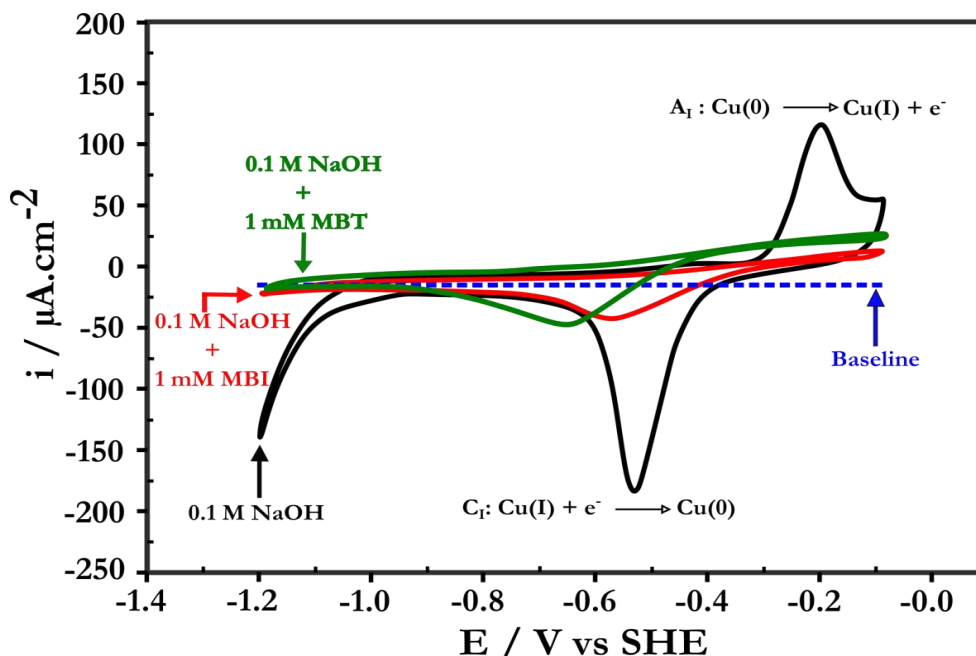


Figure 5.1: Cyclic voltammograms in the ECTM cell for microcrystalline copper in 0.1 M NaOH(aq) with and without MBT and MBI as indicated, scan rate = 1 mV/s.

In pure 0.1 M NaOH(aq), during the anodic scan, a shallow anodic peak is observed at -0.42 V/SHE followed by a sharp and intense A_1 peak at -0.2 V/SHE. The latter is characteristic of the anodic oxidation of copper as labeled in Figure 5.1 [70]–[83], and the former is likely related to the adsorption of hydroxide groups in the underpotential range of oxidation, as studied on single crystals [79]–[82]. During the cathodic scan and with respect to the baseline, the reaction remains anodic until -0.38 V/SHE and is cathodic afterwards. A sharp C_1 cathodic peak is observed at -0.52 V/SHE corresponding to the reductive decomposition of the Cu(I) oxide to Cu(0) metal as labeled in Figure 5.1, after which the cathodic current decreases to a stable plateau till the onset of hydrogen evolution. The measurements are in good agreement with those from previous work in the same electrolyte [59]–[61], [79]–[82].

In 0.1 M NaOH(aq) + 1 mM MBT, during the anodic scan, the CV does not show any A_1 anodic peak of formation of the Cu(I) passive film, but instead a continuous although attenuated increase of positive current from about -0.75 V/SHE up until the anodic apex at -0.08 V/SHE. During the cathodic scan, the current remains anodic down till -0.51 V/SHE, after which it is cathodic with a small peak observed at -0.62 V/SHE. The C_1 peak observed in 0.1 M NaOH(aq) at -0.52 V/SHE, and characteristic for the reduction of the Cu(I) passive film to Cu(0) metal, is suppressed. These measurements confirm the inhibiting effect of the presence of a pre-formed layer of MBT on a reduced copper surface on the formation of the Cu(I) surface oxide, like previously observed in alkaline aqueous solution [31], [34] and in gaseous phase [52]–[54].

In the presence of 1 mM MBI in the 0.1 M NaOH(aq) electrolyte, no A_1 anodic peak is observed on polarizing the sample anodically and the C_1 reduction peak is also suppressed in the cathodic scan. Thus, the pre-formed layer of MBI also inhibits the formation of the Cu(I) surface oxide. The measured currents are lower than in the presence of MBT with an increase of positive current from about -0.60 V/SHE and slow and continuous till the anodic apex. During the cathodic scan, the current remains anodic down till -0.40 V/SHE, after which it is cathodic with a small peak observed at -0.54 V/SHE. Note that, with both MBT and MBI, the negative current measured at the cathodic apex is strongly decreased, showing that the pre-formed organic layers also inhibit the reaction of hydrogen evolution in this potential range.

Unlike in strongly and weakly acidic conditions ($\text{pH} < 5$), Cu exhibits passivity in the alkaline conditions of the present experiment ($\text{pH} = 13$). This means that, in the absence of the inhibitors, when the surface is swept anodically, a stable Cu_2O oxide is formed in the Cu(I) oxidation range that protects the surface against dissolution. The cathodic peak C_1 observed in pure 0.1 M NaOH(aq) confirms the formation of the surface oxide and corresponds to the decomposition of this Cu(I) oxide to Cu(0) metallic copper [70]–[83]. It is important to keep in mind that in 0.1 M NaOH(aq), during anodic passivation, there is a competing reaction occurring between the dissolution of copper into the electrolyte and the formation of the stable oxide. Both reactions consume metallic copper but the first one is minority and irreversible whereas the second one is reversible and largely dominant.

On integrating the measured current densities over time, we obtain charge densities for the anodic and cathodic reactions as $q_{\text{AI}} = 2357 \mu\text{C}\cdot\text{cm}^{-2}$ and $q_{\text{CI}} = 2168 \mu\text{C}\cdot\text{cm}^{-2}$, respectively, confirming a partially reversible behavior consistent with some copper being irreversibly consumed during anodic polarization since $q_{\text{AI}} > q_{\text{CI}}$. The electric charge density q associated with the irreversible reaction of copper is $189 \mu\text{C}\cdot\text{cm}^{-2}$ ($q = q_{\text{AI}} - q_{\text{CI}}$). The equivalent thickness of irreversibly dissolved copper ($\delta_{\text{Cu(IR)}}$) can be calculated using Equation 1, where V_M is the molar volume of reacting material ($V_M^{\text{Cu}} = 7.1 \text{ cm}^3\text{mol}^{-1}$ for Cu metal), z the number of exchanged electrons ($z = 1$ for Cu(I) anodic oxidation) and F the Faraday constant.

$$\delta = \frac{qV_M}{zF} \quad \text{Eq (1)}$$

From this, we get a $\delta_{\text{Cu(IR)}}$ value of 0.14 nm. This low value amounts to 0.67 equivalent monolayers (ML) of copper (one (111)-oriented ML of copper is 0.208 nm thick from the bulk *fcc* structure) being irreversibly consumed by dissolution. To calculate the equivalent thickness of the Cu(I) oxide passive film formed on the surface, we use the value q_{CI} of the reductive electric charge density in Eq (1). If one assumes the formation of $\text{Cu(I)}_2\text{O}$ oxide film and using $V_M^{\text{Cu}_2\text{O}} = 23.9 \text{ cm}^3\cdot\text{mol}^{-1}$ and $z = 2$ for the reduction of 2 Cu(I) in Eq (1), we obtain the value of $\delta_{\text{pass}} = 2.68 \text{ nm}$. This obtained value is in agreement with the previously obtained thickness values for Cu(I) oxide films [23], [24], [33], [60], [61].

Regarding the effect of MBT and MBI, we have seen in Figure 5.1 that the distinct anodic peak A_1 is absent when the CV is recorded in the presence of the inhibitor. This implies that MBT and MBI block passivation of the surface by inhibiting the formation of the surface oxide. The residual activity measured both during the anodic and cathodic scans in the presence of inhibitor may be due to the oxidation and reduction of those copper atoms that are dissociated from oxygen during the initial cathodic reduction pretreatment of the air-formed native oxide. Indeed, the cathodic pretreatment is applied in the presence of the inhibitors and it is most likely that the free Cu atoms, dissociated from oxygen by electrochemical reduction, react with the adsorbed organic molecules and are thus captured in the molecular inhibitor layer formed on the surface as illustrated by the model shown in Figure 5.2. So, we can expect the inhibitor film, pre-formed before the CV treatment, to include copper atoms originating from the native oxide and trapped in the organic film. The residual activity recorded during anodic and subsequent cathodic polarization of the surface can thus be that of the Cu atoms initially trapped in the pre-formed inhibitor surface layer.

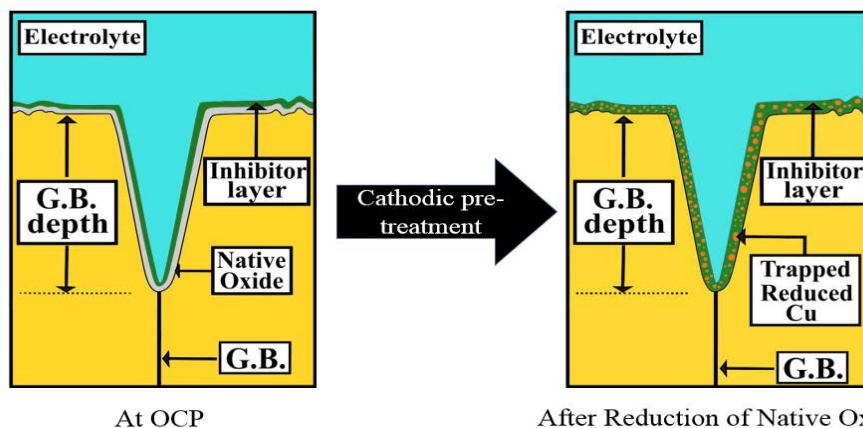


Figure 5.2: Schematic illustration of the inhibitor layer formed after cathodic pre-treatment of the surface: the reduction of the native oxide pre-covered by the inhibitor film leads to trapping of the copper atoms dissociated from the oxygen atoms in the inhibitor layer.

Since macroscopic passivation is blocked by the inhibitor layer pre-formed before electrochemical testing, the equivalent thickness δ_{pass} of the Cu(I) passive oxide film is not calculated since it is not physically meaningful. Instead, two values, $\delta_{Cu(R)}$ and $\delta_{Cu(IR)}$ can be calculated from the electrochemical data for the inhibitor. The value of $\delta_{Cu(R)}$, calculated from the cathodic charge density, is assigned to the amount of copper that is reversibly reacting during the electrochemical polarization. This value estimates the amount of copper presumably trapped in the pre-formed inhibitor layer and reversibly reacting during the CV treatment. The second quantity, $\delta_{Cu(IR)}$, calculated from the difference between anodic and cathodic charge density, estimates the amount of copper that is irreversibly consumed due to the residual dissolution occurring during the electrochemical polarization.

With MBT, the values of the charge density cumulated during the anodic and cathodic polarization scans are $1807 \mu\text{C}\cdot\text{cm}^{-2}$ and $1746 \mu\text{C}\cdot\text{cm}^{-2}$, respectively. From the cumulated cathodic charge density, we get $\delta_{Cu(R)} = 1.28 \text{ nm}$ (6.17 ML) of copper trapped in the pre-formed inhibitor film and reversibly reacting during electrochemical polarization, meaning that several equivalent monolayers of copper would be trapped in the pre-formed MBT surface layer as a result from the dissociation of the native oxide. The non-zero difference between the anodic and cathodic charge densities is consistent with an irreversible loss of copper due to residual dissolution. From the difference of $61 \mu\text{C}\cdot\text{cm}^{-2}$, $\delta_{Cu(IR)}$ is calculated from Eq. (1) using $V_M^{Cu} = 7.1 \text{ cm}^3\text{mol}^{-1}$ and $z = 1$, and we get $\delta_{Cu(IR)} = 0.045 \text{ nm}$ corresponding to a fraction of a monolayer (0.22 ML) of copper irreversibly consumed due to residual dissolution. This quite small value is consistent with efficient macroscopic inhibition of irreversible dissolution and residual dissolution being localized in the most active sites such as grain boundary surface regions. With MBI, the values of the anodic and cathodic charge densities are $847 \mu\text{C}\cdot\text{cm}^{-2}$ and $842 \mu\text{C}\cdot\text{cm}^{-2}$, respectively. For $\delta_{Cu(R)}$, we get a value of 0.62 nm (2.98 ML) from the cathodic charge density, meaning that the pre-formed MBI inhibitor layer would contain about twice as less reacting copper atoms than the pre-formed MBT inhibitor layer. The difference between anodic and cathodic charge densities is within the uncertainty range, which suggests that the pre-formed MBI inhibitor layer would more efficiently mitigate irreversible dissolution than the pre-formed MBT inhibitor layer in the most reactive surface sites.

In summary, these CV data show that the organic inhibitor layers, pre-formed before electrochemical testing, behave similarly and block the formation of a Cu(I) oxide film and thus surface passivation; however, the electrochemical reactivity is not fully suppressed. The observed residual activity is assigned for its most part to the copper atoms dissociated from the native oxide during the cathodic pretreatment and trapped in the pre-formed inhibitor surface layer. These trapped copper atoms amount to the equivalent of a few monolayers of copper metal and react reversibly upon anodic and cathodic

polarization. Irreversible anodic charge transfer is assigned to the residual anodic dissolution of copper contributed preferentially from the most reactive sites of the surface such as GB surface terminations. Although blocking passivation may seem detrimental to corrosion protection, this is efficiently compensated by the pre-formed organic layers efficiently mitigating dissolution upon anodic polarization in the Cu(I) oxidation range.

5.3.2 ECSTM images and classification of grain boundaries by their morphology

Figures 5.3 and 5.4 show *in situ* ECSTM images of the topmost surface of microcrystalline copper obtained in 0.1 M NaOH(aq) with 1 mM MBT or with 1 mM MBI in the electrolyte, respectively. For each inhibitor, the same local area is imaged in the initial metallic state, after reduction of the native oxide (Figures 5.3a and 5.4a), in the Cu(I) oxidation range (Figures 5.3b and 5.4b) and in the final metallic state, after reduction of the oxidized state (Figures 5.3c & 5.4c). The selected areas of interest show the typical copper microstructure exhibiting grains and sub-grains. The difference in measured topographic height amongst different grains is attributed to differences of local surface reactivity during the surface preparation by electrochemical etching. The GB surface regions correspond to the surface termination of GB planes and their adjacent vicinity. Some of these GB surface regions are measured higher than others, which is again assigned to differences in local surface reactivity during the surface preparation. A few GB regions are also revealed due to topographical variations between the adjacent grains.

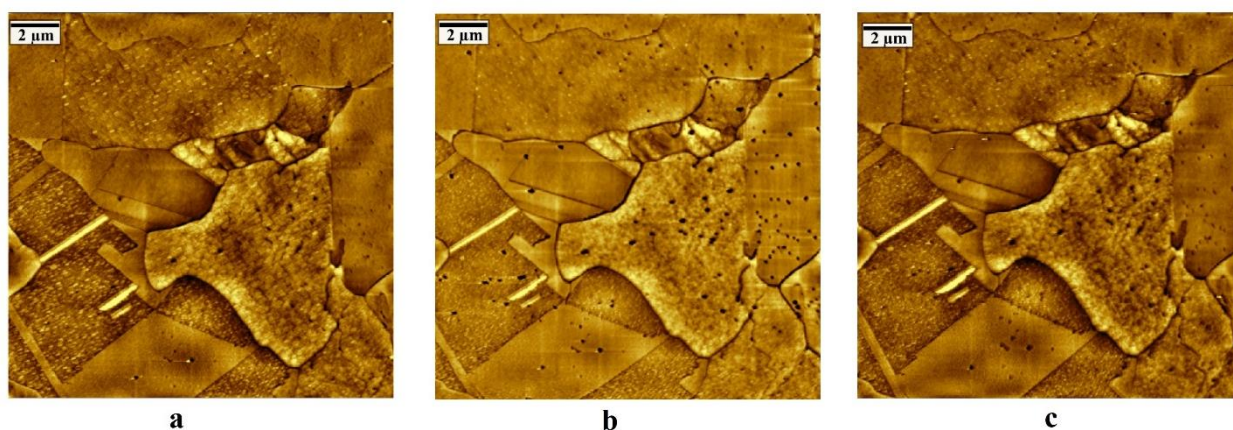


Figure 5.3: Topographic ECSTM images of microcrystalline copper as obtained *in situ* in 0.1 M NaOH(aq) +1 mM MBT: (a) Initial metallic state ($\Delta Z = 10.2$ nm, $E_{Cu} = -0.75$ V/SHE, $E_{tip} = -0.30$ V/SHE, $I_t = 0.5$ nA); (b) Surface state after anodic sweep until Cu(I) oxidation range ($\Delta Z = 13.7$ nm, $E_{Cu} = -0.08$ V, $E_{tip} = -0.30$ V, $I_{tip} = 1.5$ nA); (c) Surface state after cathodic sweep until hydrogen evolution and back to metallic state ($\Delta Z = 10.3$ nm, $E_{Cu} = -0.75$ V, $E_{tip} = -0.60$ V, $I_{tip} = 1.0$ nA).

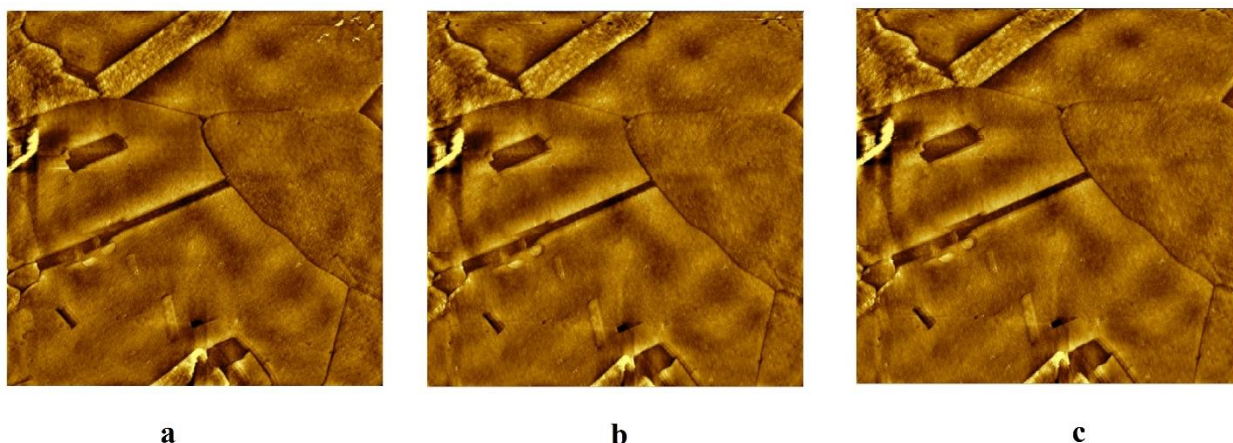


Figure 5.4: Topographic ECSTM images of microcrystalline copper as obtained *in situ* in 0.1 M NaOH(aq) +1 mM MBI: (a) Initial metallic state ($\Delta Z = 9.8$ nm, $E_{Cu} = -0.75$ V/SHE, $E_{tip} = -0.60$ V/SHE, $I_t = 0.5$ nA); (b) Surface state after anodic sweep until Cu(I) oxidation range ($\Delta Z = 9.5$ nm, $E_{Cu} = -0.08$ V, $E_{tip} = -0.30$ V, $I_{tip} = 1.5$ nA); (c) Surface state after cathodic sweep until hydrogen evolution and back to metallic state ($\Delta Z = 9.9$ nm, $E_{Cu} = -0.75$ V, $E_{tip} = -0.60$ V, $I_{tip} = 1.0$ nA).

The adopted classification of the observed grain boundaries is based on their morphology in the surface plane and is consistent with our previous work [63], [64] (Chapters 3 and 4). GBs appearing in parallel pairs and separating sub-grains are assigned to $\Sigma 3$ coherent twins, i.e. with a GB plane of {111} orientation. Short and straight GBs are assigned to low Σ CSL boundaries. Straight segments observed along a GB with locally straight or curved morphology are assigned to high Σ CSL boundaries. Finally, curved GBs or locally curved segments are assigned to the class of random boundaries. A summary of grounds used for this classification is given in Table 5.1.

Table 5.1: Summary of criteria used for classification of grain boundaries based on their morphology in the surface plane

GB morphology	Class of GBs
Two parallel GBs separating a sub-grain	$\Sigma 3$ coherent twins (with a {111}-oriented GB plane)
Short and straight GBs	Low Σ CSL boundaries
Straight GB segments	High Σ CSL boundaries
Curved GBs or curved GB segments	Random boundaries

5.3.3 Local inhibiting effects on grain boundary network

The analysis of the images displayed in Figures 5.3 and 5.4 resulted in totals of 101 local sites for MBT and 100 local sites for MBI where the depth in the GB regions could be measured geometrically in the initial Cu(o) metallic region, upon anodic polarization in the Cu(I) oxidation region, and back in the Cu(o) metallic region after reduction. For both inhibitors, comparative analysis of the variations of the measured depth of all GB sites resulted in five distinct types of local topographical evolution of the grain boundary network that are: i) no variation of the GB depth, ii) repeated increase, iii) repeated decrease, iv) decrease followed by an increase and v) increase followed by a decrease. For each type, one example of the line profile evolution is given in Figure 5.5. These are the same five types of local topographical behavior that were observed when studying the early intergranular corrosion in acidic conditions (10 mM HCl) in the presence of the inhibitors [63], [64] (Chapters 3 and 4). However, their mechanistic interpretations differ as they must take into account the inhibitor effect on surface passivation.

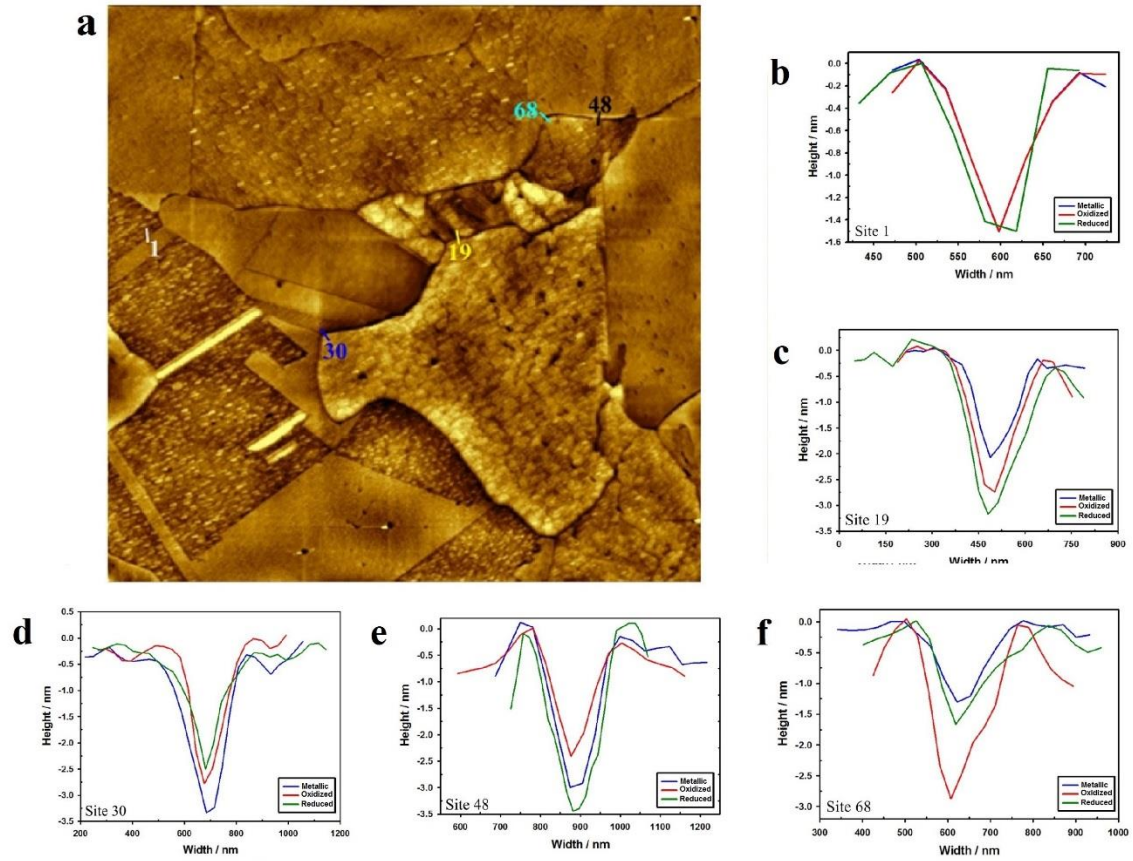
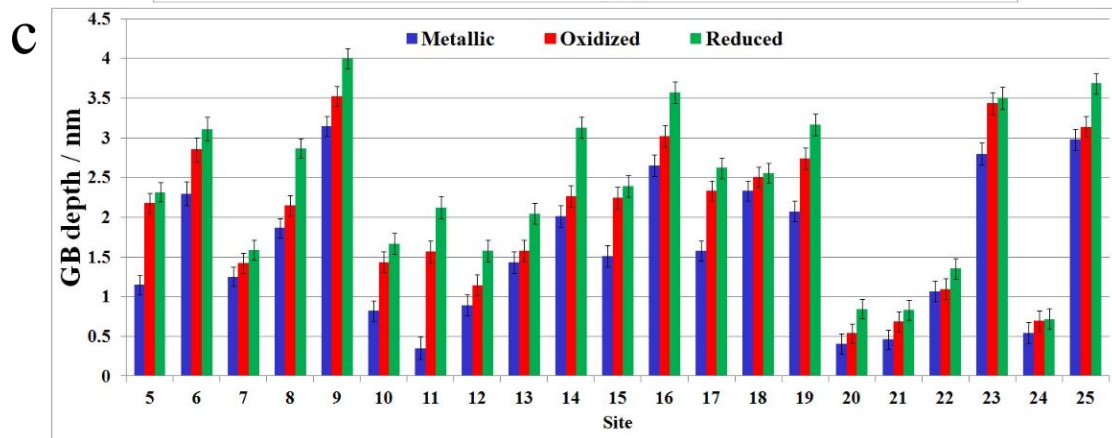
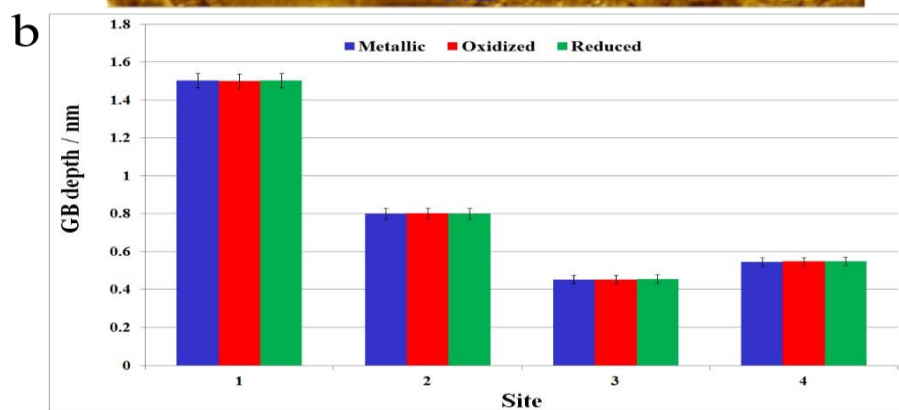
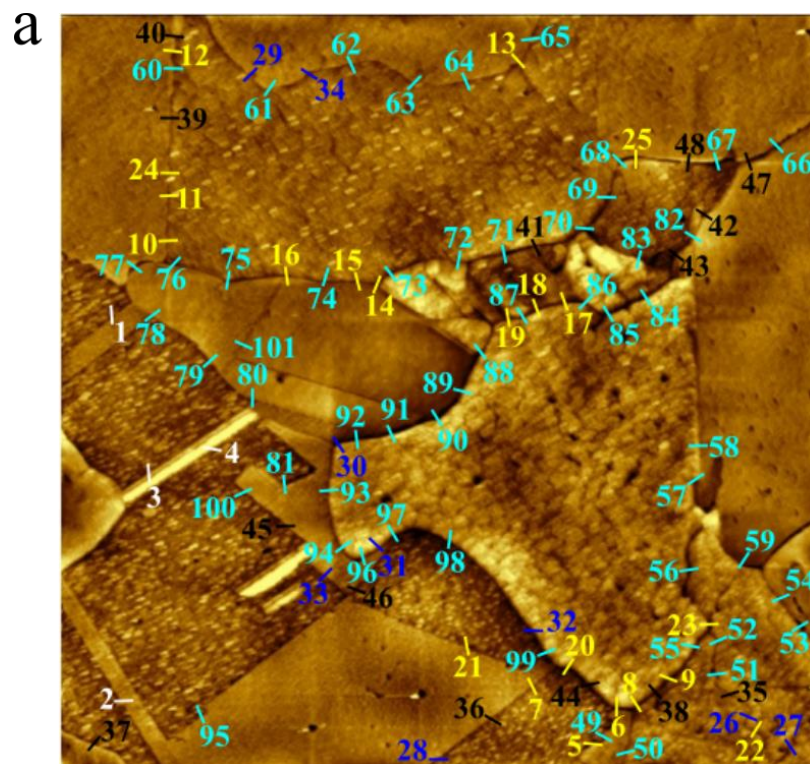


Figure 5.5: Local behavior of the topographical evolution of the GB network from average topographic line profiles measured across the GBs: (a) ECSTM topographic image of microcrystalline copper in 0.1 M NaOH(aq) + 1 mM MBT; (b) no variation of the GB depth at site # 1, (c) repeated increase at site # 19, (d) repeated decrease at site # 30, (e) decrease followed by increase at site # 48 and (f) increase followed by decrease at site # 68.

In Figures 5.6 and 5.7, we show all the analyzed local GB sites together with the histograms for all five types of behavior of the variation of the depth of the GB region observed in the presence of MBT and MBI, respectively. These five types of behavior show that both inhibitors are blocking passivation in the GB regions in agreement with the macroscopic CV data, but that residual dissolution or passivation is not completely blocked in the GB regions. Hereafter, we organize the discussion according to the type of behavior locally observed.



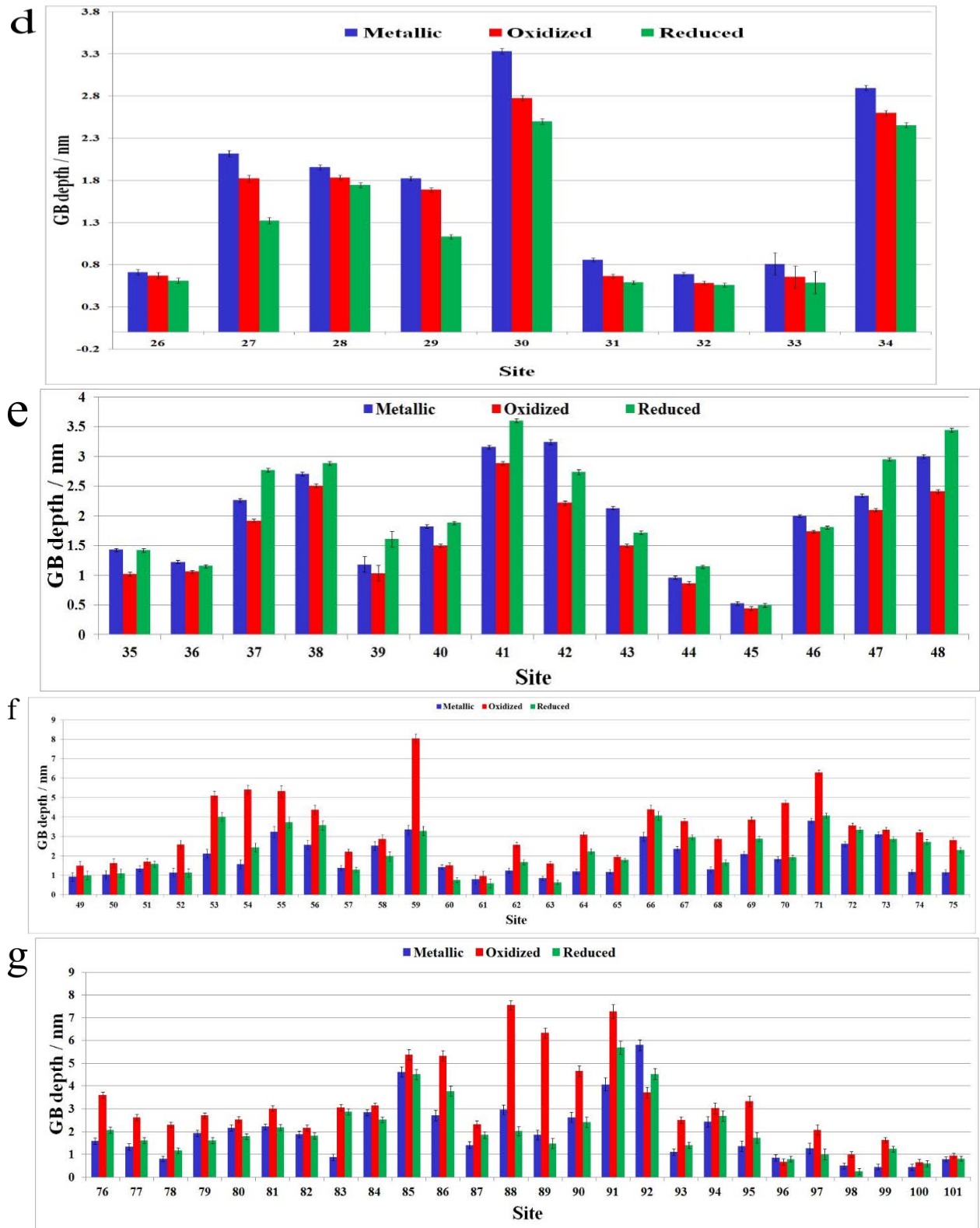
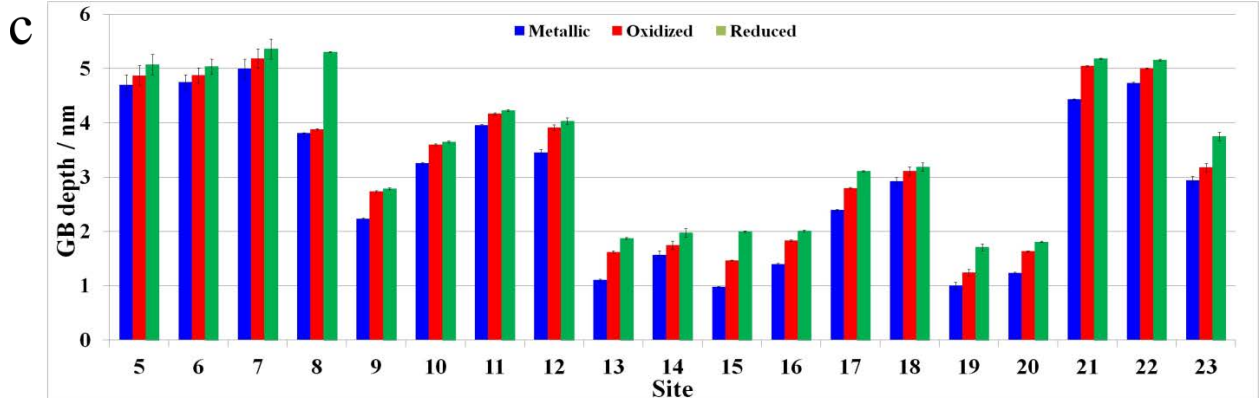
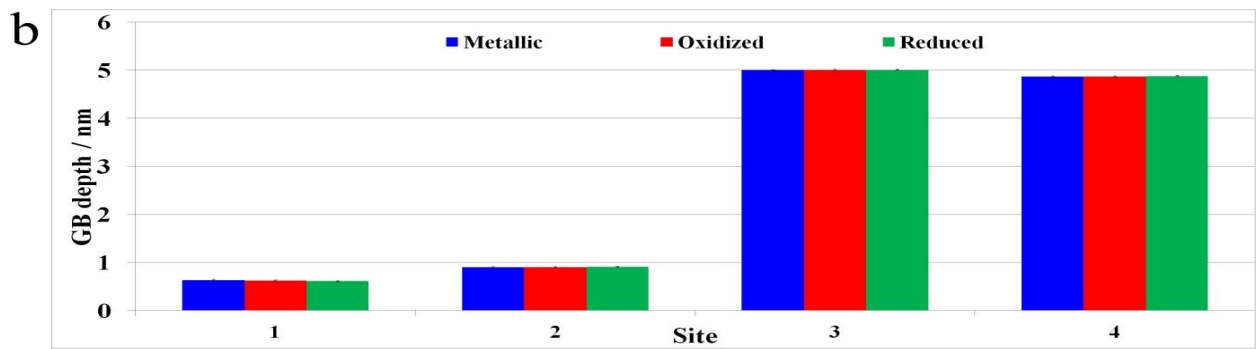
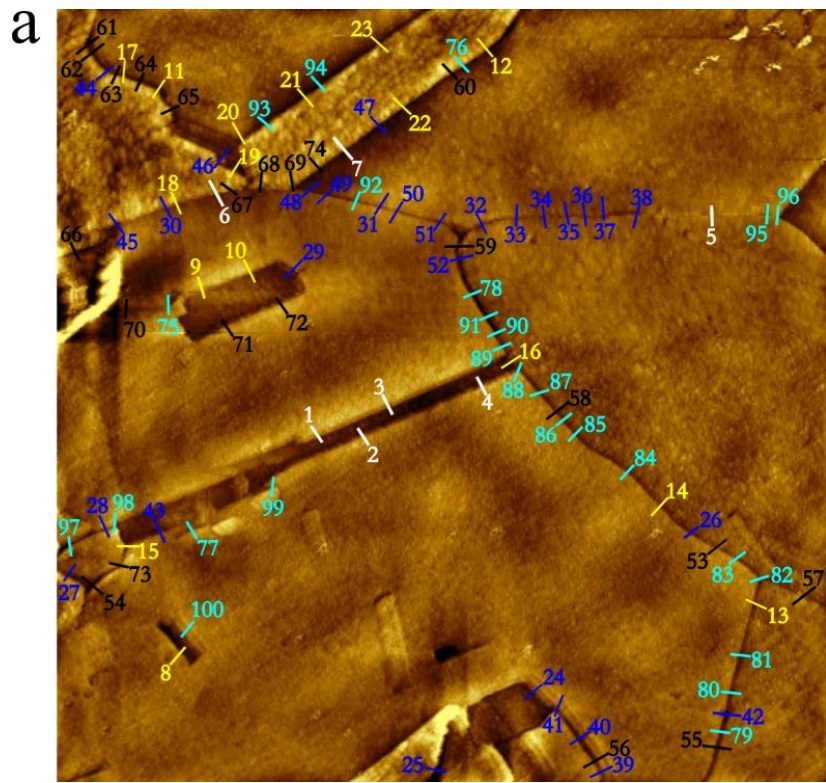


Figure 5.6: Identification of local GB behavior for microcrystalline copper in 0.1 M NaOH(aq) + 1 mM MBT: (a) Topographic ECSTM image with grain boundary sites labelled 1 to 101; (b) Bar graph of the depth measured across the GB sites (labelled in white in (a)) showing no depth variation in metallic, oxidized and reduced surface states; (c) Bar graph of the GB sites (labelled in yellow in (a)) showing continuous depth increase; (d) Bar graph of the GB sites (labelled in dark blue in (a)) showing continuous depth decrease; (e) Bar graph of the GB sites (labelled in black in (a)) showing depth decrease and subsequent increase; (f,g) Bar graphs of the GB sites (labelled in light blue in (a)) showing depth increase and subsequent decrease.



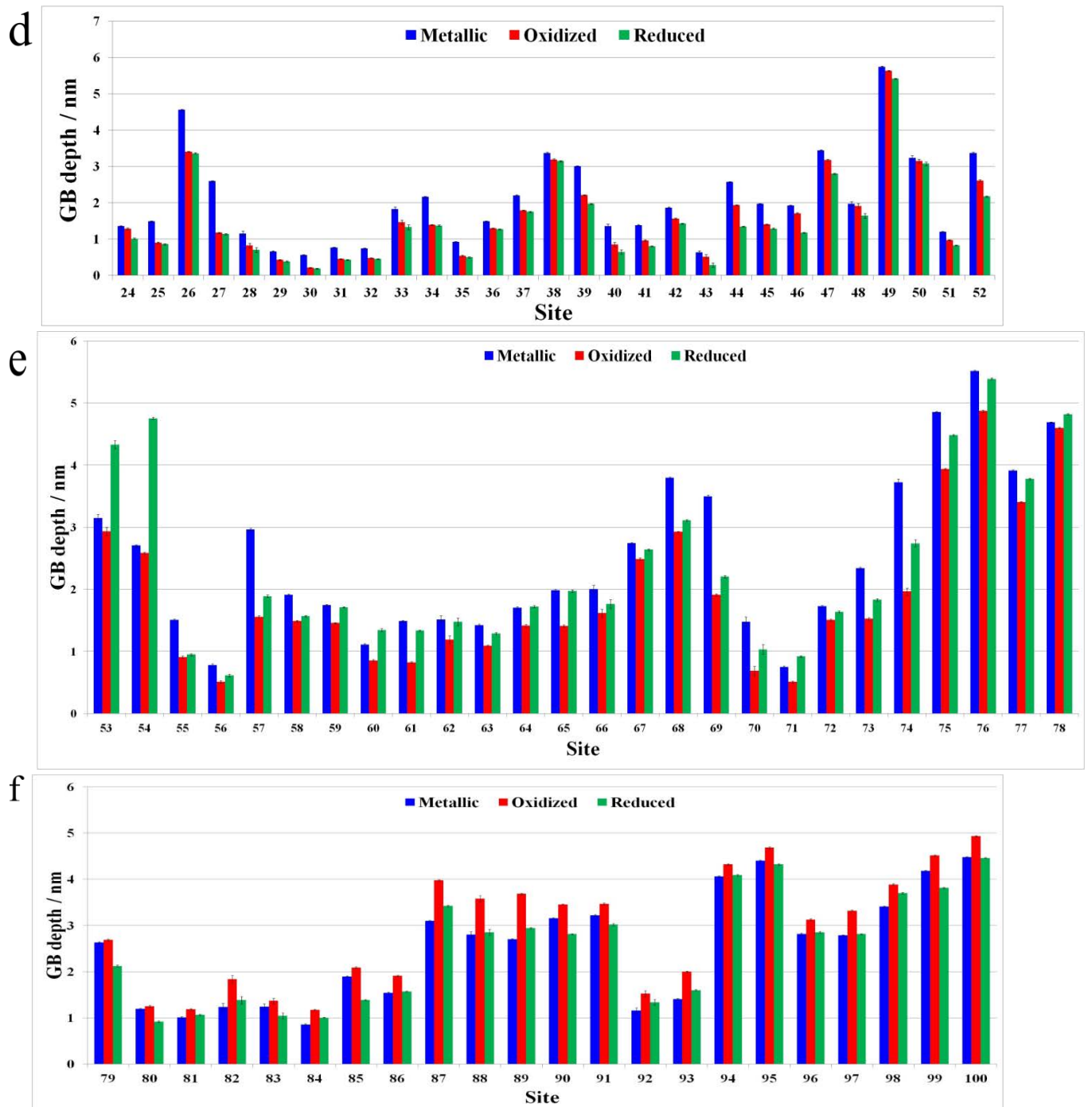


Figure 5.7: Identification of local GB behavior for microcrystalline copper in 0.1 M NaOH(aq) + 1 mM MBI: (a) Topographic ECSTM image with grain boundary sites labelled 1 to 100; (b) Bar graph of the depth measured across the GB sites (labelled in white in (a)) showing no depth variation in metallic, oxidized and reduced surface states; (c) Bar graph of the GB sites (labelled in yellow in (a)) showing continuous depth increase; (d) Bar graph of the GB sites (labelled in dark blue in (a)) showing continuous depth decrease; (e) Bar graph of the GB sites (labelled in black in (a)) showing depth decrease and subsequent increase; (f) Bar graph of the GB sites (labelled in light blue in (a)) showing depth increase and subsequent decrease.

Blocked passivation with absence of preferential intergranular reaction

Firstly, we discuss the case of the local GB sites that show no variation of the GB depth upon anodic oxidation and subsequent reduction. These sites are labelled 1 to 4 in Figures 5.6a and 5.7a, and the depth values measured across the GB sites are reported in Figures 5.6b and 5.7b for MBT and MBI, respectively. In these local sites, the absence of depth variation indicates no preferential reactivity of the GB surface regions as compared to the adjacent grains. This behavior is illustrated by the model shown in Figure 5.8.

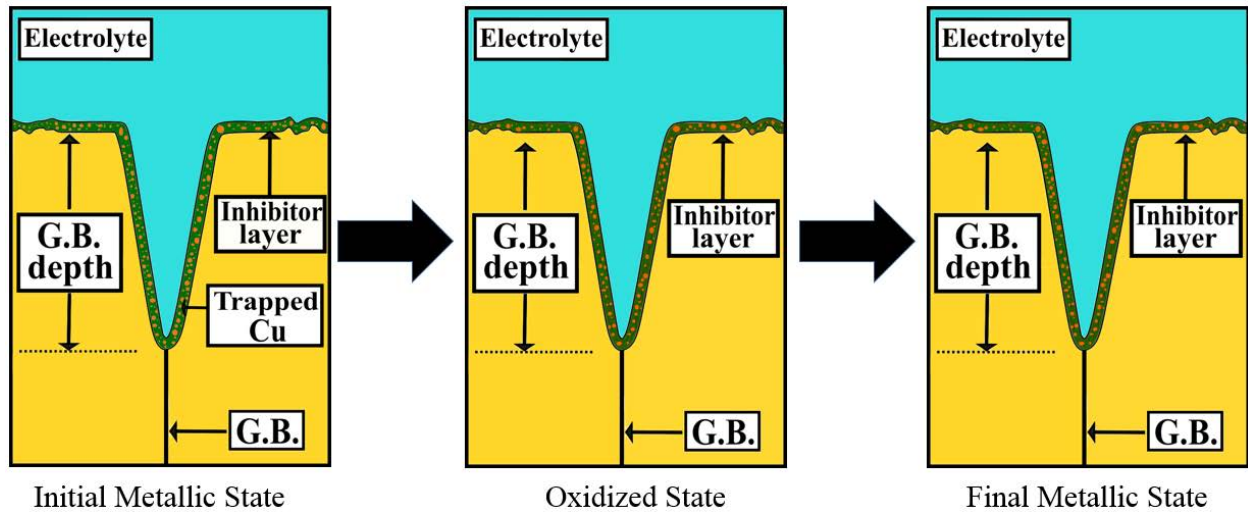


Figure 5.8: Schematic illustration of observed inhibiting effects of pre-formed MBT and MBI layers on intergranular passivation: surface passivation is blocked on grains and at GBs and there is no preferential residual reactivity at the GBs.

All the sites that displayed this behavior are located along two parallel GBs separating a sub-grain, a configuration typical of Σ_3 coherent twins. Even in the absence of inhibitors, Σ_3 CTs have been reported to have no preferential reactivity compared to adjacent grains, both in acidic [62] and alkaline [61] media. Thus, since there is passivation in the absence of the inhibitor as confirmed above, the absence of preferential local reactivity in these sites can be assigned to the pre-formed organic film of inhibitor equally blocking passivation in the GB region and on the adjacent grains, but also equally inhibiting the residual anodic dissolution or passivation that may occur in the Cu(I) potential range. The absence of preferential GB reactivity for Σ_3 coherent twins, also observed in acid conditions [63], [64] (Chapters 3 and 4), is interpreted as an intrinsic property of CTs rather than as an inhibiting effect of MBT or MBI.

Blocked passivation with residual intergranular dissolution

Secondly, we consider the case of the local GB sites that showed preferential reactivity compared to adjacent grains characterized by an increase of the depth of the GB surface region upon anodic polarization and after subsequent reduction. These sites are labelled from 5 to 25 in Figure 5.6a and from 5 to 23 in Figure 5.7a for MBT and MBI, respectively. The corresponding histograms of the GB depth values are shown in Figures 5.6c and 5.7c, respectively. The model in Figure 5.9 can help us understand this case of a continuous increase of the GB depth assigned to residual intergranular dissolution.

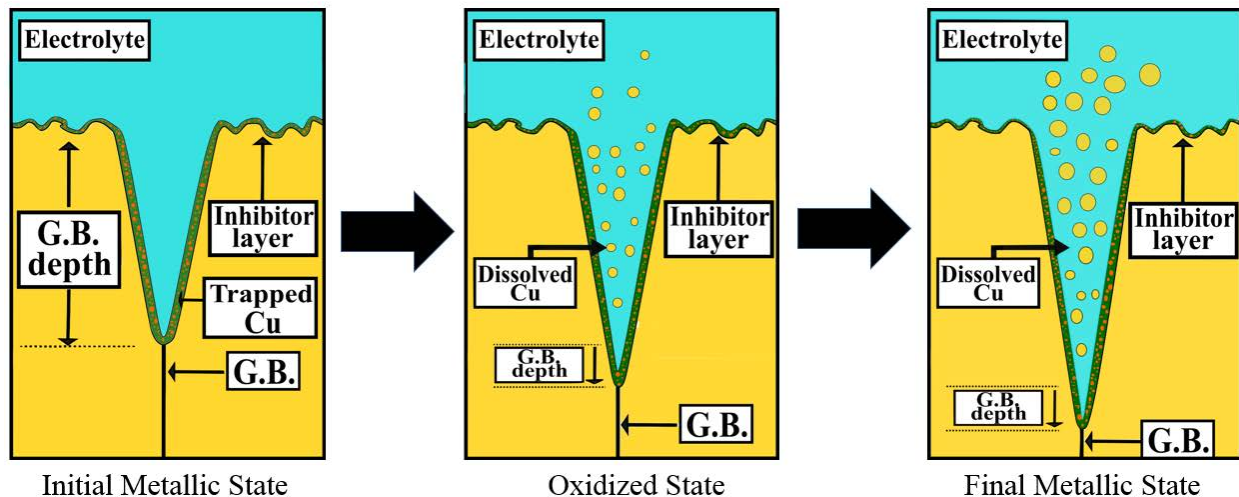


Figure 5.9: Schematic illustration of observed inhibiting effects of pre-formed MBT and MBI layers on intergranular passivation: passivation is blocked on grains and at GBs but there is residual dissolution preferentially at the GBs.

As discussed above in Section 5.3.1, in our testing conditions, when the cathodic pretreatment is applied to the surface to reduce the native oxide, there is already an inhibitor layer pre-adsorbed on the surface. Upon reductive decomposition of the native oxide, Cu atoms are released and most likely trapped in the inhibitor surface film. The reversible part of the residual electrochemical activity measured during subsequent cycling corresponds to these Cu atoms trapped in the surface inhibitor film and reacting reversibly during the anodic and cathodic sweeps. Along with the copper reacting reversibly, some copper is lost due to dissolution, which forms the irreversible part of the measured electrochemical activity. This residual dissolution in the presence of an inhibitor layer occurs preferentially from intergranular regions resulting in a continuous increase of the depth of the measured line profile. Thus, in the GB sites showing this behavior, the pre-formed inhibitor layers of MBT or MBI block anodic passivation in the Cu(I) oxidation range, like on the grains. Still, they fail to completely block residual anodic dissolution in the most reactive sites, resulting in an increase of the depth of the intergranular regions. The GB depth further increases when the surface is measured in the reduced state since, during the reverse scan, there is still polarization in the Cu(I) anodic region before entering the cathodic region.

For MBT, eighteen of the twenty-one sites in Figure 5.6a showing this type of behavior belong to the class of random boundaries (sites 5, 6, 8-20 and 23-25). The histogram in Figure 5.6c shows that the highest increase in the GB depth, and thus the largest extent of residual dissolution, is measured for this class of grain boundaries. Among the three non-random boundaries, site 7 belongs to the class of Σ_3 CTs. Unlike sites 1-4, also assigned to Σ_3 CTs, this site would not resist residual anodic dissolution, possibly as a result from a significant deviation from the ideal geometry of Σ_3 CTs [61], [62]. Sites 21 and 22 belong to the classes of low Σ and high Σ CSL boundaries, respectively. For these 3 non-random boundaries, it can be observed that MBT inhibits the local loss of Cu from the intergranular region to a greater extent than for the other 18 random GBs, in agreement with the expected more reactive character of random boundaries.

For MBI, there are nineteen sites labelled in Figure 5.7a showing this type of behavior. Eight of them, sites 6, 11, 12, 14-18, belong to the class of random boundaries, and another eight of them, sites 5, 7, 13, 19-23, to the class of high Σ CSL GBs. Three local GBs, at sites 8-10, belong to the class of Σ_3 CTs that probably deviate from the ideal geometry.

Incompletely blocked passivation with irreversible accumulation of passivation products

Third is the case of the intergranular behavior characterized by a decrease of the measured GB depth upon anodic polarization in the Cu(I) passive range and after subsequent reduction. For MBT, there were nine sites, labeled 26-34 in Figure 5.6a, showing this behavior, and for MBI, twenty-nine sites, labeled 24-52 in Figure 5.7a. The corresponding histograms of the measured GB depth are displayed in Figure 5.6d and 5.7d, respectively. The model in Figure 5.10 illustrates our interpretation of this locally observed intergranular behavior.

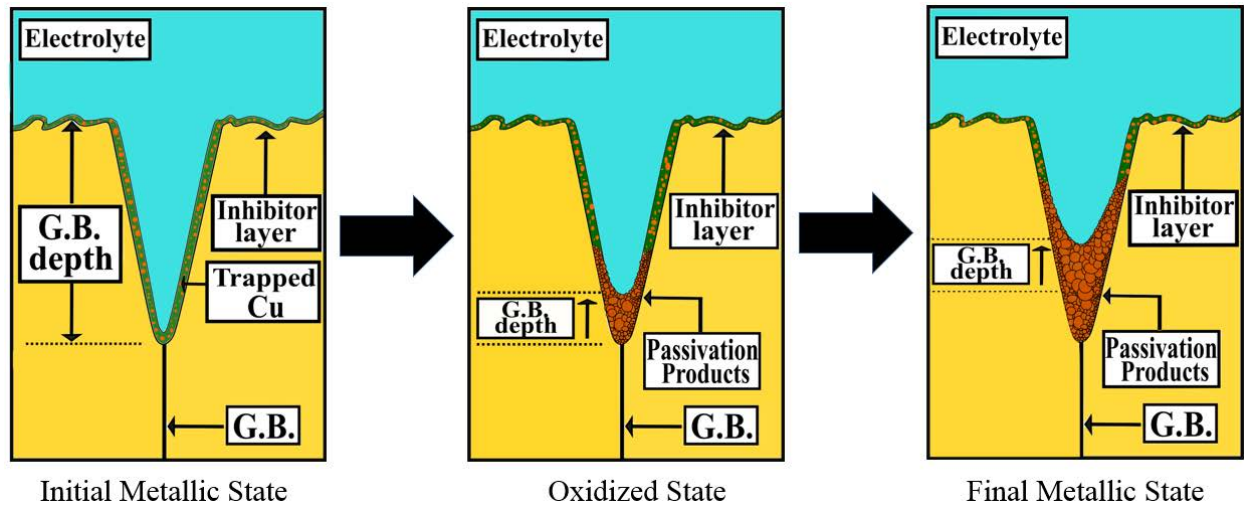


Figure 5.10: Schematic illustration of observed inhibiting effects of pre-formed MBT and MBI layers on intergranular passivation: passivation is completely blocked on grains and incompletely blocked at GBs; there is residual anodic reactivity at the GBs leading to irreversible accumulation of passivation products.

In the GB sites showing this type of behavior, copper is preferentially consumed upon anodic polarization compared to adjacent grains to form products that accumulate in the intergranular region, thus leading to the measured decrease of the depth of the GB region, like observed in acid solution [63], [64] (Chapters 3 and 4). The decrease of the measured GB depth can result from local passivation during the anodic scan to form Cu(I) oxide like observed in the absence of inhibitor [59], [60], [62]. This implies that anodic passivation would be incompletely blocked by a pre-formed inhibitor layer, more defective in the GB site than on the adjacent grains, and that Cu(I) oxide would grow in the defective site of the inhibitor film. Local accumulation of corrosion products cannot be ruled out. They might be complexes formed by the reaction of locally dissolving copper with the organic molecules present in the electrolyte and deposited in the intergranular regions. It is a limitation of this experimental technique as we cannot identify the exact nature and composition of these accumulated passivation/corrosion products. One could expect Cu(I) oxide to be reduced during the cathodic sweep thus leading to an increase of the GB depth and not the observed decrease [59], [60], [62]. However, it is unclear if the applied cathodic sweep would be sufficiently reductive to decompose the Cu(I) passivation product formed in the GB sites because of the defective pre-formed inhibitor layer.

For MBT, among the nine sites showing this intergranular behavior, one, site 28 is classified as a Σ_3 CT that, just like the above discussed site 7, might be a boundary largely deviated from the ideal geometry of CTs and thus losing its intrinsically intergranular resistant character. Sites 33 and 26 are attributed to low Σ and high Σ CSL boundaries, respectively. Six out of the nine sites are classified as random boundaries with, among them, four sites (sites 27, 29, 30 and 34) showing the largest variation of the GB depth. This preferential intergranular susceptibility is expected for random boundaries that are more

reactive than CTs and most CSL boundaries. It is here observed even in the presence of corrosion inhibitor.

For 1 mM MBI, among the twenty-nine sites showing this intergranular behavior, a majority of fifteen sites (sites 25, 26, 29, 30, 32-38, 44, 45, 51 and 52) are classified as random boundaries with preferential intergranular susceptibility to residual corrosion in the presence of the organic inhibitor. Site 43 is classified as a $\Sigma 3$ CT, likely also deviated from ideal geometry. Sites 27 and 28 are classified as low Σ CSLs, and eleven sites (24, 31, 39-42, 46-50) belongs to the high Σ CSLs.

Incompletely blocked passivation with reversible accumulation of passivation products

Next, the case of the intergranular behavior characterized by a decrease of the GB depth measured upon anodic polarization in the Cu(I) passive range followed by an increase after subsequent reduction is discussed. For MBT, there are fourteen sites, labeled 35-48 in Figure 5.6e where this behavior is observed, and, for MBI, twenty-six sites, labeled 53-78 in Figure 5.7e. This behavior can be understood using the model shown in Figure 5.11.

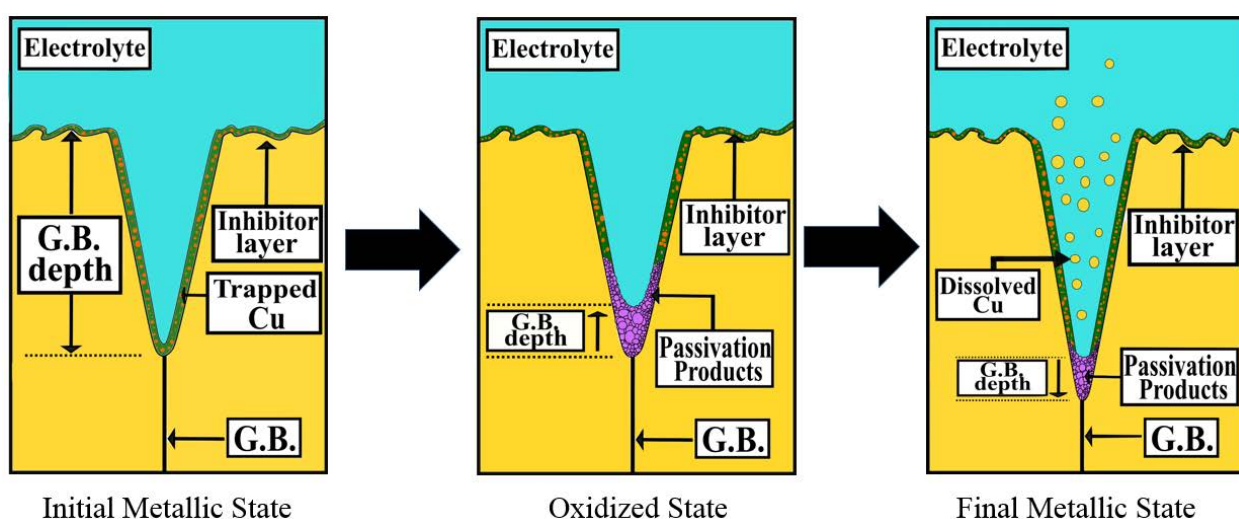


Figure 5.11: Schematic illustration of observed inhibiting effects of pre-formed MBT and MBI layers on intergranular passivation: passivation is blocked on grains and incompletely at GBs; there is residual anodic reactivity at the GBs leading to reversible accumulation of passivation products and residual corrosion.

Like in the previous case, the decrease of the depth measured in the GB surface regions is interpreted as due to the accumulation of passivation products in the intergranular region when the surface is anodically polarized in the Cu(I) passive region, as a result of a locally less efficient inhibiting effect of the pre-formed MBT or MBI layer on formation of Cu(I) oxide. Subsequently, when the surface is cathodically polarized, the increase of the GB depth might be due to electrochemical reduction of the accumulated passivation products causing a decrease of thickness. In this case, the applied cathodic sweep would be sufficiently reductive to decompose the Cu(I) passivation products formed in the GB sites. The residual dissolution of copper from the grain boundary region during the cathodic sweep cannot be excluded since there is still polarization in the Cu(I) anodic region before entering the cathodic region. This is suggested by the minority number of GB sites (sites 37-41, 44, 47 and 48 in Figure 5.6e and sites 53, 54, 60, 64 and 78 in Figure 5.7e) where the depth is measured larger after the anodic/cathodic cycling than before.

For MBT, among the fourteen sites showing this local behavior, ten (sites 38-44 and 46-48) are classified as random boundaries. Site 36 is classified as being a Σ_3 CT, likely deviated from its ideal geometry. Two sites, 37 and 45, are classified as being low Σ CSLs, and one (site 35) as being a high Σ CSL. For MBI, out of twenty-six sites with this behavior, twelve (sites 53, 54, 56, 60-62, 66, 74, 75 and 77) are random boundaries, fourteen (sites 57-59, 63-65, 67-73, 76) are high Σ CSLs and two (sites 55 and 78) are attributed to Σ_3 CTs. None of the measured sites are attributed to low Σ CSLs.

Blocked passivation with residual intergranular dissolution and accumulation of corrosion products

Finally, we consider the case of the intergranular behavior characterized by an increase of the GB depth measured upon anodic polarization in the Cu(I) passive range followed by a decrease after subsequent reduction. For MBT, this behavior is observed in fifty-two sites labeled 49-101 in Figure 5.6. The corresponding histogram is splitted in two panels shown in Figure 5.6f & 5.6g. For MBI, there are twenty-six grain sites, labeled 79-100 in Figure 5.7a, having this behavior, and the corresponding histogram is shown in Figure 5.7f. Our interpretation of this behavior is illustrated in Figure 5.12. Like in the second case examined in this Section, the increase of the depth of the GB surface regions measured upon polarization in the Cu(I) potential range is interpreted as due to the pre-formed organic layer blocking passivation in the GB region but failing to suppress anodic dissolution. Subsequently, during the cathodic sweep, there is ongoing dissolution since there is still polarization in the Cu(I) anodic region before entering the cathodic region, leading in this case to the accumulation of corrosion products in the GB region.

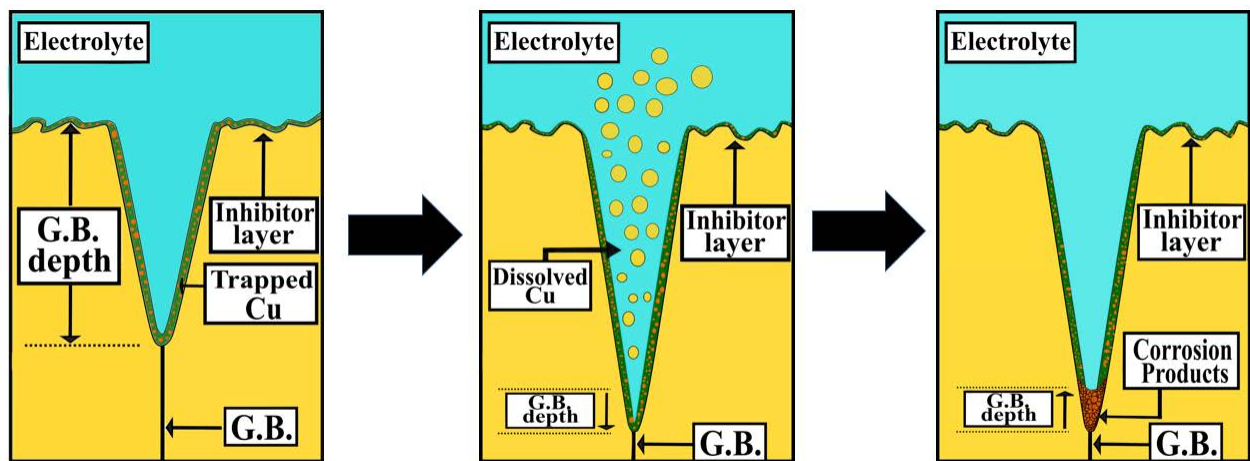


Figure 5.12: Schematic illustration of observed inhibiting effects of pre-formed MBT and MBI layers on intergranular passivation: passivation is blocked on grains and at GBs; there is residual dissolution at the GBs leading to accumulation of corrosion products.

For MBT, among the fifty-two sites showing this behavior, forty-two (sites 49, 51, 55-57, 59-77, 81-84, 87-94, 96-99) correspond to random GBs, seven (sites 50, 52-54, 58, 78, 79) belong to high Σ CSL boundaries, two (sites 80, 100) to low Σ CSLs, and one (site 95) to CTs. It has to be noted that data from more sites could be extracted for the experiment with MBT, all of them showed this behavior and correspond to random boundaries. For MBI, twenty-two sites show this local behavior. Among them, fourteen (sites 79, 80, 83 and 85-95) are classified as random boundaries. Two sites (97 and 98) belong to Σ_3 CTs, also likely deviated from ideal geometry. Two sites (96 and 99) are attributed to low Σ CSLs and four sites (81, 82, 84 and 100) to high Σ CSLs.

5.3.4 MBT & MBI effects on local passivation properties according to GB type

Tables 5.2 and 5.3 summarize the occurrences of the observed effects of MBT and MBI, respectively, on the passivation properties of the grain boundaries. They are sorted according to GB type as defined in Table 5.1. Figure 5.13 presents an overall comparative view of the data. Both inhibitors were observed to either completely or incompletely block passivation with residual preferential reactivity from the intergranular region, depending on the local effect of the pre-formed MBT or MBI surface layers and on the GB type.

Table 5.2: Observed occurrences of intergranular behavior for various types of grain boundaries for microcrystalline copper in 0.1 M NaOH(aq) + 1 mM MBT.

Intergranular behavior	C.T.s	Low Σ C.S.L.s	High Σ C.S.L.s	Random G.B.s
Blocked passivation and absence of preferential reaction	4	--	--	--
Blocked passivation with residual dissolution	1	1	1	19
Incompletely blocked passivation with irreversible accumulation of passivation products	1	1	1	6
Incompletely blocked passivation with reversible accumulation of passivation products	1	2	1	10
Blocked passivation with residual dissolution and accumulation of corrosion products	1	2	7	42

Table 5.3: Observed occurrences of intergranular behavior for various types of grain boundaries for microcrystalline copper in 0.1 M NaOH(aq) + 1 mM MBI.

Intergranular behavior	C.T.s	Low Σ C.S.L.s	High Σ C.S.L.s	Random G.B.s
Blocked passivation and absence of preferential reaction	4	--	--	--
Blocked passivation with residual dissolution	3	--	8	8
Incompletely blocked passivation with irreversible accumulation of passivation products	1	2	11	15
Incompletely blocked passivation with reversible accumulation of passivation products	2	--	14	10
Blocked passivation with residual dissolution and accumulation of corrosion products	2	2	4	14

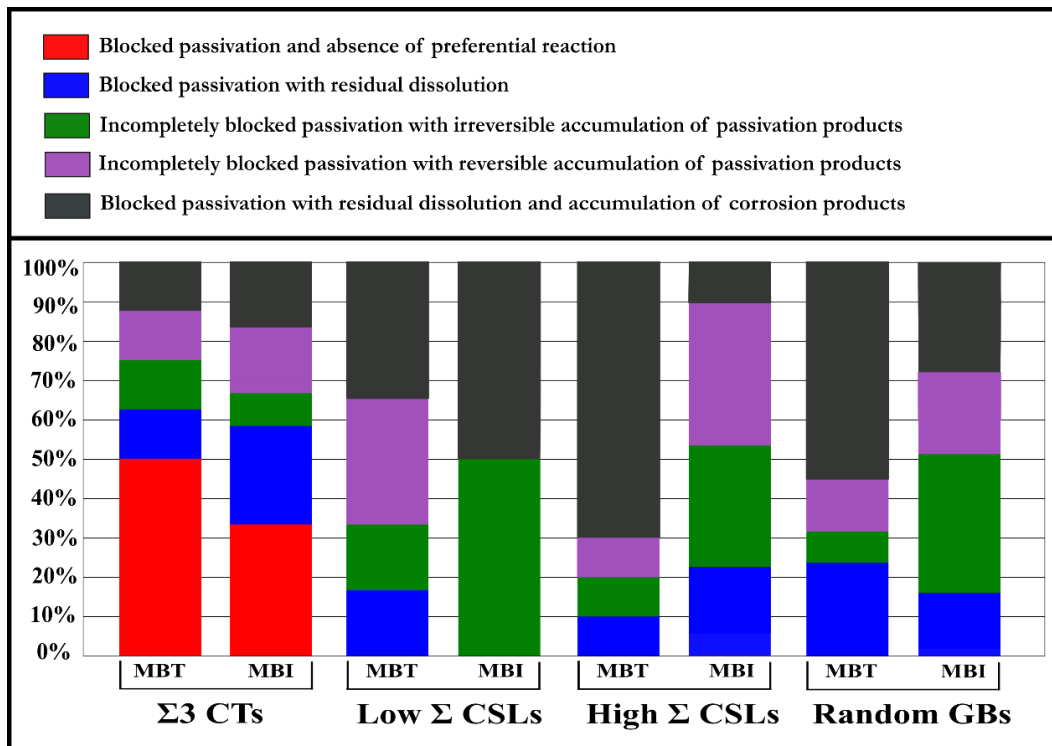


Figure 5.13: Percentage of each type of intergranular behavior observed on various types of grain boundaries for microcrystalline copper in 0.1 M NaOH(aq) + 1 mM MBI and in 0.1 M NaOH(aq) + 1 mM MBT.

Coherent twin is the only GB type for which passivation was blocked as on the adjacent grains and no residual intergranular activity was detected. With both inhibitors, this was observed for a majority, absolute or relative, of the analyzed sites, which we assign to CTs close to ideal geometry [62], and thus intrinsically resistant to intergranular corrosion. In the CT sites deviated from the ideal geometry and thus showing preferential reactivity compared to adjacent grains, all other types of intergranular behavior were observed with a rather uniform distribution of their occurrences. A larger proportion of reactive CT sites were observed with the pre-formed MBI layer than with the pre-formed MBT layer, but this may be due to the site distribution in the analyzed field of view and not to a lower inhibiting efficiency of MBI.

The intergranular behaviors observed for all other types of GBs, low Σ CSLs, high Σ CSLs and random GBs, in the presence of the inhibitors belong to two classes depending on the inhibitor effect on passivation. If intergranular passivation is blocked, residual reactivity is associated to dissolution with possible accumulation of corrosion products. This is color-coded in green and purple in Figure 5.13. Whereas, in the case of incompletely blocked, or poisoned, intergranular passivation, passivation products may also accumulate (reversibly or not) in the intergranular region. This is coded in blue and black in Figure 5.13.

Examining the data for random GBs in Figure 5.13 from this perspective, we can deduce a stronger blocking effect on intergranular passivation with MBT than with MBI. These boundaries can be expected to be the most reactive owing to their ill-defined crystallographic character. With MBI, the accumulation of passivation products, whether reversible or irreversible, for most of the random boundaries, is in agreement with previous studies showing that, due to higher reactivity of these GBs, a locally thicker film of Cu(I) oxide film is formed in the absence of inhibitor [59]–[61]. With MBT, intergranular passivation would be more strongly poisoned and the accumulation of passivation products less frequently occurring in the analyzed distribution.

For high Σ CSLs, Figure 5.13 also shows that MBT would more strongly poison passivation than MBI, thus confirming for these reactive boundaries the trend observed for random GBs. For low Σ CSLs, the distribution that could be analyzed in the field of view is smaller. However, Figure 5.13 shows that blocked passivation and incompletely blocked passivation are much more balanced for both inhibitors. In these GBs, the residual reactivity would be too low to differentiate the blocking effect on the passivation behavior, which is in line with the less reactive character of the low Σ CSLs that can be expected from their well-defined crystallographic character.

The stronger effect of MBT than MBI for blocking passivation at the intergranular sites is likely to be an effect of the barrier properties of the pre-formed inhibitor layer. As discussed above in Section 5.3.1 from the analysis of the macroscopic electrochemical data, more Cu atoms would be trapped in the pre-formed MBT than in the pre-formed MBI surface layer after reductive decomposition of the native oxide in the presence of the inhibitor. This increase in trapped Cu atoms could reflect an increase in thickness and/or a densification of the MBT surface layer compared to the MBI surface layer, which would improve the barrier properties for surface passivation, especially in the more reactive sites such as intergranular boundaries. This improved barrier properties could result from the presence in the heterocyclic structure of two S and one N atom in MBT versus one S and two N atoms in MBI, with S atoms being able to covalently bond more strongly to Cu atoms than N atoms.

5.4 Conclusions

ECSTM was applied to characterize the effects of MBT and MBI on the local passivation and corrosion properties at the surface termination of grain boundaries for copper in alkaline aqueous solution. The

macroscopic electrochemical response, characterized by CV, showed that, in the presence of 1 mM of inhibitor, both MBT and MBI block surface passivation on the grains. The observed residual activity was attributed to reversible anodic oxidation of copper atoms that were dissociated from the native oxide and trapped in the pre-formed inhibitor film and to irreversible loss of copper due to residual dissolution in the most reactive sites, including GBs.

In situ ECSTM analysis of the same GB sites in the initial Cu(o) metallic, Cu(I) oxidized and Cu(o) reduced surface states showed that Σ_3 coherent twins with close to ideal geometry did not react preferentially compared to the adjacent grains in agreement with previous reports. All the other types of GBs, including Σ_3 CTs deviated from ideal geometry, were preferential sites of reaction compared to grains. Depending on the barrier effect of the pre-formed inhibitor surface layer, intergranular passivation was found to be either completely blocked, however with residual local dissolution and accumulation of corrosion products in the GBs regions, or incompletely blocked, with residual local formation of passivation products, likely Cu(I) oxidation products.

For the less reactive GBs corresponding to low Σ CSLs, no difference of barrier effect of the pre-formed MBT and MBI organic layers for blocking passivation was observed. For the more reactive GBs corresponding to random boundaries and high Σ CSLs, the pre-formed MBT surface layer showed a stronger barrier effect for blocking passivation than the pre-formed MBI surface layer as shown by the higher occurrence of blocked intergranular behavior in the analyzed population of GB sites. It is proposed that MBT, being able to strongly bond to more Cu atoms than MBI thanks to two S atoms instead of one in its heterocyclic structure, would more efficiently trap Cu atoms from the surface, thus providing improved barrier properties to the pre-formed MBT surface layer, including in the most reactive surface sites such as GBs

Acknowledgments

This project has received funding from the European Research Council (ERC) under the European Union's Horizon 2020 research and innovation programme (ERC Advanced Grant agreement No 741123).

References

- [1] J. Mieluch and M. Smialowski, "The behaviour of grain boundaries in iron during anodic polarization in ammonium nitrate solution," *Corrosion Science*, vol. 4, no. 1, pp. 237–243, Jan. 1964, doi: 10.1016/0010-938X(64)90022-8.
- [2] P. Lin, G. Palumbo, U. Erb, and K. T. Aust, "Influence of grain boundary character distribution on sensitization and intergranular corrosion of alloy 600," *Scripta Metallurgica et Materialia*, vol. 33, no. 9, pp. 1387–1392, Nov. 1995, doi: 10.1016/0956-716X(95)00420-Z.
- [3] VINOGRADOV, A, MIMAKI, T, HASHIMOTO, S, and VALIEV, R, "On the corrosion behavior of ultra-fine grain copper," *Scripta materialia*, vol. 41, no. Num 3, pp. 319–326, 1999.
- [4] L. Lu, M. L. Sui, and K. Lu, "Superplastic Extensibility of Nanocrystalline Copper at Room Temperature | Science," *Science*, vol. 287, no. 5457, pp. 1463–1466, Feb. 2000.
- [5] V.Y. Gertsman and S.M. Gruemer, "Grain Boundary Character Along Intergranular Stress Corrosion Crack Paths in Austenitic Stainless Alloys Removed from High-Temperature Water," *Acta Materialia*, vol. 49, pp. 1589–1598, 2001.
- [6] S.H. Kim, U. Erb, and K.T. Aust, "Grain Boundary Character Distribution and Intergranular Corrosion Behavior in High Purity Aluminum," *Scripta Materialia*, vol. 44, pp. 835–839, 2001.
- [7] E. M. Lehockey, A. M. Brennenstuhl, and I. Thompson, "On the relationship between grain boundary connectivity, coincident site lattice boundaries, and intergranular stress corrosion cracking," *Corrosion Science*, vol. 10, no. 46, pp. 2383–2404, 2004, doi: 10.1016/j.corsci.2004.01.019.

- [8] H. Miyamoto, K. Yoshimura, T. Mimaki, and M. Yamashita, "Behavior of intergranular corrosion of $\langle 011 \rangle$ tilt grain boundaries of pure copper bicrystals," *Corrosion Science*, vol. 44, no. 8, pp. 1835–1846, Aug. 2002, doi: 10.1016/S0010-938X(01)00158-5.
- [9] M. Shimada, H. Kokawa, Z. J. Wang, Y. S. Sato, and I. Karibe, "Optimization of grain boundary character distribution for intergranular corrosion resistant 304 stainless steel by twin-induced grain boundary engineering," *Acta Materialia*, vol. 50, no. 9, pp. 2331–2341, May 2002, doi: 10.1016/S1359-6454(02)00064-2.
- [10] V. Randle, "'Special' Boundaries and Grain Boundary Plane Engineering," *Scr. Mater.*, vol. 54, pp. 1011–1015, 2006.
- [11] S. Xia, B. Zhou, and W. Chen, "Effect of single-step strain and annealing on grain boundary character distribution and intergranular corrosion in Alloy 690," *J Mater Sci*, vol. 43, no. 9, pp. 2990–3000, May 2008, doi: 10.1007/s10853-007-2164-y.
- [12] R. Jones and V. Randle, "Sensitisation behaviour of grain boundary engineered austenitic stainless steel," *Materials Science and Engineering*, vol. 527, no. A, pp. 4275–4280, 2010.
- [13] CL Changliang *et al.*, "Improving the intergranular corrosion resistance of 304 stainless steel by grain boundary network control," *Corros. Sci.*, vol. 53, pp. 1880–1886, 2011.
- [14] K. D. Ralston and N. Birbilis, "Effect of Grain Size on Corrosion: A Review," *CORROSION*, vol. 66, no. 7, pp. 075005–075005–13, Jul. 2010, doi: 10.5006/1.3462912.
- [15] C. Luo, X. Zhou, G. E. Thompson, and A. E. Hughes, "Observations of intergranular corrosion in AA2024-T351: The influence of grain stored energy," *Corrosion Science*, vol. 61, pp. 35–44, Aug. 2012, doi: 10.1016/j.corsci.2012.04.005.
- [16] S. K. B., B. S. Prasad, V. Kain, and J. Reddy, "Methods for making alloy 600 resistant to sensitization and intergranular corrosion," *Corrosion Science*, vol. 70, pp. 55–61, May 2013, doi: 10.1016/j.corsci.2012.12.021.
- [17] Y. Takehara, , H. Fujiwara, and H Miyamoto, "'Special' to 'general' transition of intergranular corrosion in Sigma 3{111} grain boundary with gradually changed misorientation," *Corros. Sci.*, vol. 77, pp. 171–175, 2013.
- [18] A. Stratulat, J.A. Duff, T.J. Marrow, and T. James, "Grain boundary structure and intergranular stress corrosion crack initiation in high temperature water of a thermally sensitised austenitic stainless steel, observed in situ," *Corros. Sci.*, vol. 85, pp. 428–435, 2014.
- [19] E. Martinez Lombardia, L. Lapeire, I. De Graeve, H. Terryn, and K. Verbeken, "Influence of grain size on the electrochemical behavior of pure copper," *J Mater Sci*, vol. 52, no. 3, pp. 1501–1510, Feb. 2017, doi: 10.1007/s10853-016-0445-z.
- [20] B. V. Mahesh and R. K. S. Raman, "Role of Nanostructure in Electrochemical Corrosion and High Temperature Oxidation: A Review," *Metall Mater Trans A*, vol. 45, no. 12, pp. 5799–5822, Nov. 2014, doi: 10.1007/s11661-014-2452-5.
- [21] N. Srinivasan, V. Kain, N. Birbilis, K. V. Mani Krishna, S. Shekhawat, and I. Samajdar, "Near boundary gradient zone and sensitization control in austenitic stainless steel," *Corrosion Science*, vol. 100, pp. 544–555, Nov. 2015, doi: 10.1016/j.corsci.2015.08.027.
- [22] A. Fateh, M. Aliofkhazraei, and A. R. Rezvanian, "Review of corrosive environments for copper and its corrosion inhibitors," *Arabian Journal of Chemistry*, vol. 13, no. 1, pp. 481–544, Jan. 2020, doi: 10.1016/j.arabjch.2017.05.021.
- [23] D. Chadwick and T. Hashemi, "Electron spectroscopy of corrosion inhibitors: Surface films formed by 2-mercaptobenzothiazole and 2-mercaptobenzimidazole on copper," *Surface Science*, vol. 89, no. 1, pp. 649–659, Jan. 1979, doi: 10.1016/0039-6028(79)90646-0.
- [24] M. Ohsawa and W. Suëtaka, "Spectro-electrochemical studies of the corrosion inhibition of copper by mercaptobenzothiazole," *Corrosion Science*, vol. 19, no. 10, pp. 709–722, Jan. 1979, doi: 10.1016/S0010-938X(79)80142-0.
- [25] J. C. Marconato, L. O. Bulhões, and M. L. Temperini, "A spectroelectrochemical study of the inhibition of the electrode process on copper by 2-mercaptobenzothiazole in ethanolic solutions," *Electrochimica Acta*, vol. 43, no. 7, pp. 771–780, Jan. 1998, doi: 10.1016/S0013-4686(97)00204-1.
- [26] R. Woods, G. A. Hope, and K. Watling, "A SERS spectroelectrochemical investigation of the interaction of 2-mercaptobenzothiazole with copper, silver and gold surfaces," *Journal of Applied Electrochemistry*, vol. 30, no. 11, pp. 1209–1222, Nov. 2000, doi: 10.1023/A:1026561914338.
- [27] C. W. Yan, H. C. Lin, and C. N. Cao, "Investigation of inhibition of 2-mercaptobenzoxazole for copper corrosion," *Electrochimica Acta*, vol. 45, no. 17, pp. 2815–2821, May 2000, doi: 10.1016/S0013-4686(00)00385-6.

- [28] M. M. Antonijević and M. B. Petrović, *Review Copper Corrosion Inhibitors. A review.* .
- [29] M. M. Antonijević, S. M. Milić, and M. B. Petrović, "Films formed on copper surface in chloride media in the presence of azoles," *Corrosion Science*, vol. 51, no. 6, pp. 1228–1237, Jun. 2009, doi: 10.1016/j.corsci.2009.03.026.
- [30] F. M. A. Kharafi, N. A. Al-Awadi, I. M. Ghayad, R. M. Abdullah, and M. R. Ibrahim, "Novel Technique for the Application of Azole Corrosion Inhibitors on Copper Surface," *Materials Transactions*, vol. 51, no. 9, pp. 1671–1676, 2010, doi: 10.2320/matertrans.M2010141.
- [31] G. Gece and Drugs, "A review of promising corrosion inhibitors," *Corrosion Science*, vol. 53, pp. 3873–3898, 2011.
- [32] L. P. Kazansky, I. A. Selyaninov, and Yu. I. Kuznetsov, "Adsorption of 2-mercaptobenzothiazole on copper surface from phosphate solutions," *Applied Surface Science*, vol. 258, no. 18, pp. 6807–6813, Jul. 2012, doi: 10.1016/j.apsusc.2012.03.097.
- [33] M. Finšgar and D. Kek Merl, "An electrochemical, long-term immersion, and XPS study of 2-mercaptobenzothiazole as a copper corrosion inhibitor in chloride solution," *Corrosion Science*, vol. 83, pp. 164–175, Jun. 2014, doi: 10.1016/j.corsci.2014.02.016.
- [34] N. Kovačević, I. Milošev, and A. Kokalj, "The roles of mercapto, benzene, and methyl groups in the corrosion inhibition of imidazoles on copper: II. Inhibitor-copper bonding," *Corrosion Science*, vol. 98, pp. 457–470, Sep. 2015, doi: 10.1016/j.corsci.2015.05.041.
- [35] M. Petrović Mihajlović and M. Antonijević, "Copper corrosion inhibitors. period 2008–2014. a review," *International journal of electrochemical science*, vol. 10, pp. 1027–1053, 2015.
- [36] Y.-H. Chen and A. Erbe, "The multiple roles of an organic corrosion inhibitor on copper investigated by a combination of electrochemistry-coupled optical in situ spectroscopies," *Corrosion Science*, vol. 145, pp. 232–238, Dec. 2018, doi: 10.1016/j.corsci.2018.09.018.
- [37] M. M. Antonijević, S. M. Milic, and M. B. Petrović, "Films formed on copper surface in chloride media in the presence of azoles," *Corrosion Science*, vol. 51, pp. 1228–1237, 2009.
- [38] T. Shahrabi, H. Tavakholi, and M. G. Hosseini, "Corrosion inhibition of copper in sulphuric acid by some nitrogen heterocyclic compounds," *Anti-Corrosion Methods and Materials*, vol. 54, no. 5, pp. 308–313, Jan. 2007, doi: 10.1108/00035590710822161.
- [39] P. M. Niamien, F. K. Essy, A. Trokourey, A. Yapi, H. K. Aka, and D. Diabate, "Correlation between the molecular structure and the inhibiting effect of some benzimidazole derivatives," *Materials Chemistry and Physics*, vol. 136, no. 1, pp. 59–65, Sep. 2012, doi: 10.1016/j.matchemphys.2012.06.025.
- [40] M. Finšgar, "2-Mercaptobenzimidazole as a copper corrosion inhibitor: Part I. Long-term immersion, 3D-profilometry, and electrochemistry," *Corrosion Science*, vol. 72, pp. 82–89, Jul. 2013, doi: 10.1016/j.corsci.2013.03.011.
- [41] G. Žerjav and I. Milošev, "Protection of copper against corrosion in simulated urban rain by the combined action of benzotriazole, 2-mercaptobenzimidazole and stearic acid," *Corrosion Science*, vol. 98, pp. 180–191, 2015, doi: 10.1016/j.corsci.2015.05.023.
- [42] T. Yoshida, "An X-Ray Photoelectron Spectroscopic Study of Several Metal Complexes of 2-Mercaptobenzimidazole and 2-Mercaptobenzoxazole," *BCSJ*, vol. 53, no. 5, pp. 1449–1450, May 1980, doi: 10.1246/bcsj.53.1449.
- [43] G. Xue, X.-Y. Huang, J. Dong, and J. Zhang, "The formation of an effective anti-corrosion film on copper surfaces from 2-mercaptobenzimidazole solution," *Journal of Electroanalytical Chemistry and Interfacial Electrochemistry*, vol. 310, no. 1, pp. 139–148, Jul. 1991, doi: 10.1016/0022-0728(91)85257-P.
- [44] G. Xue* and Q. Dai, "SERS and IR Studies of the Reaction of an Oxidized Surface and an Etched Surface of Copper with 2-Mercaptobenzimidazole," *Spectroscopy Letters*, vol. 27, no. 3, pp. 341–351, Mar. 1994, doi: 10.1080/00387019408000849.
- [45] G. Xue, X. Huang, and J. Ding, "Surface reaction of 2-mercaptobenzimidazole on metals and its application in adhesion promotion," *Journal of the Chemical Society Faraday Transactions*, vol. 87, no. 8, pp. 1229–1232, 1991.
- [46] F. X. Perrin and J. Pagetti, "Characterization and mechanism of direct film formation on a cu electrode through electro-oxidation of 2-mercaptobenzimidazole," *Corrosion Science*, vol. 40, no. 10, pp. 1647–1662, Oct. 1998, doi: 10.1016/S0010-938X(98)00060-2.
- [47] B. Trachli, M. Keddami, H. Takenouti, and A. Srhiri, "Protective effect of electropolymerized 2-mercaptobenzimidazole upon copper corrosion," 2002, doi: 10.1016/S0300-9440(01)00205-3.
- [48] J. Izquierdo, J. J. Santana, S. González, and R. M. Souto, "Scanning microelectrochemical characterization of the anti-corrosion performance of inhibitor films formed by 2-

- mercaptobenzimidazole on copper,” *Progress in Organic Coatings*, vol. 74, no. 3, pp. 526–533, Jul. 2012, doi: 10.1016/j.porgcoat.2012.01.019.
- [49] M. Finšgar, “2-Mercaptobenzimidazole as a copper corrosion inhibitor: Part II. Surface analysis using X-ray photoelectron spectroscopy,” *Corrosion Science*, vol. 72, pp. 90–98, Jul. 2013, doi: 10.1016/j.corsci.2013.03.010.
- [50] D.-Q. Zhang, L.-X. Gao, and G. Zhou, “Inhibition of copper corrosion in aerated hydrochloric acid solution by heterocyclic compounds containing a mercapto group,” *Corrosion Science - CORROSION SCI*, vol. 46, pp. 3031–3040, Dec. 2004, doi: 10.1016/j.corsci.2004.04.012.
- [51] Z. Zhang, Q. Wang, X. Wang, and L. Gao, “The influence of crystal faces on corrosion behavior of copper surface: First-principle and experiment study,” *Applied Surface Science*, vol. 396, pp. 746–753, Feb. 2017, doi: 10.1016/j.apsusc.2016.11.020.
- [52] X. Wu, F. Wiame, V. Maurice, and P. Marcus, “Adsorption and thermal stability of 2-mercaptobenzothiazole corrosion inhibitor on metallic and pre-oxidized Cu(111) model surfaces,” *Applied Surface Science*, vol. 508, p. 145132, Apr. 2020, doi: 10.1016/j.apsusc.2019.145132.
- [53] X. Wu, F. Wiame, V. Maurice, and P. Marcus, “2-Mercaptobenzothiazole corrosion inhibitor deposited at ultra-low pressure on model copper surfaces,” *Corrosion Science*, vol. 166, p. 108464, Apr. 2020, doi: 10.1016/j.corsci.2020.108464.
- [54] X. Wu, F. Wiame, V. Maurice, and P. Marcus, “Moiré Structure of the 2-Mercaptobenzothiazole Corrosion Inhibitor Adsorbed on a (111)-Oriented Copper Surface,” *J. Phys. Chem. C*, vol. 124, no. 29, pp. 15995–16001, Jul. 2020, doi: 10.1021/acs.jpcc.0c04083.
- [55] E. Vernack, D. Costa, P. Tingaut, and P. Marcus, “DFT studies of 2-mercaptobenzothiazole and 2-mercaptobenzimidazole as corrosion inhibitors for copper,” *Corrosion Science*, vol. 174, p. 108840, Sep. 2020, doi: 10.1016/j.corsci.2020.108840.
- [56] F. Chiter, D. Costa, V. Maurice, and P. Marcus, “DFT investigation of 2-mercaptobenzothiazole adsorption on model oxidized copper surfaces and relationship with corrosion inhibition,” *Applied Surface Science*, vol. 537, p. 147802, Jan. 2021, doi: 10.1016/j.apsusc.2020.147802.
- [57] X. Wu, F. Wiame, V. Maurice, and P. Marcus, “2-mercaptobenzimidazole films formed at ultra-low pressure on copper: adsorption, thermal stability and corrosion inhibition performance,” *Applied Surface Science*, vol. 527, p. 146814, 2020.
- [58] I. Milošev, N. Kovačević, J. Kovač, and A. Kokalj, “The roles of mercapto, benzene and methyl groups in the corrosion inhibition of imidazoles on copper: I. Experimental characterization,” *Corrosion Science*, vol. 98, pp. 107–118, Sep. 2015, doi: 10.1016/j.corsci.2015.05.006.
- [59] H. Chen *et al.*, “Grain boundary passivation studied by in situ scanning tunneling microscopy on microcrystalline copper,” *J Solid State Electrochem*, vol. 19, no. 12, pp. 3501–3509, Dec. 2015, doi: 10.1007/s10008-015-2787-x.
- [60] H. Chen *et al.*, “Local passivation of metals at grain boundaries: In situ scanning tunneling microscopy study on copper,” *Corrosion Science*, vol. 111, pp. 659–666, Oct. 2016, doi: 10.1016/j.corsci.2016.04.013.
- [61] M. Bettayeb, V. Maurice, L. H. Klein, L. Lapeire, K. Verbeken, and P. Marcus, “Combined in situ microstructural study of the relationships between local grain boundary structure and passivation on microcrystalline copper,” *Electrochimica Acta*, vol. 305, pp. 240–246, May 2019, doi: 10.1016/j.electacta.2019.03.054.
- [62] M. Bettayeb, V. MAURICE, L. H. Klein, L. Lapeire, K. Verbeken, and P. Marcus, “Nanoscale Intergranular Corrosion and Relation with Grain Boundary Character as Studied In Situ on Copper,” *Journal of The Electrochemical Society*, vol. 165, no. 11, pp. 835–841, 2018, doi: 10.1149/2.134181jes.
- [63] S. B. Sharma, V. Maurice, L. H. Klein, and P. Marcus, “Local Inhibition by 2-mercaptobenzothiazole of Early Stage Intergranular Corrosion of Copper,” *J. Electrochem. Soc.*, 2020, doi: 10.1149/1945-7111/abcc36.
- [64] S. B. Sharma, V. Maurice, L. H. Klein, and P. Marcus, “In situ scanning tunneling microscopy study of 2-mercaptobenzimidazole local inhibition effects on copper corrosion at grain boundary surface terminations,” *Electrochimica Acta (2021)*, *in press*.
- [65] E. Martinez-Lombardia *et al.*, “Scanning electrochemical microscopy to study the effect of crystallographic orientation on the electrochemical activity of pure copper,” *Electrochimica Acta*, vol. 116, pp. 89–96, Jan. 2014, doi: 10.1016/j.electacta.2013.11.048.

- [66] E. Martinez-Lombardia *et al.*, "In situ scanning tunneling microscopy study of the intergranular corrosion of copper," *Electrochemistry Communications*, vol. 41, pp. 1–4, Apr. 2014, doi: 10.1016/j.elecom.2014.01.007.
- [67] E. Martinez-Lombardia *et al.*, "In Situ Scanning Tunneling Microscopy Study of Grain-Dependent Corrosion on Microcrystalline Copper," *J. Phys. Chem. C*, vol. 118, no. 44, pp. 25421–25428, Nov. 2014, doi: 10.1021/jp507089f.
- [68] R. Lindström, V. Maurice, and L.H. Klein, *The Use of Electrochemical Scanning Tunnelling Microscopy (EC-STM) in Corrosion Analysis* | ScienceDirect. Woodhead Publishing, 2007.
- [69] Gwyddion – Free SPM (AFM, SNOM/NSOM, STM, MFM ...) data analysis software. .
- [70] H.-H. Strehblow and B. Titze, "The investigation of the passive behaviour of copper in weakly acid and alkaline solutions and the examination of the passive film by esca and ISS," *Electrochimica Acta*, vol. 25, no. 6, pp. 839–850, Jun. 1980, doi: 10.1016/0013-4686(80)90036-5.
- [71] U. Sander, H. H. Strehblow, and J. K. Dohrmann, "In situ photoacoustic spectroscopy of thin oxide layers on metal electrodes. Copper in alkaline solution," *J. Phys. Chem.*, vol. 85, no. 4, pp. 447–450, Feb. 1981, doi: 10.1021/j150604a025.
- [72] W. Kautek and J. G. G. Li, "XPS Studies of Anodic Surface Films on Copper Electrodes," *J. Electrochem. Soc.*, vol. 137, no. 9, p. 2672, Sep. 1990, doi: 10.1149/1.2087008.
- [73] B. Millet, "Etude électrochimique et photoélectrochimique de couches d'oxydes de cuivre semi-conductrices. Rôle d'un inhibiteur de corrosion du cuivre," l'université Paris VI, 1994.
- [74] Y. Feng, K.-S. Siow, W.-K. Teo, K.-L. Tan, and A.-K. Hsieh, "Corrosion Mechanisms and Products of Copper in Aqueous Solutions at Various pH Values," *CORROSION*, vol. 53, no. 5, pp. 389–398, May 1997, doi: 10.5006/1.3280482.
- [75] C. A. Melendres, G. A. Bowmaker, J. M. Leger, and B. Beden, "In-situ synchrotron far infrared spectroscopy of surface films on a copper electrode in aqueous solutions," *Journal of Electroanalytical Chemistry*, vol. 449, no. 1, pp. 215–218, Jun. 1998, doi: 10.1016/S0022-0728(97)00609-8.
- [76] M.R.G. De Chialvo, R.C. Salvarezza, and A. Arvia, "The mechanism of oxidation of copper in alkaline solutions," *J. Appl. Electrochem*, vol. 14, pp. 165–175, 1984.
- [77] S. T. Mayer and R. H. Muller, "An In Situ Raman Spectroscopy Study of the Anodic Oxidation of Copper in Alkaline Media," *J. Electrochem. Soc.*, vol. 139, no. 2, p. 426, Feb. 1992, doi: 10.1149/1.2069234.
- [78] H.Y.H. Chan, C.G. Takoudis, and M.J. Weaver, "Oxide film formation and oxygen adsorption on copper in aqueous media as probed by surface-enhanced Raman spectroscopy," *J. Phys. Chem. B*, vol. 103, pp. 357–365, 1999.
- [79] V. Maurice, H.-H. Strehblow, and P. Marcus, "In situ STM study of the initial stages of oxidation of Cu(III) in aqueous solution," *Surface Science*, vol. 458, no. 1, pp. 185–194, Jun. 2000, doi: 10.1016/S0039-6028(00)00442-8.
- [80] J. Kunze, V. Maurice, L. H. Klein, H.-H. Strehblow, and P. Marcus, "In Situ Scanning Tunneling Microscopy Study of the Anodic Oxidation of Cu(III) in 0.1 M NaOH," *J. Phys. Chem. B*, vol. 105, no. 19, pp. 4263–4269, May 2001, doi: 10.1021/jp004012i.
- [81] H.-H. Strehblow, V. Maurice, and P. Marcus, "Initial and later stages of anodic oxide formation on Cu, chemical aspects, structure and electronic properties," *Electrochimica Acta*, vol. 46, no. 24, pp. 3755–3766, Aug. 2001, doi: 10.1016/S0013-4686(01)00657-0.
- [82] J. Kunze, V. Maurice, L. H. Klein, H.-H. Strehblow, and P. Marcus, "In situ STM study of the anodic oxidation of Cu(001) in 0.1 M NaOH," *Journal of Electroanalytical Chemistry*, vol. 554–555, pp. 113–125, Sep. 2003, doi: 10.1016/S0022-0728(03)00115-3.
- [83] J. Kunze, V. Maurice, L. H. Klein, H.-H. Strehblow, and P. Marcus, "In situ STM study of the duplex passive films formed on Cu(III) and Cu(001) in 0.1 M NaOH," *Corrosion Science*, vol. 46, no. 1, pp. 245–264, Jan. 2004, doi: 10.1016/S0010-938X(03)00140-9.

Conclusions and perspectives

In this work, local inhibition effects of 2-mercaptobenzothiazole (MBT, $C_7H_5NS_2$) and 2-mercaptobenzimidazole (MBI, $C_7H_6N_2S$) on intergranular corrosion of copper were studied in situ at the surface termination of various types of grain boundaries. Electrochemical scanning tunneling microscopy was used to characterize microscopic effects at the nanometric scale, and combined with cyclic voltammetry applied in the same testing conditions to characterize macroscopic inhibiting effects. Both in the acidic and alkaline environments studied, the applied protocols included a pre-treatment of the copper surface allowing to electrochemically reduce the native oxide film and to study the inhibitor effects on active dissolution and on passivation starting from a surface in the metallic state.

MBT and MBI inhibition effects on early active dissolution of grain boundary network

MBT efficiently inhibits the macroscopic active dissolution of copper as shown by CV analysis performed in acidic HCl medium, where no stable copper oxide can be formed. A drastic decrease of the current density associated with Cu(I) anodic dissolution was observed in the presence of MBT in the electrolyte. The inhibition activity of MBT was also evidenced by a positive shift of the onset of anodic dissolution. From the analysis of the residual current, it can be concluded that the MBT surface layer, pre-formed before testing corrosion by active dissolution, efficiently blocks the dissolution of copper from the grains, but not completely from the preferential sites of reactivity such as grain boundary surface terminations, and thus that the GB network remains susceptible to early intergranular corrosion in the active state.

In situ ECSTM analysis showed that the efficiency of MBT on blocking the dissolution from the grain boundaries is a function of the type of grain boundaries. Based on their morphology in the surface plane, grain boundaries were classified into four broad categories: coherent twins, low Σ CSLs, high Σ CSLs and random boundaries. Analysis of the topographical evolution of the intergranular surface regions showed that coherent twins were not intergranular sites of preferential reactivity compared to adjacent grains. The resistance to preferential dissolution of such boundaries was attributed to their intrinsic property of resistance to intergranular corrosion and not to the protection provided by MBT. The low Σ CSLs were observed to be preferential sites of reactivity with respect to the adjacent grains, and it was found that such boundaries could be well protected by MBT against active dissolution. All analyzed high Σ CSLs and random GBs were observed to react preferentially to various degrees compared to grains, indicating a defective protection by the pre-formed MBT layer. Some of these GBs showed continuous dissolution while others could be protected by the accumulation of corrosion products. This accumulation, and the related protection, could be continuous, transient, or delayed after repeated cycling of the polarization in the Cu(I) anodic dissolution region. For high Σ CSLs, protection by local accumulation of corrosion products was found to be stable upon repeated cycling, whereas for random boundaries, this

protection effect of accumulated corrosion products was generally found to be transient. This is assigned to the intrinsically more reactive character of random GBs, less effectively combated by the local formation of reaction products in the intergranular sites incompletely protected by the pre-formed MBT surface layer.

MBI also efficiently blocks the active dissolution of copper on the grains in HCl solution as shown by CV analysis of the macroscopic electrochemical behavior after the cathodic reduction of native oxide. However, unlike with MBT, a passivation-like behavior was evidenced by a peak observed in the Cu(I) dissolution range in the presence of MBI. From the CV data, it is clear that the pre-treatment conditions in which the MBI layer is pre-formed on the surface is a key factor for the inhibition efficiency of the molecular layer. If the molecules are pre-adsorbed on the surface covered by the native oxide film and the surface is subsequently reduced, this results in higher residual activity with characteristic passivation-like behavior, which we assigned to the anodic formation of a protective film of Cu(I)-MBI reaction products on the surface. In contrast, if the MBI molecules are pre-adsorbed on the surface in the metallic state cathodically reduced prior to exposure to MBI, then this leads to the formation of a presumably more homogenous barrier molecular film, more efficiently blocking atomic transport across the interface and suppressing residual anodic and cathodic activity.

In situ ECSTM analysis was conducted in conditions of MBI pre-adsorption on the native oxide film subsequently reduced by cathodic pre-treatment for the sake of comparison with MBT pre-adsorbed in exactly the same conditions. Coherent twins showed no preferential intergranular corrosion compared to adjacent grains. Like with MBT, this is assigned to the intrinsically intergranular corrosion resistant character of coherent twins rather than to the inhibition effect of MBI. All other CSLs and random boundaries were found to be preferential sites of corrosion compared to adjacent grains. The presence of MBI did lead to the mitigation of the dissolution from the intergranular region, either due to the anodically formed Cu(I)-MBI surface layer or due to the preferential accumulation of the Cu(I) corrosion products in the grain boundary region. The preferential accumulation of the product was found to be either stable, transient or delayed in conditions where the anodic oxidation was forced by repeated application of anodic cycles. CSL grain boundaries other than coherent twins were found to be efficiently protected by the anodically formed Cu(I)-MBI surface layer. For random boundaries, this anodically formed surface layer was less protective and the local protection was due to preferential accumulation of corrosion products, which was assigned to the intrinsically more reactive character of the random boundaries.

Comparison of corrosion inhibition by MBI with MBT showed that MBT is a more efficient corrosion inhibitor than MBI in the same pre-adsorption and testing conditions. For MBI, the formation of a surface film of Cu(I) reaction products was generated on the grains and the preferential accumulation of reaction products was more frequently observed in the intergranular regions.

MBT and MBI inhibition effects on local passivation of grain boundary network

CV macroscopic analysis performed after the cathodic reduction of the native oxide showed that in basic NaOH solution, where stable copper oxides can be formed, the presence of MBT or MBI in the electrolyte blocked surface passivation on the grains in the range of Cu(I) oxidation. The observed residual activity was attributed to two processes: the reversible anodic oxidation of those copper atoms embedded in the pre-formed organic layer after dissociation from the native oxide, and the irreversible residual dissolution of copper from the most reactive sites of the surface including the GBs.

In situ ECSTM analysis of the local topography of the GB network was performed in the initial Cu(o) metallic range with the surface covered by the pre-formed organic layer, after polarizing the surface in the Cu(I) oxidation range and subsequently back in the Cu(o) metallic range. The analysis confirmed the intergranular behavior of coherent twins with close to ideal geometry, with no preferential reactivity compared to adjacent grains like in acid solution. Again this is assigned to the intergranular corrosion resistant character of the coherent twins and not to the effect of the pre-formed inhibitor layer. All the other types of GBs, including coherent twins deviated from ideal geometry, were sites of preferential reaction compared to adjacent grains. Depending on the barrier effect of the pre-formed inhibitor surface layer, intergranular passivation was either completely blocked, however with local residual dissolution and accumulation of corrosion products in the intergranular regions, or incompletely blocked, with residual local formation of passivation products, likely Cu(I) oxidation products.

For low Σ CSLs, which are comparatively less reactive than high Σ CSLs and random GBs, passivation was equally blocked with no difference of barrier effect between the pre-formed organic layers of MBT or MBI. For high Σ CSLs and random boundaries, the pre-formed MBT surface layer has a stronger barrier effect for blocking passivation than the pre-formed MBI surface layer, as characterized by higher occurrence of this intergranular behavior in the analyzed GBs sites. This might be an effect of the presence of two S atoms in the heterocyclic structure of MBT instead of one in MBI, allowing MBT to more efficiently capture Cu atoms upon release from the surface. This would provide the pre-formed MBT surface layer with improved barrier properties including in the most reactive surface sites such as GBs.

Although blocking passivation is a detrimental effect for corrosion protection, the results obtained in this work show that this is compensated by the formation of organic barrier films of MBT or MBI that also block the surface reactions of corrosion by anodic dissolution. Only the most reactive sites such as random GBs are defectively protected by the organic inhibitor films and remain susceptible to the initiation of intergranular corrosion, however less than in the absence of inhibitor.

Perspectives

Further work can be envisaged to complete and develop the present study:

- The composition and thickness of the inhibitor films of MBT and MBI could be analyzed with surface analytical techniques such as XPS and ToF-SIMS in relation with their conditions of formation, by exposing the copper substrate before or after removal of the native oxide film.
- The inhibition efficiency of MBT and MBI could also be studied in low pH and highly acidic electrolytes such as H_2SO_4 in absence of highly aggressive Cl^- ions in the medium.
- The same study could be performed in a neutral environment where the effects of MBT and MBI could be studied in saline conditions to better understand their efficiency in real-life conditions such as for copper in seawater.
- In 0.1 M NaOH, it would be interesting to explore the macroscopic electrochemical behavior when the pre-formed MBT and MBI are formed with copper in the metallic state rather than with the surface covered by native oxide.
- The inhibition efficiency of MBT and MBI for copper passivation in the Cu(II) oxidation range could also be studied.
- In situ ECSTM analysis of copper in similar experimental conditions could be performed with benzotriazole, which is another widely used inhibitor for the copper system. This would provide a comparative study of efficiency of the three corrosion inhibitors.
- Corrosion inhibition by MBT and MBI on different copper alloys such as Brass and Bronze would also be of interest.

Annexe : Résumé Étendu de Thèse

Etat de l'art

La corrosion intergranulaire est l'une des principales formes de corrosion localisée des matériaux métalliques polycristallins. Elle s'initie à la terminaison des joints de grains en surface du matériau, et peut se propager sous la surface jusqu'à mettre en péril toute la microstructure. Il est très important de mieux la comprendre pour mieux la contrôler. De nombreuses études ont conclu que la corrosion intergranulaire dépend de l'énergie et du type de joints de grains. Pour étudier la corrosion intergranulaire, il est donc important de bien comprendre quelques concepts sur les joints de grains.

Les joints de grains sont des interfaces qui sont formées entre deux réseaux de même structure cristalline et même composition, mais orientés différemment. En fonction de l'angle de désorientation, les joints de grains sont répertoriés comme d'angle faible ou d'angle élevé. Les joints de grains d'angle faible ont moins de 15° de désorientation. De nombreuses études ont montré que les joints de grains d'angle faible ne sont pas sensibles à la corrosion intergranulaire contrairement aux joints de grains de grand angle. Les joints de grains de grand angle, caractérisés par une désorientation supérieure à 15° , présentent des degrés variables de résistance à la corrosion intergranulaire. Les joints de grains qui ont une meilleure résistance sont dits « spéciaux » et peuvent être décrits par un réseau de sites de coïncidence (dénommé CSL en anglais). L'autre sous-catégorie de joints de grains de grand angle n'obéissant pas à une description de type CSL correspond aux joints de grains aléatoires, qui ne présentent pas de résistance particulière à la corrosion. Les joints de grains de type CSL peuvent avoir un comportement particulier du fait de leur plus faible énergie. Les joints de grains CSL sont désignés par un indice Σ qui est un nombre impair dans le réseau cubique. Pour un joint de grains CSL Σ_n , $1/n$ désigne la fraction de sites partagés à l'interface par les deux réseaux voisins. Il a été démontré que, pour les matériaux cubiques à faces centrées comme le cuivre, les joints de macles sont résistants à la corrosion intergranulaire lorsqu'ils sont cohérents. Les joints de macles cohérents sont des joints de grains de type CSL Σ_3 dont le plan est peu dévié de son orientation théorique (111). Les autres joints de grains CSL Σ_n ($n < 29$) ont des degrés variables de sensibilité à la corrosion intergranulaire. Tout joint de grains d'angle élevé avec Σ supérieur à 29 est répertorié comme joint aléatoire. L'angle de désorientation peut dévier de sa valeur cristallographique théorique et il y a donc des critères de déviation tolérée. Le critère de Brandon est le plus utilisé. Un autre critère plus restrictif est le critère Palumbo-Aust.

Ainsi, afin d'améliorer la durée de vie d'un matériau métallique polycristallin, une stratégie envisageable est d'augmenter, à l'intérieur du matériau, la proportion de joints de grains CSL Σ_n dits spéciaux car résistants à la corrosion intergranulaire. C'est l'objet principal de l'ingénierie des joints de grains. Les procédés métallurgiques alors mis en œuvre consistent en une alternance de traitements mécaniques et thermiques. Cependant, il existe des limites à l'ingénierie des joints de grains pour améliorer la résistance à la corrosion intergranulaire. Une autre méthode largement utilisée pour mitiger la corrosion consiste à utiliser des inhibiteurs de corrosion.

Cette thèse a pour objectif d'étudier l'effet de deux inhibiteurs largement utilisés pour ralentir la corrosion du cuivre, le 2-mercaptobenzothiazole et le 2-mercaptobenzimidazole, sur les premiers stades de corrosion intergranulaire et sur la passivation du cuivre en surface, à la terminaison des joints de

grains. Avant de discuter des effets de ces inhibiteurs, il est important de préciser le comportement à la corrosion du cuivre.

Le cuivre est un des métaux largement utilisé comme métal ou alliage métallique en raison de ses propriétés chimiques et électriques. À faible pH, le cuivre existe sous sa forme active au contact de l'eau et se corrode car aucun oxyde de cuivre stable ne peut se former dans des conditions acides et lui permettre de s'auto-protéger contre la corrosion par passivation. Pour un pH supérieur à 5,5, des oxydes de cuivre stables peuvent se former et le cuivre être sous forme «passive» dans laquelle sa surface est recouverte d'un film passif constitué d'oxyde protecteur contre la corrosion. Le cuivre forme deux oxydes : l'oxyde Cu_2O (cuprite) à l'état oxydé Cu(I) et l'oxyde CuO (ténorite) à l'état oxydé Cu(II). L'oxyde Cu(II) n'est formé qu'à des potentiels positifs plus élevés. La formation de CuO n'est possible que lorsque la surface est recouverte de couches suffisamment épaisses de Cu_2O . Dans le domaine passif Cu(I), le substrat métallique est couvert par 1 à 2 nm d'oxyde Cu_2O . Dans le domaine passif Cu(II), la surface du métal est recouverte par 1 nm de Cu_2O et 2 à 4 nm de CuO et $\text{Cu}(\text{OH})_2$ (hydroxyde cuivreux). Les diagrammes potentiel-pH, introduits par Pourbaix, sont un moyen pour prévoir les différents états dans lesquels le cuivre peut exister au contact de l'eau ainsi que les domaines de potentiel et de pH dans lesquels ces états peuvent exister. En présence d'ions Cl^- , qui sont des espèces agressives, il se forme une autre couche au-dessus de l'oxyde Cu(II) qui est soit de l'atacamite $[\text{Cu}_2(\text{OH})_3\text{Cl}]$ soit de la malachite $[\text{CuCO}_3, \text{Cu}(\text{OH})_2]$. La stabilité de cet oxyde dans les milieux chlorés dépend principalement du pH et de la quantité d'oxygène dissous. Quel que soit l'oxyde, la corrosion localisée du cuivre au contact des ions chlorures est inévitable.

Outre l'électrolyte ou l'environnement, la microstructure du matériau joue également un rôle prépondérant sur sa corrosion. Il a été démontré que la taille des grains a un impact sur la corrosion du cuivre polycristallin. La cinétique de corrosion du cuivre à grains ultra fins est plus lente que celle du cuivre à gros grains. De plus, il a été observé que plus la taille moyenne du grain était petite, plus son potentiel de corrosion était négatif. Les grains de plus petite taille se corrodent plus uniformément que les grains plus gros. Non seulement la taille, mais également la structure des grains influence la corrosion du cuivre. Il a été observé que la formation de couches d'oxyde de cuivre dépend de l'orientation cristallographique des grains. Les joints de grains, comme déjà discuté, ont également un impact sur la corrosion du cuivre. Il existe donc des besoins en inhibiteurs de corrosion pour protéger le cuivre de la corrosion dans divers environnements.

Les inhibiteurs de corrosion sont des molécules qui diminuent la vitesse de corrosion des métaux et alliages. Les inhibiteurs de corrosion sont classés suivant leur nature chimique (molécules organiques ou inorganiques), ou suivant leur mode d'action (anodique, cathodique ou mixte). Les inhibiteurs anodiques augmentent la valeur du potentiel de corrosion dans le milieu alors, qu'en revanche, les inhibiteurs cathodiques diminuent la vitesse de réaction cathodique et donc le potentiel de corrosion. Les inhibiteurs de corrosion mixtes ont une action à la fois sur l'activité anodique et cathodique du matériau. Les inhibiteurs inorganiques sont des molécules inorganiques pouvant être des inhibiteurs non passivant ou passivant. Les inhibiteurs organiques, comme leur nom l'indique, sont des molécules fabriquées à partir d'hydrocarbures, qui peuvent avoir une structure cyclique benzénique ainsi que des groupes fonctionnels qui leur permettent de fortement s'adsorber sur la surface. Certains ont également des hétéroatomes qui interagissent avec le métal pour former les liaisons σ . L'adsorption de ces molécules en surface conduit à la formation d'une barrière physique qui protège le métal du milieu agressif. De nombreux inhibiteurs organiques ont également un groupe fonctionnel terminal qui rend la surface hydrophobe.

Le 2-mercaptobenzothiazole (MBT, $C_7H_5NS_2$) est un inhibiteur organique largement utilisé en particulier pour le cuivre et ses alliages. Il peut exister sous sa forme thiol ou thione. Il appartient à la catégorie des inhibiteurs mixtes car il inhibe les réactions anodiques et cathodiques. Le MBT protégerait le cuivre par la formation de complexes Cu^+ -MBT. Il est un inhibiteur efficace pour le cuivre dans les milieux acides, neutres et alcalins. Des études théoriques par fonctionnelle de densité (DFT) de l'adsorption de MBT sur une surface de $Cu(111)$ recouverte d'un film ultramince de $Cu_2O(111)$ ont montré que la forme thione et le thiolate interagissent fortement avec la surface et peuvent se substituer à H_2O ou des groupes OH à la surface.

Le 2-mercaptobenzimidazole (MBI, $C_7H_6N_2S$) a une structure moléculaire similaire à celle du MBT mais avec un S et 2 N au lieu de 2 S et 1 N dans la structure hétérocyclique. Il existe également sous deux formes tautomères. C'est également un inhibiteur de corrosion de type mixte qui s'adsorbe fortement via ses hétéroatomes S et N pour former un film organique barrière qui protège la surface. Il a été montré que l'adsorption isolée de MBI est plus exothermique que celle de MBT. De plus, le film moléculaire de MBI est plus fortement lié à la surface.

Techniques expérimentales, instrumentation et protocoles

Le comportement électrochimique global du cuivre en présence de MBT et MBI en solution a été étudié par voltamétrie cyclique dans une cellule électrochimique classique avec une électrode au calomel saturé et reproduit dans une cellule spécialement adaptée pour les mesures de microscopie à effet tunnel in situ. Les effets des inhibiteurs de corrosion ont été étudiés en milieu acide dans une solution $HCl(aq)$ de concentration 10 mM et en milieu basique dans une solution $NaOH(aq)$ de concentration 0,1 mM. Les solutions étaient préparées à partir d'eau-ultra-pure Millipore. En milieu $HCl(aq)$ 10 mM, la poudre MBI a pu être dissoute à la concentration de 1 mM par agitation mécanique après quatre jours de préparation. En revanche, la poudre de MBT n'a pu être dissoute après quatre jours de préparation qu'à une concentration de 0,1 mM en raison de sa plus faible solubilité. En milieu $NaOH(aq)$ 0,1 mM, MBT et MBI ont été plus facilement dissout à la concentration de 1 mM.

Le comportement local du cuivre à l'émergence des joints de grains en surface a été étudié en solution par microscopie à effet tunnel in situ sous contrôle électrochimique (ECSTM). Nous avons utilisé une cellule spécialement conçue et fabriquée en Kel-F. La cellule possède une électrode de travail qui est notre échantillon, et une contre-électrode et une pseudo électrode de référence qui sont constituées par des fils de platine. Le potentiel de l'électrode de référence est calibré par rapport à celui de l'électrode à hydrogène standard. En fonctionnement ECSTM, la pointe sonde du microscope constitue une quatrième électrode dont le potentiel par rapport à la référence est contrôlé simultanément avec celui de l'électrode de travail par un bipotentiostat. Cette pointe est taillée par électroérosion à partir d'un fil de tungstène et recouverte d'un matériau isolant (cire Apiezon) afin de minimiser le courant faradique et optimiser la mesure du courant tunnel. L'étanchéité entre échantillon et cellule est assurée par un joint torique VITON délimitant une surface de travail de 0,16 cm^2 . La capacité de la cellule est d'environ 360 μL . La cellule avec ses électrodes en platine préinstallées est nettoyée en suivant un protocole strict par ébullition d'abord dans HNO_3 concentré, puis dans un mélange « piranha » de H_2SO_4 et H_2O_2 à 30% dans un rapport 2: 1 en volume. Elle est rincée cinq fois par ébullition dans l'eau Millipore pour éliminer l'acide résiduel. Le joint torique en VITON est également nettoyé dans le mélange « piranha » porté à ébullition, puis rincé.

La microscopie à effet tunnel est une technique d'analyse de surface maintenant largement utilisée sous ultra-haut vide pour caractériser localement à haute résolution, jusqu'à l'échelle atomique, les surfaces

conductrices et semi-conductrices. Elle a été développée dans les laboratoires IBM de Zurich par G. Binnig et H. Rohrer qui ont reçu un prix Nobel en 1986. Ce microscope utilise une sonde locale qui est une pointe très fine, terminée par une protubérance de dimension atomique, qui scanne la surface. Cette sonde est maintenue à une distance de quelques angströms de la surface étudiée par un tube piézoélectrique. Le microscope fonctionne sur le principe de l'effet tunnel quantique et peut être opéré selon deux modes : en mode courant constant pour mesurer les variations locales de topographie ou en mode hauteur constante pour mesurer les variations locales de courant tunnel. Le courant tunnel mesuré entre la surface et la sonde, polarisées à l'aide d'un potentiostat, décroît exponentiellement avec la distance entre sonde et surface. La théorie du courant tunnel est basée sur la présence d'une barrière de potentiel entre sonde et surface. Théoriquement, la pointe STM est considérée comme une fonction d'onde sphérique. Lorsque la différence de potentiel appliquée est inférieure au travail de sortie des électrodes et que la distance entre sonde et surface est suffisamment proche, un courant tunnel circule. La direction du courant tunnel qui circule est fixée par le signe de la polarisation appliquée. La microscopie à effet tunnel électrochimique in situ est une extension où la sonde est le quatrième composant de la cellule électrochimique. Ce microscope peut imager la surface, en principe jusqu'à une résolution atomique, tout en contrôlant le potentiel électrochimique appliqué à la surface, ce qui permet d'effectuer des mesures in situ des altérations de topographie et de structure engendrées par des réactions électrochimiques. Un microscope Agilent PicoSPM et un bipotentiostat PicoStat contrôlés par le logiciel PicoScan 5.3.3 ont été utilisés pour cette thèse. Le scanner piézoélectrique était un scanner Keysight avec un champ de vision maximal de 30 μm x 30 μm .

Les échantillons de cuivre microcristallin utilisés ont été préparés préalablement à cette thèse à l'Université de Gand, Belgique par laminage cryogénique de cuivre de haute pureté (ETP-Cu). Le recuit de recristallisation était limité à 1 min à 200 °C afin de conserver une taille de grain compatible avec le champ de vision local du microscope STM. Des analyses par diffraction des électrons rétrodiffusés (EBSD) ont montré une granulométrie moyenne de 1,4 μm avec une dispersion très large allant de 0,1 à 37 μm . La texture est aléatoire avec absence d'orientation cristallographique préférentielle. Typiquement, le réseau de joints de grains se caractérisait par une proportion d'environ 66% de joints de grains de type CSL Σ_3 et la majeure partie des 34% restants de joints de grains de type aléatoire. La taille de grain relativement faible augmente la probabilité d'isoler différents types de joints de grains dans le champ de vision local du STM.

L'analyse de surface par ECSTM nécessite des surfaces très planes et des pointes très fines. La surface de l'échantillon a été préparée par polissage mécanique à l'aide d'une solution diamantée. Quatre étapes de polissage ont été utilisées allant de 6 μm jusqu'à 0,25 μm . Le polissage mécanique moyen dure 150 minutes. L'échantillon est ensuite rincé avec de l'acétone, de l'éthanol puis de l'eau Millipore. La préparation de surface est suivie d'un polissage électrochimique réalisé dans de l'acide orthophosphorique à 66% pendant 15 secondes à 3 V par rapport à une plaque de cuivre utilisée comme cathode. L'échantillon est ensuite rincé avec de l'acide orthophosphorique à 10% puis dans l'eau Millipore. L'étape d'électropolissage permet d'éliminer la couche écrouie laissée en surface par le polissage mécanique et ainsi d'exposer directement le réseau de joints de grains à l'électrolyte.

La dernière étape de préparation des échantillons avant étude par voltamétrie cyclique et par ECSTM est la réduction cathodique de l'oxyde natif couvrant la surface. Ce prétraitement est réalisé par cyclage de la polarisation dans le domaine de potentiel où le cuivre reste à l'état métallique. En partant du potentiel de circuit ouvert, le potentiel est balayé d'abord cathodiquement jusqu'au seuil de dégagement d'hydrogène puis en retour jusqu'à une borne anodique inférieure au potentiel de circuit ouvert et où le cuivre reste à l'état métallique et inerte. Le traitement est répété deux fois. Ces trois cycles de

prétraitement permettent de dissocier complètement l'oxyde natif, y compris en présence des inhibiteurs en solution.

La pointe sonde STM est obtenue à partir d'un fil rectiligne de tungstène de 0,5 mm de diamètre taillé électrochimiquement dans NaOH 3 M en deux étapes, la première pour amincir le fil et la seconde pour le sectionner. La pointe est ensuite recouverte de cire Apiezon sauf à sa doute dernière extrémité de manière à minimiser le courant faradique généré par immersion dans l'électrolyte et optimiser la mesure du courant tunnel nécessaire à l'analyse ECSTM.

Inhibition locale par le 2-mercaptobenzothiazole de l'initiation de la corrosion intergranulaire du cuivre

Dans cette partie, l'effet local du 2-mercaptobenzothiazole (MBT) sur l'initiation de la corrosion intergranulaire du cuivre a été étudié en milieu HCl(aq) 10 mM. Dans ce milieu acide (pH de 2), les oxydes de cuivre sont instables et ne permettent pas à la surface de s'auto-protéger par passivation.

La figure 1 caractérise le comportement électrochimique étudié par voltamétrie cyclique dans la cellule ECSTM. Les voltammogrammes obtenus avec et sans inhibiteur permettent de discuter les effets de MBT sur l'activité électrochimique globale de la surface. Lorsqu'une activité anodique substantielle est enregistrée dans le domaine de formation des ions cuivreux Cu(I), comme observé en l'absence d'inhibiteur, la réponse peut être attribuée essentiellement à la réactivité des grains qui se corrodent par dissolution active du cuivre à l'état Cu(I). En effet, la fraction surfacique associée au réseau de joints de grains est petite par rapport à celle associée aux grains comme le confirme les images ECSTM de la microstructure. En présence de MBT, seule une activité résiduelle est enregistrée dans le domaine d'oxydation Cu(I), jusqu'à la borne anodique de -0.18 V/EHS (figure 1 (a)). Elle traduit la réactivité résiduelle, également par dissolution active du cuivre à l'état Cu(I), attribuable aux sites préférentiels de réaction tels que les joints de grains. Sans inhibiteur de la dissolution anodique, l'analyse des densités de charge transférées montre qu'une épaisseur équivalente de 19,7 nm de cuivre réagit lors de la polarisation anodique dans les conditions testées, soit l'équivalent de 95 monocouches de cuivre. En présence de MBT, le voltammogramme est quasiment plat jusqu'à la borne anodique car la dissolution du cuivre est fortement inhibée par la couche de MBT préformée en surface. Seule une épaisseur équivalente de 0,03 nm (0,13 monocouche) de cuivre réagit lors de la polarisation anodique, contrairement aux 19,7 nm (95 monocouches) mesurés en l'absence de MBT. En présence de MBT, le seuil de dissolution anodique est déplacé positivement de 0,15-0,20 V (figure 1 (b)), montrant qu'une force motrice plus élevée est requise pour dissoudre le Cu(I) à travers le film barrière de MBT préformé en surface. Le prétraitement de réduction de la couche d'oxyde natif étant réalisé en présence d'une couche de MBT pré-adsorbé sur la surface, il est probable que le film barrière de MBT préformé avant le test de corrosion inclut des atomes de cuivre dissociés de l'oxygène lors du prétraitement cathodique.

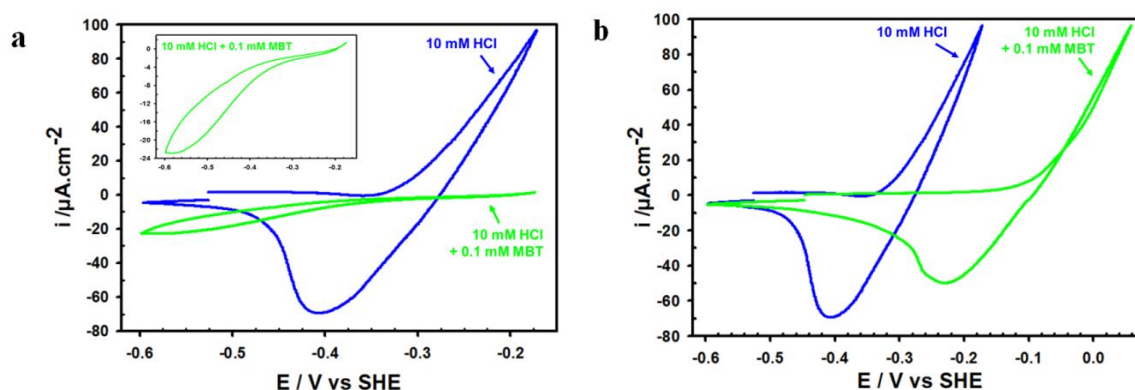


Figure 1 Voltammogrammes obtenus dans la cellule ECTM et caractérisant l'effet inhibiteur de MBT sur le comportement en corrosion du cuivre en milieu HCl (aq) : (a) CVs enregistrés sans et avec MBT. L'encart montre un CV agrandi obtenu en présence de MBT. (b) CVs enregistrés sans et avec MBT.

L'analyse par ECSTM de la surface en présence de MBT dans l'électrolyte a été réalisée avant et après application de 2 et 4 cycles électrochimiques pour initier la corrosion du cuivre dans le domaine anodique de formation des ions cuivreux Cu(I). Les cycles sont identiques à ceux réalisés pour l'étude par voltamétrie cyclique et permettent de contrôler les altérations topographiques induites par l'initiation de la corrosion. La microstructure observée localement est présentée figure 2. Les joints de grains émergeant en extrême surface ont été répertoriés suivant leur morphologie dans le plan de la surface. Les joints rectilignes qui forment des paires parallèles, séparant un sous-grain, sont répertoriés comme des joints de grains CSL Σ_3 de type joint de macles. Les joints rectilignes mais non appariés sont répertoriés comme des joints de grains CSL de bas indice Σ . Les joints présentant une morphologie localement rectiligne sont répertoriés comme des joints de grains CSL de haut indice Σ . Enfin, les joints courbés ou présentant une morphologie localement courbe sont répertoriés comme des joints de grains aléatoires.

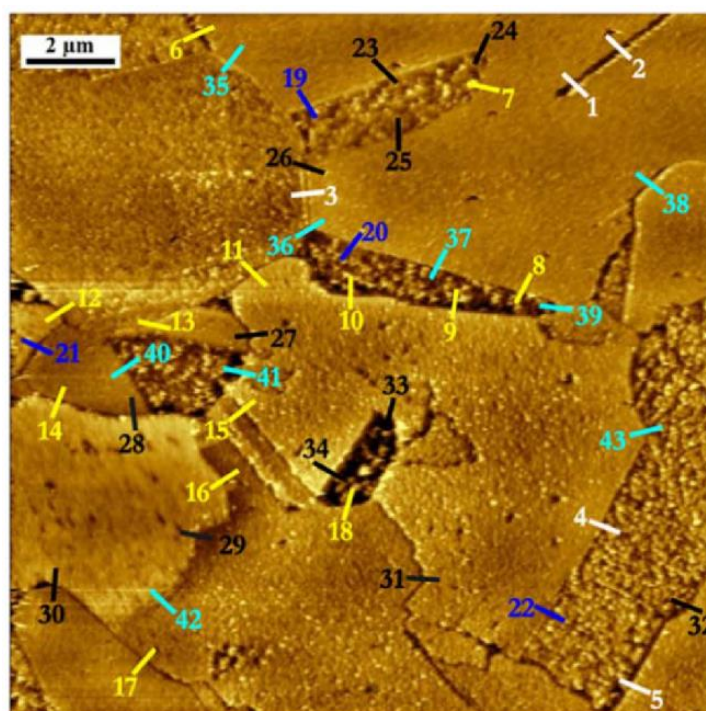


Figure 2 Identification locale du comportement en corrosion intergranulaire des joints de grains du cuivre microcristallin dans HCl(aq) 10 mM + MBT 0,1 mM. Les sites indexés correspondent aux joints de grains émergents en surface et dont la profondeur a été mesurée avant et après application de cycles électrochimiques permettant d'initier la corrosion.

L'analyse topographique de l'émergence en surface des joints de grains a permis de mesurer localement les variations de profondeur d'un même site intergranulaire induites par les cycles électrochimiques. Cinq comportements distincts ont été observés. Après application de 2 et 4 CVs pour initier la corrosion du cuivre, ces comportements se caractérisent par : i) une absence de variation de la profondeur du site intergranulaire (sites indexés en blanc sur la figure 2), ii) une augmentation répétée de la profondeur du site intergranulaire (sites indexés en jaune sur la figure 2), iii) une diminution répétée de la profondeur du site intergranulaire (sites indexés en bleu sur la figure 2), iv) une diminution suivie par une augmentation de la profondeur du site intergranulaire (sites indexés en noir sur la figure 2), et v) une augmentation suivie d'une diminution de la profondeur du site intergranulaire (sites indexés en cyan sur la figure 2). Tous les sites à partir desquels des données topographiques locales ont pu être extraites après 0, 2 et 4 CVs sont indexés sur la figure 2 selon un code de couleur associé au comportement observé.

Le comportement caractérisé par l'absence de variation de profondeur du site intergranulaire peut s'interpréter par la résistance intrinsèque du joint de grain à la corrosion intergranulaire ou par la formation d'une couche organique inhibant uniformément la surface. Pour les joints de macles, ce comportement peut être attribué à la résistance intrinsèque du joint à la corrosion intergranulaire. En effet, contrairement à d'autres types de joints de grains, les joints de macles ne sont pas des sites préférentiels de réaction en l'absence d'inhibiteur. L'absence d'initiation de la corrosion localisée n'est donc pas un effet de l'inhibiteur pour ce type de joints de grains. Cependant, pour d'autres types de joints de grains, l'absence de variation de la profondeur mesurée peut être due à une protection identique apportée par l'inhibiteur aux joints de grains et aux grains adjacents.

Le comportement caractérisé par une augmentation répétée de la profondeur du site intergranulaire est attribué à la consommation locale et irréversible du matériau par dissolution, plus rapide au joint de grains que sur les grains adjacents. Dans ce cas, la couche de MBT préformée en surface ne parvient pas à protéger les joints les plus réactifs lorsque la polarisation anodique est cyclée dans le domaine de dissolution active du cuivre.

Le comportement caractérisé par la diminution répétée de la profondeur du site intergranulaire est attribué à une accumulation préférentielle de produits de corrosion conduisant à une diminution de la profondeur mesurée. Dans ce cas, l'accumulation de produits de corrosion est reproduite lorsque la dissolution est forcée par répétition de la polarisation anodique dans le domaine Cu(I). Cette accumulation de produits de corrosion peut être transitoire ou retardée suivant le nombre de cycles de polarisation anodique appliqués, conduisant aux deux autres comportements observés. Dans le cas d'une accumulation transitoire, après 2 cycles, les produits accumulés dans le site intergranulaire conduisent à une diminution de sa profondeur. Cependant, cet effet est transitoire car lors des cycles suivants le film formé par ces produits est altéré et il y a une dissolution préférentielle qui augmente la profondeur du site intergranulaire. Dans le cas d'une accumulation retardée, observée après 4 cycles, il y a tout d'abord dissolution préférentielle conduisant à une augmentation de la profondeur du site intergranulaire. Puis, après répétition du cyclage anodique, il y a formation et accumulation locale de produits de corrosion conduisant à la diminution de profondeur du site intergranulaire.

L'analyse des comportements intergranulaires observés en fonction du type de joint de grains montre que, sur 43 sites analysés, ceux appartenant à des joints de macles présentent une absence de réactivité préférentielle attribuable à leur résistance intrinsèque à la corrosion intergranulaire, et non à un effet de l'inhibiteur. Le seul joint de grains CSL d'indice Σ bas identifié a montré une absence de réactivité préférentielle dans ce cas attribuable à une protection homogène par la couche MBT préformée. Les joints de grains CSL d'indice Σ élevé ont présenté les cinq types de comportement local décrits ci-dessus,

montrant une variabilité de l'effet inhibiteur de MBT pour ce type de site intergranulaire. Tous les joints de grains aléatoires ont présenté une réactivité préférentielle par rapport aux grains adjacents, avec cependant une accumulation de produits de corrosion dans la majorité des cas. L'absence de protection parfaite des joints de grains aléatoires par la couche MBT préformée est en accord avec la réactivité plus élevée de ce type de joints de grains. La réactivité observée traduit une variabilité de l'effet inhibiteur de MBT sur l'initiation de la corrosion intergranulaire des joints de grains aléatoires comme des joints de grains CSL d'indice Σ élevé. L'accumulation locale de produits de corrosion dans le site intergranulaire peut conduire à une protection contre la dissolution qui peut être stable, transitoire ou retardée selon le cyclage dans le domaine anodique Cu(I).

Inhibition locale de la corrosion intergranulaire du cuivre par le 2-mercaptobenzimidazole

Cette partie traite des effets d'inhibition du 2-mercaptobenzimidazole (MBI) sur l'initiation de la corrosion intergranulaire du cuivre. Le cuivre microcristallin est analysé à l'échelle macroscopique par voltamétrie cyclique et à l'échelle nanométrique par ECSTM in situ en milieu avec HCl(aq) 10 mM contenant 1 mM de MBI. L'instrumentation utilisée, la préparation de surface, et les protocoles expérimentaux sont identiques à ceux utilisés pour l'étude avec MBT afin de permettre la comparaison entre les deux inhibiteurs.

La figure 3 (a) montre les voltammogrammes caractérisant le comportement électrochimique du cuivre en l'absence et en présence de MBI dans l'électrolyte. Ceux obtenus en présence de MBI sont représentés agrandis sur la figure 3b. En l'absence d'inhibiteur, le cuivre subit une corrosion importante par dissolution active lorsqu'il est polarisé dans le domaine de formation des ions cuivreux Cu(I). Une épaisseur équivalente de 19,7 nm de cuivre réagit anodiquement dans les conditions testées. En présence de MBI, la dissolution active est très fortement inhibée et la figure 3 (b) montre que l'activité résiduelle dépend de la présence ou de l'absence de MBI lors du prétraitement de réduction de l'oxyde natif. L'activité électrochimique résiduelle du cuivre est plus élevée dans le cas du prétraitement réalisé en présence de MBI.

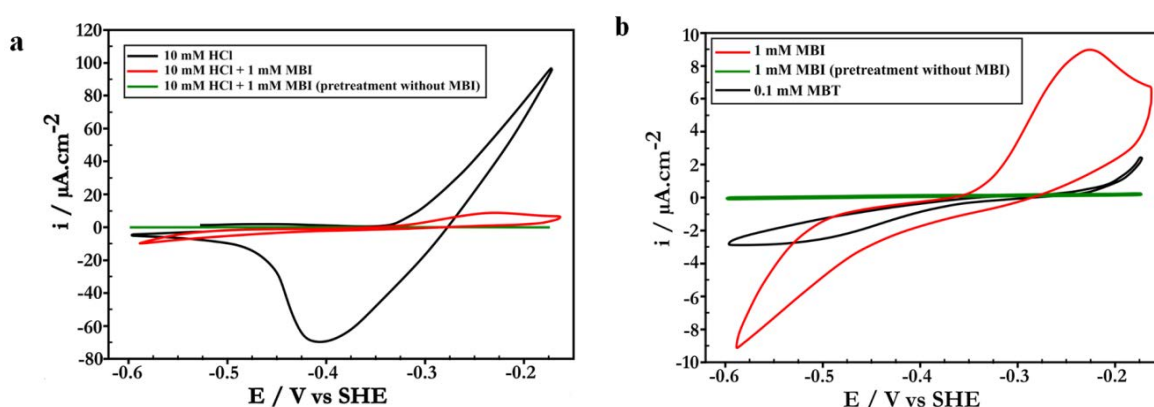


Figure 3 Voltammogrammes obtenus dans la cellule ECTM caractérisant l'effet inhibiteur de MBI sur le comportement en corrosion du cuivre en milieu HCl(aq) : (a) CVs enregistés sans et avec MBI dans la solution. (b) CVs élargis obtenus en présence de MBI après un prétraitement cathodique avec et sans MBI dans la solution. En (b), le CV obtenu dans HCl(aq) 10 mM + MBT 0,1 M est présenté à titre de comparaison.

Dans ce cas, l'inhibiteur présent dans l'électrolyte s'adsorbe sur le cuivre initialement couvert par le film d'oxyde natif et le processus de réduction se produit donc en présence d'une couche organique moléculaire de MBI. De ce fait, les atomes de Cu, libres et instables en surface après dissociation de

l'oxygène par électro-réduction, peuvent être capturés par la couche moléculaire pré-adsorbée. Il en résulte la formation d'un film barrière moins efficace pour bloquer le transport atomique à travers l'interface. Dans le domaine Cu(I), la réaction anodique initiée par l'augmentation du potentiel diminue en intensité pour former un pic dans un processus similaire à un processus de passivation. Les charges transférées lors du balayage anodique indiquent qu'une épaisseur équivalente de 1,7 nm de cuivre a réagi et a été capturée par la formation du film de surface dans ces conditions de polarisation anodique. Lors du balayage inverse, aucun pic cathodique n'est observé comme en l'absence de MBI et le transfert de charge indique que l'équivalent de 1,55 nm de cuivre a réagi. Les épaisseurs calculées correspondent à plusieurs monocouches de cuivre et suggèrent que la couche organique formée en surface est constituée de produits de réaction Cu(I)-MBI, éventuellement des complexes organométalliques, et tridimensionnels en épaisseur.

Dans le cas du prétraitement réalisé en l'absence de MBI, le CV obtenu après ajout de MBI est plat montrant une inhibition très efficace de la dissolution anodique du cuivre ainsi que de l'activité cathodique. Dans ce cas, le MBI s'adsorbe sur la surface du cuivre à l'état métallique obtenu après réduction de l'oxyde natif. Le CV obtenu montre que ces conditions de pré-adsorption optimisent l'efficacité inhibitrice de la couche moléculaire adsorbée en raison de la formation d'une barrière moléculaire bloquant plus efficacement le transport atomique à travers l'interface. Le CV montre également, dans le domaine Cu(I), l'absence de pic indicatif de la formation anodique d'une couche 3D constituée de produits de réaction Cu(I)-MBT. La densité de courant positive totale mesurée montre que, pour cette condition de prétraitement, seule une fraction infime de monocouche de cuivre a réagi (épaisseur équivalente de 0,03 nm). Il est probable que la couche de MBI préformée dans ces conditions est une couche organique de haute pureté contenant très peu voire pas de cuivre piégé et lui conférant des propriétés barrière optimisées.

Les résultats obtenus avec MBT ont montré que, dans les mêmes conditions de prétraitement, les grains de surface sont très efficacement protégés et que l'activité électrochimique résiduelle ne provient que des sites préférentiels de réaction. Avec MBI, les résultats montrent que la couche moléculaire préformée ne fait qu'atténuer l'oxydation anodique globale de la surface, conduisant à un comportement de type passivation avec formation d'une couche de surface 3D probablement constituée de produits de réaction Cu(I)-MBI. Cette couche superficielle se forme à la surface des grains et protège le cuivre de la dissolution anodique comme le montre la réponse électrochimique macroscopique. Cette couche se forme également dans les sites intergranulaires de surface comme le montre l'analyse locale des variations topographiques mesurées lors du cyclage électrochimique.

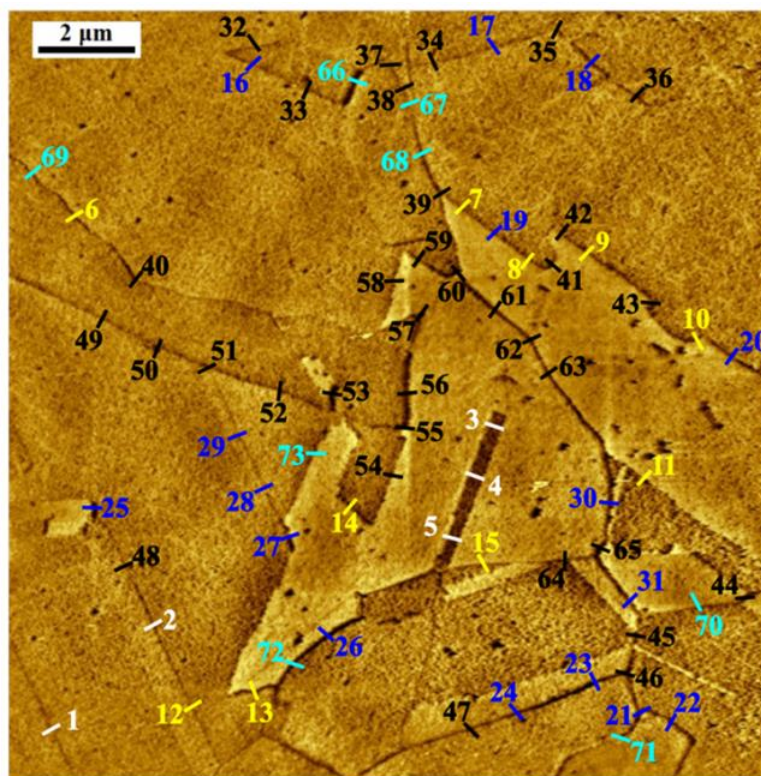


Figure 4 Identification locale du comportement en corrosion intergranulaire des joints de grains du cuivre microcristallin dans HCl(aq) 10 mM + MBI 1 mM. Les sites indexés correspondent aux joints de grains émergents en surface et dont la profondeur a été mesurée avant et après application de cycles électrochimiques permettant d'initier la corrosion.

La figure 4 montre la microstructure observée par ECSTM en présence de MBI dans l'électrolyte, avant et après application de 2 et 4 cycles pour initier la corrosion du cuivre dans le domaine anodique Cu(I). Les voltammogrammes sont identiques à ceux réalisés pour l'étude par voltamétrie cyclique et permettent la comparaison directe des données avec celles obtenues en présence de MBT. Les joints de grains sont classifiés en fonction de leur morphologie en surface et selon les mêmes critères que ceux appliqués pour l'étude avec MBT. La série d'images obtenues in situ a permis de localiser 74 sites où la variation de la profondeur du site intergranulaire en surface a pu être analysée géométriquement avant et après cyclage anodique. Ces 74 sites sont indexés sur la figure 4. Comme lors de l'étude avec MBT, 5 types de comportement intergranulaire local, marqués par un code de couleur, ont pu être identifiés : i) profondeur inchangée du site intergranulaire (sites indexés en blanc sur la figure 4), ii) augmentation répétée de la profondeur du site intergranulaire (sites indexés en jaune sur la figure 4), iii) diminution répétée de la profondeur du site intergranulaire (sites indexés en bleu sur la figure 4), iv) diminution suivie d'une augmentation de la profondeur du site intergranulaire (sites indexés en noir sur la figure 4), et v) augmentation suivie d'une diminution de la profondeur du site intergranulaire (sites indexés en cyan sur la figure 4).

Dans le cas d'une profondeur inchangée du site intergranulaire, la couche superficielle constituée de produits de réaction Cu(I)-MBI se forme indifféremment au joint de grains et sur les grains adjacents. Tous les sites pour lesquels ce comportement est observé correspondent à des joints de macles. Ainsi, le comportement intergranulaire observé est compatible avec le caractère intrinsèquement résistant des joints de macles à la corrosion intergranulaire. Les joints de macles réagissent comme les grains adjacents dans le domaine anodique Cu(I) et la couche organométallique formée localement est indifférenciée par rapport à celle formée sur les grains.

Dans le cas d'une augmentation nette et répétée de la profondeur du site, il y a consommation préférentielle du matériau par dissolution irréversible et plus rapide au joint de grain que sur les grains adjacents. Cette dissolution préférentielle est due à la protection imparfaite apportée localement par la couche de produits de réaction Cu(I)-MBI qui atténue moins fortement la réactivité locale, plus grande au joint de grain que sur les grains adjacents.

Dans le cas d'une diminution nette et répétée de la profondeur du site intergranulaire, il y a accumulation locale plus marquée de produits de réaction dans le joint de grains que sur les grains adjacents en raison de la réactivité localement plus élevée du joint de grain. Dans ce cas, les joints de grains sont protégés par les produits de corrosion localement formés. En présence de MBI, la réponse électrochimique obtenue par voltamétrie est indicative d'un comportement de type passivation non observé dans HCl(aq) uniquement. Ainsi, plus de cuivre réagirait dans le site intergranulaire lors de la polarisation anodique conduisant à la formation d'une couche localement plus épaisse de produits de réaction Cu(I)-MBI que sur les grains adjacents. Le processus serait répété à chaque cycle de traitement conduisant ainsi à l'augmentation plus marquée d'épaisseur du film formé dans le site intergranulaire et donc à sa diminution de profondeur par rapport aux grains adjacents.

Dans le cas d'une diminution de la profondeur du site intergranulaire après 2 CVs puis d'une augmentation après 4 CVs, il y a protection transitoire du joint de grains par les produits de corrosion formés puis dissolution localement préférentielle du matériau. Ce comportement suggère que la couche plus épaisse de produits de réaction formés localement dans le site intergranulaire fournit d'abord une protection locale contre la dissolution anodique comme observée sur les grains par voltamétrie. Cependant, cette protection initiale apportée par la couche de surface n'est pas stable et altérée lors des cycles ultérieurs comme le montre l'augmentation de la profondeur du site intergranulaire.

Enfin, dans le cas d'une augmentation de la profondeur du site intergranulaire après 2 CVs puis d'une diminution après 4 CVs, il y a dissolution nette, moins atténuée au joint de grains par la couche superficielle de produits de réaction que sur les grains adjacents, puis accumulation préférentielle des produits de réaction Cu(I)-MBI dans la région intergranulaire. La profondeur du joint de grains diminue du fait de la formation d'une couche superficielle plus épaisse que sur les grains adjacents.

Les joints de macles ne montrent aucune réactivité intergranulaire préférentielle par rapport aux grains adjacents dans la plupart des sites analysés, et ceci indépendamment de la présence de MBI ou MBT dans la solution et en accord avec la résistance intrinsèque de ce type de joint de grains à la corrosion intergranulaire. En présence de MBI, ces joints de grains réagissent de façon identique aux grains adjacents pour former une couche de produits de réaction Cu(I)-MBI a priori uniforme.

Tous les autres types de joints de grains ont montré une réactivité préférentielle. Pour les joints de grains aléatoires, qui sont intrinsèquement les plus réactifs, la protection locale engendrée par accumulation de produits de réaction Cu(I)-MBI a été observée de façon largement prédominante. Avec MBI, comme avec MBT, la majeure partie des sites intergranulaires mesurés de type joint de grains aléatoire n'a pas montré de protection stable après une polarisation anodique répétée dans le domaine de dissolution du cuivre, montrant la fragilité de la protection apportée par les produits de réaction accumulés dans les régions intergranulaires.

Pour les joints de type CSL d'indice Σ élevé, la protection du site intergranulaire par une couche plus épaisse de produits de réaction Cu(I)-MBI est également observée. Toutefois la dissolution locale du matériau y est plus fréquemment observée sans accumulation de produits de réaction, ce qui suggère

une plus faible réactivité des joints de grains type CSL d'indice Σ élevé par rapport à la plupart des joints de grains aléatoires.

Pour les joints de type CSL de faible indice Σ , la protection par une couche plus épaisse de produits de réaction Cu(I)-MBI est plus fréquemment observée que la dissolution atténuée par la couche MBI. Cela suggère que certains joints de type CSL pourraient être initialement aussi réactifs que les joints aléatoires pour former des produits de corrosion Cu(I)-MBI. Une plus grande fraction des joints CSL de bas indice Σ que des joints aléatoires formeraient une couche protectrice de produits de corrosion stable dans les conditions de test étudiées.

Effets du 2-mercaptobenzothiazole et du 2-mercaptobenzimidazole sur la passivation locale aux joints de grains du cuivre

Dans cette partie, les effets du 2-mercaptobenzothiazole et du 2-mercaptobenzimidazole sur la réactivité locale du cuivre à l'émergence des joints de grains en surface ont été étudiés en milieu alcalin NaOH (aq) 0,1 M. Dans ce milieu, le cuivre est protégé contre la corrosion par la formation d'une couche passive constituée d'oxyde Cu_2O dans le domaine de formation des ions cuivreux Cu(I) et d'oxyde Cu_2O en partie interne et $\text{CuO}/\text{Cu}(\text{OH})_2$ en partie externe dans le domaine de formation des ions cuivriques Cu(II). Les effets de MBT et MBI sur la passivation dans le domaine Cu(I) ont été étudiés dans cette thèse.

La figure 5 montre les voltammogrammes obtenus en l'absence et en présence des inhibiteurs dans l'électrolyte. En l'absence d'inhibiteur, le voltammogramme est typique de la passivation de la surface par la formation d'une couche d'oxyde Cu(I), caractérisée par un pic de courant anodique A_1 , et de la réduction de cette couche passive, caractérisée par un pic de courant cathodique C_1 . A partir de la densité de transfert de charge cathodique mesurée, nous pouvons déterminer l'épaisseur équivalente de la couche passive formée dans ces conditions, soit 2,68 nm d'oxyde Cu_2O . La différence entre densité de transfert de charge anodique et densité de transfert de charge cathodique permet d'estimer l'épaisseur équivalente de cuivre consommé de façon irréversible par dissolution lors du processus de passivation, soit 0,14 nm correspondant à 0,67 monocouche.

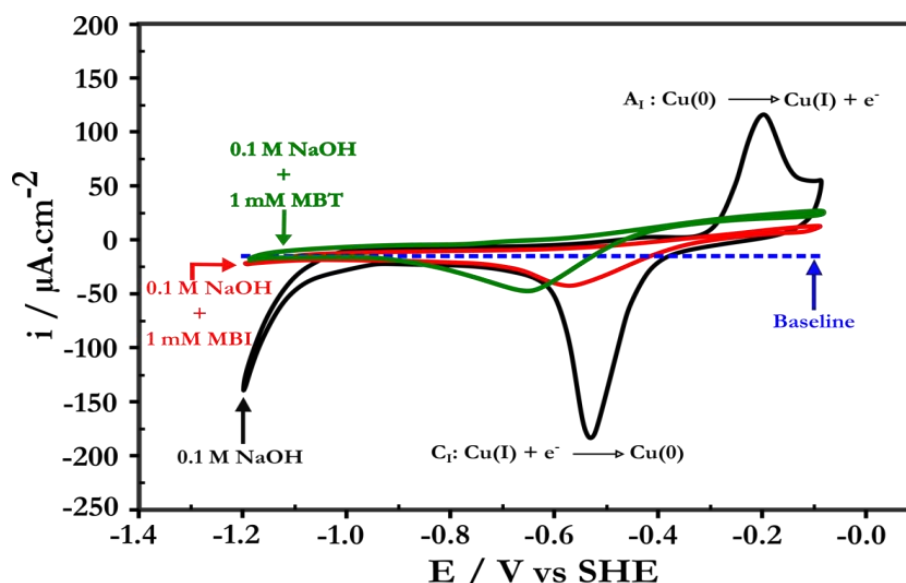


Figure 5 Voltammogrammes obtenus dans la cellule ECSTM et caractérisant les effets des inhibiteurs MBT et MBI sur la passivation du cuivre en milieu NaOH (aq).

En présence des inhibiteurs MBT ou MBI dans l'électrolyte, les voltammogrammes ne présentent pas le pic A_1 caractéristique de la passivation. Le pic C_1 caractéristique de la réduction d'un film passif d'oxyde Cu(I) est également absent. Cela implique que la couche organique de MBT ou MBI, formée en surface préalablement au test de passivation, bloque la formation d'oxyde en surface empêchant ainsi le cuivre de se passiver. L'activité résiduelle mesurée pendant les balayages anodique et cathodique en présence des inhibiteurs est attribuée à l'oxydation et à la réduction des atomes de cuivre présents dans la couche organique préformée en surface. En effet, le prétraitement cathodique de l'oxyde natif est réalisé en présence des inhibiteurs et il est très probable que les atomes de Cu provenant de la dissociation de l'oxyde par réduction électrochimique et libres de se lier sur la surface, réagissent avec les molécules organiques pré-adsorbées et soient ainsi capturés dans la couche moléculaire. Ainsi, on peut s'attendre à ce que le film organique, préformé en surface avant le test de passivation, contienne une majeure partie des atomes de cuivre provenant de l'oxyde natif.

En présence de MBT, on obtient, à partir de la densité de transfert de charge cathodique mesurée, une épaisseur équivalente de 1,28 nm (ou 6,17 monocouches) de cuivre piégé dans le film organique et qui réagirait donc de manière réversible lors du cycle oxydo-réduction réalisé dans le domaine de formation des ions cuivreux Cu(I). A partir de la différence entre densités de transfert de charge anodique et cathodique, nous obtenons une épaisseur équivalente de 0,045 nm de cuivre, soit une fraction de monocouche (0,22 monocouche), qui serait consommée de manière irréversible par dissolution résiduelle lors de ce même cycle d'oxydo-réduction. Cette valeur, très faible, est cohérente avec une inhibition macroscopique sur l'ensemble de la surface de la dissolution irréversible du cuivre lors du cyclage électrochimique dans le domaine de formation des ions Cu(I). La dissolution résiduelle mesurée serait localisée dans les sites de surface les plus actifs tels que les sites d'émergence des joints de grains.

En présence de MBI, nous obtenons une épaisseur équivalente de 0,62 nm (ou 2,98 monocouches) de cuivre piégé dans la couche organique préformée et qui réagirait donc de manière réversible lors du cycle d'oxydo-réduction. La couche organique de MBI préformée après réduction de l'oxyde natif contiendrait ainsi environ deux fois moins d'atomes de cuivre que la couche de MBT. La différence entre les densités de charge anodique et cathodique est trop faible pour être significative compte tenu de l'incertitude, ce qui suggère que la couche de MBI préformée dans ces conditions atténuerait plus efficacement que la couche de MBT la dissolution irréversible du cuivre dans les sites de surface les plus réactifs.

Ces données électrochimiques macroscopiques montrent que les couches organiques, préformées avant le test de passivation, se comportent de manière similaire et bloquent la formation d'un film d'oxyde Cu (I) en surface et ainsi la passivation du cuivre. La réactivité résiduelle observée est attribuée pour l'essentiel aux atomes de cuivre dissociés de l'oxyde natif lors du prétraitement cathodique et piégés dans la couche organique superficielle préformée. Le blocage de la passivation peut paraître préjudiciable à la protection contre la corrosion du matériau. Toutefois cet effet négatif des inhibiteurs sur la passivation semble efficacement contrebalancé par la formation de couches organiques qui atténuent fortement la dissolution du cuivre lors de la polarisation anodique dans le domaine de formation des ions cuivreux Cu(I).

La figure 6 montre les microstructures locales étudiées par ECSTM en présence de MBT (figure 6 (a)) ou de MBI (figure 6 (b)) dans l'électrolyte NaOH(aq). Les images ont été enregistrées après réduction de l'oxyde natif : i) dans le domaine de polarisation correspondant au cuivre à l'état métallique Cu(o), ii) dans le domaine de polarisation correspondant à l'état oxydé Cu(I), et iii) après retour à l'état métallique Cu(o). Le même critère de classification des joints de grains selon leur morphologie dans le plan de surface que pour l'étude en milieu HCl(aq) a été adopté. L'analyse topographique des sites intergranulaires de surface a également été réalisée selon les mêmes critères afin de caractériser les variations locales induites par la polarisation électrochimique.

L'analyse des images a permis de localiser 101 sites intergranulaires de surface pour l'étude avec MBT et 100 sites pour l'étude avec MBI dans lesquels les variations de profondeur locale induites par la polarisation dans le domaine anodique Cu(I) et le retour dans le domaine métallique Cu(o) ont pu être mesurées géométriquement. Ces sites sont indexés sur les images présentées figure 6 avec un code de couleur associé au comportement mesuré localement. En présence de MBT comme en présence de MBI, le comportement observé localement se distingue par cinq types de variations topographiques locales : i) profondeur inchangée du site intergranulaire (sites indexés en blanc), ii) augmentation répétée (sites indexés en jaune), iii) diminution répétée (sites indexés en bleu), iv) diminution suivie d'une augmentation (sites indexés en noir), et v) augmentation suivie d'une diminution (sites indexés en cyan). Ces cinq types de variations sont similaires à ceux observés en milieu acide HCl(aq) mais leur interprétation mécanistique diffère car en milieu alcalin NaOH(aq) elle doit prendre en compte l'effet des inhibiteurs sur la passivation de la surface.

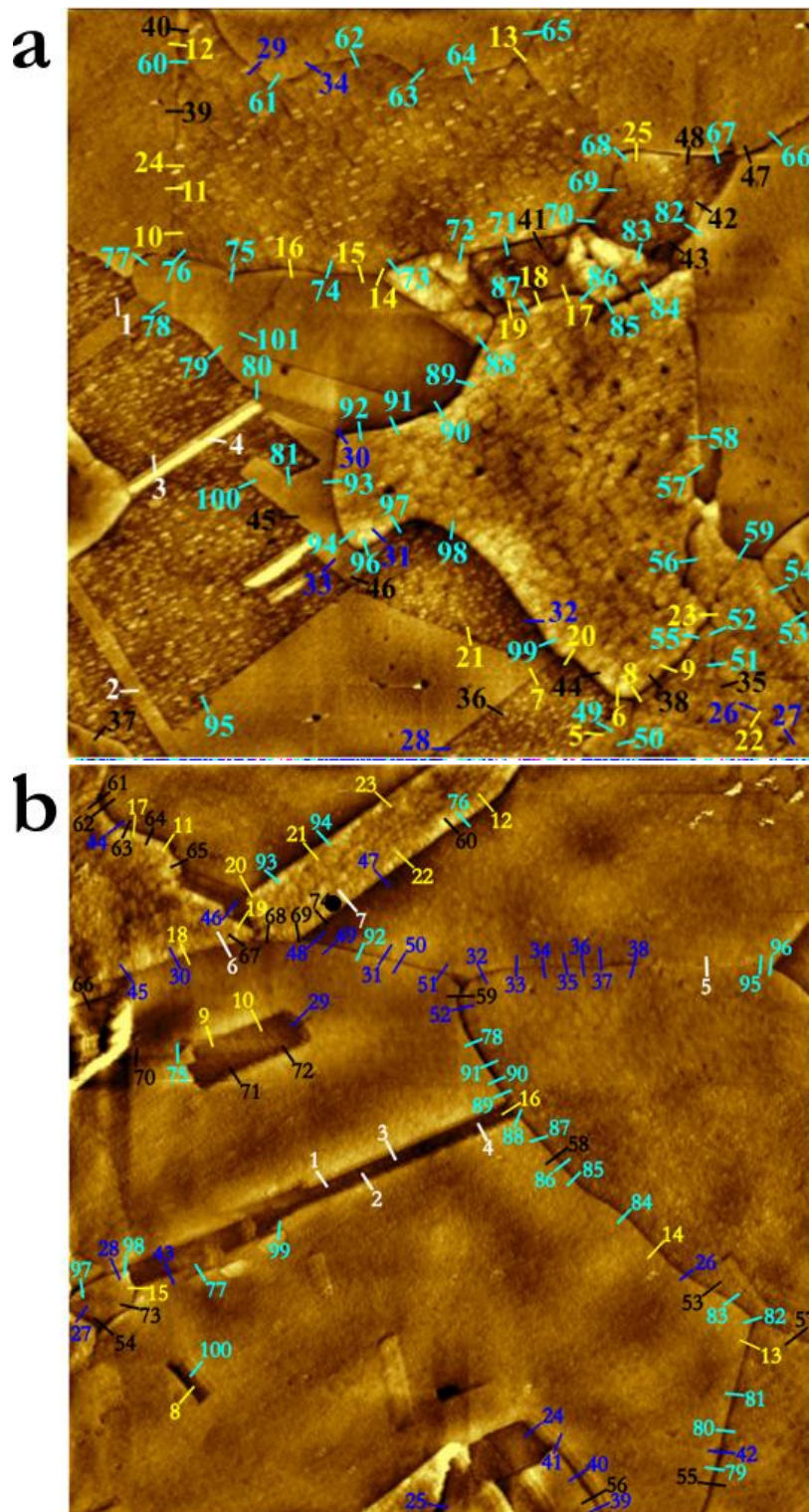


Figure 6 Identification locale du comportement en passivation des joints de grains du cuivre microcristallin en milieu alcalin en présence d'inhibiteur de corrosion : (a) dans NaOH(aq) 0,1 M + MBT 1 mM, (b) dans NaOH(aq) 0,1 M + MBI 1 mM. Les sites indexés correspondent aux joints de grains émergeants en surface et dont la profondeur a été mesurée avant et après application de la polarisation anodique dans le domaine de formation des ions cuivreux Cu(I).

Dans le cas d'une profondeur inchangée du site intergranulaire, la passivation est bloquée à l'émergence en surface du joint de grains comme sur les joints adjacents et la réactivité résiduelle y est identique. Ce comportement est observé aux joints de macles. L'absence de réactivité préférentielle locale pour ce type de joints de grains est interprétée comme une propriété intrinsèque des joints de macles. La couche

organique préformée par l'inhibiteur aux joints de macles ne se différencie pas de celle préformée sur les grains dans les conditions testées du fait de l'absence de réactivité préférentielle des joints de macles.

Le cas d'une augmentation répétée de la profondeur du site intergranulaire traduit une réactivité préférentielle à l'émergence en surface du joint de grains par rapport aux grains adjacents. Les données de voltamétrie cyclique ont montré qu'il existe deux processus de réaction concurrents lors du traitement d'oxydo-réduction appliqué : l'oxydation réversible des atomes de Cu piégés dans la couche organique préformée et la dissolution irréversible du cuivre dans les sites les plus réactifs de la surface. L'augmentation répétée de la profondeur observée correspond donc aux sites intergranulaires de surface où la passivation est localement bloquée par la couche organique, comme sur les grains, mais où cette couche organique ne bloque pas complètement la dissolution résiduelle, préférentielle aux joints de grains et conduisant à l'augmentation de la profondeur du site intergranulaire.

Le cas d'une diminution répétée de la profondeur du site intergranulaire est interprété par une passivation partiellement ou imparfaitement bloquée aux joints de grains par la couche organique préformée et conduisant à l'accumulation locale de produits de réaction lors de la polarisation anodique. La diminution de la profondeur du site intergranulaire étant persistante après réduction de la surface, l'accumulation de produits de réaction est irréversible. Aux joints de grains, le cuivre est préférentiellement consommé lors de la polarisation anodique par rapport aux grains adjacents pour former des produits qui s'accumulent dans la région intergranulaire conduisant à la diminution de la profondeur mesurée. La diminution de la profondeur aux joints de grains peut résulter de la passivation locale du site intergranulaire pour former des oxydes de Cu(I), la passivation n'y étant pas complètement bloquée par la couche organique préformée. L'accumulation locale de produits de corrosion ne peut être exclue. Ces produits de corrosion peuvent se former par réaction du cuivre dissous localement avec les molécules organiques présentes dans l'électrolyte. La nature et la composition des produits de réactions accumulés aux joints de grains n'ont pas pu être identifiées dans ce travail.

Le cas d'une diminution suivie d'une augmentation de la profondeur du site intergranulaire correspond également aux joints de grains où la passivation est partiellement ou imparfaitement bloquée par la couche organique préformée conduisant à l'accumulation locale de produit de réaction lors de la polarisation anodique, du fait de la consommation préférentielle de cuivre dans le site intergranulaire. Cependant, contrairement au cas précédent, cette accumulation de produits de réaction est réversible. Dans ce cas, le balayage cathodique ultérieur à la polarisation anodique serait insuffisamment réducteur pour décomposer les produits de réactions formés, plus probablement des oxydes de Cu(I) formés et accumulés localement dans le site intergranulaire. La dissolution résiduelle du cuivre dans le site intergranulaire ne peut être exclue pour expliquer l'augmentation de profondeur.

Enfin, le cas d'une augmentation suivie d'une diminution de la profondeur du site intergranulaire correspond, comme dans le deuxième cas, aux joints de grains où la passivation est bloquée par la couche organique préformée et où il subsiste une dissolution résiduelle conduisant à la consommation irréversible de cuivre dans la région intergranulaire lors de la polarisation anodique. Cependant, pour les joints de grains présentant ce comportement, le maintien transitoire de la polarisation dans la région anodique de formations des ions cuivreux Cu(I) avant d'entrer dans la région cathodique lors du balayage retour en potentiel conduirait à l'accumulation des produits de corrosion formés par les ions cuivreux dans le site intergranulaire et ainsi à la diminution de la profondeur mesurée.

Les joints de macle sont le seul type de joint de grains pour lequel nous avons observé un comportement caractérisé par le blocage de la passivation par la couche organique préformée au joint de grains comme sur les grains adjacents avec absence d'activité intergranulaire résiduelle. En présence de MBT comme

en présence de MBI, ce comportement a été observé pour la majorité des joints de macles analysés, que nous attribuons à des joints de macles cohérents, c'est-à-dire proches de la géométrie idéale et donc intrinsèquement résistants à la corrosion intergranulaire. Pour une minorité des joints de macles analysés, tous les autres types de comportement intergranulaire ont été observés avec une distribution assez uniforme de leurs occurrences. Ces joints de macles plus réactifs seraient des joints de macles incohérents, c'est-à-dire déviés de leur géométrie idéale.

Pour tous les autres types de joints de grains, les comportements intergranulaires observés en présence de MBT et de MBI se répartissent en deux classes en fonction de l'effet bloquant de l'inhibiteur sur la passivation. Si la passivation intergranulaire est bloquée, la réactivité résiduelle est associée à une dissolution avec accumulation possible de produits de corrosion. Si la passivation intergranulaire n'est que partiellement bloquée, la réactivité résiduelle est associée à l'accumulation réversible ou irréversible de produits de réaction qui protègent le site intergranulaire contre la dissolution et donc passivants.

Pour les joints de grains de type aléatoire, plus réactifs, nous observons un effet de blocage sur la passivation intergranulaire plus fort avec la couche de MBT préformée qu'avec celle de MBI. Avec MBI, l'accumulation, réversible ou irréversible, de produits de passivation résiduelle observée sur la plupart des joints de grains aléatoires, est en accord avec les études précédentes qui montrent, qu'en raison de la réactivité plus élevée de ces joints de grains, un film d'oxyde Cu(I) localement plus épais se forme en l'absence d'inhibiteur. Avec MBT, la passivation intergranulaire est fortement empoisonnée et l'accumulation de produits de passivation résiduelle est observée moins fréquemment dans la distribution analysée.

Pour les joints de grains de type CSL de haut indice Σ , nous observons que la couche de MBT préformée empoisonne plus fortement la passivation que celle de MBI, confirmant ainsi pour ces joints de grains également plus réactifs la tendance observée pour les joints de grains aléatoires. Pour les joints de grains de type CSL de bas indice Σ , la distribution qui a pu être analysée dans le champ de vision local du microscope est plus petite. Cependant nous observons que la répartition entre blocage complet ou partiel de la passivation est beaucoup plus équilibrée pour les deux inhibiteurs. Pour ce type de joints de grains, qui peuvent être moins réactifs de par leur caractère cristallographique la réactivité résiduelle serait trop faible pour différencier l'effet bloquant des couches organiques de MBT et MBI préformées sur le comportement en passivation du joint de grains.

L'effet bloquant plus fort de MBT que de MBI sur la passivation des sites intergranulaires résulte probablement des propriétés de barrière de la couche organique préformée. D'après l'analyse des données voltamétriques, plus d'atomes de Cu seraient piégés dans la couche de MBT préformée après décomposition de l'oxyde natif en présence de l'inhibiteur adsorbé que dans celle de MBI. Cette augmentation de la quantité d'atomes de Cu piégés pourrait résulter en une épaisseur et/ou une densification plus grande de la couche préformée de MBT que de celle de MBI, ce qui améliorerait les propriétés de barrière bloquant la passivation de surface, en particulier dans les sites plus réactifs que sont les joints de grains.

RÉSUMÉ

Les effets locaux de deux inhibiteurs organiques de corrosion, le 2-mercaptobenzothiazole (MBT) et le 2-mercaptobenzimidazole (MBI), sur la dissolution et la passivation à l'émergence en surface de différents types de joints de grains (JdG) ont été étudiés sur le cuivre microcristallin par voltamétrie cyclique (CV) et, in situ, à l'échelle nanométrique, par microscopie à effet tunnel électrochimique (ECSTM). En solution acide HCl(aq), MBT protège efficacement la surface des grains en bloquant la dissolution active des ions Cu(I). La couche de MBT préformée protège parfaitement les JdG CSL de bas Σ alors que les JdG aléatoires, plus réactifs, peuvent être protégés par l'accumulation de produits de réaction dans le site intergranulaire. Avec MBI, l'inhibition est moins efficace qu'avec MBT avec plus de produits de réaction Cu(I) générés sur les grains pour former un film de surface protecteur et une accumulation préférentielle locale se produisant plus fréquemment parmi les sites intergranulaires analysés. En solution alcaline NaOH(aq), les couches superficielles organiques, préformées après dissociation de l'oxyde natif en présence d'inhibiteur, bloquent la formation d'oxyde cuivreux Cu(I). L'analyse ECSTM locale révèle une réactivité intergranulaire résiduelle, sauf aux joints de macles cohérents. Aux JdG CSL et aléatoires, la formation d'oxyde Cu(I) est soit bloquée avec dissolution résiduelle et accumulation de produits de corrosion, soit incomplètement bloquée avec passivation résiduelle, en fonction de l'effet barrière de la couche organique préformée. Pour les JdG CSL de Σ élevé et les JdG aléatoires, plus réactifs, la couche organique préformée de MBT a un effet barrière plus marqué sur la formation d'oxyde Cu(I) que celle de MBI. La molécule MBT, pouvant se lier fortement à plus d'atomes de Cu que celle de MBI en raison de deux atomes de S au lieu d'un seul dans sa structure hétérocyclique, piègerait plus efficacement les atomes de Cu relâchés par la surface, offrant ainsi des propriétés de barrière améliorées à la couche organique MBT préformée, y compris dans les sites de surface les plus réactifs tels que les JdG. Ces résultats permettent de mieux comprendre les mécanismes locaux de protection conférés aux sites intergranulaires de surface par la préformation de couches moléculaires organiques d'inhibiteurs de corrosion.

MOTS CLÉS

Corrosion intergranulaire, inhibition de la corrosion, 2-mercaptobenzothiazole (MBT), 2-mercaptobenzimidazole (MBI), cuivre, STM, échelle nanométrique, in situ, film passif, joints de grains.

ABSTRACT

The local effects of two organic corrosion inhibitors, 2-mercaptobenzothiazole (MBT) and 2-mercaptobenzimidazole (MBI), on dissolution and passivation at the surface termination of different types of grain boundaries (GBs) were investigated on microcrystalline copper by cyclic voltammetry (CV) and in situ, at nanometric scale, by electrochemical scanning tunneling microscopy (ECSTM). In acid HCl(aq) solution, macroscopic CV analysis showed efficient corrosion inhibition by MBT that protects the grains by blocking Cu(I) active dissolution. Local ECSTM analysis showed that the pre-formed MBT layer perfectly protects the low Σ CSL GBs while the more reactive random GBs are protected by local accumulation of reaction products. MBI inhibition was less efficient than MBT inhibition with Cu(I) reaction products generated on the grains to form a protective surface film and their preferential local accumulation occurring more frequently in the analyzed population of GB sites. In alkaline NaOH(aq) solution, the organic surface layers, pre-formed after reductive dissociation of the native oxide in the presence of the inhibitors, block the formation of a Cu(I) surface oxide. Local ECSTM analysis revealed residual intergranular reactivity except for coherent twins. On CSL and random GBs, Cu(I) surface oxide formation was either blocked with residual dissolution and accumulation of corrosion products, or incompletely blocked with residual passivation, depending on the barrier effect of the pre-formed organic layer. For the more reactive high Σ CSL and random GBs, the pre-formed MBT surface layer showed a stronger barrier effect on surface oxide formation than the pre-formed MBI surface layer. MBT, being able to strongly bond to more Cu atoms than MBI due to two S atoms instead of one in its heterocyclic structure, would more efficiently trap Cu atoms released from the surface, thus providing improved barrier properties to the pre-formed MBT surface layer, including in the most reactive surface sites present in GBs. These results bring new insight into how surface reactivity is altered by a pre-formed surface layer of organic molecules and on local mitigation of corrosion at various types of GBs.

KEYWORDS

Intergranular corrosion, corrosion inhibition, 2-mercaptobenzothiazole (MBT), 2-mercaptobenzimidazole (MBI), copper, STM, nanometer scale, in situ, passive film, grain boundary.